Surface and interface properties of glass-ceramic garnet-type solid electrolytes for the application in solid-state batteries

Dissertation zur Erlangung des Grades

„**Doktor der Naturwissenschaften**“

– Dr. rer. nat. –

Vorgelegt dem

Fachbereich Biologie und Chemie

der

Justus-Liebig-Universität Gießen

von

Nina Hoinkis

Mainz, 2023

Die vorliegende Arbeit wurde im Zeitraum von Oktober 2019 bis September 2022 am Physikalisch-Chemischen Institut der Justus-Liebig-Universität Gießen in Kooperation mit der SCHOTT AG in Mainz unter Betreuung von Prof. Dr. Jürgen Janek angefertigt.

Einreichungsdatum/Submission date:	15. Juni 2023
Disputation/Disputation:	11. September 2023
Dekan/Dean:	Prof. Dr. Thomas Wilke
1. Gutachter/1st reviewer:	Prof. Dr. Jürgen Janek
2. Gutachter/2nd reviewer:	Prof. Dr. Maren Lepple

Eidestattliche Erklärung

Ich erkläre: Ich habe die vorgelegte Dissertation selbstständig und ohne unerlaubte fremde Hilfe und nur mit den Hilfen angefertigt, die ich in der Dissertation angegeben habe. Alle Textstellen, die wörtlich oder sinngemäß aus veröffentlichten Schriften entnommen sind, und alle Angaben, die auf mündlichen Auskünften beruhen, sind als solche kenntlich gemacht. Ich stimme einer evtl. Überprüfung meiner Dissertation durch eine Antiplagiat-Software zu. Bei den von mir durchgeführten und in der Dissertation erwähnten Untersuchungen habe ich die Grundsätze guter wissenschaftlicher Praxis, wie sie in der „Satzung der Justus-Liebig-Universität Gießen zur Sicherung guter wissenschaftlicher Praxis“ niedergelegt sind, eingehalten.

Mainz, 15. Juni 2023

Ort, Datum Nina Hoinkis

Abstract

Next-generation secondary batteries with enhanced energy and power density gain in importance, especially due to the growing demand for electric vehicles. Solid-state batteries (SSBs) are considered as one of the most promising alternatives to state-of-the-art lithium ion batteries. Conventional liquid electrolytes, that are volatile and flammable, are replaced by solid electrolytes (SEs). In addition to improved cell safety due to the high thermal stability of SEs, they promise to enable the application of the lithium metal anode (LMA). The LMA provides a very high theoretical capacity, offering significantly improved gravimetric and volumetric energy density.

SEs comprise polymers, oxides, sulfides, halides, phosphates or composites thereof. In the class of oxides, the garnet-type $Li_7La_3Zr_2O_{12}$ (LLZO) has attracted significant interest. In addition to its high room-temperature ionic conductivity, it is one of the few candidate materials that is stable in contact with lithium metal. However, several obstacles still hinder the practical application of LLZO, such as its instability in ambient air. Most importantly, despite the high mechanical stability of LLZO, lithium dendrite propagation in interconnected pores, grain boundaries and even single crystals, which leads to internal short circuits, is a severe issue.

The focus of this thesis is on the application of the novel class of glass-ceramic LLZO and its surface and interface properties. It is produced at the SCHOTT AG in a specific and industrially scalable melting route. Firstly, the surface properties of the powder and the related degradation mechanism in ambient air were studied by kinetic analysis. Both hydration and carbonation were found to follow the core shrinking model with the hydration being an essential intermediate step. A linear dependence on the specific surface area of the powders was observed. Secondly, the effect of the amorphous phase intrinsically contained in glass-ceramic LLZO on the sintering and the interface to the LMA was investigated. Besides its potential to reduce sintering temperature and time due to liquid phase sintering, it was found to segregate into the grain boundaries and pores, mechanically and electrochemically preventing the growth and propagation of lithium metal dendrites. Thirdly, another strategy to overcome the obstacles of LLZO is the integration of LLZO particles into a polymer solid electrolyte (PSE). However, the effect of the garnet/PSE interface on the lithium ion transport in such hybrid electrolytes remains unclear. Hence, the influence of the phase compatibility between LLZO and a polyethylene oxide (PEO)-based PSE on the interface resistance was investigated, finding no positive correlation. The interface resistance is too high to achieve ion transport through LLZO in the HSE, resulting in decreased ionic conductivity compared with the pure PSE.

Overall, the results of this thesis provide profound insights into the application of glass-ceramic LLZO. Besides practical knowledge on its surface properties for the processing of LLZO, this work revealed the outstanding properties of the amorphous phase at the interface with potential LMAs, making it a promising material for future SSBs.

Zusammenfassung

Im Zuge der Energiewende und der damit verbundenen Elektrifizierung des Mobilitätssektors gewinnen Sekundärbatterien der nächsten Generation mit höheren Energie- und Leistungsdichten immer mehr an Bedeutung. Festkörperbatterien (FKB) gelten als eine der vielversprechendesten Alternativen zu herkömmlichen Lithiumionenbatterien, in denen der brennbare und flüchtige Flüssigelektrolyt durch einen Festelektrolyten (FE) ersetzt wird. Durch dessen hohe thermische Stabilität wird nicht nur eine erhöhte Sicherheit der Batteriezelle erreicht, sondern vor allem der Einsatz einer Lithiummetallanode (LMA) ermöglicht. LMAs zeichnen sich durch eine der höchsten theoretischen Kapazitäten aus, die etwa zehnmal so hoch wie die von gängigen Graphitanoden ist.

Als FE-Materialien kommen Polymere, Oxide, Sulfide, Halogenide, Phosphate oder Komposite davon in Frage. In der Klasse der Oxide hat besonders $Li_7La_3Zr_2O_7$ (LLZO) mit Granat-Struktur an Bedeutung gewonnen. Neben der hohen Ionenleitfähigkeit bei Raumtemperatur ist es eines der wenigen Materialien, die im Kontakt mit Lithiummetall stabil sind. Dennoch gibt es einige Herausforderungen, die die praktische Anwendung von LLZO behindern, so wie z. B. dessen Instabilität in Umgebungsluft. Darüber hinaus ist die Bildung von Lithiumdendriten in Poren und Korngrenzen trotz der hohen mechanischen Stabilität des LLZO das nach wie vor größte Problem.

Die vorliegende Dissertation beschäftigt sich mit den Oberflächen- und Grenzflächeneigenschaften der neuen glaskeramischen Variante von LLZO, die bei der SCHOTT AG in einem speziellen Schmelzprozess hergestellt wird. Im ersten Teil wurde die Degradation an der Pulveroberfläche in Umgebungsluft mithilfe von kinetischen Messungen näher untersucht. Sowohl Hydratation und Karbonisierung folgen dem *Core Shrinking* Modell, bei dem die Hydratation ein unabdingbarer Zwischenschritt darstellt. Es wurde eine lineare Abhängigkeit von der spezifischen Oberfläche des Pulvers festgestellt. Im zweiten Teil wurde der Effekt der intrinsisch enthaltenen amorphen Phase auf das Sinterverhalten und die Grenzfläche zur LMA analysiert. Neben der effektiven Reduzierung der Sintertemperatur und -zeit durch Flüssigphasensintern, konnte gezeigt werden, dass die amorphe Phase in den Korngrenzen und Poren die Bildung und Ausbreitung von Lithiumdendriten verhindert. Im dritten Teil wurde die Applikation in Hybridelektrolyten (HE) beleuchtet, wobei der Einfluss der Phasenkompatibilität zwischen LLZO und einer Polyethylenoxid (PEO)-basierten Matrix auf deren Grenzflächenwiderstand im Fokus stand. Letzterer erwies sich jedoch trotz erhöhter Kompatibilität als zu hoch, um einen Ionentransport durch die LLZO Partikel zu ermöglichen. Die Leitfähigkeiten der HE waren gegenüber der reinen PEO-Matrix deutlich verringert.

Insgesamt zeigen die Ergebnisse dieser Dissertation neben von den Oberflächeneigenschaften abgeleiteten praktischen Erkenntnissen für die Handhabung von LLZO, dass glaskeramisches LLZO aufgrund seiner besonderen amorphen Phase besonders an der Grenzfläche zu einer LMA ein vielversprechendes Material für die zukünftige Anwendung in FKBs ist.

Contents

General Remarks

This thesis begins with an introduction to the topic and the definition of scientific goals, followed by the theoretical fundamentals. The results of three different projects are presented and discussed in three subsections with individually numbered figures, tables and schemes as well as individual bibliographies. Each subsection is introduced by a brief summary that puts the subsection into context with the overall scientific goals of the thesis and specifies the contribution of the authors.

The first two of the three subsections have been previously published in peer-reviewed journals. For those, the publication is listed below as well as referenced at the beginning of each subsection. The graphical design, numbering, formatting, etc., of the original publication has been adjusted for the design of the present thesis with the permission of the co-authors and publishers. The supporting information of each subsection is given in the appendix.

For all other graphics that have been adapted or reproduced from other publications, the permission of the publishers has been given as stated in the respective figure caption. All graphics have been created or adapted with Microsoft PowerPoint. Data plots have been generated with OriginPro 2021b. Software for data analysis and fitting are given in the experimental section of each subsection.

Section 3.1: Publication 1: „Particle size-dependent degradation kinetics of garnet-type $Li_7La_3Zr_2O_{12}$ solid electrolyte powders in ambient air"

N. Hoinkis, J. Schuhmacher, S. Leukel, C. Loho, A. Roters, F. H. Richter, J. Janek, *Journal of Physical Chemistry C*, **2023**, DOI: https://doi.org/10.1021/acs.jpcc.3c01027.

Section 3.2: Publication 2: „Amorphous phase induced lithium dendrite suppression in glass-ceramic garnet-type solid electrolyte"

N. Hoinkis, J. Schuhmacher, S. Leukel, C. Loho, A. Roters, F. H. Richter, J. Janek, *ACS Applied Materials & Interfacesl*, **2023**, DOI: https://doi.org/10.1021/acsami.3c01667.

Section 3.3: Manuscript: „The role of ceramic/polymer interfaces in garnet-polymer hybrid electrolytes: Understanding the influence of phase compatibility on electrochemical performance"

N. Hoinkis, J. Schuhmacher, S. Leukel, A. Roters, F. H. Richter, J. Janek, *manuscript*, **2023**.

List of Abbreviations and Symbols

EU	European Union
BEV	Battery electric vehicle
LIB	Lithium-ion battery
SSB	Solid-state battery
SE	Solid electrolyte
LMA	Lithium metal anode
ISE	Inorganic solid electrolyte
PSE	Polymer electrolyte
LLZO	Lithium lanthanum zirconium oxide
HSE	Hybrid electrolyte
PEO	Polyethylene oxide
AAM	Anode active material
CAM	Cathode active material
LiTFSI	Lithium bis(trifluoromethanesulfonyl)imide
W_{grav}	Gravimetric energy density
W_{vol}	Volumetric energy density
NaSICON	Sodium superionic conductor
LATP	Lithium aluminum titantium phosphate
LAGP	Lithium germanium titantium phosphate
LLTO	Lithium lanthanum titanate
LiSICON	Lithium superionic conductor
SPS	Spark plasma sintering
FAST	Field-assisted sintering technology
c-LLZO	cubic LLZO
t-LLZO	tetragonal LLZO
pfu	per formula unit
DFT	Density functional theory
PAN	Polyacrylonitrile
PVDF	Polyvinylidene fluoride

PEC	Polyethylene carbonate
VTF	Vogel-Tammann-Fulcher
R_{int}	Interface resistance
ESW	Electrochemical stability window
MCI	Mixed conducting interphase
SEI	Solid electrolyte interphase
XPS	X-ray photoelectron spectroscopy
$J_{Li\ diffusion}$	Flux of lithium metal diffusion
$J_{Li\ creep}$	Flux of lithium metal creep
$J_{Li+\ migration}$	Flux of lithium ion transport
CCD	Critical current density

Greek letters are integrated into the English alphabet. SI units and physical constants are not listed.

1 Introduction

1.1 Background and Motivation

The human-made climate change is one of the biggest challenges of our times. According to current scenarios, global warming of 1.5 °C and 2 °C will be exceeded during the 21st century if global emissions are not reduced significantly.[1] In line with the UN Paris Agreement on Climate Change, the European Union (EU) adopted the European Green Deal in 2019 that aims to cut emissions by 55 % by 2030 to become climate neutral by 2050. One major goal is the decarbonization of the energy and transport sector, the latter accounting for a quarter of the EU's emissions with tendency to rise.[2] This aims for an energy transition including not only energy production from renewable sources, but also efficient use and storage of energy that can compensate fluctuations in production. Especially decentralized energy storage in the form of rechargeable battery systems will play an important role. Therefore, regarding transport, the need for a transition from combustion engine vehicles towards zero-emission battery electric vehicles (BEV) is particularly high.[3–6]

The state-of-the-art technology for BEVs is the lithium-ion battery (LIB) that is well established due to its high energy density, large cyclability and reliability.[7] However, the demand for longer driving ranges and fast battery charging, i.e, higher energy and power density, is tremendous, which will soon exceed the physicochemical limits of the LIB technology. Especially the limited capacity of the graphite electrode (372 mAh g^{-1}) as well as the safety issue of thermal runaway of cells using the liquid electrolyte are major obstacles to further improve its performance.[8–11]

One promising candidate for next-generation battery systems is the solid-state battery (SSB).[8,12] It is a term for a battery class in which the liquid electrolyte of conventional LIBs is replaced by a solid electrolyte (SE). Besides the improved safety by the inherent thermal stability of SEs compared with flammable organic liquid electrolytes, solid materials are mechanically stable intrinsically having the ability to suppress the growth of lithium dendrites.[13] The latter are detrimental for battery operation because they lead to internal short circuit of the battery cell. Most importantly, SEs enable the use of lithium metal anodes (LMA) provided they are electrochemically stable against them. Due to its superior theroretical capacity (3860 mAh g^{-1}) together with its low density (0.59 g cm^{-3}) and the lowest negative electrochemical potential (–3.04 V *vs*. standard hydrogen electrode) it can boost both the gravimetric and volumetric energy density, as well as cyclability of the battery.[11,14]

SEs range from inorganic, ceramic (or glassy) to organic (often semi-solid) polymer electrolytes that contain conducting lithium salts, or a combination thereof.[15–17] While inorganic solid electrolytes (ISE) offer the benefit of high ionic conductivity and mechanical strength, polymer solid electrolytes (PSE) provide flexibility, processability and enhanced contact with the electrodes reducing the interface resistance.[18,19] In the class of oxides, the garnet-type $Li_7La_3Zr_2O_{12}$ (LLZO) has attracted great interest. In addition to its high ionic conductivity at room-temperature, it is one of the few ISEs that is stable in contact with lithium metal.[20] However, even though research has immensely progressed in terms of ionic conductivity optimization, several challenges related to surface and interface issues still remain for its practical application.

First, its instability in ambient air and the formation of impurities such as lithium carbonate at its surface is detrimental to the electrochemical performance and interface contact with the electrodes.[21] Moreover, forming a sufficently low interfacial resistance with the electrodes is further limited by its inherent brittleness as well as the challenge to achieve a microstructure with high density and low grain boundary resistance.[13] Most importantly, the application of LMAs is still hindered due to the growth of lithium dendrites during cycling at relevant current densities, leading to an internal short circuit.[22,23] The main reason is inhomogeneous lithium deposition at the Li|SE interface, which is accelerated by current focusing at the tip once a lithium protrusion has formed. The uneven deposition is caused by poor interfacial contact because of voids, surface impurities and grain boundaries in polycrystalline material.[24] Strategies to suppress dendrite growth include advanced sintering techniques to reach superior densification, surface cleaning procedures, and introduction of artificial or self-generated interlayers.[25–28] Even though these strategies have improved the cycling stability of LLZO, the issue of dendrite formation still remains.[22] Another promising strategy is the combination with PSEs in a hybrid solid electrolyte (HSE) that can probably enhance the dendrite stability.[29] However, the effect of the arising interface between LLZO and the polymer matrix on the ion transport in such HSEs remains unclear.

Further investigation of both the surface and interface properties for the fruitful application of LLZO are required. Open questions remain regarding the surface properties and the related degradation mechanism. Especially the surface composition of LLZO powders is of high importance, which is rarely considered in the literature. With regard to the interface properties at the LMA, approaches to achieve superior microstructure that are industrially scalable and easy to implement are essential to effectively benefit from the LMA application. In HSE applications, the interface with the adjoining polymer matrix needs further attention, especially in terms of the compatibility of the two phases.

1.2 Scientific goals

At the SCHOTT AG, LLZO is manufactured in a specific synthesis as glass-ceramic material. Contrary to conventional solid-state reaction routes, the educts are processed in a melting route, intrinsically forming an amorphous phase upon cooling besides the highly conductive crystalline phase. The volume fraction and chemistry of the amorphous phase can be adjusted during the process. The melting block is further processed via coarse grinding and fine dry-milling resulting in a Li-ion conductive powder.

The applicability of the novel class of glass-ceramic LLZO in SSBs is subject of this thesis, focusing on current issues of LLZO application regarding both scientific understanding and industrial feasibility. The overall goal of this work is to understand and enhance the surface and interface properties of glass-ceramic LLZO that are relevant for its implementation into SSBs. In addition to the surface properties of pristine LLZO powders, it addresses the interfacial issues in two conceivable application scenarios. The first is a pure ISE manufactured by sintering and the second is a HSE, in which LLZO particles are embedded in a PSE matrix. This results in three subprojects implemented as publications or manuscripts, which are graphically represented in Figure 1.2.1. Their objectives are highlighted in the following section.

A key property for processing of powders is a clean surface without impurities, which is especially important in the case of LLZO due to its environmental instability and the related formation of lithium carbonate. Therefore, the first publication, entitled „*Particle size dependent degradation kinetics of garnet-type $Li_7La_3Zr_2O_{12}$ solid electrolyte powders in ambient air*" addresses the degradation mechanism of LLZO with different particle sizes relevant for battery applications. It aims to provide insights into the kinetics of the mechanism, the dependence of surface area, as well as to give suggestions for handling and manufacturing of LLZO.

The second publication, entitled „*Amorphous phase induced lithium dendrite suppression in glass-ceramic garnet-type solid electrolyte*" deals with the application of glass-ceramic LLZO as sintered ISE, which is a potentially industrially scalable method for the use of a LMA. The main objective is to improve interfacial issues with the LMA by the unique properties of the glass-ceramic and thus, the ability of dendrite suppression in order to reach high current densities. Therefore, the effect of the amorphous phase, which is intrinsically contained in glass-ceramic LLZO, on the sintering behavior and the resulting microstructure is investigated and correlated with the electrochemical performance and dendrite stability of the sintered LLZO.

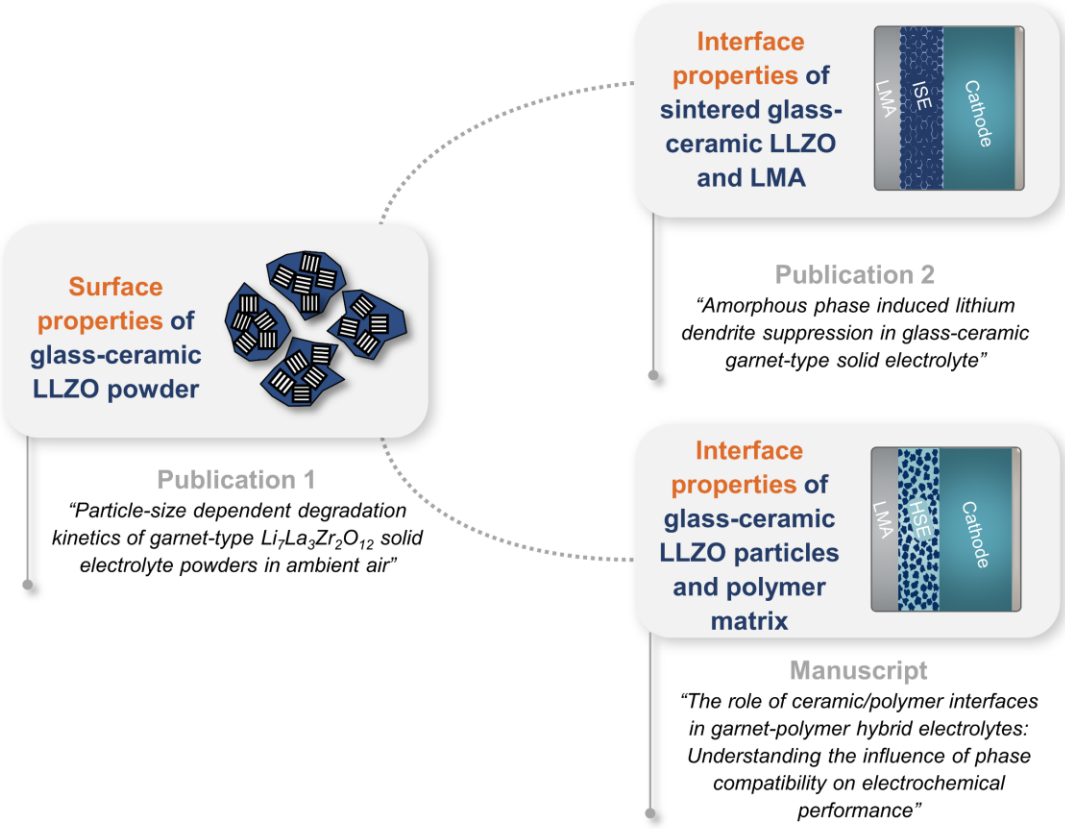

Figure 1.2.1. Graphical representation of the three subprojects implemented as publications and manuscripts being the basis of this thesis.

The application of glass-ceramic LLZO in a HSE is highlighted within the manuscript with the title „*The role of ceramic/polymer interfaces in garnet-polymer hybrid electrolytes: Understanding the influence of phase compatibility on electrochemical performance*". The overall goal of the study is to understand the influence of the compatibility between the LLZO and PSE (based on widely common polyethylene oxide (PEO)) phase on the interface resistance and the electrochemical performance of the HSE. Therefore, the phase compatibility is altered by the use of differing glass-ceramic LLZO variants as well as surface modification. Effects on the interface resistance and the ionic conductivity of the HSEs are investigated.

1.3 References

(1) Shukla, P. R.; Skea, J.; Slade, R.; Al Khourdajie, A.; van Diemen, R.; McCollum, D.; Pathak, M.; Some, S.; Vyas, P.; Fradera, R.; Belkacemi, M.; Hasija, A.; Lisboa, G.; Luz, S.; Malley, J., Eds. *Climate Change 2022: Mitigation of Climate Change. Contribution of Working Group III to the Sixth Assessment Report of the Intergovernmental Panel on Climate Change*:*Summary for Policymakers*; Cambridge University Press. **2022**.

(2) *The European Green Deal*; Communication from the Commission COM(2019) 640 final. **2019**.

(3) *'Fit for 55': Delivering the EU's 2030 Climate Target on the Way to Climate Neutrality*; Communication from the Commission COM(2021) 550 final. **2021**.

(4) Thielmann, A.; Neef, C.; Hettesheimer, T.; Döscher, H.; Wietschel, M.; Tübke, J. *Energiespeicher-Roadmap (Update 2017): Hochenergie-Batterien 2030+ und Perspektiken zukünftiger Batterietechnologien*; Fraunhofer-Institut für System- und Innovationsforschung ISI. **2017**.

(5) La Mata Pérez, M. d. E.; Scholten, D.; Smith Stegen, K. The Multi-Speed Energy Transition in Europe: Opportunities and Challenges for EU Energy Security. *Energy Strategy Reviews* **2019**, *26*, 100415.

(6) Nilsson, M.; Nykvist, B. Governing the Electric Vehicle Transition – Near Term Interventions to Support a Green Energy Economy. *Appl. Energy* **2016**, *179*, 1360–1371.

(7) Tarascon, J. M. The Li-Ion Battery: 25 Years of Exciting and Enriching Experiences. *Electrochem. Soc. Interface* **2016**, *25*, 79–83.

(8) Janek, J.; Zeier, W. G. A Solid Future for Battery Development. *Nat. Energy* **2016**, *1*, 16141.

(9) Goodenough, J. B.; Park, K.-S. The Li-Ion Rechargeable Battery: A Perspective. *J. Am. Chem. Soc.* **2013**, *135*, 1167–1176.

(10) Randau, S.; Weber, D. A.; Kötz, O.; Koerver, R.; Braun, P.; Weber, A.; Ivers-Tiffée, E.; Adermann, T.; Kulisch, J.; Zeier, W. G.*; et al.* Benchmarking the Performance of All-Solid-State Lithium Batteries. *Nat. Energy* **2020**, *5*, 259–270.

(11) Boaretto, N.; Garbayo, I.; Valiyaveettil-SobhanRaj, S.; Quintela, A.; Li, C.; Casas-Cabanas, M.; Aguesse, F. Lithium Solid-State Batteries: State-of-the-art and Challenges for Materials, Interfaces and Processing. *J. Power Sources* **2021**, *502*, 229919.

(12) Albertus, P.; Babinec, S.; Litzelman, S.; Newman, A. Status and Challenges in Enabling the Lithium Metal Electrode for High-Energy and Low-Cost Rechargeable Batteries. *Nat. Energy* **2017**, *3*, 16–21.

(13) Hatzell, K. B.; Chen, X. C.; Cobb, C. L.; Dasgupta, N. P.; Dixit, M. B.; Marbella, L. E.; McDowell, M. T.; Mukherjee, P. P.; Verma, A.; Viswanathan, V.*; et al.* Challenges in Lithium Metal Anodes for Solid-State Batteries. *ACS Energy Lett.* **2020**, *5*, 922–934.

(14) Guo, Y.; Li, H.; Zhai, T. Reviving Lithium-Metal Anodes for Next-Generation High-Energy Batteries. *Adv. Mater.* **2017**, *29*.

(15) Pasta, M.; Armstrong, D.; Brown, Z. L.; Bu, J.; Castell, M. R.; Chen, P.; Cocks, A.; Corr, S. A.; Cussen, E. J.; Darnbrough, E.*; et al.* 2020 Roadmap on Solid-State Batteries. *J. Phys.: Energy* **2020**, *2*, 32008.

(16) Placke, T.; Kloepsch, R.; Dühnen, S.; Winter, M. Lithium Ion, Lithium Metal, and Alternative Rechargeable Battery Technologies: The Odyssey for High Energy Density. *J. Solid State Electrochem.* **2017**, *21*, 1939–1964.

(17) Sen, S.; Trevisanello, E.; Niemöller, E.; Shi, B.-X.; Simon, F. J.; Richter, F. H. The Role of Polymers in Lithium Solid-State Batteries with Inorganic Solid Electrolytes. *J. Mater. Chem. A* **2021**, *9*, 18701–18732.

(18) Zhang, Z.; Shao, Y.; Lotsch, B.; Hu, Y.-S.; Li, H.; Janek, J.; Nazar, L. F.; Nan, C.-W.; Maier, J.; Armand, M.*; et al.* New Horizons for Inorganic Solid State Ion Conductors. *Energy Environ. Sci.* **2018**, *11*, 1945–1976.

(19) Zhang, Q.; Liu, K.; Ding, F.; Liu, X. Recent Advances in Solid Polymer Electrolytes for Lithium Batteries. *Nano Res.* **2017**, *10*, 4139–4174.

(20) Connell, J. G.; Fuchs, T.; Hartmann, H.; Krauskopf, T.; Zhu, Y.; Sann, J.; Garcia-Mendez, R.; Sakamoto, J.; Tepavcevic, S.; Janek, J. Kinetic versus Thermodynamic Stability of LLZO in Contact with Lithium Metal. *Chem. Mater.* **2020**, *32*, 10207–10215.

(21) Huo, H.; Luo, J.; Thangadurai, V.; Guo, X.; Nan, C.-W.; Sun, X. Li_2CO_3: A Critical Issue for Developing Solid Garnet Batteries. *ACS Energy Lett.* **2020**, *5*, 252–262.

(22) Cao, D.; Sun, X.; Li, Q.; Natan, A.; Xiang, P.; Zhu, H. Lithium Dendrite in All-Solid-State Batteries: Growth Mechanisms, Suppression Strategies, and Characterizations. *Matter* **2020**, *3*, 57–94.

(23) Krauskopf, T.; Richter, F. H.; Zeier, W. G.; Janek, J. Physicochemical Concepts of the Lithium Metal Anode in Solid-State Batteries. *Chem. Rev.* **2020**, *120*, 7745–7794.

(24) Yang, L.; Lu, Z.; Qin, Y.; Wu, C.; Fu, C.; Gao, Y.; Liu, J.; Jiang, L.; Du, Z.; Xie, Z.*; et al.* Interrelated Interfacial Issues between $Li_7La_3Zr_2O_{12}$-Based Garnet Electrolyte and Li Anode in the Solid-State Lithium Battery: A Review. *J. Mater. Chem. A* **2021**, *9*, 5952–5979.

(25) Yamada, H.; Ito, T.; Hongahally Basappa, R. Sintering Mechanisms of High-Performance Garnet-type Solid Electrolyte Densified by Spark Plasma Sintering. *Electrochim. Acta* **2016**, *222*, 648–656.

(26) Sharafi, A.; Kazyak, E.; Davis, A. L.; Yu, S.; Thompson, T.; Siegel, D. J.; Dasgupta, N. P.; Sakamoto, J. Surface Chemistry Mechanism of Ultra-Low Interfacial Resistance in the Solid-State Electrolyte Li 7 La 3 Zr 2 O 12. *Chem. Mater.* **2017**, *29*, 7961–7968.

(27) Han, X.; Gong, Y.; Fu, K. K.; He, X.; Hitz, G. T.; Dai, J.; Pearse, A.; Liu, B.; Wang, H.; Rubloff, G.*; et al.* Negating Interfacial Impedance in Garnet-Based Solid-State Li Metal Batteries. *Nat. Mater.* **2017**, *16*, 572–579.

(28) Huo, H.; Chen, Y.; Li, R.; Zhao, N.; Luo, J.; Da Pereira Silva, J. G.; Mücke, R.; Kaghazchi, P.; Guo, X.; Sun, X. Design of a Mixed Conductive Garnet/Li Interface for Dendrite-Free Solid Lithium Metal Batteries. *Energy Environ. Sci.* **2020**, *13*, 127–134.

(29) Huo, H.; Chen, Y.; Luo, J.; Yang, X.; Guo, X.; Sun, X. Rational Design of Hierarchical "Ceramic-in-Polymer" and "Polymer-in-Ceramic" Electrolytes for Dendrite-Free Solid-State Batteries. *Adv. Energy Mater.* **2019**, *9*, 1804004.

2 Fundamentals

This chapter provides theoretical fundamentals of next-generation solid-state batteries that will be compared to conventional lithium-ion batteries. Two classes of solid electrolytes are highlighted including their synthesis and their lithium ion transport mechanism. The interface between SEs and lithium metal anode is presented in detail including the stationary and dynamic state while stripping and plating. Different dendrite growth mechanisms are discussed.

2.1 Lithium-ion batteries

In general, batteries and accumulators are energy storage systems that are based on several types of galvanic cells. Providing the reversibility of the electrochemical reactions, the term accumulator or secondary battery is used and battery (or primary battery) for irreversible reactions, respectively. However, both systems are colloquially referred to as “battery”.[1]

Since their commercialization by Sony in 1991, LIBs have established as one of the most important energy storage systems. They have become the leading market share in small format battery market for portable devices due to their high energy density, cycle life and high efficiency, compared to other currently available battery technologies given in Figure 2.1.1A.[2–4] Recently, they also have been successfully implemented as the technology of choice for the automotive sector, e.g., hybrid, plug-in or fully BEVs. Driven by the increasing demand, its total worldwide battery production has more than quadrupled in the recent decade and is expected to continuously grow.[5–7]

The design of the state-of-the-art LIB is given in Figure 2.1.1B. The following section is based on refs. [1] and [8]. LIB cells consist of two electrodes, the anode and cathode, each composed of an active storage component, a current collector and inactive materials like binders and conductive agents. The anode active material (AAM, negative electrode) is typically made of porous graphite and the cathode active material (CAM, positive electrode) of porous layered lithium transition metal oxides, mainly lithium cobalt, nickel and manganese oxide. Copper and aluminum foil are used as current collectors on the negative and positive electrode, respectively. The electrodes are separated by a thin separator (polymer membrane usually made of polyethylene and polypropylene). Both the separator and the electrodes are infiltrated by a liquid electrolyte that ensures fast lithium ion transfer between the electrodes and prevents electronic short-circuiting. Typical liquid electrolytes are mixtures of organic compounds, mainly linear ethers and carbonates as well as cyclic carbonates in which conducting

lithium salts are dissolved. Common examples are ethylene carbonate and dimethyl carbonate and lithium hexafluorophosphate ($LiPF_6$) or lithium bis(trifluoromethanesulfonyl)imide (LiTFSI).

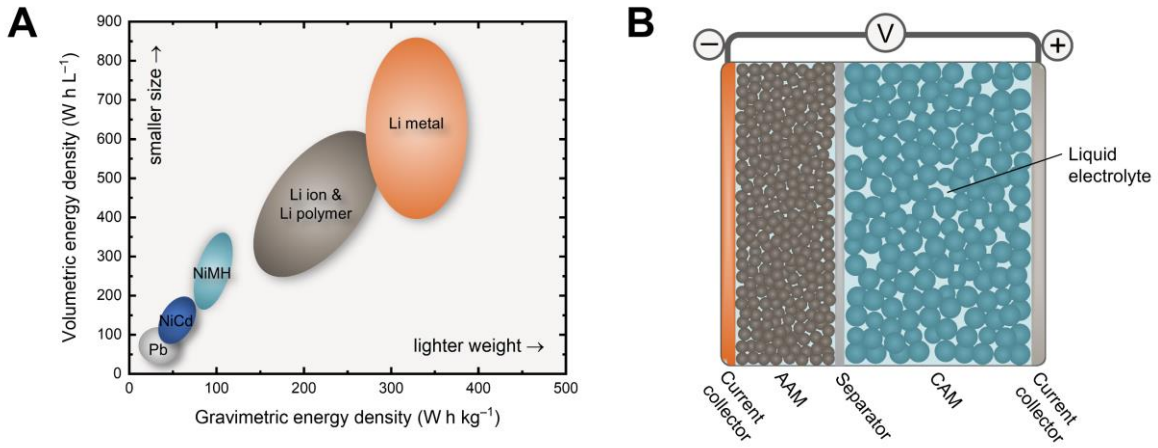

Figure 2.1.1. (A) Comparison of the different battery technologies in terms of volumetric vs. gravimetric energy density. Adapted from [4]. (B) Typical battery design of the conventional LIB with the anode (AAM) and cathode active material (CAM) infiltrated by a liquid electrolyte. Adapted from [9].

The operating principle of the LIB is based on lithium ion insertion reactions from both electrodes, i.e., oxidation and reduction processes, where the lithium ions act as the charge carrier. During discharging, lithium ions intercalated in the graphite anode move through the electrolyte towards the cathode in which they are incorporated in the layered structure. Correspondingly, electrons from the anode (i.e., oxidation) are transferred through the external circuit and recombine at the cathode side (i.e., reduction). When the cell is operated in charge mode, the electron current and lithium ion flow are reversed. In state-of-the-art LIBs, several cells are connected in series and/or in parallel to provide the required voltage and capacity, e.g., for EV application, cells are arranged into modules that are placed into a battery pack.

At cell level, LIBs nowadays reach volumetric and gravimetric energy densities up to 750 Wh L^{-1} and 300 Wh kg^{-1}, respectively by constant optimization over the years (see Figure 2.1.1A), e.g., due to reducing the amount of inactive components as well as reducing the thickness of separator layers. However, they are considered as mature technology as they will soon reach their physicochemical limit.[9–11] Silicon is a promising replacement with a capacity of 4,200 mAh g^{-1} compared with 372 mAh g^{-1} for graphite, but the significant volume change during cell cycling (~300 %) and an unstable electrolyte interface results in capacity fading over time.[12] Therefore, its widespread commercial application is hindered and it is rather used as additive for graphite anodes. The most promising high-capacity anode is lithium metal with its superior capacity of 3,860 mAh g^{-1}.[13] However, its use in liquid-electrolyte cells is limited because of lithium dendrite formation.[14] Furthermore, LIBs suffer from severe safety issues associated with the use of toxic and flammable

liquid electrolytes. Thermal management systems lower volumetric energy density at the pack level.[15]

2.2 Solid-state batteries

The concept of the SSB has gained particular importance for research of both academia and industry in the last decade due to the upcoming limitations of LIBs in terms of energy density and safety. The main goal is to boost the energy density of battery cells, especially for longer driving ranges of EVs. Conceivable designs of SSBs are demonstrated in Figure 2.2.1. The basic principle is based on the replacement of the electrolyte-filled separator membrane and the liquid electrolyte in the electrodes by a solid electrolyte (SE). It therefore provides both lithium ion conduction and electronic separation. It can either be implemented in a conventional AAM (A) or the latter can be replaced by a high-capacity LMA (B).[9] SEs can range from sintered, completely inorganic solid electrolytes (ISEs) to (semi-)solid polymer solid electrolytes (PSEs) and hybrid solid electrolytes (HSEs) (C).[16]

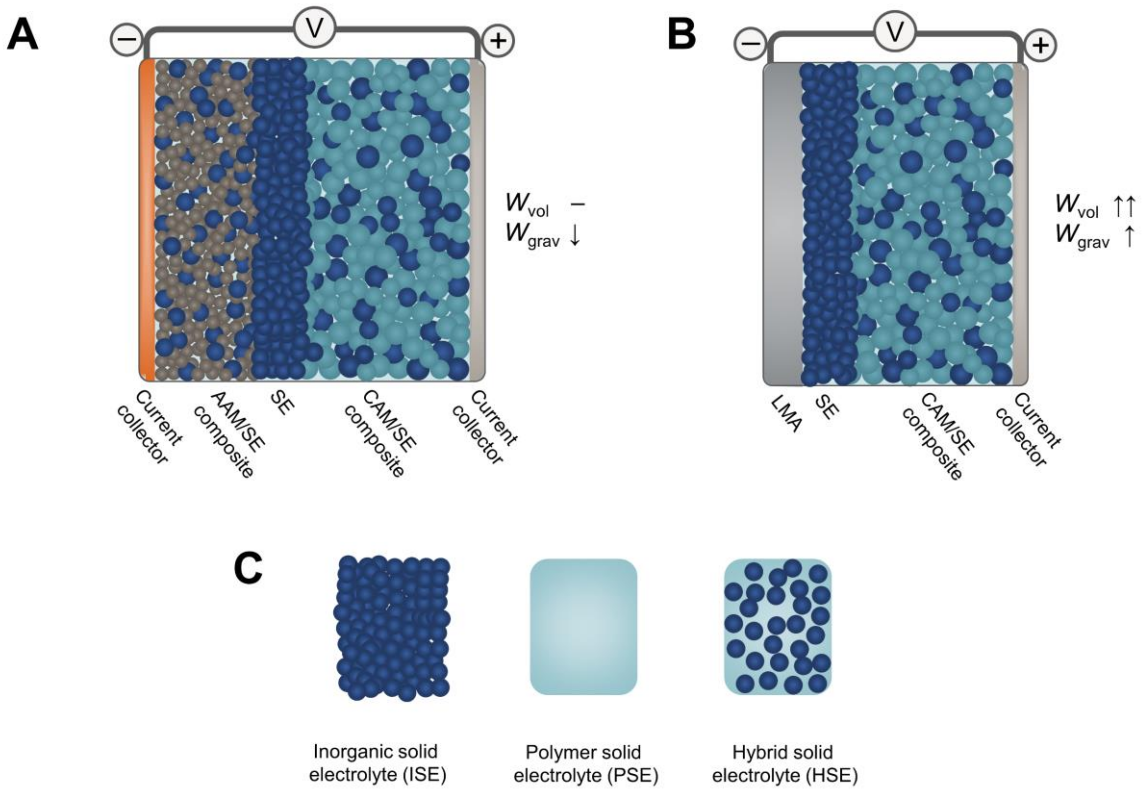

Figure 2.2.1. SSB design principles with SE as separator and different anode concepts: (A) SE implementation into conventional AAM and (B) replacement of the conventional AAM by LMA. The change in volumetric (W_{vol}) and gravimetric energy density (W_{grav}) compared with LIBs is given schematically on the right-hand side for each design principle. Adapted from [9]. (C) Schematic representation of different types of SEs including ISE, PSE and HSE.

In terms of energy density, the sole replacement of the liquid electrolyte would not provide an improvement in volumetric (W_{vol}) as well as gravimetric energy density (W_{grav}) due to the higher density of SEs. Contrarily, the use of high-capacity LMA can significantly increase the energy density provided that the SE is stable against lithium metal. Due to the natural mechanical strength of SEs, they may also prevent the formation of lithium dendrites upon cycling, overall facilitating the use of a LMA.[17]

Moreover, most SEs have a superior thermal stability compared to liquid electrolytes allowing wider temperature ranges and improving battery safety. In fact, their ionic conductivity even increases at elevated temperatures reaching that of liquid electrolytes.[9] It is also only dominated by lithium ions compared with lithium ions plus anions from the conducting salt in liquid electrolytes, therefore enabling higher current densities and quicker charging, i.e., higher power density.[18]

2.3 Solid electrolytes

SEs are the key components to construct SSBs. The requirements for SEs are manifold and may differ for particular applications either as separator or catholyte material. First, SEs must have ionic conductivies of several mS cm^{-1} to be an adequate substitute for liquid electrolytes. At the same time, their electronic resistance must be high to reliably perform as separator. To ensure low internal cell resistance, the interfaces between the SE and the electrodes should have low resistance, the ideal case would be $\leq 1\,\Omega\,cm^2$.[19] Surface layers from atmosphere reaction, degradation reactions and nonuniform wetting can have substantial influence on the interface resistance.[20] Moreover, the SE requires a wide electrochemical stability window, i.e., it must be stable at anode and cathode potentials. Especially for the use of LMA, the (electro-)chemical stability against lithium, one of the most electropositive elements, is of major importance as well as superior mechanical strength to withstand lithium dendrite propagation through the electrolyte.[21] On the other hand, some flexibility and softness is beneficial to reach good wettability with the electrodes and to accommodate volume changes.[22] In Figure 2.3.1, the most important performance properties of the three main classes of SEs ranging from ISE to PSE and HSE are demonstrated in radar plots. In the class of ISEs, the two most predominant systems of oxides and sulfides are highlighted. While ISEs mainly offer the benefit of high ionic conductivities and high thermal and mechanical strength, PSEs are poor ion conductors but have the advantage of high flexibility and easy processability. HSEs can combine these two systems but reaching high conductivities is still challenging, plus they have high processing costs.[23] In the following sections, the properties and related benefits and challenges of ISEs and HSEs will be presented in detail.

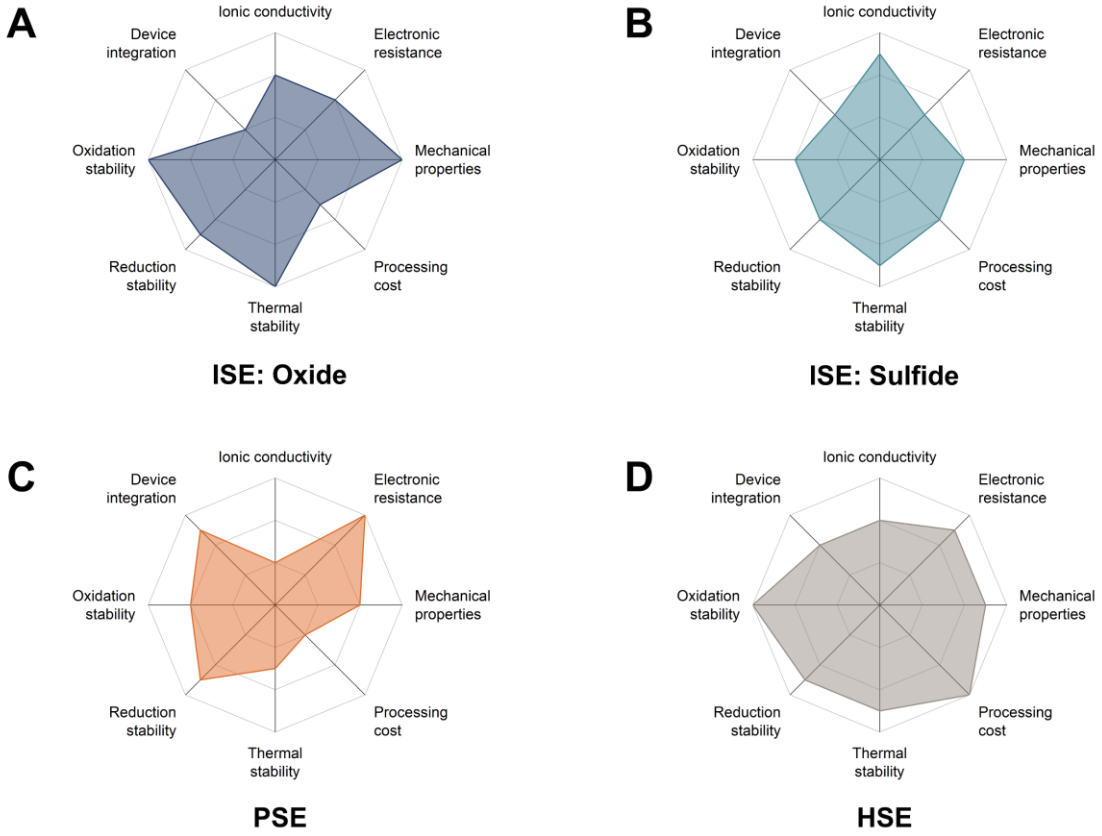

Figure 2.3.1. Radar plots of the performance properties of different SE materials: (A) oxide ISE, (B) sulfide ISE, (C) PSE, and (D) HSE. Adapted from [23].

2.3.1 Inorganic solid electrolytes

ISEs range from lithium metal oxides, sulfides, phosphates and nitrides to halides and crystalline ceramic to glass-ceramic and glassy systems. They have been proven to exhibit high ionic conductivities, as summarized in Figure 2.3.2. Besides early lithium ion conductors, such as Li_3N and Li–β–Al_2O_3, two groups of SEs have emerged as the most practical choice, namely oxides and sulfides.[24]

Most oxide-based SEs can be categorized by their crystal structure into NaSICON-type, perovskite-type and garnet-type SEs. The first family is named after a sodium superionic conductor $NaM_2(PO_4)_3$ (M = Ge, Ti, Zr) in which the Na^+ ions are replaced with Li^+ ions without the change of the crystalline NaSICON structure. The most popular are $Li_{1+x}Al_xTi_{2-x}(PO_4)_3$ (LATP) and $Li_{1+x}Al_xGe_{2-x}(PO_4)_3$ (LAGP) that are characterized by partial Al substitution of Ti and Ge, respectively.[25] Ionic conductivities up to 10^{-2} S cm^{-1} have been reported[26], however, due to their reductive instability against lithium metal, their application with a LMA is restricted. On the cathode side, the main challenge is to achieve sufficient interface contact.[27] Perovskite-type SEs have the general crystal structure ABO_3 (A = Ca, Sr, La; B = Al, Ti) with the A-sites partially occupied by Li or La giving

$Li_{3x}La_{2/3-x}TiO_3$ (LLTO). Even though they exhibit bulk ionic conductivities > 10^{-3} S cm^{-1}, the high grain boundary and interfacial resistance as well as the instability of Ti^{4+} with LMA hinder their practical application.[28] Garnet-type SEs show a variety of chemistries with the ideal chemical formula $A_3B_2M_3O_{12}$ (A = Ca, Mg, Fe; B = Al, Fe, Ga, Cr, V; X = Si, Ge) and crystallize in a face-centered-cubic structure with eight (A), six (B) and four (M) oxygen-coordinated cation sites.[29] Early studies focused on lithium garnets with low lithium content (e.g., $Li_3Ln_3Te_2O_{12}$ with Ln = Y, Pr, Nd), $Li_5La_3M_2O_{12}$ (M = Nb, Ta) and $Li_6Ala_2M_2O_{12}$ (A = Ca, Sr, Ba; M = Nb, Ta))[29], but they were developed to so-called lithium-stuffed garnets that exhibit higher ionic conductivity (10^{-4}–10^{-3} S cm^{-1}), with the most prominent one $Li_7La_3Zr_2O_{12}$ (LLZO).[30] Garnets are very attractive due to their broad electrochemical window and high chemical stability against lithium metal. As LLZO is the subject of this thesis, it will be discussed in detail in the sections 2.3.1.2 and 2.3.1.3.

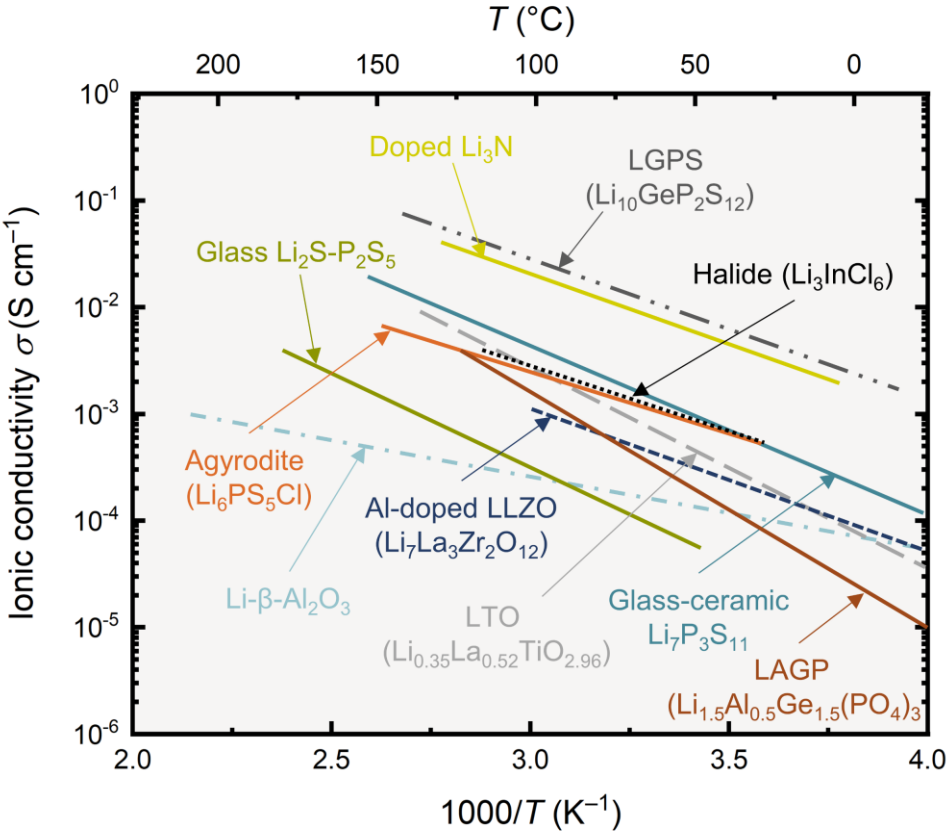

Figure 2.3.2. Temperature-dependant ionic conductivity of common ISEs ranging from oxides, sulfides, phosphates and nitrides to halides. Both crystalline and glassy systems are shown. Data values are reproduced with permission from [31–40].

Sulfide-based SEs comprise multiple different chemistries, with the most prominent families of thio-LiSICONs, LGPS ($Li_{10}GeP_2S_{12}$), agyrodites (Li_6PS_5X (X = Cl, Br, I) and a variety of Li–P–S glasses or glass-ceramics.[41] They have the highest ionic conductivities among ISEs at ambient temperature reaching those of liquid electrolytes (Figure 2.3.2). O^{2-} anions are replaced with S^{2-} anions that are highly polarizable leading to less pronounced interaction of Li^+ ions with the anionic sub-lattice.

Moreover, the soft mechanical properties of sulfides offer easy processability and better wettability with the electrodes.[24] However, their severe (electro-)chemical instability against both LMA and cathode active materials as well as poor air stability releasing toxic H_2S gas hinders their practical application.[42]

Overall, the benefits and challenges of oxide- and sulfide-based SEs are summarized in the radar plots in Figure 2.3.1.[43] Sulfides have the advantage of very high ionic conductivities, but lack in (electro-)chemical stability, whereas oxides offer superior stability and high mechanical strength, while maintaining sufficient ionic conductivities. On the one hand, the stiffness of oxide-based SEs causes significant issues to reach good wettability, i.e., low interfacial resistance towards the electrodes including LMA. On the other hand, their rigid mechanical properties are considered to be favorable for the suppression of lithium dendrites. However, in practice, they still suffer from lithium dendrite growth along grain boundaries despite their high shear modulus.[44] The interface and behavior while cycling with a LMA will be highlighted in section 2.4.

2.3.1.1 Ion transport mechanism

In crystalline ISEs, the ion conduction mechanism is based on classical diffusion, in which mobile ions hop from one lattice site to an adjacent vacant site. Therefore, the prerequisite for ion conduction are interstitials, vacancies, and partial occupancy on lattice sites or interstices in the crystal structure. These are either present intrinsically due to entropic effects or they can be generated extrinsically by substitution of aliovalent cations (called doping).[45] Different types of diffusion processes are schematically depicted in Figure 2.3.3A involving (i) exchange diffusion, (ii) vacancy diffusion, (iii) ring diffusion, and (iv) interstitial diffusion.[46]

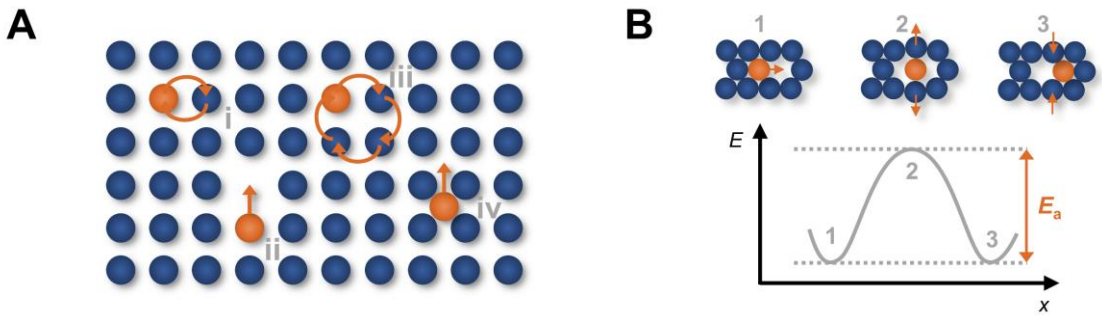

Figure 2.3.3. (A) Schematic representation of diffusion processes in solid-state materials based on (i) the direct exchange mechanism, (ii) the vacancy mechanism, (iii) the ring mechanism, and (iv) the interstitial mechanism. (B) Schematic representation of the potential barrier determined by the activation energy E_a that needs to be overcome during the diffusion process. Adapted from [46].

Lithium ion conductivity σ is strongly related to the number of mobile lithium ions n per unit volume, their charge q and their mobility μ in the crystal structure:

$$\sigma = nq\mu \tag{2.1}$$

The mobility μ can be described analogously to diffusion of mobile lithium ions in the ISEs, but caused by an external electric field. It is therefore highly governed by the crystal structure and its defects that determines the energy barrier, i.e., the activation energy, for hopping between two lithium sites.[24]

Thus, ionic conductivity can be expressed as follows, where E_A is the activation energy, T the temperature and k_B the Boltzmann constant:

$$\sigma = \frac{\sigma_0}{T} \exp\left(\frac{-E_A}{k_B T}\right) \tag{2.2}$$

A low activation energy and a high concentration of mobile lithium ions are favorable for high ionic conductivity. Even though the concentration of mobile ions can be increased by doping to create vacancies and interstitials, the ionic conductivity often starts to decrease after passing through a maximum because of the strong lithium ion interaction upon addition of more mobile species.[45] In crystalline ISEs, the mobile ions are typically only lithium ions. Hence, the lithium ion transference number t_{Li+}, that is defined as the ratio of the conductivity of lithium ions to the sum of the conductivities of all charge carriers, is close to unity. Conversely, t_{Li+} of liquid electrolytes is about 0.2–0.5 due to the presence of anions from the conducting salt.[47]

In polycrystalline ISEs, the grain boundaries are a structural discontinuity, which is often detrimental for lithium ion transport due to the high energy barrier caused by changes in local structure.[24] Compared to (poly-)crystalline ISEs, amorphous or glassy SEs exhibit isotropic conduction properties due to the lack in long-range order and grain boundaries, resulting in a disordered energy landscape for lithium ion hopping. Therefore, the exact ion transport mechanism in amorphous materials and the effect on ionic conductivity is still under debate.[48,49] However, amorphous phases located in the grain boundaries of polycrystalline ISEs, e.g., in glass-ceramics or by the addition of a second phase, have been proven to reduce grain boundary resistance and hence, overall ionic conductivity.[50–52]

2.3.1.2 Synthesis and sintering of LLZO

Due to the variety of synthesis methods for different SE classes, solely the manufacturing of LLZO being the focus of this thesis will be highlighted. Various methods exist for the synthesis of LLZO bulk powder, of which wet-chemical methods and solid-state synthesis have established. One of the most common wet-chemical methods is the sol-gel route including the following steps: (1) the reagents (usually metal chlorides, nitrates, acetates) are dissolved in alcohol to form metal alkoxides; (2) hydrolysis and partial condensation of the latter resulting in a colloidal suspension called 'sol'; (3) polycondensation to metal-oxo-metal bonds forming a 'gel'; (4) drying the gel and (5) calcination for complete removal of solvent.[53] One limitation is to get stable metal alkoxides, therefore, an alternative route called Pechini process has been developed. Usually the metal nitrates in combination with a chelating agent, mostly citric acid, are used, which then form a gel upon heating.[54] The sol-gel method offers small particle sizes and low calcination temperatures compared with the solid-state synthesis (~900 °C), however, finding a suitable precursor and solvent can be challenging.[53]

The solid-state synthesis is one of the easiest accessible and most straightforward methods. The reagents (mostly metal oxides, hydroxides, and in the case of lithium often carbonates) are ground and homogenized by mortar or ball milling (optionally, organic solvents can be added), subsequently calcined to drive their reaction (900–1100 °C) and then milled to give a lithium ion-conductive powder. Sometimes repeated milling/calcination steps are required.[55] Major drawbacks of this method are the high calcination temperatures and long annealing times required. This impedes synthesis at industrial scale, especially regarding energy consumption.[42]

The SCHOTT AG with its expertise in melting technology recently has developed a specific melting route to produce glass-ceramic LLZO.[56] A schematic representation of the procedure is given in Figure 2.3.4. Basically, the reagents are melted and homogenized first. Upon cooling, crystallization seeds of LLZO start to form that continously grow to give a glass-ceramic with a high volume fraction of Li-ion conductive crystalline phase and an additonal amorphous phase. The volume fraction and the composition of the amorphous phase, e.g., stabilization due to glass-forming agents, can be adjusted during the process. The bulk material is subsequently milled to give a powder. The melting route has been proven to be fast and industrially scalable.

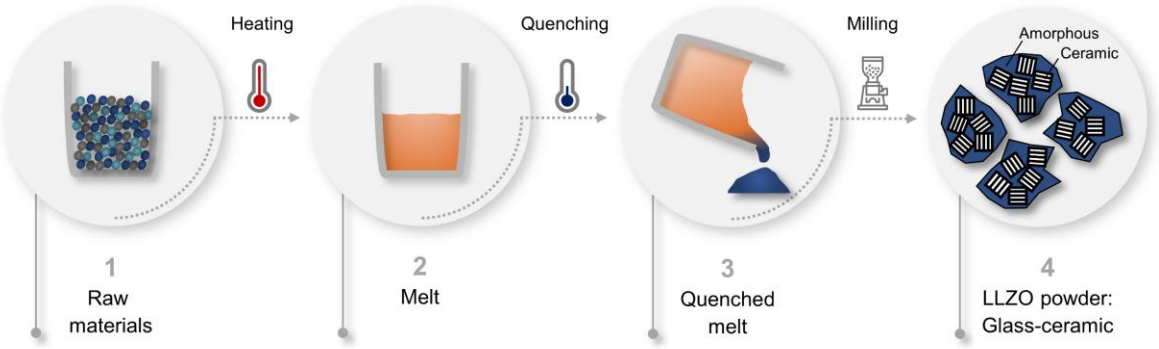

Figure 2.3.4. Schematic representation of the melting route developed at the SCHOTT AG to produce glass-ceramic LLZO.

All of the methods above are followed by a sintering step. A wide variation of techniques have been successfully proven to perform the sintering, e.g., furnace heating sintering[53], spark plasma sintering (SPS) or field-assisted sintering (FAST)[57,58], and microwave-assisted sintering[59]. Furnace heating sintering is the most commonly used method as it has the lowest instrumentational requirements, even though high sintering temperatures (~1200 °C) as well as long sintering times (~12 h) are needed. A major drawback is the Li volatilization at such high temperatures, which can cause the formation of unwanted Li-deficient phases such as $La_2Zr_2O_7$.[60] An excess amount of lithium reagent is often added and/or sacrificial powder (also called mother powder) is used to prevent changes in stoichiometry. Yet, techniques with lower sintering temperature as well as time are favorable. Besides fast-sintering techniques like SPS/FAST, liquid phase sintering is a feasible approach. Contrarily to conventional sintering, a sintering additive with a low melting point is added to the ceramic LLZO affecting the material transport and densification.[61]

According to classical sintering theory, i.e., the two-sphere sintering model, the main driving force of sintering is the reduction in surface energy.[62] The quality of the pressed green pellet is essential for the densification process, i.e., homogeneity and narrow particle size distribution of the powder. Driven by different transport mechanisms, the particles coalesce and compact to give a dense material. Transport mechanisms can be divided into mechanisms with and without densification, which is schematically represented in Figure 2.3.5A. Surface diffusion and transport upon vaporisation and condensation at the surface are sole transport mechanisms (i–iii), while diffusion processes at the grain boundary promote densification (iv–v). Typical sintering stages include neck formation, followed by the formation of a network of interconnected pores by compaction and lastly, those pores are closed off and become isolated from each other. Pore shrinking and densification are very slow at that stage and are mainly determined by the grains surrounding the pores. Often smaller grains are eliminated, while larger grains grow, a phenomenon called Ostwald ripening, which can lead to unwanted abnormal grain growth.[62] To reach effective pore shrinking, the sintering

atmosphere is crucial, e.g., oxygen atmosphere is often used for sintering of LLZO to facilitate pore transportation to the surface.[63]

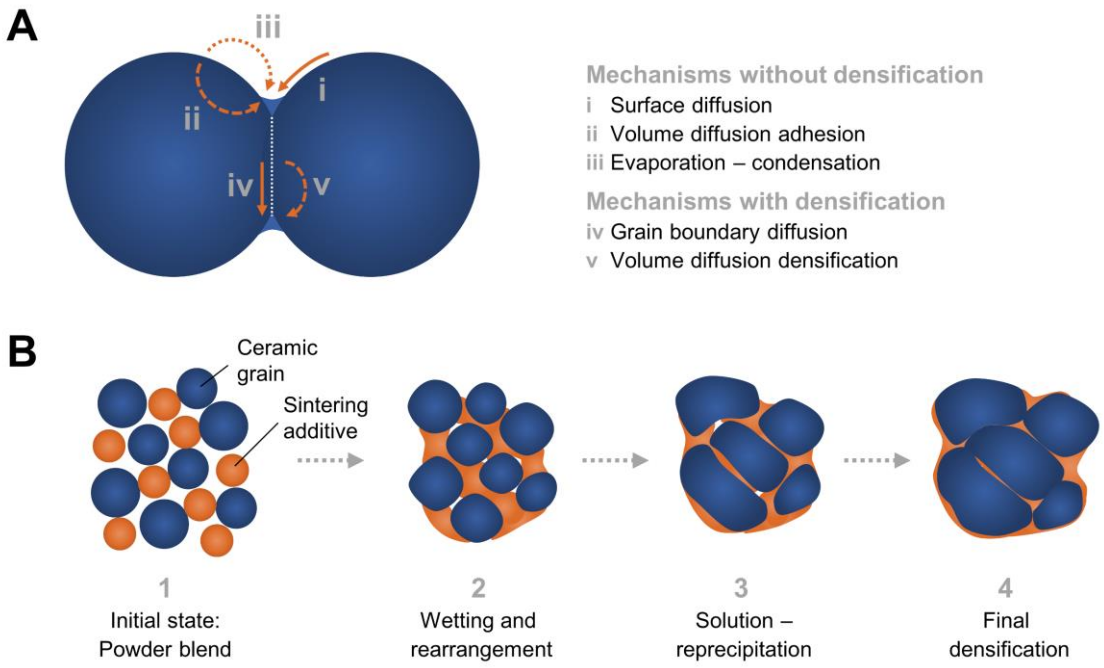

Figure 2.3.5. Schematic representation of (A) the sintering mechanism according the two-sphere model and the related transport mechanisms divided into processes without densification (i–iii) and with densification (iv–v) and (B) of the sintering stages of liquid phase sintering starting from a powder blend (1) to wetting and rearrangement (2) and solution – reprecipitation (3) to final densification (4). Adapted from [62] and [61].

In liquid phase sintering, the diffusion processes at the surfaces of the particles are enhanced drastically because of the surrounding liquid phase. Figure 2.3.5B demonstrates the different stages during liquid phase sintering starting from a powder blend comprising of ceramic grains and a sintering additive (1). Upon temperature increase, the sintering additive melts to give a liquid phase that wets the ceramic grains and interparticle voids due to capillary forces, followed by rearrangement of the grains (2). The solubility and the resulting contact angle between the solid and liquid phase are crucial at this stage. Due to subsequent solution-precipitation processes (3), densification and grain coarsening is promoted (4).[61] The main advantages of liquid phase sintering are the reduction of sintering temperature as well as time and high final densities. For sintering of LLZO, typical sintering additives are lithium compounds, such as Li_2O, LiOH, Li_3PO_4, just to name a few.[64–66] They are usually mixed and homogenized with the initial LLZO powder. In glass-ceramic LLZO, the amorphous phase acts directly as sintering additive and is intrinsically included in the initial LLZO powder.

2.3.1.3 Properties and current challenges of LLZO

The garnet-type LLZO crystallizes in two stable phases: a cubic modification (c-LLZO) with the space group $Ia\bar{3}d$, that was discovered by Murugan *et al.*[30] and a tetragonal modification (t-LLZO) with the $I4_1/acd$ space group first reported by Awaka *et al.*[67]. Their crystal structures together with important Li positions are demonstrated in Figure 2.3.6. Both polymorphs consist of La^{3+} at dodecahedral sites and Zr^{4+} at octahedral sites, with the LaO_8 and ZrO_6 polyhedra connected by edge-sharing. In c-LLZO, the lithium ions only partially and randomly occupy a tetragonal site (Li1: 24d) and a distorted octahedral site (Li2: 48g or more specifically, two off-centered 96h sites upon splitting of the 48g site due to high Li^+–Li^+ repulsion).[68] The LiO_4 tetrahedra share faces with the LiO_6 polyhedra and form a 3D network structure that enables a fast lithium ion conduction pathway. Theoretically, two different pathways exist, one only includes the migration between adjacent Li2 sites and according to the other one, lithiums ions migrate along the Li2–Li1–Li2 pathway (i.e., 96h–24d–96h). From *ab initio* calculations, it was found that the latter is favored due to its lower activation energy (0.8 eV *vs*. 0.28 eV).[69] However, pure c-LLZO is not stable at room temperature and t-LLZO is formed instead. t-LLZO is slightly elongated along one axis compared with c-LLZO, which results in a transformation of the tetrahedral 24d site into a fully occupied 8a (Li1) and an unoccupied 16e site. The 96h site also transforms into two distorted fully occupied octahedral sites (Li2: 16f and Li3: 32g).[68]

The major difference between c- and t-LLZO is the ordering of Li atoms and occupation of lithium sites. While in t-LLZO the lithium ions are of higher order due to the fully occupied Li sites, c-LLZO has more available vacancies because of the lithium ion disorder (see insets in Figure 2.3.6). This enables fast single ion hopping along the 3D network of c-LLZO. Therefore, the ionic conductivity of c-LLZO is two orders of magnitude higher compared with t-LLZO (~10^{-4} *vs*. ~10^{-6} S cm^{-1}).[70] At room temperature, t-LLZO is the stable polymorph that undergoes a phase transitition into c-LLZO only at elevated temperatures (> ~150–200 °C).[71] A strategy to stabilize c-LLZO at room temperature is the incorporation of dopants. There are various studies proving that the inclusion of a wide array of dopants is possible on all three cation sites (see [72] for refs.). Both hypervalent and subvalent dopants can be used that generate either lithium vacancies or increase the number of lithium ions per formula unit (pfu) (beyond 7 Li^+ pfu), respectively, disrupting the lithium ordering. The most common dopants are supervalent cations,e.g., Al^{3+} and Ga^{3+} on the Li site. Even though Al^{3+} for example is very attractive in terms of costs, doping on the Li site is very sensitive to the amount of Al^{3+} due to the occupation of lithium transport channel sites.[73] A more robust doping strategy is to substitute Ta^{5+} and Nb^{5+} on the Zr site. However, a major drawback of Nb^{5+} doping is the reduction instability in contact with lithium metal.[74] The highest ionic conductivities have been observed for about 6.5 Li^+ pfu (up to $2 \cdot 10^{-3}$ S cm^{-1})[75], but further strategies are subject of research to reach ionic conductivities comparable to liquid electrolytes, such as co-doping.[76]

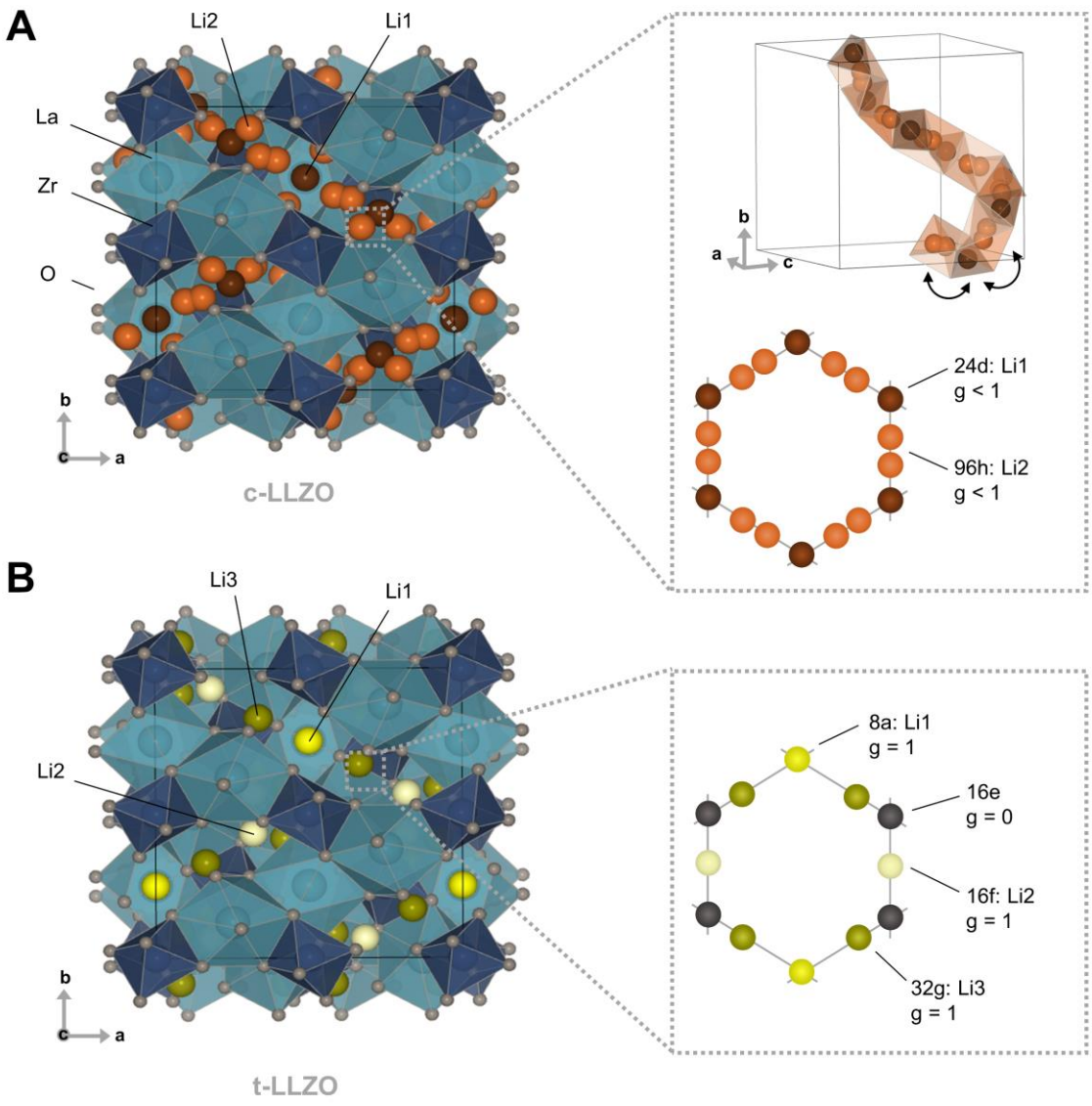

Figure 2.3.6. Crystal structure of LLZO (A) in cubic modification (c-LLZO) with tetrahedral Li1 site (24d) and octahedral Li2 site (96h) and (B) in tetragonal modification (t-LLZO) together with tetrahedral Li1 site (8a) and octahedral Li2 and Li3 sites (16f and 32g). The inset of c-LLZO shows a detailed representation of the lithium sublattice illustrating the predominent lithium pathway along Li2–Li1–Li2 sites. For both c- and t-LLZO, the insets further display a schematic representation of the occupancy of the different Li sites. The value *g* is a dimensionless occupancy value. Adapted from [76].

While recent research has progressed immensely in terms of optimizing the ionic conductivity of LLZO, the main challenges of LLZO are related to surface and interfacial issues upon integration in a battery cell. On the one hand, surface impurities are a major issues due to its environmental instability. Combining Density functional theory (DFT) calculations with experimental analyses exhibited that it readily undergoes Li^+/H^+ exchange from moisture in ambient air or from protic solvents forming LiOH as intermediate.[77] This subsequently reacts with environmental CO_2 to Li_2CO_3 which forms an insulating layer due to its very low ionic and electronic conductivity. Therefore, such an impurity layer is not only detrimental for ionic conductivity but also dramatically increases the interface resistance with the electrodes as well as with the polymer matrix within the

HSE approach.[78] On the other hand, further interfacial issues at the electrodes are caused by chemical instability and poor wetting ability of LLZO. Regarding the cathode side, key issues are poor interface contact due to the rigidity of both materials and interdiffusion and degradation processes being detrimental for cycle stability. However, the LLZO/cathode interface is beyond the scope of this thesis and details can be found in the literature ([76] and refs. therein). In terms of the LMA side, the major issue is related to lithium dendrite formation upon cycling, which will be covered in detail in section 2.4.

2.3.2 Polymer-based hybrid solid electrolytes

The basic principle of the HSE approach is to benefit from the advantages of both ISE and PSE. The most common HSE is a composite consisting of ISE filler particles incorporated into a polymer electrolyte matrix. While the soft and flexible PSE solves the mismatch and wettability issues at the interface with the electrodes, the ISE maintains high ionic conductivity at room temperature. Moreover, the rigid ISE particles have the potential to overcome the poor cycling stability of bare PSEs as they are easily penetrated by lithium filaments short circuiting the cell (see section 2.4.4).[79] Other types of HSEs are multilayer structures where PSE layers are placed on both sides of an ISE pellet or instead of PSE layers, trace amounts of conventional liquid electrolyte can be used in order to ensure proper contact with the electrodes. However, in this section only composite systems will be highlighted. Details for the other HSE can be found elsewhere.[80,81]

The polymer matrix is usually composed of a host polymer with a high dielectric constant that can effectively dissolve a lithium conducting salt. Several polymers can be used, e.g., polyacrylonitrile (PAN), polyvinylidene flouride (PVDF) or polyethylene carbonate (PEC), however, polyethylene oxide (PEO)-based PSEs are the most widely studied due to their excellent salt-solvating ability and interfacial compatibility with electrodes.[82] The most prominent conducting salt is lithium bis(trifluoromethane-sulfonyl)imide (LiTFSI) that easily dissociates because of its delocalized anion. The major drawback of PSEs is their low ionic conductivity in the range of 10^{-5}–10^{-7} S cm^{-1} at room temperature, hence, they can only be operated at elevated temperatures such as 70 °C. Moreover, they suffer from severe lithium dendrite penetration due to their low mechanical strength and are not electrochemically stable against most cathode materials.[83]

Regarding the ISE particles, in principle every type can be used as filler but amongst the most studied are garnet-based ISEs due to their outstanding properties described in section 2.3.1.3. However, not only ion conductive ISE particles can be integrated into the polymer matrix. Before the development of the hybrid electrolyte concept, composites with insulating or so-called *passive* fillers, such as Al_2O_3, TiO_2, and SiO_2, have already been intensively investigated.[84–86] Besides enhancement of both the mechanical and thermal stability in the same manner as ISE fillers, they differ in their influence on the overall ionic conductivity. They indeed have a positive effect on the ionic conductivity due to

reduction of the crystalline phase in the polymer matrix (details on the ion transport mechanism in section 2.3.2.1), but cannot provide an extra ion transport pathway compared to ISE filler particles, i.e., *active* fillers.[80] Moreover, another advantage of garnet-based ISE fillers is that they have the potential to increase the electrochemical stability of the HSE due to their wide electrochemical window, especially at the interface with the LMA.[87] Therefore, most reports focus on the electrochemical performance and study the influence of filler content ranging from polymer-rich (< 50 vol% filler content) to inorganic-rich systems (> 50 vol% filler content), which will be discussed in the next section together with current challenges.

2.3.2.1 Ion transport mechanism

Polymer electrolytes

When compositing PSE and ISE materials, the different ion transport mechanisms of the two components need to be taken into account. In contrast to the hopping mechanism in defect sites of the ISE (section 2.3.1.1), the ionic conduction in PSEs is realized via lithium ion hopping from one coordinating site to another with the segmental motion of the polymer chains, as illustrated for PEO in Figure 2.3.7. This free motion is only effectively possible in amorphous regions of the polymer.[88]

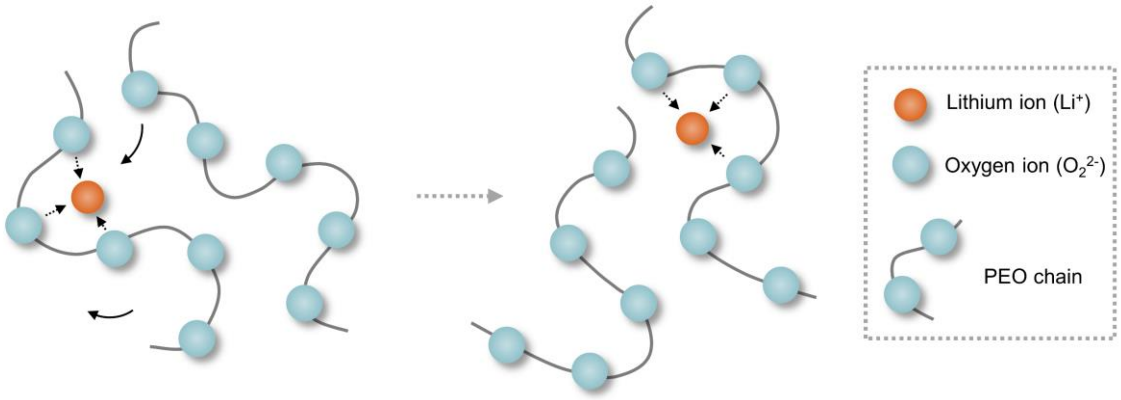

Figure 2.3.7. Lithium ion transport mechanism by segmental motion of polymer chains in the amorphous phase of an PEO-based PSE. Adapted from [88].

At room temperature, both amorphous and crystalline regions are present, hence, ion transport can drastically enhance above the melting temperature of the crystalline phase (for PEO at about 64 °C).[89] Therefore, the ionic conductivity of PSEs is highly dependent on their degree of crystallinity and its temperature dependence is modeled by the non-linear Vogel-Tammann-Fulcher (VTF) equation, where E_A is the activation energy, k_B the Boltzmann constant, T the temperature and T_0 the reference temperature, which is usually 10–50 K below the glass transition temperature of the polymer[90,91]:

$$\sigma = \sigma_0 T^{-\frac{1}{2}} \exp\left(\frac{-E_A}{k_B(T - T_0)}\right) \quad (2.3)$$

Most PSEs are dual-ion conductors in which both lithium ions and anions are mobile. As the lithium ions are coordinated with Lewis basic sites of the PEO backbone, the anions are more mobile and hence, the transference number of PEO-based PSEs are usually lower than 0.5.[83]

Hybrid electrolytes

The overall ionic conductivity of the HSE depends on the individual ionic conductivities of the PSE and ISE and their volume fraction, which strongly affects the contribution of the different pathways. In Figure 2.3.8A and B, the possible pathways for polymer-rich and inorganic-rich HSEs are depicted.[80,92] In general, lithium ions can move (i) only through the PSE phase, (ii) along PSE|ISE interface/interphases, (iii) through both components crossing the PSE|ISE interface, and (iv) only through the ISE phase. The latter is only present when the percolation limit is reached, i.e., for inorganic-rich HSEs.

For polymer-rich systems, the pathways (i)–(iii) are principally possible, however, the corresponding contributions highly depend on the PSE|ISE interface properties. Pathway (ii) is mainly determined by surface phenomena, which are also well known from *passive* fillers, e.g., increased ion pair dissociation of the conducting salt and potentially anion attraction on the ISE surface due to Lewis acid-base interactions, and enhanced lithium ion transport due to reduced crystallinity of the polymer at the ISE surface.[93] For *active* fillers, lithium ion redistribution from the ISE into the PSE driven by the gradient of chemical potential μ at the interface (Figure 2.3.8D) is also discussed as possible positive factor on the lithium ion transport near the surface.[94–97] Here, the concentration of the conducting salt in the polymer also plays an important role.

Such surface phenomena are not only related to the surface chemistry of the fillers and its compatibility with the polymer matrix, but also to the size and shape of the particles. It was reported that ionic conductivities of HSEs using nano-sized filler particles can be effectively increased due to amplification of surface-related transport mechanisms.[98–100] Variation of the shape, e.g., nanowires or vertically aligned fillers also have a positive impact because of fast anisotropic lithium ion pathways (Figure 2.3.8C).[101–104]

A prerequisite for pathway (iii) is the ionic transport, i.e., charge transfer, across the PSE|ISE interface. As depicted in a simplified manner in Figure 2.3.8E, the charge transfer includes both the desolvation of lithium ions at the interface and the transport through a potential solid-polymer electrolyte interphase layer (SPEI, e.g., by Lewis acid-base reaction, chemical reaction and/or impurities on the ISE surface, e.g., Li_2CO_3 for LLZO). The desolvation is considered to be the rate-determining step and its activation energy is influenced by the difference in chemical potential across the interface.[105,106] The chemical potential itself is determined by the activity of lithium ions, i.e., concentration, and the electrostatic interaction between the lithium ions, the anions and the polymer backbone or host structure.[107] Experimental characterization of the interfacial charge transfer and its

activation energy is very challenging, as the phenomena are usually limited to sub-micron range. One approach is a macroscopic model system using a symmetrical sandwich-type cell setup where the ISE is sandwiched between two PSEs and blocking electrodes. With this method, the interface resistance for PEO-based PSE and LLZO was analyzed and found to be in the range from 100 Ω cm^2 to 10 kΩ cm^2.[108–111] Such high interfacial resistances can block pathway (iii), which is often overlooked in literature.

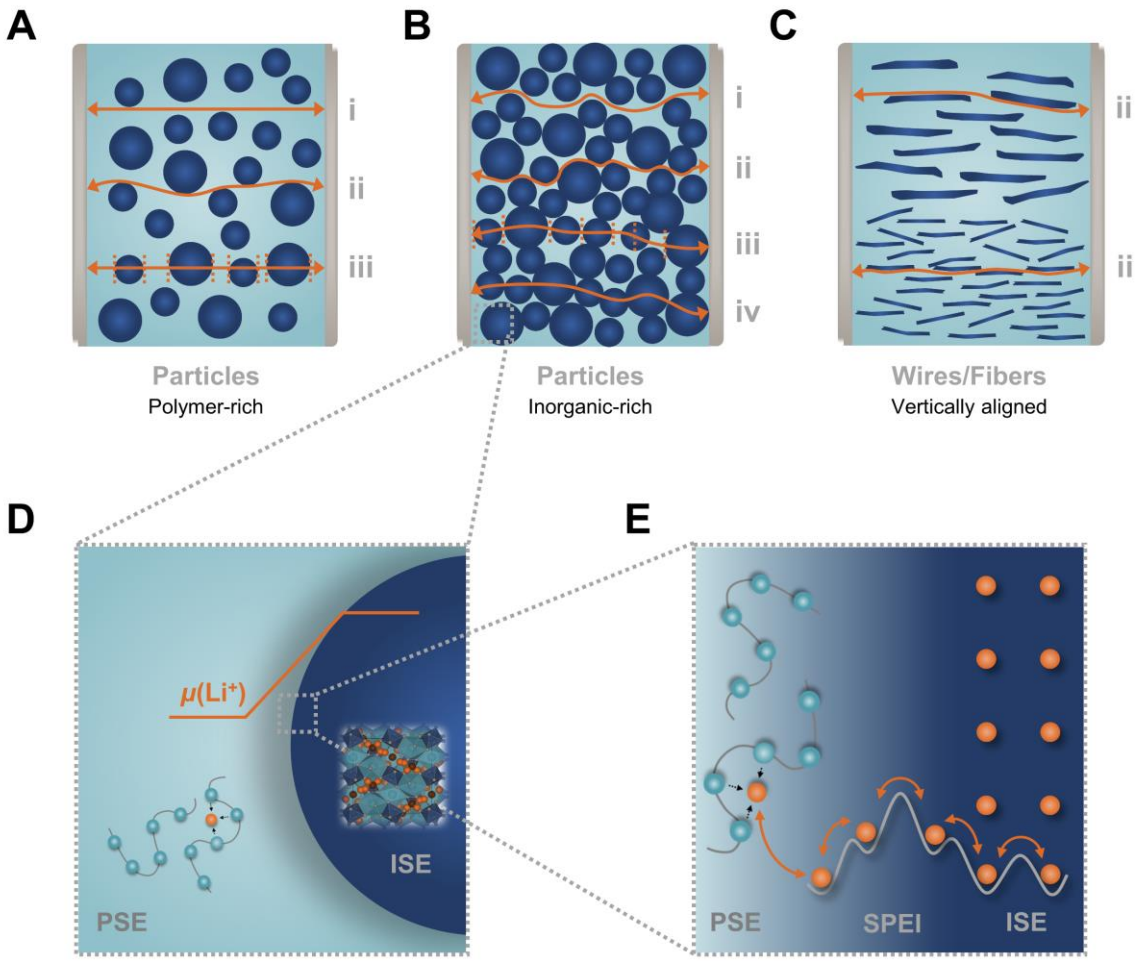

Figure 2.3.8. Schematic representation of the ion transport pathways in (A) polymer-rich and (B) inorganic-rich HSEs incorporating particles as fillers as well as (C) vertically aligned fibers or wires. Pathways include ion transport (i) only through the PSE phase, (ii) along PSE|ISE interface/interphases, (iii) through both components crossing the PSE|ISE interface, and (iv) only through the ISE phase. Adapted from [92]. (D) Scheme of the chemical potential of lithium ions within the two phases of a HSE. Adapted from [80]. (E) Schematic representation of the lithium ion transport and the related potential barriers across the polymer-solid electrolyte interface (SPEI). Adapted from [112].

Many reports have focused on elucidating the ion transport pathways in polymer-and inorganic-rich HSEs, and several models have been developed to describe the different mechanisms.[97,113,114] However, the results are contradictory and the mechanism has not been clarified yet. For polymer-rich systems, both synergistic and negative effects on the ionic conductivity of the HSE compared to the pure PSE have been reported. Synergies are explained by mostly surface-related phenomena as

described above (pathway (ii)), but also by contribution of pathway (iii).[98,100,115–119] This was also experimentally proven by solid-state Li nuclear magnetic resonance spectroscopy (NMR) with lithium isotope labeling, by which the authors could confirm the preferred pathway through the ISE particles (in this case LLZO).[120] Reduced ionic conductivities are ascribed to the sole contribution of the pathway through the PSE (pathway (i)). The incorporation of the ISE particles then only leads to lower cross-sectional area and higher tortuosity of the polymer matrix.[96,121,122] For inorganic-rich HSEs, increased ionic conductivities through percolation of ISE particles (pathway (iv)) are observed[123–125], but other studies showed that the percolating network cannot be formed by simple ISE contact.[96,126] However, what all systems have in common is that they are all below the ionic conductivitiy of the pure ISE.

One explanation for the contrasting results is that the performance of HSEs is greatly affected by the chemical nature of the components, including lithium salt concentration and polymer chain length, the size and shape of the filler particles, and the compounding process together with potential impurities. Therefore, comparibility is challenging and results need to be carefully interpreted. In fact, comparison between active and passives filler should be included in every study.

2.3.2.2 Synthesis

The most common preparation method of HSEs is the solution casting method where all components (polymer, conducting salt and ISE filler) are intimately mixed in an inert solvent. The resulting slurry is cast into a mold or by doctor blade on a substrate.[127] Upon subsequent evaporation of the solvent, the electrolyte solidifies and can be detached from the mold or substrate. For PEO-based PSEs, mostly acetonitrile is used as a solvent because of its good solubility with PEO and high vapor pressure. The solution casting method is relatively facile, low cost and scalable. However, the solvent needs to be carefully chosen in terms of solubility, volatility and chemical stability with all components. For systems where the elimination of solvents is required, e.g., solvent-sensitive sulfide-based ISEs, the mechanochemical method can be used that includes solvent-free mixing of the components, e.g., by ball milling or kneading process, followed by hot-pressing.[121,128–130] For both methods, the careful pre-drying of all components is crucial as water residues can lead to overestimation of the ionic conductivity of the HSE. This is especially important for the ISE LLZO that is very sensitive to humidity because it can form insulating Li_2CO_3 on its surface (see section 2.3.1.3).[78] However, not only water residues can impair the electrochemical performance but also solvent residues. Even though vacuum drying is widely used, the complete removal of solvent remains challenging.[86] This issue is easily often overlooked. Therefore, solvent-free techniques are of high interest for the processing of HSEs.

For inorganic-rich HSEs with filler contens > 50 %, the described blending methods reach their limits due to strong agglomeration of the particles.[131] Instead, porous ISE 3D frameworks (made by

electrospinning or from hydrogels) can be infiltrated by a polymer electrolyte solution with low viscosity of which the solvent is subsequently evaporated. The resulting HSEs profit from the high ISE content and hence, have high room temperature conductivities.[132,133] However, this method strongly depends on the capillarity and is not very appealing for large-scale application.

2.4 Challenges of the lithium metal anode

The lithium metal anode (LMA) is considered to be one of the most promising anode materials to boost both the volumetric and gravimetric density of next-generation lithium batteries. Lithium metal has the optimum properties due to its very low density (0.59 g cm^{-3}), the most negative electrochemical potential (–3.04 V *vs*. standard hydrogen electrode) and one of the highest theoretical capacities among all anode materials (3,860 mAh g^{-1} and 2061 mAh cm^{-3}, respectively). A key prerequisite for electrolytes is therefore (electro-)chemical stability against lithium metal to provide stable cycling. While liquid electrolytes in conventional LIBs are prone to unstable side reactions and are easily penetrated by lithium dendrites, SEs that are (electro-)chemically stable against lithium metal are considered to be able to suppress these negative effects, especially due to their intrinsic high shear modulus.[21]

In order to displace the current state-of-the-art graphite anode and to effectively increase the energy density, several cell performance parameters need to be achieved, such as high cycle areal capacity (> 3 mAh cm^{-2}), high current density (> 5 mA cm^{-2}), and high energy efficiency, which requires a low internal resistance (< 40 Ω cm^2) on the cell level.[134] With regard to the LMA, these targets are translated into requirements for both the Li|SE interface and the SE itself. The former should have very low and stable interfacial resistance (R_{int}) without minor influence of side reactions to retain all active lithium, and the latter has to be chemically stable against lithium metal and resistant to lithium dendrite formation. However, few reports come close to these targets because of poor interfacial contact of Li|SE caused by impurities, voids, or defects, and/or SE microstructure prone to lithium dendrite penetration while cycling due to low mechanical strength, i.e., pores, cracks, and vulnerable grain boundaries in the case of ISEs.[44]

This section firstly highlights the stationary Li|SE interface including chemical stability and strategies to reach low R_{int}. Secondly, the effects of current load, i.e., lithium stripping and plating, on the Li|SE interface will be discussed including interface kinetics and morphological aspects of both the SE and lithium metal. Thirdly, different mechanisms of lithium dendrite propagation are summarized with respect to the microstructure of the SE as well as lithium mechanics. Within all sections, the focus is on ISE systems and therein especially on LLZO. PSE systems with the focus on PEO-based PSEs are briefly highlighted at the end of each section.

2.4.1 Stationary interface with electrolyte

Interfacial phenomena of Li|SE are considered the bottleneck limiting high rate capabilities and stable cycling of the LMA. They determine not only the transport properties at the interface and related charge transfer kinetics in the stationary state (without external applied field), but also the lithium stripping and plating processes upon current load (see section 2.4.2).

In principle, the ideal SE is (electro-)chemically stable in contact with lithium metal. The interfacial stability is defined by the electrochemical stability window (ESW) that generally describes the thermodynamic stability of electrolytes in contact with electrodes. Due to the very high chemical potential of lithium metal, most SEs are not thermodynamically stable in contact with lithium metal, leading to the formation of an interphase layer consisting of decomposition products.[21] It can either conduct both ions and electrons resulting in progressive growth of the interphase (mixed conducting interphase, MCI), e.g, Ti^{4+} in LATP[135], or exclusively ions forming a kinetically self-limiting interphase (solid electrolyte interphase, SEI). Such an SEI can protect the SE from further reduction, which was found for PEO-based PSE, for example.[136,137] Incorporation of electrochemically more stable ISEs into PSEs (HSE approach) is proven to increase the ESW compared with the pure PSEs.[98,116] A special case in terms of (electro-)chemical stability is LLZO, as is the only practically relevant SE that is thermodynamically stable in contact with lithium metal. Even though recent reports have shown a nanoscale layer of reduced Zr^{4+} (oxygen-deficient interphase) by X-ray photoelectron spectroscopy (XPS) studies[74], this interphase was proven to have negligible influence on the charge transfer kinetics across the interface.[138]

In the other cases, interphase formation leads to substantial morphological and structural changes impeding interfacial charge transfer and ion transport at the interface. As a consequence, high interfacial resistances are observed over time affecting stripping/plating upon cycling (see section 2.4.2). Moreover, space charge can also cause resistive layers at the interface due to the depletion of ion species.[139] This especially applies for PSEs (and HSEs) as the anions are mobile (the transference number is mostly < 0.5).[109] Contrarily, space charge layers have marginal contribution for single ion conducting ISEs, as their transference number is close to unity. For LLZO, due to the absence of a bulk interphase, it could be shown theoretically and experimentally that the charge transfer is negligible (< 0.1 Ω cm^2) enabling fast kinetics sufficient for application.[140]

Despite the fact that LLZO has high stability and fast charge transfer kinetics, high interfacial impedences are observed in practical application.[141] These are mainly caused by current constriction phenomena from insufficient interfacial contact because of impurities (e.g., Li_2CO_3 due to environmental instability), voids and porosity in the microstructure, and local surface defects in both LLZO and lithium metal. Therefore, the true area of contact is often effectively smaller than the apparent, geometrical contact area.[142] Such inhomogeneous current distribution dramatically affect

the interface during lithium stripping and plating, which will be discussed in the next section. Even though PSEs (and HSEs) instrinsically should form an intimate contact with lithium metal due to their soft nature, they often suffer from the same interfacial issues in practical application.[143]

2.4.2 Dynamic interface: Stripping-Plating

During both anodic load, i.e., lithium stripping, and cathodic load, i.e., lithium plating, morphological changes are one of the major issues for stable cycling. These are caused by strong volume changes of lithium metal at the Li|SE interface and the related inhomogeneous current distribution. In the following sections, mechanisms during stripping are highlighted first and subsequently the plating mechanisms.

Stripping

During stripping, the diffusional properties of lithium metal are crucial. As every stripped metal ion leaves one vacant site, the replenishment of lithium to the interface highly depends on the diffusion of lithium atoms, i.e., more specifically vacancy diffusion ($J_{\text{Li diffusion}}$ with J being the flux), as well as on lithium metal creep ($J_{\text{Li creep}}$). The latter has minor influence when no external pressure is applied. If the vacancy diffusion limit in the lithium metal is not exceeded by the stripping current that removes lithium ions from the Li|ISE interface ($J_{\text{Li+ migration}}$), the interface remains structurally stable (Figure 2.4.1A).[141]

Above a critical current density, the stripping current removes lithium ions faster from the interface than lithium can be replenished according to Equation (2.4)[144]:

$$J_{\text{Li diffusion}} + J_{\text{Li creep}} < J_{\text{Li+ migration}} \qquad (2.4)$$

As a result, vacancies supersaturate and form voids and pores in the lithium metal, wherein adatam diffusion of the lithium pore is the limiting diffusional pathway (Figure 2.4.1B). Overall, such pore generation leads to contact loss at the interface. The remaining contact areas are hotspots for lithium plating during cathodic load triggering dendrite formation.[141,144]Plating mechanisms will be discussed in the following section. However, pore growth can be prevented by an externally applied pressure, stimulating the plastic deformation and creep of the lithium metal ($J_{\text{Li creep}}$), which is schematically represented in Figure 2.4.1C (see also strategies in section 2.4.4).[141]

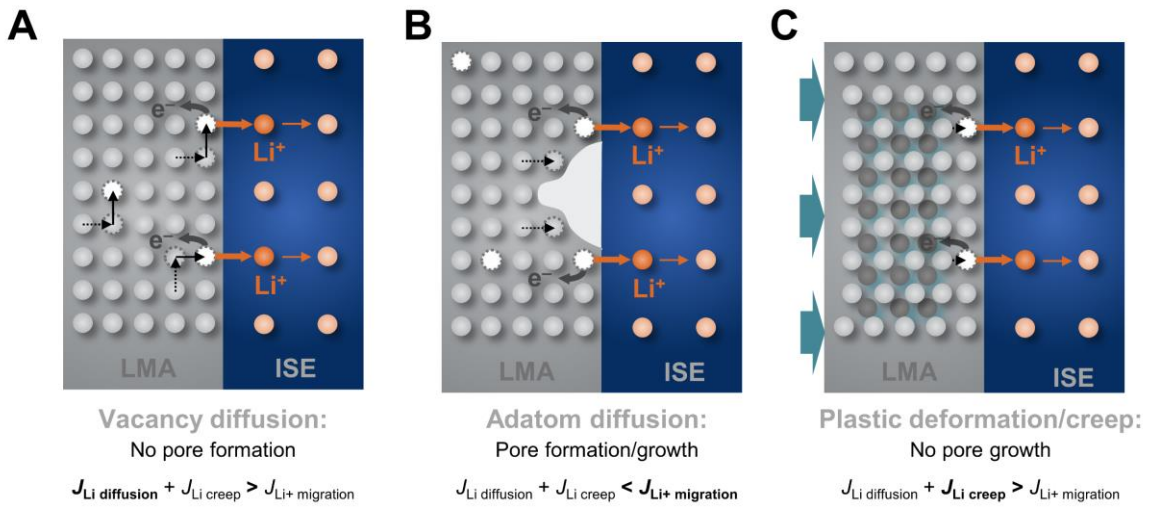

Figure 2.4.1. Schematic representation of the different mechanisms at the Li|ISE interface under anodic load, i.e., lithium stripping. (A) The interface remains structurally stable, if the stripping current that removes lithium ions from the interface ($J_{Li+\ migration}$) does not exceed the vacancy diffusion limit ($J_{Li\ diffusion}$) in the lithium metal. Lithium creep has minor influence without externally applied pressure. (B) If the stripping current removes lithium ions faster that lithium is replenished, pores will form and grow at the interface leading to contact loss. Herein, adatom diffusion of the pore is the limiting mechanism. (C) Upon externally applied pressure, plastic deformation and creep of the lithium metal prevent pore growth and contact loss. Adapted from [141].

Plating

During lithium plating, a layer-by-layer deposition of lithium metal at the interface would be favorable, which is not achievable in real application, especially at high current densities. Instead, lithium deposition is strongly affected by the interfacial properties and the related current distribution. Uneven current distribution at the interface leads to focusing of the current forming hotspots for lithium dendrite formation. The latter can propagate into the SE and lead to failure of the cell eventually (see section 2.4.3).[44] The main causes for current focusing are summarized in Figure 2.4.2 for a Li|ISE interface. They range from (i) poor interfacial contact, e.g., caused by the aforementioned void formation during stripping to (ii–iii) contaminations and surface defects or flaws at the interface of both the ISE and the lithium metal. Even for ideally contacted interfaces, current focusing can occur (iv) due to deviating ion transport properties along grain boundaries in polycrystalline materials. On the one hand, grain boundaries are prone to lithium deposition due to their mechanically softer nature.[145] On the other hand, the locally increased electro-chemo-mechanical potential due to the higher resistivity of the grain boundaries compared to the grains can lead to enhanced lithium deposition in the grain boundaries.[146] Therefore, reducing the grain size and thereby increasing the grain boundary area, achieves higher current densities.[147] However, there are also studies reporting the opposite, which the authors explained by the fact that less grain boundaries lead to less hotspots.[148]

By several *in situ* and *ex situ* microscopy techniques, mostly whisker-like structures have been observed at the Li|ISE interface as well as lateral dendritic growth at high current densities, which can locally be present due to current focusing.[140,149–151] Interestingly, optimized clean surfaces of LLZO with minimal inhomogeneities have shown that lithium plating at several A cm^{-2} is in principal possible, confirming the fast charge transfer kinetics of the Li|LLZO interface.[140]

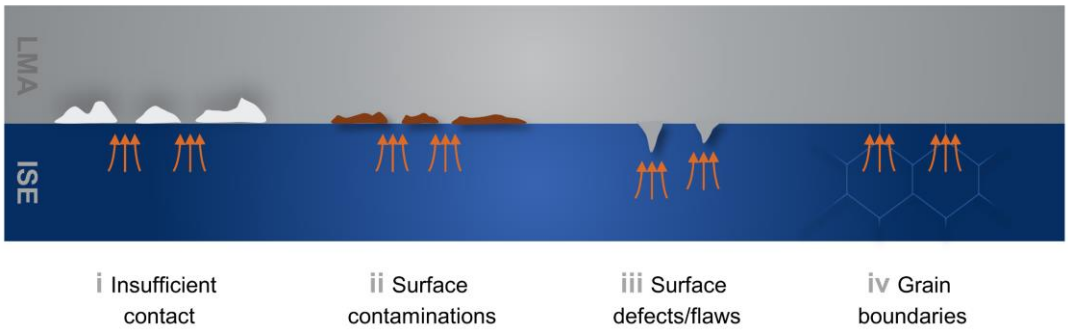

Figure 2.4.2. Different reasons for current focusing at the Li|ISE interface under cathodic load, i.e., lithium plating, ranging from poor interfacial contact/void formation (i), surface contaminations and surface defects/flaws at both the ISE and the lithium surface (ii–iii), and grain boundaries as potential hotspots for lithium dendrite formation. Adapted with permission from [21].

For PSEs, the main reason for lithium dendrite formation is also attributed to the issue of current dfocusing. In the same manner as for ISEs, impurities, defects and voids at the interface act as hotspots for lithium nucleation. In contrast, the distribution of charge at the interface substantially differs from that in single ion conducting ISEs. Due to the low Li^+ transference number of PSEs, space charge layers are easily formed at the Li|PSE interface due to the high anion mobility, which enhances lithium deposition during cathodic load.[44,79]

2.4.3 Dendrite growth mechanisms

Lithium metal depositions at the interface are usually the starting point of dendrite growth inside the SE, self-catalyzed by intensifying current focusing with increasing length of the dendrite.[149] The current density, above which a cell fails due to occurrence of short circuits, is defined as the critical current density (CCD). It is typically determined by the abrupt decrease of the cell's overpotential measured via galvanostatic cycling of lithium-symmetric cells. Caution is required for so-called "soft shorts" that are caused by very small lithium filaments and only induce a slight drop in overpotential. Therefore, they are easily overlooked and lead to overestimation of CCDs.[15,152] However, there is no standard protocol for CCD measurements, making literature values difficult to compare, as it is affected by measurement parameters, such as temperature, pressure, cycling duration, and thickness of the pellet. Most importantly, it strongly depends on the interfacial contact and it is also discussed to introduce a critical current *stripping* density or a critical potential instead.[144,153]

The growth of lithium filaments inside the SE highly depends on the microstructure and the mechanical properties of the SE. A model by Monroe and Newman predicted that SEs with roughly twice the shear modulus, i.e., elastic stiffness, of lithium metal (4.8 GPa at room temperature) are required for effective suppression of lithium dendrites.[154] Most ISEs (e.g., LLZO ~100 GPa[155]) and also some PSEs[156] fulfill this criterion but are still penetrated by lithium dendrites. CCD values are usually reported as lower than 1 mA cm^{-2} indicating that the factors determining dendrite formation are manifold (see ref. [21] for references).

For ISEs, stress-induced fracture upon lithium filament growth is a severe problem for both polycrystalline and single-crystalline materials. Figure 2.4.3A schematically shows the stress accumulation at the tip of the lithium surface flaw inducing crack opening in the ISE.[157,158] Following an electro-chemo-mechanical model, the maximum stress at the tip was found to increase with current density. Resulting current focusing at the tip can be accompanied by intensive Joule heating. Such local temperature fluctuations together with mechanical deformation also affect lithium mechanics, i.e., plastic deformation via creep, potentially amplifying crack opening.[159] Once a crack has formed, it can easily propagate and is a hotspot for further lithium deposition, which is shown by *in situ* recorded SEM images in Figure 2.4.3B.

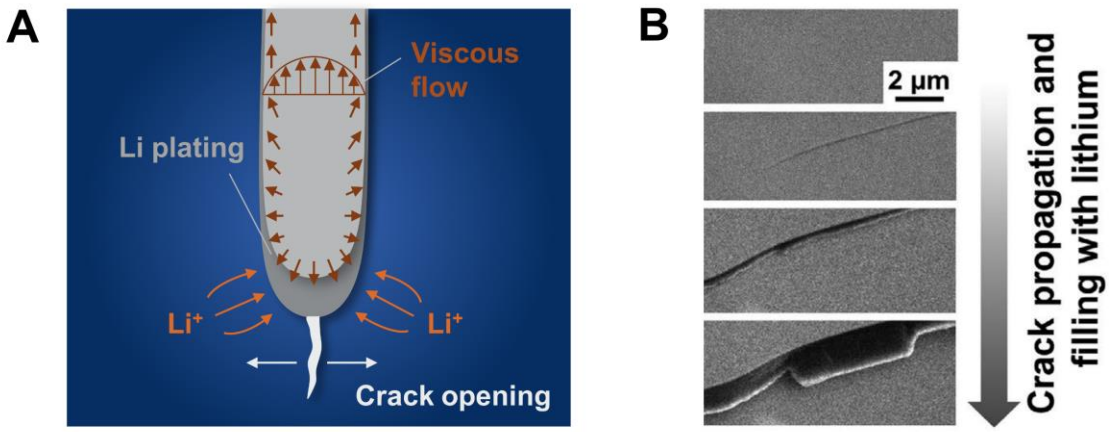

Figure 2.4.3. (A) Schematical representation of the mechanism of lithium dendrite growth in ISEs upon lithium plating. The stress accumulation at the dendrite tip leads to crack opening and propagation within the ISE. Adapted with permission from [159]. (B) *In situ* SEM images of a propagating crack in the ISE material LLZO that is directly filled with lithium metal. Reproduced with permission from [140].

Therefore, the fracture toughness of ISEs plays an important role, where oxides should be much more tolerant to this failure mode than sulfides.[21] Moreover, it is correlated to the microstructure, e.g., it was found that grain boundaries in polycrystalline LLZO are "soft spots" for dendrite susceptibility[160] as well as porosity, i.e. interconnected pores.[150,161] There is also a second failure mode discussed in literature, which is the nucleation of lithium metal inside the ISE due to partial electronic

conductivity, e.g., from the oxygen framework. However, this has probably minor influence and details can be found in several references.[153,162,163]

PSEs, including PEO-based PSEs, usually do not fulfill the shear modulus criterion of Monroe and Newman, as they have typically 2–3 orders of magnitude lower modulus than lithium metal.[164] Besides, most PSEs need to be operated at elevated temperatures due to their low room-temperature ionic conductivity, which reduces their elastic stiffness. Therefore, sharp lithium filaments nucleated at the Li|PSE interface can easily penetrate and grow in PSEs. Mostly mossy and needle-like structures have been observed *in situ*, pushing away the polymer and leading to delamination from the LMA.[165–167] As lithium filaments exhibit diameters in the range of microns, the growth mechanism through nanopores in the PSE has been considered unlikely.[164,168] Instead of solely considering elastic shear modulus, the elastic properties, i.e., the yield strength of both the PSE and lithium metal should be considered. Barai *et al.* postulated that dendrite formation can be suppressed by increasing the yield strength of the PSE, even with a shear modulus smaller than lithium metal.[79]

2.4.4 Strategies of lithium dendrite suppression

The manifold strategies to suppress lithium dendrite formation and penetration can roughly be divided into strategies related to the interface and to the SE itself, i.e., stiffness, microstructure, etc. While for ISEs the focus is mainly on interfacial improvements and microstructure optimization, reinforcing the mechanical strength is of higher importance for PSEs. Figure 2.4.4 schematically represents an overview of the most common strategies for lithium dendrite suppression in ISEs and PSEs that will be highlighted in this section.

One of the most straightforward strategies is to apply uniaxial pressure during current load in order to overcome interfacial issues. Especially, contact loss at the Li|ISE interface while stripping can be avoided due to plastic deformation of lithium metal (see Figure 2.4.1). For ISEs, stack pressures in the low MPa range (about 10 MPa) were found to be optimal for high CCDs.[169] However, such high pressures are detrimental for lithium plating because they can amplify mechanical stresses at the crack tip.[170] Therefore, applying intermediate pressure is inalienable for cell design. Conversely, elevated temperature has mainly positive effects on cycling performance. Higher temperature facilitates ionic transport in the ISE, charge transfer, and the mechanical properties of lithium metal, improving surface wetting.[171–174] Moreover, increasing the temperature, e.g. by a battery management system, can help to decrease the stack pressure required for practical application.

With respect to ISEs, other interface related strategies include primarily cleaning protocols, e.g., removing insulating Li_2CO_3 from the LLZO surface by polishing[175], annealing[176] or acid treatment[177], or introduction of very thin interphase layers. These can either be (1) electronically conducting metal interlayers (alloy-based, e.g., sputtering of an Au layer on LLZO *in situ* forms a Li–Au alloy[178]

(Li–Mg, Li–Ag, Li–Sn were reported as well[179–181]), (2) ionically conducting SEI layers (Li_3N, $Li_2Al_4O_7$ by ALD coating with Al_2O_3, or PSE coatings[182–184]) or (3) mixed conducting interlayers (LiC_6, Li_2S-Mo, and Li_3N-Cu from conversion reactions[185–187]). They all aim to decrease the interfacial resistance and provide homogeneous current upon cycling. However, most researchers postulate that the ideal interphase layer should be highly ionically conducting, but electronically insulating to prevent electron injection into the ISE.[188]

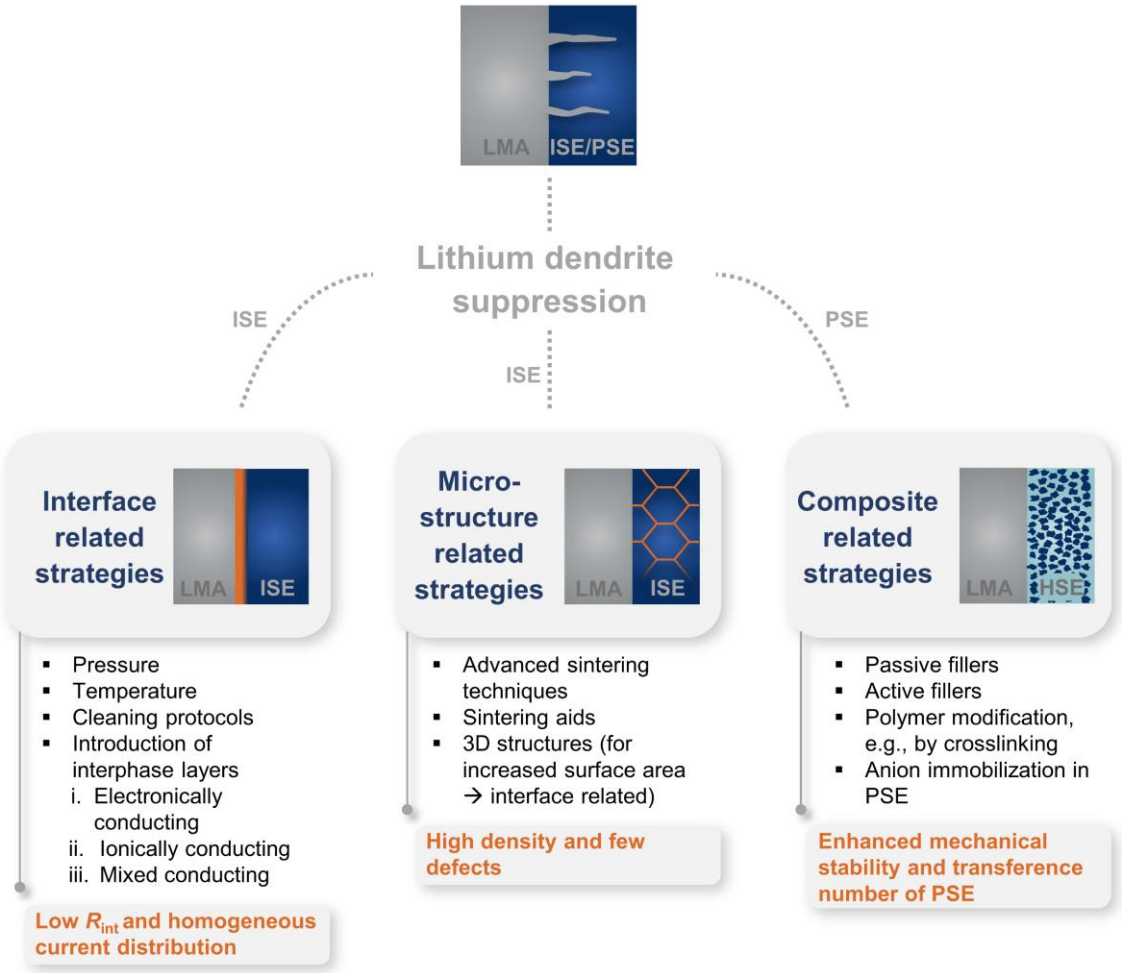

Figure 2.4.4. Summary of most common strategies to overcome lithium dendrite formation in ISEs including interface and microstructure related approaches as well as in PSEs comprising composite related strategies.

Several approaches have been applied to optimize the microstructure of the ISE in terms of density and grain boundary modification. Besides different pressing strategies, such as conventional uniaxial cold or hot pressing, isostatic pressing and fast-sintering techniques (e.g., spark plasma sintering, SPS)[189–191], liquid phase sintering has broadly been used (see section 2.3.1.2). The sintering aid often segregates into the grain boundaries and thereby improves lithium dendrite suppression.[65,66,192,193] In addition to high-density approaches, porous ISE structures have proven to exhibit high CCDs

(e.g., porous LLZO in a trilaminar setup with dense LLZO in-between, CCD up to 10 mA cm^{-2} [194]) due to extensive increase of contact area.

A common strategy for PSEs is the HSE approach in order to increase mechanical stability. As described in section 2.3.2, both inactive (mostly SiO_2 and Al_2O_3) and active fillers can be used. It has been shown by several examples that the tensile modulus of the PSE can be increased up to tenfold, thereby increasing the CCD compared to the pure PSE.[195,196] Another approach, similar to the addition of inactive fillers, is to add another polymer for crosslinking, e.g., via photopolymerization, resulting in a rigid network.[156] The use of ISE particles as active filler is expected to not only enhance the mechanical strength but also the ionic conductivity. Furthermore, it can compensate the space charge effects at the Li|PSE interface as the polymer matrix and the filler particles can potentially constrict anion movement, thereby increasing the transference number of the HSE and regulating homogeneous lithium plating.[197–199] However, up to now, the ion transport mechanism of HSEs is not fully understood (see section 2.3.2.1). The optimum setting of the polymer to filler ratio is also challenging in order to balance the different requirements, i.e., high polymer content for good interfacial contact with electrodes and high filler ratio for sufficient dendrite suppression. There are manifold reports related to that topic but they differ substantially in measurement parameters, filler properties, and manufacturing processes, impeding direct comparability.[96,100,130,200,201]

The lithium metal itself can also be optimized by 3D structuring for example, but this goes beyond the scope of this work, and the reader is referred to the following references.[202,203]

2.5 References

(1) Korthauer, R., Ed. *Handbuch Lithium-Ionen-Batterien*, 1st ed.; Springer Berlin / Heidelberg. **2013**.

(2) Goodenough, J. B.; Park, K.-S. The Li-Ion Rechargeable Battery: A Perspective. *J. Am. Chem. Soc.* **2013**, *135*, 1167–1176.

(3) Placke, T.; Kloepsch, R.; Dühnen, S.; Winter, M. Lithium Ion, Lithium Metal, and Alternative Rechargeable Battery Technologies: The Odyssey for High Energy Density. *J. Solid State Electrochem.* **2017**, *21*, 1939–1964.

(4) Tarascon, J. M.; Armand, M. Issues and Challenges Facing Rechargeable Lithium Batteries. *Nature* **2001**, *414*, 359–367.

(5) Dr. Thomas Schmaltz; Tim Wicke; Dr. Lukas Weymann; Philipp Voß; Dr. Christoph Neef; Dr. Axel Thielmann. *Solid-State Battery Roadmap 2035+*; Fraunhofer-Institut für System- und Innovationsforschung ISI. **2022**.

(6) Blomgren, G. E. The Development and Future of Lithium Ion Batteries. *J. Electrochem. Soc.* **2017**, *164*, A5019-A5025.

(7) Thielmann, A.; Neef, C.; Hettesheimer, T.; Döscher, H.; Wietschel, M.; Tübke, J. *Energiespeicher-Roadmap (Update 2017): Hochenergie-Batterien 2030+ und Perspektiken zukünftiger Batterietechnologien*; Fraunhofer-Institut für System- und Innovationsforschung ISI. **2017**.

(8) Kurzweil, P.; Dietlmeier, O. *Elektrochemische Speicher*:*Superkondensatoren, Batterien, Elektrolyse-Wasserstoff, rechtliche Grundlagen*; Lehrbuch; Springer Vieweg. **2015.** DOI: 10.1007/978-3-658-10900-4.

(9) Janek, J.; Zeier, W. G. A Solid Future for Battery Development. *Nat. Energy* **2016**, *1*, 16141.

(10) Pasta, M.; Armstrong, D.; Brown, Z. L.; Bu, J.; Castell, M. R.; Chen, P.; Cocks, A.; Corr, S. A.; Cussen, E. J.; Darnbrough, E.*; et al.* 2020 Roadmap on Solid-State Batteries. *J. Phys.: Energy* **2020**, *2*, 32008.

(11) Wieser, M.; Moroz, S. Rechargeable Batteries - Past, Present and Future. *Energy News* **2018**, *36*, 5–7.

(12) Jin, Y.; Zhu, B.; Lu, Z.; Liu, N.; Zhu, J. Challenges and Recent Progress in the Development of Si Anodes for Lithium-Ion Battery. *Adv. Energy Mater.* **2017**, *7*, 1700715.

(13) Guo, Y.; Li, H.; Zhai, T. Reviving Lithium-Metal Anodes for Next-Generation High-Energy Batteries. *Adv. Mater.* **2017**, *29*.

(14) Love, C. T.; Baturina, O. A.; Swider-Lyons, K. E. Observation of Lithium Dendrites at Ambient Temperature and Below. *ECS Electrochemistry Letters* **2014**, *4*, A24-A27.

(15) Albertus, P.; Babinec, S.; Litzelman, S.; Newman, A. Status and Challenges in Enabling the Lithium Metal Electrode for High-Energy and Low-Cost Rechargeable Batteries. *Nat. Energy* **2017**, *3*, 16–21.

(16) Zhao, W.; Yi, J.; He, P.; Zhou, H. Solid-State Electrolytes for Lithium-Ion Batteries: Fundamentals, Challenges and Perspectives. *Electrochem. Energ. Rev.* **2019**, *2*, 574–605.

(17) Liu, H.; Cheng, X.-B.; Huang, J.-Q.; Yuan, H.; Lu, Y.; Yan, C.; Zhu, G.-L.; Xu, R.; Zhao, C.-Z.; Hou, L.-P.*; et al.* Controlling Dendrite Growth in Solid-State Electrolytes. *ACS Energy Lett.* **2020**, *5*, 833–843.

(18) Weiss, M.; Ruess, R.; Kasnatscheew, J.; Levartovsky, Y.; Levy, N. R.; Minnmann, P.; Stolz, L.; Waldmann, T.; Wohlfahrt-Mehrens, M.; Aurbach, D.*; et al.* Fast Charging of Lithium-Ion Batteries: A Review of Materials Aspects. *Adv. Energy Mater.* **2021**, *11*, 2101126.

(19) Taylor, N. J.; Sakamoto, J. Solid-State Batteries: Unlocking Lithium's Potential with Ceramic Solid Electrolytes. *Am. Ceram. Soc. Bull.* **2019**, *98*, 26–31.

(20) Jiang, Z.; Han, Q.; Wang, S.; Wang, H. Reducing the Interfacial Resistance in All-Solid-State Lithium Batteries Based on Oxide Ceramic Electrolytes. *ChemElectroChem* **2019**, *6*, 2970–2983.

(21) Krauskopf, T.; Richter, F. H.; Zeier, W. G.; Janek, J. Physicochemical Concepts of the Lithium Metal Anode in Solid-State Batteries. *Chem. Rev.* **2020**, *120*, 7745–7794.

(22) Liang, J.; Luo, J.; Sun, Q.; Yang, X.; Li, R.; Sun, X. Recent Progress on Solid-State Hybrid Electrolytes for Solid-State Lithium Batteries. *Energy Stor. Mater.* **2019**, *21*, 308–334.

(23) He, F.; Hu, Z.; Tang, W.; Wang, A.; Wen, B.; Zhang, L.; Luo, J. Vertically Heterostructured Solid Electrolytes for Lithium Metal Batteries. *Adv. Funct. Mater.* **2022**, *32*, 2201465.

(24) Zhang, Z.; Shao, Y.; Lotsch, B.; Hu, Y.-S.; Li, H.; Janek, J.; Nazar, L. F.; Nan, C.-W.; Maier, J.; Armand, M.*; et al.* New Horizons for Inorganic Solid State Ion Conductors. *Energy Environ. Sci.* **2018**, *11*, 1945–1976.

(25) DeWees, R.; Wang, H. Synthesis and Properties of NaSICON-type LATP and LAGP Solid Electrolytes. *ChemSusChem* **2019**, *12*, 3713–3725.

(26) Kumar, B.; Thomas, D.; Kumar, J. Space-Charge-Mediated Superionic Transport in Lithium Ion Conducting Glass–Ceramics. *J. Electrochem. Soc.* **2009**, *156*, A506.

(27) Hou, M.; Liang, F.; Chen, K.; Dai, Y.; Xue, D. Challenges and Perspectives of NASICON-Type Solid Electrolytes for All-Solid-State Lithium Batteries. *Nanotechnology* **2020**, *31*, 132003.

(28) Lu, J.; Li, Y. Perovskite-Type Li-Ion Solid Electrolytes: A Review. *J. Mater. Sci.: Mater. Electron.* **2021**, *32*, 9736–9754.

(29) Thangadurai, V.; Narayanan, S.; Pinzaru, D. Garnet-Type Solid-State Fast Li Ion Conductors for Li Batteries: Critical Review. *Chem. Soc. Rev.* **2014**, *43*, 4714–4727.

(30) Murugan, R.; Thangadurai, V.; Weppner, W. Schnelle Lithiumionenleitung in Granatartigem $Li_7La_3Zr_2O_{12}$. *Angew. Chem.* **2007**, *119*, 7925–7928.

(31) Alpen, U. v.; Rabenau, A.; Talat, G. H. Ionic Conductivity in Li_3N Single Crystals. *Appl. Phys. Lett.* **1977**, *30*, 621–623.

(32) Wang, K.; Ye, Q.; Zhang, J.; Huang, H.; Gan, Y.; He, X.; Zhang, W. Halide Electrolyte Li_3InCl_6-Based All-Solid-State Lithium Batteries With Slurry-Coated $LiNi_{0.8}Co_{0.1}Mn_{0.1}O_2$ Composite Cathode: Effect of Binders. *Front. Mater.* **2021**, *8*.

(33) Hikima, K.; Huy Phuc, N. H.; Tsukasaki, H.; Mori, S.; Muto, H.; Matsuda, A. High Ionic Conductivity of Multivalent Cation Doped Li_6PS_5Cl Solid Electrolytes Synthesized by Mechanical Milling. *RSC Adv.* **2020**, *10*, 22304–22310.

(34) Zhijian Sun; Lei Liu; Yuxiao Lu; Guangyue Shi; Jiajun Li; Lei Ma; Jie Zhao; Hongli An. Preparation and Ionic Conduction of $Li_{1.5}Al_{0.5}Ge_{1.5}(PO_4)_3$ Solid Electrolyte Using Inorganic Germanium as Precursor. *J. Eur. Ceram. Soc.* **2019**, *39*, 402–408.

(35) Düvel, A.; Kuhn, A.; Robben, L.; Wilkening, M.; Heitjans, P. Mechanosynthesis of Solid Electrolytes: Preparation, Characterization, and Li Ion Transport Properties of Garnet-Type Al-Doped $Li_7La_3Zr_2O_{12}$ Crystallizing with Cubic Symmetry. *J. Phys. Chem. C* **2012**, *116*, 15192–15202.

(36) Kamaya, N.; Homma, K.; Yamakawa, Y.; Hirayama, M.; Kanno, R.; Yonemura, M.; Kamiyama, T.; Kato, Y.; Hama, S.; Kawamoto, K.*; et al.* A Lithium Superionic Conductor. *Nat. Mater.* **2011**, *10*, 682–686.

(37) Minami, K.; Hayashi, A.; Tatsumisago, M. Crystallization Process for Superionic $Li_7P_3S_{11}$ Glass-Ceramic Electrolytes. *J. Am. Ceram. Soc.* **2011**, *94*, 1779–1783.

(38) Mizuno, F.; Hayashi, A.; Tadanaga, K.; Tatsumisago, M. New, Highly Ion-Conductive Crystals Precipitated from Li_2S-P_2S_5 Glasses. *Adv. Mater.* **2005**, *17*, 918–921.

(39) Adachi, G.; Imanaka, N.; Aono, H. Fast Li+ Conducting Ceramic Electrolytes. *Adv. Mater.* **1996**, *8*, 127–135.

(40) Inaguma, Y.; Liquan, C.; Itoh, M.; Nakamura, T.; Uchida, T.; Ikuta, H.; Wakihara, M. High Ionic Conductivity in Lithium Lanthanum Titanate. *Solid State Commun.* **1993**, *86*, 689–693.

(41) Chen, S.; Xie, D.; Liu, G.; Mwizerwa, J. P.; Zhang, Q.; Zhao, Y.; Xu, X.; Yao, X. Sulfide Solid Electrolytes for All-Solid-State Lithium Batteries: Structure, Conductivity, Stability and Application. *Energy Stor. Mater.* **2018**, *14*, 58–74.

(42) Jonderian, A.; McCalla, E. The Role of Metal Substitutions in the Development of Li Batteries, Part II: Solid Electrolytes. *Mater. Adv.* **2021**, *2*, 2846–2875.

(43) Manthiram, A.; Yu, X.; Wang, S. Lithium Battery Chemistries Enabled by Solid-State Electrolytes. *Nat. Rev. Mater.* **2017**, *2*.

(44) Cao, D.; Sun, X.; Li, Q.; Natan, A.; Xiang, P.; Zhu, H. Lithium Dendrite in All-Solid-State Batteries: Growth Mechanisms, Suppression Strategies, and Characterizations. *Matter* **2020**, *3*, 57–94.

(45) Bachman, J. C.; Muy, S.; Grimaud, A.; Chang, H.-H.; Pour, N.; Lux, S. F.; Paschos, O.; Maglia, F.; Lupart, S.; Lamp, P.*; et al.* Inorganic Solid-State Electrolytes for Lithium Batteries: Mechanisms and Properties Governing Ion Conduction. *Chem. Rev.* **2016**, *116*, 140–162.

(46) Richard J.D. Tilley. *Understanding Solids: The Science of Materials*; John Wiley & Sons Ltd. **2013**.

(47) Xu, K. Nonaqueous Liquid Electrolytes for Lithium-Based Rechargeable Batteries. *Chem. Rev.* **2004**, *104*, 4303–4417.

(48) Schweiger, L.; Hogrefe, K.; Gadermaier, B.; Rupp, J. L. M.; Wilkening, H. M. R. Ionic Conductivity of Nanocrystalline and Amorphous $Li_{10}GeP_2S_{12}$: The Detrimental Impact of Local Disorder on Ion Transport. *J. Am. Chem. Soc.* **2022**, *144*, 9597–9609.

(49) Wohlmuth, D.; Epp, V.; Bottke, P.; Hanzu, I.; Bitschnau, B.; Letofsky-Papst, I.; Kriechbaum, M.; Amenitsch, H.; Hofer, F.; Wilkening, M. Order vs. Disorder - A Huge Increase in Ionic Conductivity of Nanocrystalline $LiAlO_2$ Embedded in an Amorphous-Like Matrix of Lithium Aluminate. *J. Mater. Chem. A* **2014**, *2*, 20295–20306.

(50) Chen, S.; Hu, X.; Bao, W.; Wang, Z.; Yang, Q.; Nie, L.; Zhang, X.; Zhang, J.; Jiang, Y.; Han, Y.*; et al.* Low-Sintering-Temperature Garnet Oxides by Conformal Sintering-Aid Coating. *Cell Rep. Phys. Sci.* **2021**, *2*, 100569.

(51) Zheng, C.; Ruan, Y.; Su, J.; Song, Z.; Xiu, T.; Jin, J.; Badding, M. E.; Wen, Z. Grain Boundary Modification in Garnet Electrolyte to Suppress Lithium Dendrite Growth. *Chem. Eng. J.* **2021**, *411*, 128508.

(52) Schirmeisen, A.; Taskiran, A.; Fuchs, H.; Bracht, H.; Murugavel, S.; Roling, B. Fast Interfacial Ionic Conduction in Nanostructured Glass Ceramics. *Phys. Rev. Lett.* **2007**, *98*, 225901.

(53) Banik, A.; Famprikis, T.; Ghidiu, M.; Ohno, S.; Kraft, M. A.; Zeier, W. G. On the Underestimated Influence of Synthetic Conditions in Solid Ionic Conductors. *Chem. Sci.* **2021**, *12*, 6238–6263.

(54) Kokal, I.; Somer, M.; Notten, P.; Hintzen, H. T. Sol–gel Synthesis and Lithium Ion Conductivity of $Li_7La_3Zr_2O_{12}$ with Garnet-Related Type Structure. *Solid State Ionics* **2011**, *185*, 42–46.

(55) Chen, R.-J.; Huang, M.; Huang, W.-Z.; Shen, Y.; Lin, Y.-H.; Nan, C.-W. Effect of Calcining and Al Doping on Structure and Conductivity of $Li_7La_3Zr_2O_{12}$. *Solid State Ionics* **2014**, *265*, 7–12.

(56) Schneider, M.; Hochrein, O.; Wolfgang, S.; Kunze, M. Ionenleitende Glaskeramik mit Granatartiger Kristallstruktur. DE102014100684A1, **2015**.

(57) Yamada, H.; Ito, T.; Hongahally Basappa, R. Sintering Mechanisms of High-Performance Garnet-type Solid Electrolyte Densified by Spark Plasma Sintering. *Electrochim. Acta* **2016**, *222*, 648–656.

(58) Botros, M.; Djenadic, R.; Clemens, C.; Möller, M.; Hahn, H. Field Assisted Sintering of Fine-Grained $Li_{7-3x}La_3Zr_2Al_xO_{12}$ Solid Electrolyte and the Influence of the Microstructure on the Electrochemical Performance. *J. Power Sources* **2014**, *309*, 108–115.

(59) Gao, D.; Wu, R.; Chen, P.; Hong, T.; Cheng, J. Microwave Assisted Reactive Sintering for Al Doped $Li_7La_3Zr_2O_{12}$ Lithium Ion Solid State Electrolyte. *Mater. Res. Express* **2019**, *6*, 125539.

(60) Paolella, A.; Zhu, W.; Bertoni, G.; Savoie, S.; Feng, Z.; Demers, H.; Gariepy, V.; Girard, G.; Rivard, E.; Delaporte, N.*; et al.* Discovering the Influence of Lithium Loss on Garnet $Li_7La_3Zr_2O_{12}$ Electrolyte Phase Stability. *ACS Appl. Energy Mater.* **2020**, *3*, 3415–3424.

(61) German, R. M.; Suri, P.; Park, S. J. Review: Liquid Phase Sintering. *J. Mater. Sci.* **2009**, *44*, 1–39.

(62) Telle, R. *Keramik*, 7th ed.; Springer Berlin / Heidelberg. **2007**.

(63) Li, Y.; Wang, Z.; Li, C.; Cao, Y.; Guo, X. Densification and Ionic-Conduction Improvement of Lithium Garnet Solid Electrolytes by Flowing Oxygen Sintering. *J. Power Sources* **2014**, *248*, 642–646.

(64) Li, Y.; Cao, Y.; Guo, X. Influence of Lithium Oxide Additives on Densification and Ionic Conductivity of Garnet-Type $Li_{6.75}La_3Zr_{1.75}Ta_{0.25}O_{12}$ Solid Electrolytes. *Solid State Ionics* **2013**, *253*, 76–80.

(65) Basappa, R. H.; Ito, T.; Morimura, T.; Bekarevich, R.; Mitsuishi, K.; Yamada, H. Grain Boundary Modification to Suppress Lithium Penetration through Garnet-Type Solid Electrolyte. *J. Power Sources* **2017**, *363*, 145–152.

(66) Xu, B.; Li, W.; Duan, H.; Wang, H.; Guo, Y.; Li, H.; Liu, H. Li_3PO_4-Added Garnet-Type $Li_{6.5}La_3Zr_{1.5}Ta_{0.5}O_{12}$ for Li-Dendrite Suppression. *J. Power Sources* **2017**, *354*, 68–73.

(67) Awaka, J.; Kijima, N.; Hayakawa, H.; Akimoto, J. Synthesis and Structure Analysis of Tetragonal $Li_7La_3Zr_2O_{12}$ with the Garnet-Related Type Structure. *J. Solid State Chem.* **2009**, *182*, 2046–2052.

(68) Samson, A. J.; Hofstetter, K.; Bag, S.; Thangadurai, V. A Bird's-Eye View of Li-Stuffed Garnet-Type $Li_7La_3Zr_2O_{12}$ Ceramic Electrolytes for Advanced All-Solid-State Li Batteries. *Energy Environ. Sci.* **2019**, *12*, 2957–2975.

(69) Xu, M.; Park, M. S.; Lee, J. M.; Kim, T. Y.; Park, Y. S.; Ma, E. Mechanisms of Li+ Transport in Garnet-Type Cubic $Li_{3+x}La_3M_2O_{12}$ (M = Te, Nb, Zr). *Phys. Rev. B* **2012**, *85*.

(70) Thangadurai, V.; Pinzaru, D.; Narayanan, S.; Baral, A. K. Fast Solid-State Li Ion Conducting Garnet-Type Structure Metal Oxides for Energy Storage. *J. Phys. Chem. Lett.* **2015**, *6*, 292–299.

(71) Adams, S.; Rao, R. P. Ion Transport and Phase Transition in $Li_{7-x}La_3(Zr_{2-x}M_x)O_{12}$ (M = Ta^{5+}, Nb^{5+}, x = 0, 0.25). *J. Mater. Chem.* **2012**, *22*, 1426–1434.

(72) Miara, L. J.; Richards, W. D.; Wang, Y. E.; Ceder, G. First-Principles Studies on Cation Dopants and Electrolyte|Cathode Interphases for Lithium Garnets. *Chem. Mater.* **2015**, *27*, 4040–4047.

(73) Shin, D. O.; Oh, K.; Kim, K. M.; Park, K.-Y.; Lee, B.; Lee, Y.-G.; Kang, K. Synergistic Multi-Doping Effects on the $Li_7La_3Zr_2O_{12}$ Solid Electrolyte for Fast Lithium Ion Conduction. *Scientific Reports* **2015**, *5*, 18053.

(74) Zhu, Y.; Connell, J. G.; Tepavcevic, S.; Zapol, P.; Garcia-Mendez, R.; Taylor, N. J.; Sakamoto, J.; Ingram, B. J.; Curtiss, L. A.; Freeland, J. W.*; et al.* Dopant-Dependent Stability of Garnet Solid Electrolyte Interfaces with Lithium Metal. *Adv. Energy Mater.* **2019**, *9*, 1803440.

(75) Qin, S.; Zhu, X.; Jiang, Y.; Ling, M.; Hu, Z.; Zhu, J. Growth of Self-Textured Ga^{3+}-substituted $Li_7La_3Zr_2O_{12}$ Ceramics by Solid State Reaction and their Significant Enhancement in Ionic Conductivity. *Appl. Phys. Lett.* **2018**, *112*, 113901.

(76) Zhang, L.; Zhuang, Q.; Zheng, R.; Wang, Z.; Sun, H.; Arandiyan, H.; Wang, Y.; Liu, Y.; Shao, Z. Recent Advances of $Li_7La_3Zr_2O_{12}$-Based Solid-State Lithium Batteries towards High Energy Density. *Energy Stor. Mater.* **2022**, *49*, 299–338.

(77) Sharafi, A.; Yu, S.; Naguib, M.; Lee, M.; Ma, C.; Meyer, H. M.; Nanda, J.; Chi, M.; Siegel, D. J.; Sakamoto, J. Impact of Air Exposure and Surface Chemistry on Li–$Li_7La_3Zr_2O_{12}$ Interfacial Resistance. *J. Mater. Chem. A* **2017**, *5*, 13475–13487.

(78) Huo, H.; Luo, J.; Thangadurai, V.; Guo, X.; Nan, C.-W.; Sun, X. Li_2CO_3: A Critical Issue for Developing Solid Garnet Batteries. *ACS Energy Lett.* **2020**, *5*, 252–262.

(79) Barai, P.; Higa, K.; Srinivasan, V. Lithium Dendrite Growth Mechanisms in Polymer Electrolytes and Prevention Strategies. *Phys. Chem. Chem. Phys.* **2017**, *19*, 20493–20505.

(80) Keller, M.; Varzi, A.; Passerini, S. Hybrid Electrolytes for Lithium Metal Batteries. *J. Power Sources* **2018**, *392*, 206–225.

(81) Li, S.; Zhang, S.-Q.; Shen, L.; Liu, Q.; Ma, J.-B.; Lv, W.; He, Y.; Yang, Q.-H. Progress and Perspective of Ceramic/Polymer Composite Solid Electrolytes for Lithium Batteries. *Adv. Sci.* **2020**, *7*, 1903088.

(82) Jiang, Y.; Yan, X.; Ma, Z.; Mei, P.; Xiao, W.; You, Q.; Zhang, Y. Development of the PEO Based Solid Polymer Electrolytes for All-Solid State Lithium Ion Batteries. *Polymers* **2018**, *10*.

(83) Ding, P.; Lin, Z.; Guo, X.; Wu, L.; Wang, Y.; Guo, H.; Li, L.; Yu, H. Polymer Electrolytes and Interfaces in Solid-State Lithium Metal Batteries. *Mater. Today* **2021**, *51*, 449–474.

(84) Croce, F. Nanocomposite Polymer Electrolytes and Their Impact on the Lithium Battery Technology. *Solid State Ionics* **2000**, *135*, 47–52.

(85) Lin, D.; Liu, W.; Liu, Y.; Lee, H. R.; Hsu, P.-C.; Liu, K.; Cui, Y. High Ionic Conductivity of Composite Solid Polymer Electrolyte via In Situ Synthesis of Monodispersed SiO_2 Nanospheres in Poly(ethylene Oxide). *Nano Lett.* **2016**, *16*, 459–465.

(86) Xi, J.; Qiu, X.; Ma, X.; Cui, M.; Yang, J.; Tang, X.; Zhu, W.; Chen, L. Composite Polymer Electrolyte Doped with Mesoporous Silica SBA-15 for Lithium Polymer Battery. *Solid State Ionics* **2005**, *176*, 1249–1260.

(87) Li, L.; Deng, Y.; Chen, G. Status and Prospect of Garnet/Polymer Solid Composite Electrolytes for All-Solid-State Lithium Batteries. *J. Energy Chem.* **2020**, *50*, 154–177.

(88) Xia, S.; Wu, X.; Zhang, Z.; Cui, Y.; Liu, W. Practical Challenges and Future Perspectives of All-Solid-State Lithium-Metal Batteries. *Chem* **2019**, *5*, 753–785.

(89) Money, B. K.; Swenson, J. Dynamics of Poly(ethylene Oxide) around Its Melting Temperature. *Macromolecules* **2013**, *46*, 6949–6954.

(90) Ratner, M. A.; Johansson, P.; Shriver, D. F. Polymer Electrolytes: Ionic Transport Mechanisms and Relaxation Coupling. *MRS Bull.* **2000**, *25*, 31–37.

(91) Quartarone, E.; Mustarelli, P. Electrolytes for Solid-State Lithium Rechargeable Batteries: Recent Advances and Perspectives. *Chem. Soc. Rev.* **2011**, *40*, 2525–2540.

(92) Sen, S.; Trevisanello, E.; Niemöller, E.; Shi, B.-X.; Simon, F. J.; Richter, F. H. The Role of Polymers in Lithium Solid-State Batteries with Inorganic Solid Electrolytes. *J. Mater. Chem. A* **2021**, *9*, 18701–18732.

(93) Srivastava, S.; Schaefer, J. L.; Yang, Z.; Tu, Z.; Archer, L. A. 25th Anniversary Article: Polymer-Particle Composites: Phase Stability and Applications in Electrochemical Energy Storage. *Adv. Mater.* **2014**, *26*, 201–234.

(94) Wang, W.; Yi, E.; Fici, A. J.; Laine, R. M.; Kieffer, J. Lithium Ion Conducting Poly(ethylene Oxide)-Based Solid Electrolytes Containing Active or Passive Ceramic Nanoparticles. *J. Phys. Chem. C* **2017**, *121*, 2563–2573.

(95) Zhang, J.; Zang, X.; Wen, H.; Dong, T.; Chai, J.; Li, Y.; Chen, B.; Zhao, J.; Dong, S.; Ma, J.; *et al.* High-Voltage and Free-Standing Poly(propylene Carbonate)/$Li_{6.75}La_3Zr_{1.75}Ta_{0.25}O_{12}$ Composite Solid Electrolyte for Wide Temperature Range and Flexible Solid Lithium Ion Battery. *J. Mater. Chem. A* **2017**, *5*, 4940–4948.

(96) Zagórski, J.; Del López Amo, J.; Cordill, M. J.; Aguesse, F.; Buannic, L.; Llordés, A. Garnet-Polymer Composite Electrolytes: New Insights on Local Li-Ion Dynamics and Electrodeposition Stability with Li Metal Anodes. *ACS Appl. Energy Mater.* **2019**, 1734–1746.

(97) Li, Z.; Huang, H.-M.; Zhu, J.-K.; Wu, J.-F.; Yang, H.; Wei, L.; Guo, X. Ionic Conduction in Composite Polymer Electrolytes: Case of PEO:Ga-LLZO Composites. *ACS Appl. Mater. Interfaces* **2019**, *11*, 784–791.

(98) Zhang, J.; Zhao, N.; Zhang, M.; Li, Y.; Chu, P. K.; Guo, X.; Di, Z.; Wang, X.; Li, H. Flexible and Ion-Conducting Membrane Electrolytes for Solid-State Lithium Batteries: Dispersion of Garnet Nanoparticles in Insulating Polyethylene Oxide. *Nano Energy* **2016**, *28*, 447–454.

(99) Croce, F.; Appetecchi, G. B.; Persi, L.; Scrosati, B. Nanocomposite Polymer Electrolytes for Lithium Batteries. *Nature* **1998**, *394*, 456–458.

(100) Huo, H.; Chen, Y.; Luo, J.; Yang, X.; Guo, X.; Sun, X. Rational Design of Hierarchical "Ceramic-in-Polymer" and "Polymer-in-Ceramic" Electrolytes for Dendrite-Free Solid-State Batteries. *Adv. Energy Mater.* **2019**, *9*, 1804004.

(101) Liu, W.; Lee, S. W.; Lin, D.; Shi, F.; Wang, S.; Sendek, A. D.; Cui, Y. Enhancing Ionic Conductivity in Composite Polymer Electrolytes with Well-Aligned Ceramic Nanowires. *Nat. Energy* **2017**, *2*.

(102) Cai, D.; Wang, D.; Chen, Y.; Zhang, S.; Wang, X.; Xia, X.; Tu, J. A Highly Ion-Conductive Three-Dimensional LLZAO-PEO/LiTFSI Solid Electrolyte for High-Performance Solid-State Batteries. *Chem. Eng. J.* **2020**, *394*, 124993.

(103) Yang, T.; Zheng, J.; Cheng, Q.; Hu, Y.-Y.; Chan, C. K. Composite Polymer Electrolytes with $Li_7La_3Zr_2O_{12}$ Garnet-Type Nanowires as Ceramic Fillers: Mechanism of Conductivity Enhancement and Role of Doping and Morphology. *ACS Appl. Mater. Interfaces* **2017**, *9*, 21773–21780.

(104) Zhai, H.; Xu, P.; Ning, M.; Cheng, Q.; Mandal, J.; Yang, Y. A Flexible Solid Composite Electrolyte with Vertically Aligned and Connected Ion-Conducting Nanoparticles for Lithium Batteries. *Nano Lett.* **2017**, *17*, 3182–3187.

(105) Sagane, F.; Abe, T.; Iriyama, Y.; Ogumi, Z. Li^+ and Na^+ Transfer Through Interfaces Between Inorganic Solid Electrolytes and Polymer or Liquid Electrolytes. *J. Power Sources* **2005**, *146*, 749–752.

(106) Abe, T.; Sagane, F.; Ohtsuka, M.; Iriyama, Y.; Ogumi, Z. Lithium-Ion Transfer at the Interface Between Lithium-Ion Conductive Ceramic Electrolyte and Liquid Electrolyte-A Key to Enhancing the Rate Capability of Lithium-Ion Batteries. *J. Electrochem. Soc.* **2005**, *152*, A2151.

(107) Sagane, F.; Abe, T.; Ogumi, Z. Sodium-Ion Transfer at the Interface Between Ceramic and Organic Electrolytes. *J. Power Sources* **2010**, *195*, 7466–7470.

(108) Tenhaeff, W. E.; Perry, K. A.; Dudney, N. J. Impedance Characterization of Li Ion Transport at the Interface between Laminated Ceramic and Polymeric Electrolytes. *J. Electrochem. Soc.* **2012**, *159*, A2118-A2123.

(109) Brogioli, D.; Langer, F.; Kun, R.; La Mantia, F. Space-Charge Effects at the $Li_7La_3Zr_2O_{12}$/Poly(Ethylene Oxide) Interface. *ACS Appl. Mater. Interfaces* **2019**, *11*, 11999–12007.

(110) Gupta, A.; Sakamoto, J. Controlling Ionic Transport through the PEO-LiTFSI/LLZTO Interface. *Electrochem. Soc. Interface* **2019**, *28*, 63–69.

(111) Trevisanello, E.; Ates, T.; Passerini, S.; Richter, F. H.; Janek, J. Influence of the Polymer Structure and its Crystallization on the Interface Resistance in Polymer-LATP and Polymer-LLZO Hybrid Electrolytes. *J. Electrochem. Soc.* **2022**, *169*, 110547.

(112) Weiss, M.; Simon, F. J.; Busche, M. R.; Nakamura, T.; Schröder, D.; Richter, F. H.; Janek, J. From Liquid- to Solid-State Batteries: Ion Transfer Kinetics of Heteroionic Interfaces. *Electrochem. Energ. Rev.* **2020**, *3*, 221–238.

(113) Kalnaus, S.; Sabau, A. S.; Tenhaeff, W. E.; Dudney, N. J.; Daniel, C. Design of Composite Polymer Electrolytes for Li Ion Batteries Based on Mechanical Stability Criteria. *J. Power Sources* **2012**, *201*, 280–287.

(114) Zaman, W.; Hortance, N.; Dixit, M. B.; Andrade, V. de; Hatzell, K. B. Visualizing Percolation and Ion Transport in Hybrid Solid Electrolytes for Li–Metal Batteries. *J. Mater. Chem. A* **2019**, *7*, 23914–23921.

(115) Cheng, S. H.-S.; He, K.-Q.; Liu, Y.; Zha, J.-W.; Kamruzzaman, M.; Ma, R. L.-W.; Dang, Z.-M.; Li, R. K.; Chung, C. Y. Electrochemical Performance of All-Solid-State Lithium Batteries Using Inorganic Lithium Garnets Particulate Reinforced PEO/$LiClO_4$ Electrolyte. *Electrochim. Acta* **2017**, *253*, 430–438.

(116) Chen, F.; Yang, D.; Zha, W.; Zhu, B.; Zhang, Y.; Li, J.; Gu, Y.; Shen, Q.; Zhang, L.; Sadoway, D. R. Solid Polymer Electrolytes Incorporating Cubic $Li_7La_3Zr_2O_{12}$ for All-Solid-State Lithium Rechargeable Batteries. *Electrochim. Acta* **2017**, *258*, 1106–1114.

(117) Buvana, P.; Vishista, K.; Shanmukaraj, D.; Murugan, R. Lithium Garnet Oxide Dispersed Polymer Composite Membrane for Rechargeable Lithium Batteries. *Ionics* **2017**, *23*, 541–548.

(118) Tong, R.; Chen, L.; Shao, G.; Wang, H.; Wang, C.-A. An Integrated Solvent-Free Modification and Composite Process of $Li_{6.4}La_3Zr_{1.4}Ta_{0.6}O_{12}$/Poly(Ethylene Oxide) Solid Electrolytes: Enhanced Compatibility and Cycle Performance. *J. Power Sources* **2021**, *492*, 229672.

(119) Zhuang, H.; Ma, W.; Xie, J.; Liu, X.; Li, B.; Jiang, Y.; Huang, S.; Chen, Z.; Zhao, B. Solvent-Free Synthesis of PEO/Garnet Composite Electrolyte for High-Safety All-Solid-State Lithium Batteries. *J. Alloys Compd.* **2021**, *860*, 157915.

(120) Zheng, J.; Tang, M.; Hu, Y.-Y. Lithium Ion Pathway within $Li_7La_3Zr_2O_{12}$-Polyethylene Oxide Composite Electrolytes. *Angew. Chem.* **2016**, *128*, 12726–12730.

(121) Keller, M.; Appetecchi, G. B.; Kim, G.-T.; Sharova, V.; Schneider, M.; Schuhmacher, J.; Roters, A.; Passerini, S. Electrochemical Performance of a Solvent-Free Hybrid Ceramic-Polymer Electrolyte Based on $Li_7La_3Zr_2O_{12}$ in $P(EO)_{15}$LiTFSI. *J. Power Sources* **2017**, *353*, 287–297.

(122) Langer, F.; Bardenhagen, I.; Glenneberg, J.; Kun, R. Microstructure and Temperature Dependent Lithium Ion Transport of Ceramic–Polymer Composite Electrolyte for Solid-State Lithium Ion Batteries Based on Garnet-Type $Li_7La_3Zr_2O_{12}$. *Solid State Ionics* **2016**, *291*, 8–13.

(123) Choi, J.-H.; Lee, C.-H.; Yu, J.-H.; Doh, C.-H.; Lee, S.-M. Enhancement of Ionic Conductivity of Composite Membranes for All-Solid-State Lithium Rechargeable Batteries Incorporating Tetragonal $Li_7La_3Zr_2O_{12}$ into a Polyethylene Oxide Matrix. *J. Power Sources* **2015**, *274*, 458–463.

(124) Jung, Y.-C.; Lee, S.-M.; Choi, J.-H.; Jang, S. S.; Kim, D.-W. All Solid-State Lithium Batteries Assembled with Hybrid Solid Electrolytes. *J. Electrochem. Soc.* **2015**, *162*, A704-A710.

(125) Wang, C.; Yang, Y.; Liu, X.; Zhong, H.; Xu, H.; Xu, Z.; Shao, H.; Ding, F. Suppression of Lithium Dendrite Formation by Using LAGP-PEO (LiTFSI) Composite Electrolyte and Lithium Metal Anode Modified by PEO (LiTFSI) in All-Solid-State Lithium Batteries. *ACS Appl. Mater. Interfaces* **2017**, 13694–13702.

(126) Waidha, A. I.; Ferber, T.; Donzelli, M.; Hosseinpourkahvaz, N.; Vanita, V.; Dirnberger, K.; Ludwigs, S.; Hausbrand, R.; Jaegermann, W.; Clemens, O. Compositional Dependence of Li-Ion Conductivity in Garnet-Rich Composite Electrolytes for All-Solid-State Lithium-Ion Batteries-Toward Understanding the Drawbacks of Ceramic-Rich Composites. *ACS Appl. Mater. Interfaces* **2021**, *13*, 31111–31128.

(127) Zhang, Y.; Zhao, Y.; Gosselink, D.; Chen, P. Synthesis of Poly(ethylene-Oxide)/Nanoclay Solid Polymer Electrolyte for All Solid-State Lithium/Sulfur Battery. *Ionics* **2015**, *21*, 381–385.

(128) Xiong, S.; Liu, Y.; Jankowski, P.; Liu, Q.; Nitze, F.; Xie, K.; Song, J.; Matic, A. Design of a Multifunctional Interlayer for NASCION‐Based Solid‐State Li Metal Batteries. *Adv. Funct. Mater.* **2020**, *30*, 2001444.

(129) Samsinger, R. F.; Schopf, S. O.; Schuhmacher, J.; Treis, P.; Schneider, M.; Roters, A.; Kwade, A. Influence of the Processing on the Ionic Conductivity of Solid-State Hybrid Electrolytes Based on Glass-Ceramic Particles Dispersed in PEO with LiTFSI. *J. Electrochem. Soc.* **2020**, *167*, 120538.

(130) Huang, Z.; Tong, R.; Zhang, J.; Chen, L.; Wang, C.-A. Blending Poly(ethylene oxide) and $Li_{6.4}La_3Zr_{1.4}Ta_{0.6}O_{12}$ by Haake Rheomixer without Any Solvent: A Low-Cost Manufacture Method for Mass Production of Composite Polymer Electrolyte. *J. Power Sources* **2020**, *451*, 227797.
(131) Huang, Z.; Pang, W.; Liang, P.; Jin, Z.; Grundish, N.; Li, Y.; Wang, C.-A. A Dopamine Modified $Li_{6.4}La_3Zr_{1.4}Ta_{0.6}O_{12}$/PEO Solid-State Electrolyte: Enhanced Thermal and Electrochemical Properties. *J. Mater. Chem. A* **2019**, *7*, 16425–16436.
(132) Fu, K. K.; Gong, Y.; Dai, J.; Gong, A.; Han, X.; Yao, Y.; Wang, C.; Wang, Y.; Chen, Y.; Yan, C.*; et al.* Flexible, Solid-State, Ion-Conducting Membrane with 3D Garnet Nanofiber Networks for Lithium Batteries. *Proceedings of the National Academy of Sciences of the United States of America* **2016**, *113*, 7094–7099.
(133) Bae, J.; Li, Y.; Zhang, J.; Zhou, X.; Zhao, F.; Shi, Y.; Goodenough, J. B.; Yu, G. A 3D Nanostructured Hydrogel-Framework-Derived High-Performance Composite Polymer Lithium-Ion Electrolyte. *Angew. Chem.* **2018**, *57*, 2096–2100.
(134) Randau, S.; Weber, D. A.; Kötz, O.; Koerver, R.; Braun, P.; Weber, A.; Ivers-Tiffée, E.; Adermann, T.; Kulisch, J.; Zeier, W. G.*; et al.* Benchmarking the Performance of All-Solid-State Lithium Batteries. *Nat. Energy* **2020**, *5*, 259–270.
(135) Hartmann, P.; Leichtweiss, T.; Busche, M. R.; Schneider, M.; Reich, M.; Sann, J.; Adelhelm, P.; Janek, J. Degradation of NASICON-Type Materials in Contact with Lithium Metal: Formation of Mixed Conducting Interphases (MCI) on Solid Electrolytes. *J. Phys. Chem. C* **2013**, *117*, 21064–21074.
(136) Ushakova, E. E.; Frolov, A.; Reveguk, A. A.; Usachov, D. Y.; Itkis, D. M.; Yashina, L. V. Solid Electrolyte Interface Formation between Lithium and PEO-Based Electrolyte. *Appl. Surf. Sci.* **2022**, *589*, 153014.
(137) Mirsakiyeva, A.; Ebadi, M.; Araujo, C. M.; Brandell, D.; Broqvist, P.; Kullgren, J. Initial Steps in PEO Decomposition on a Li Metal Electrode. *J. Phys. Chem. C* **2019**, *123*, 22851–22857.
(138) Connell, J. G.; Fuchs, T.; Hartmann, H.; Krauskopf, T.; Zhu, Y.; Sann, J.; Garcia-Mendez, R.; Sakamoto, J.; Tepavcevic, S.; Janek, J. Kinetic versus Thermodynamic Stability of LLZO in Contact with Lithium Metal. *Chem. Mater.* **2020**, *32*, 10207–10215.
(139) Shen, Y.; Zhang, Y.; Han, S.; Wang, J.; Peng, Z.; Chen, L. Unlocking the Energy Capabilities of Lithium Metal Electrode with Solid-State Electrolytes. *Joule* **2018**, *2*, 1674–1689.
(140) Krauskopf, T.; Mogwitz, B.; Hartmann, H.; Singh, D. K.; Zeier, W. G.; Janek, J. The Fast Charge Transfer Kinetics of the Lithium Metal Anode on the Garnet‐Type Solid Electrolyte $Li_{6.25}Al_{0.25}La_3Zr_2O_{12}$. *Adv. Energy Mater.* **2020**, *10*, 2000945.
(141) Krauskopf, T.; Hartmann, H.; G. Zeier, W.; Janek, J. Toward a Fundamental Understanding of the Lithium Metal Anode in Solid-State Batteries - An Electrochemo-Mechanical Study on the Garnet-Type Solid Electrolyte $Li_{6.25}Al_{0.25}La_3Zr_2O_{12}$. *ACS Appl. Mater. Interfaces* **2019**, *11*, 14463–14477.

(142) Flatscher, F.; Philipp, M.; Ganschow, S.; Wilkening, H. M. R.; Rettenwander, D. The Natural Critical Current Density Limit for $Li_7La_3Zr_2O_{12}$ Garnets. *J. Mater. Chem. A* **2020**, *8*, 15782–15788.

(143) Gupta, A.; Kazyak, E.; Craig, N.; Christensen, J.; Dasgupta, N. P.; Sakamoto, J. Evaluating the Effects of Temperature and Pressure on Li/PEO-LiTFSI Interfacial Stability and Kinetics. *J. Electrochem. Soc.* **2018**, *165*, A2801-A2806.

(144) Kasemchainan, J.; Zekoll, S.; Jolly, D. S.; Ning, Z.; Hartley, G. O.; Marrow, J.; Bruce, P. G. Critical Stripping Current leads to Dendrite Formation on Plating in Lithium Anode Solid Electrolyte Cells. *Nat. Mater.* **2019**, *18*, 1105–1111.

(145) Barai, P.; Higa, K.; Ngo, A. T.; Curtiss, L. A.; Srinivasan, V. Mechanical Stress Induced Current Focusing and Fracture in Grain Boundaries. *J. Electrochem. Soc.* **2019**, *166*, A1752-A1762.

(146) Raj, R.; Wolfenstine, J. Current Limit Diagrams for Dendrite Formation in Solid-State Electrolytes for Li-Ion Batteries. *J. Power Sources* **2017**, *343*, 119–126.

(147) Cheng, L.; Chen, W.; Kunz, M.; Persson, K.; Tamura, N.; Chen, G.; Doeff, M. Effect of Surface Microstructure on Electrochemical Performance of Garnet Solid Electrolytes. *ACS Appl. Mater. Interfaces* **2015**, *7*, 2073–2081.

(148) Sharafi, A.; Haslam, C. G.; Kerns, R. D.; Wolfenstine, J.; Sakamoto, J. Controlling and Correlating the Effect of Grain Size with the Mechanical and Electrochemical Properties of $Li_7La_3Zr_2O_{12}$ Solid-State Electrolyte. *J. Mater. Chem. A* **2017**, *5*, 21491–21504.

(149) Kazyak, E.; Garcia-Mendez, R.; LePage, W. S.; Sharafi, A.; Davis, A. L.; Sanchez, A. J.; Chen, K.-H.; Haslam, C.; Sakamoto, J.; Dasgupta, N. P. Li Penetration in Ceramic Solid Electrolytes: Operando Microscopy Analysis of Morphology, Propagation, and Reversibility. *Matter* **2020**, *2*, 1025–1048.

(150) Ren, Y.; Shen, Y.; Lin, Y.; Nan, C.-W. Direct Observation of Lithium Dendrites inside Garnet-Type Lithium-Ion Solid Electrolyte. *Electrochem. Commun.* **2015**, *57*, 27–30.

(151) Cheng, E. J.; Sharafi, A.; Sakamoto, J. Intergranular Li Metal Propagation through Polycrystalline $Li_{6.25}Al_{0.25}La_3Zr_2O_{12}$ Ceramic Electrolyte. *Electrochim. Acta* **2017**, *223*, 85–91.

(152) Krauskopf, T.; Dippel, R.; Hartmann, H.; Richter, F. H.; Zeier, W. G.; Janek, J. Lithium-Metal Growth Kinetics on LLZO Garnet-Type Solid Electrolytes. *Joule* **2019**, *3*, 1–20.

(153) Han, F.; Westover, A. S.; Yue, J.; Fan, X.; Wang, F.; Chi, M.; Leonard, D. N.; Dudney, N. J.; Wang, H.; Wang, C. High Electronic Conductivity as the Origin of Lithium Dendrite Formation within Solid Electrolytes. *Nat. Energy* **2019**, *4*, 187–196.

(154) Monroe, C.; Newman, J. The Impact of Elastic Deformation on Deposition Kinetics at Lithium/Polymer Interfaces. *J. Electrochem. Soc.* **2005**, *152*, A396.

(155) Ni, J. E.; Case, E. D.; Sakamoto, J. S.; Rangasamy, E.; Wolfenstine, J. B. Room Temperature Elastic Moduli and Vickers Hardness of Hot-Pressed LLZO Cubic Garnet. *J. Mater. Sci.* **2012**, *47*, 7978–7985.

(156) Zeng, X.-X.; Yin, Y.-X.; Li, N.-W.; Du, W.-C.; Guo, Y.-G.; Wan, L.-J. Reshaping Lithium Plating/Stripping Behavior via Bifunctional Polymer Electrolyte for Room-Temperature Solid Li Metal Batteries. *J. Am. Chem. Soc.* **2016**, *138*, 15825–15828.

(157) Porz, L.; Swamy, T.; Sheldon, B. W.; Rettenwander, D.; Frömling, T.; Thaman, H. L.; Berendts, S.; Uecker, R.; Carter, W. C.; Chiang, Y.-M. Mechanism of Lithium Metal Penetration through Inorganic Solid Electrolytes. *Adv. Energy Mater.* **2017**, *7*, 1701003.

(158) Li, G.; Monroe, C. W. Dendrite Nucleation in Lithium-Conductive Ceramics. *Phys. Chem. Chem. Phys.* **2019**, *21*, 20354–20359.

(159) LePage, W. S.; Chen, Y.; Kazyak, E.; Chen, K.-H.; Sanchez, A. J.; Poli, A.; Arruda, E. M.; Thouless, M. D.; Dasgupta, N. P. Lithium Mechanics: Roles of Strain Rate and Temperature and Implications for Lithium Metal Batteries. *J. Electrochem. Soc.* **2019**, *166*, A89-A97.

(160) Yu, S.; Siegel, D. J. Grain Boundary Softening: A Potential Mechanism for Lithium Metal Penetration through Stiff Solid Electrolytes. *ACS Appl. Mater. Interfaces* **2018**, *10*, 38151–38158.

(161) Shen, F.; Dixit, M. B.; Xiao, X.; Hatzell, K. B. Effect of Pore Connectivity on Li Dendrite Propagation within LLZO Electrolytes Observed with Synchrotron X-ray Tomography. *ACS Energy Lett.* **2018**, *3*, 1056–1061.

(162) Aguesse, F.; Manalastas, W.; Buannic, L.; Del Lopez Amo, J. M.; Singh, G.; Llordés, A.; Kilner, J. Investigating the Dendritic Growth during Full Cell Cycling of Garnet Electrolyte in Direct Contact with Li Metal. *ACS Appl. Mater. Interfaces* **2017**, *9*, 3808–3816.

(163) Tian, H.-K.; Xu, B.; Qi, Y. Computational Study of Lithium Nucleation Tendency in $Li_7La_3Zr_2O_{12}$ (LLZO) and Rational Design of Interlayer Materials to Prevent Lithium Dendrites. *J. Power Sources* **2018**, *392*, 79–86.

(164) Harry, K. J.; Higa, K.; Srinivasan, V.; Balsara, N. P. Influence of Electrolyte Modulus on the Local Current Density at a Dendrite Tip on a Lithium Metal Electrode. *J. Electrochem. Soc.* **2016**, *163*, A2216-A2224.

(165) Golozar, M.; Hovington, P.; Paolella, A.; Bessette, S.; Lagacé, M.; Bouchard, P.; Demers, H.; Gauvin, R.; Zaghib, K. In Situ Scanning Electron Microscopy Detection of Carbide Nature of Dendrites in Li-Polymer Batteries. *Nano Lett.* **2018**, *18*, 7583–7589.

(166) Dollé, M.; Sannier, L.; Beaudoin, B.; Trentin, M.; Tarascon, J.-M. Live Scanning Electron Microscope Observations of Dendritic Growth in Lithium/Polymer Cells. *Electrochem. Solid-State Lett.* **2002**, *5*, A286.

(167) Harry, K. J.; Hallinan, D. T.; Parkinson, D. Y.; MacDowell, A. A.; Balsara, N. P. Detection of Subsurface Structures Underneath Dendrites Formed on Cycled Lithium Metal Electrodes. *Nat. Mater.* **2014**, *13*, 69–73.

(168) Harry, K. J.; Parkinson, D. Y.; Balsara, N. P. Failure Analysis of Batteries Using Synchrotron-based Hard X-ray Microtomography. *J. Visualized Exp.* **2015**, e53021.
(169) Sakamoto, J. More Pressure Needed. *Nat. Energy* **2019**, *4*, 827–828.
(170) Barroso-Luque, L.; Tu, Q.; Ceder, G. An Analysis of Solid-State Electrodeposition-Induced Metal Plastic Flow and Predictions of Stress States in Solid Ionic Conductor Defects. *J. Electrochem. Soc.* **2020**, *167*, 20534.
(171) Krauskopf, T.; Mogwitz, B.; Rosenbach, C.; Zeier, W. G.; Janek, J. Diffusion Limitation of Lithium Metal and Li–Mg Alloy Anodes on LLZO Type Solid Electrolytes as a Function of Temperature and Pressure. *Adv. Energy Mater.* **2019**, *9*, 1902568.
(172) Wang, M.; Wolfenstine, J. B.; Sakamoto, J. Temperature Dependent Flux Balance of the $Li/Li_7La_3Zr_2O_{12}$ Interface. *Electrochim. Acta* **2019**, *296*, 842–847.
(173) Kinzer, B.; Davis, A. L.; Krauskopf, T.; Hartmann, H.; LePage, W. S.; Kazyak, E.; Janek, J.; Dasgupta, N. P.; Sakamoto, J. Operando Analysis of the Molten Li|LLZO Interface: Understanding how the Physical Properties of Li affect the Critical Current Density. *Matter* **2021**, *4*, 1947–1961.
(174) A. Sharafi; Meyer, H. M.; Nanda, J.; Wolfenstine, J.; Sakamoto, J. Characterizing the Li–$Li_7La_3Zr_2O_{12}$ Interface Stability and Kinetics as a Function of Temperature and Current Density. *J. Power Sources* **2016**, *302*, 135–139.
(175) Cheng, L.; Crumlin, E. J.; Chen, W.; Qiao, R.; Hou, H.; Franz Lux, S.; Zorba, V.; Russo, R.; Kostecki, R.; Liu, Z.*; et al.* The Origin of High Electrolyte-Electrode Interfacial Resistances in Lithium Cells Containing Garnet Type Solid Electrolytes. *Phys. Chem. Chem. Phys.* **2014**, *16*, 18294–18300.
(176) Wu, J.-F.; Pu, B.-W.; Da Wang; Shi, S.-Q.; Zhao, N.; Guo, X.; Guo, X. In Situ Formed Shields Enabling Li2CO3-Free Solid Electrolytes: A New Route to Uncover the Intrinsic Lithiophilicity of Garnet Electrolytes for Dendrite-Free Li-Metal Batteries. *ACS Appl. Mater. Interfaces* **2019**, *11*, 898–905.
(177) Huo, H.; Chen, Y.; Zhao, N.; Lin, X.; Luo, J.; Yang, X.; Liu, Y.; Guo, X.; Sun, X. In-situ Formed Li_2CO_3-Free Garnet/Li Interface by Rapid Acid Treatment for Dendrite-Free Solid-State Batteries. *Nano Energy* **2019**, *61*, 119–125.
(178) Tsai, C.-L.; Roddatis, V.; Chandran, C. V.; Ma, Q.; Uhlenbruck, S.; Bram, M.; Heitjans, P.; Guillon, O. $Li_7La_3Zr_2O_{12}$ Interface Modification for Li Dendrite Prevention. *ACS Appl. Mater. Interfaces* **2016**, *8*, 10617–10626.
(179) Fu, K. K.; Gong, Y.; Fu, Z.; Xie, H.; Yao, Y.; Liu, B.; Carter, M.; Wachsman, E.; Hu, L. Transient Behavior of the Metal Interface in Lithium Metal-Garnet Batteries. *Angew. Chem.* **2017**, *56*, 14942–14947.
(180) Feng, W.; Dong, X.; Li, P.; Wang, Y.; Xia, Y. Interfacial Modification of Li/Garnet Electrolyte by a Lithiophilic and Breathing Interlayer. *J. Power Sources* **2019**, *419*, 91–98.

(181) He, M.; Cui, Z.; Chen, C.; Li, Y.; Guo, X. Formation of Self-Limited, Stable and Conductive Interfaces between Garnet Electrolytes and Lithium Anodes for Reversible Lithium Cycling in Solid-State Batteries. *J. Mater. Chem. A* **2018**, *6*, 11463–11470.

(182) Xu, H.; Li, Y.; Zhou, A.; Wu, N.; Xin, S.; Li, Z.; Goodenough, J. B. Li_3N-Modified Garnet Electrolyte for All-Solid-State Lithium Metal Batteries Operated at 40 °C. *Nano Lett.* **2018**, *18*, 7414–7418.

(183) Han, X.; Gong, Y.; Fu, K. K.; He, X.; Hitz, G. T.; Dai, J.; Pearse, A.; Liu, B.; Wang, H.; Rubloff, G.*; et al.* Negating Interfacial Impedance in Garnet-Based Solid-State Li Metal Batteries. *Nat. Mater.* **2017**, *16*, 572–579.

(184) Zhou, W.; Zhu, Y.; Grundish, N.; Xin, S.; Wang, S.; You, Y.; Wu, N.; Gao, J.; Cui, Z.; Li, Y.*; et al.* Polymer Lithium-Garnet Interphase for an All-Solid-State Rechargeable Battery. *Nano Energy* **2018**, *53*, 926–931.

(185) Duan, J.; Wu, W.; Nolan, A. M.; Wang, T.; Wen, J.; Hu, C.; Mo, Y.; Luo, W.; Huang, Y. Lithium-Graphite Paste: An Interface Compatible Anode for Solid-State Batteries. *Adv. Mater.* **2019**, *31*, e1807243.

(186) Fu, J.; Yu, P.; Zhang, N.; Ren, G.; Zheng, S.; Huang, W.; Long, X.; Li, H.; Liu, X. In Situ Formation of a Bifunctional Interlayer Enabled by a Conversion Reaction to Initiatively Prevent Lithium Dendrites in a Garnet Solid Electrolyte. *Energy Environ. Sci.* **2019**, *12*, 1404–1412.

(187) Huo, H.; Chen, Y.; Li, R.; Zhao, N.; Luo, J.; Da Pereira Silva, J. G.; Mücke, R.; Kaghazchi, P.; Guo, X.; Sun, X. Design of a Mixed Conductive Garnet/Li Interface for Dendrite-Free Solid Lithium Metal Batteries. *Energy Environ. Sci.* **2020**, *13*, 127–134.

(188) Wang, S.; Xu, H.; Li, W.; Dolocan, A.; Manthiram, A. Interfacial Chemistry in Solid-State Batteries: Formation of Interphase and Its Consequences. *J. Am. Chem. Soc.* **2018**, *140*, 250–257.

(189) Sharafi, A.; Meyer, H. M.; Nanda, J.; Wolfenstine, J.; Sakamoto, J. Characterizing the Li-$Li_7La_3Zr_2O_{12}$ Interface Stability and Kinetics as a Function of Temperature and Current Density. *J. Power Sources* **2016**, *302*, 135–139.

(190) Zhang, Y.; Chen, F.; Tu, R.; Shen, Q.; Zhang, L. Field Assisted Sintering of Dense Al-Substituted Cubic Phase $Li_7La_3Zr_2O_{12}$ Solid Electrolytes. *J. Power Sources* **2014**, *268*, 960–964.

(191) Baek, S.-W.; Lee, J.-M.; Kim, T. Y.; Song, M.-S.; Park, Y. Garnet Related Lithium Ion Conductor Processed by Spark Plasma Sintering for All Solid State Batteries. *J. Power Sources* **2014**, *249*, 197–206.

(192) Hosokawa, H.; Takeda, A.; Inada, R.; Sakurai, Y. Tolerance for Li Dendrite Penetration in Ta-Doped $Li_7La_3Zr_2O_{12}$ Solid Electrolytes Sintered with $Li_{2.3}C_{0.7}B_{0.3}O_3$ Additive. *Mater. Lett.* **2020**, *279*, 128481.

(193) Liu, K.; Ma, J.-T.; Wang, C.-A. Excess Lithium Salt Functions more than Compensating for Lithium Loss when Synthesizing $Li_{6.5}La_3Ta_{0.5}Zr_{1.5}O_{12}$ in Alumina Crucible. *J. Power Sources* **2014**, *260*, 109–114.

(194) Hitz, G. T.; McOwen, D. W.; Zhang, L.; Ma, Z.; Fu, Z.; Wen, Y.; Gong, Y.; Dai, J.; Hamann, T. R.; Hu, L.; *et al*. High-Rate Lithium Cycling in a Scalable Trilayer Li-Garnet-Electrolyte Architecture. *Mater. Today* **2019**, *22*, 50–57.

(195) Lin, D.; Yuen, P. Y.; Liu, Y.; Liu, W.; Liu, N.; Dauskardt, R. H.; Cui, Y. A Silica-Aerogel-Reinforced Composite Polymer Electrolyte with High Ionic Conductivity and High Modulus. *Adv. Mater.* **2018**, *30*, e1802661.

(196) Tang, W.; Tang, S.; Zhang, C.; Ma, Q.; Xiang, Q.; Yang, Y.-W.; Luo, J. Simultaneously Enhancing the Thermal Stability, Mechanical Modulus, and Electrochemical Performance of Solid Polymer Electrolytes by Incorporating 2D Sheets. *Adv. Energy Mater.* **2018**, *8*, 1800866.

(197) Zhao, C.-Z.; Zhang, X.-Q.; Cheng, X.-B.; Zhang, R.; Xu, R.; Chen, P.-Y.; Peng, H.-J.; Huang, J.-Q.; Zhang, Q. An Anion-Immobilized Composite Electrolyte for Dendrite-Free Lithium Metal Anodes. *Proc. Natl. Acad. Sci. U. S. A.* **2017**, *114*, 11069–11074.

(198) Chen, L.; Li, W.; Fan, L.-Z.; Nan, C.-W.; Zhang, Q. Intercalated Electrolyte with High Transference Number for Dendrite‐Free Solid‐State Lithium Batteries. *Adv. Funct. Mater.* **2019**, *29*, 1901047.

(199) Lu, Y.; Tikekar, M.; Mohanty, R.; Hendrickson, K.; Ma, L.; Archer, L. A. Stable Cycling of Lithium Metal Batteries Using High Transference Number Electrolytes. *Adv. Energy Mater.* **2015**, *5*, 1402073.

(200) Cheng, J.; Hou, G.; Chen, Q.; Li, D.; Li, K.; Yuan, Q.; Wang, J.; Ci, L. Sheet-Like Garnet Structure Design for Upgrading PEO-Based Electrolyte. *Chem. Eng. J.* **2021**, 132343.

(201) Wang, S.; Sun, Q.; Peng, W.; Ma, Y.; Zhou, Y.; Song, D.; Zhang, H.; Shi, X.; Li, C.; Zhang, L. Ameliorating the Interfacial Issues of All-Solid-State Lithium Metal Batteries by Constructing Polymer/Inorganic Composite Electrolyte. *J. Energy Chem.* **2020**.

(202) Shim, J.; Lee, J. W.; Bae, K. Y.; Kim, H. J.; Yoon, W. Y.; Lee, J.-C. Dendrite Suppression by Synergistic Combination of Solid Polymer Electrolyte Crosslinked with Natural Terpenes and Lithium-Powder Anode for Lithium-Metal Batteries. *ChemSusChem* **2017**, *10*, 2274–2283.

(203) Chi, S.-S.; Liu, Y.; Zhao, N.; Guo, X.; Nan, C.-W.; Fan, L.-Z. Solid Polymer Electrolyte Soft Interface Layer with 3D Lithium Anode for All-Solid-State Lithium Batteries. *Energy Stor. Mater.* **2019**, *17*, 309–316.

3 Results and Discussion

Garnet-type SEs and especially the lithium-stuffed $Li_7La_3Zr_2O_{12}$ (LLZO)-based garnets have attracted immense interest. Since their discovery by Murugan *et al.* in 2007, significant advances have been achieved, especially in terms of the ionic conductivity. As a result of intensive research on the choice of doping element and optimum compositions thereof, ionic conductivities of about 2 mS cm^{-1} at room temperature were reached, which is about a magnitude higher than initial values. However, as ideal compositions have already been found, current research mainly focuses on materials processing and application-related issues.

Regarding the materials processing, alternatives to the conventional, energy-intensive solid-state synthesis are required for large-scale applications. In terms of the issues related to the application, engineering the garnet/electrode interfaces is one of the major obstacles. With regard to this, the surface properties of the garnet itself and its instability in ambient air negatively affects the interface with the electrodes. Additional degradation issues arise with typical cathode materials, while the cycling stability and formation of lithium metal dendrites at the interface with the potential LMA remains as the main issue. Moreover, the microstructure and the related brittleness of LLZO are prone to be penetrated by lithium dendrites. Therefore, HSEs with the benefits of flexible polymer electrolytes have emerged as potential alternative. However, the influence of the interface between LLZO and the polymer matrix on the lithium ion transport and its correlation with the phase compatibility remains unclear.

This thesis covers the investigation of such surface and interface properties of novel glass-ceramic LLZO. It is manufactured at the SCHOTT AG in an industrially scalable melting process that is industrially scalable and therefore promising for the large-scale production of LLZO. The first publication addresses the surface properties of glass-ceramic LLZO powders in terms of their degradation in ambient air. Detailed insights into the mechanism are given by kinetic data, from which suggestions for the handling of LLZO can be derived. In the second publication, the effect of the amorphous phase in glass-ceramic LLZO on the sintering process and the electrochemical performance is presented. In addition, its impact on the formation and propagation of lithium metal dendrites is described. The manuscript provides knowledge about the role of LLZO glass-ceramic/polymer interfaces in HSEs. The correlation between phase compatibility and interface resistance is investigated, including its influence on the electrochemical performance.

3.1 Publication 1: "Particle size-dependent degradation kinetics of garnet-type $Li_7La_3Zr_2O_{12}$ solid electrolyte powders in ambient air"

In publication 1 of this thesis, the surface properties and the related degradation, i.e., hydration and carbonation of glass-ceramic LLZO was studied in detail. The focus was on the pristine powders, as investigations of the degradation have mainly been made for sintered pellets in the literature. The objective is to gain insights into the mechanism and provide understanding of the handling conditions of LLZO powders. Powders with different surface areas relevant for battery applications were subjected to several kinetic analyses, such as SEM, XRD, and Raman spectroscopy. A LLZO variant with a low volume fraction of amorphous phase was chosen in order to provide comparability to stoichiometric LLZO used in the literature.

The correlated analyses revealed that the degradation mechanism in ambient air follows a two-step consecutive reaction for all powders investigated. By exploring the temporal evolution, it could be shown that both hydration and carbonation are self-limited by diffusion processes on the surface, which is in accordance with the core shrinking model. While the hydration and the related expansion of the lattice upon Li^+/H^+ exchange was studied by XRD, Raman spectroscopy enabled the simultaneous observation of the hydration and carbonation by analysing the reaction products LiOH and Li_2CO_3. Moreover, the study revealed that the hydration is an essential intermediate step by adjusting the atmosphere from ambient air to dry room conditions, excluding the direct carbonation of LLZO. A linear dependence of the rate constant on the surface area of the powder was found for both the hydration and carbonation.

Overall, the results of the first publication provide profound insights into the degradation of LLZO powders. In addition to the elucidation of the mechanism, this work gives guidance on the handling and processing of LLZO powders, which is of main importance for its application in future battery applications.

The idea for this study was developed by the first author under the supervision of J. Schuhmacher and S. Leukel. C. Loho performed and assisted the SEM experiments the SCHOTT AG. All other experiments were performed and analyzed by the first author with the support of the analytics division at the SCHOTT AG. J. Schuhmacher, S. Leukel, F. H. Richter and J. Janek assisted the scientific discussion of the data. The manuscript was written by the first author and edited by six co-authors.

The manuscript has been accepted for publication in Journal of Physical Chemistry C **2023**, *127*, 8320-8331. DOI: https://doi.org/10.1021/acs.jpcc.3c01027.

THE JOURNAL OF PHYSICAL CHEMISTRY C
A JOURNAL OF THE AMERICAN CHEMICAL SOCIETY

pubs.acs.org/JPCC

Article

Particle Size-Dependent Degradation Kinetics of Garnet-Type $Li_{6.5}La_3Zr_{1.5}Ta_{0.5}O_{12}$ Solid Electrolyte Powders in Ambient Air

Nina Hoinkis, Jörg Schuhmacher, Sebastian Leukel, Christoph Loho, Andreas Roters,* Felix H. Richter, and Jürgen Janek*

Cite This: *J. Phys. Chem. C* 2023, 127, 8320−8331

Read Online

ACCESS | Metrics & More | Article Recommendations | Supporting Information

ABSTRACT: Garnet-type $Li_7La_3Zr_2O_{12}$ (LLZO) is a promising solid electrolyte for the application in solid-state lithium batteries (SSBs). However, its reaction with water and carbon dioxide in ambient air and the resulting formation of insulating lithium carbonate is one of the major obstacles for its large-scale manufacturing and processing. Especially when processed as powder with large surface areas, e.g., for the application in hybrid electrolytes, where LLZO powders are incorporated into a polymer matrix, uncontaminated surfaces are crucial. In this work, the kinetics of the hydration and carbonation mechanism is studied in detail for Ta-doped LLZO powders by time-dependent analyses of morphology, structure, and composition. Common particle sizes for battery applications, i.e., powders with different specific surface areas, are investigated. It is shown that the degradation mechanism follows a two-step consecutive reaction for all particle sizes investigated. It is self-limited by diffusion processes in the reaction layer in accordance with the core shrinking model. The hydration reaction is an essential intermediate step that precedes carbonation, which is demonstrated by systematically adjusting the atmosphere from dry room conditions up to ambient air. Moreover, the reaction rate of the hydration and carbonation depends strongly on the particle size and thus on the surface area. A linear correlation of the reaction rate and the specific surface area is found. Altogether, the novel insights into the degradation mechanism of LLZTO powder scrutinized in this work provide guidance on how to select, handle, and process LLZTO powders according to the surface quality requirements in future battery applications.

1. INTRODUCTION

Solid-state batteries (SSBs) with solid electrolytes (SEs) and lithium metal anodes have attracted significant attention as potential next-generation Li batteries because they can provide superior energy density and enhanced battery safety.[1−3] One of the most promising SEs among various types is the ceramic Li-ion conductor $Li_7La_3Zr_2O_{12}$ (LLZO) with its cubic garnet-type structure due to its high ionic conductivity, excellent thermal stability, and broad electrochemical window, particularly its chemical stability against Li metal.[4,5] This allows for LLZO not only to be used as single, completely inorganic SE, but also as a protective separator in combination with other electrolytes that are prone to degradation in contact with Li metal.[6] Another attractive application is the use of LLZO powders in solid or gel-like hybrid electrolytes (HSEs), in which the particles are incorporated into a Li-ion conductive polymer matrix providing enhanced flexibility in cell design.[7] However, the environmental instability of LLZO, arising from the reaction with water (hydration) and carbon dioxide (carbonation) in ambient air, still impairs its large-scale manufacturing and processing. For future application of LLZO-based components and batteries, it is therefore crucial to develop a fundamental understanding of the mechanism and kinetics of the interaction of LLZO with ambient air, so that tailored countermeasures can be taken.

In contrast to an early work that demonstrated chemical stability of LLZO in ambient air,[5] recent studies have found that it readily undergoes hydration in water[8,9] and other protic solvents[10−12] as well as by water vapor from ambient air.[13−16] During the hydration step, Li^+ ions in the LLZO structure are exchanged for protons from the water (Li^+/H^+ exchange), resulting in the formation of lithium hydroxide (LiOH). With a moderate amount of Li^+/H^+ exchange, LLZO retains its cubic structure in the space group $Ia\bar{3}d$, whereas it changes to a slightly distorted non-centrosymmetric space group $I\bar{4}3d$ upon intensive exchange (>75%).[10,17,18] In ambient air, it was found that the hydration is readily followed by carbonation with

Received: February 14, 2023
Revised: April 8, 2023
Published: April 20, 2023

https://doi.org/10.1021/acs.jpcc.3c01027
J. Phys. Chem. C 2023, 127, 8320−8331

atmospheric carbon dioxide (CO_2). The formed intermediate LiOH either reacts directly with CO_2 to form Li_2CO_3 or via an intermediate hydration to $LiOH{\cdot}H_2O$ that reacts subsequently to the final product Li_2CO_3.[14−16,19] Conversely, it has been also discussed that LLZO directly reacts with CO_2 via a single-step reaction pathway. Whereas Cheng *et al.* and Li *et al.* suggested that the direct carbonation of LLZO is the energetically preferred pathway,[20,21] Sharafi *et al.* postulated that the Li^+/H^+ exchange mechanism is energetically more favorable compared with the direct carbonation based on DFT calculations.[15] Xia *et al.* confirmed by experiments in dry air (containing an unknown content of CO_2) that no Li_2CO_3 was formed, from which they hypothesized that humidity is crucial for Li_2CO_3 formation.[14] In summary, consensus on the exact reaction pathway and its intermediate steps has not been reached so far. A systematic study that differentiates between experimental conditions with or without CO_2 and/or H_2O would be helpful to unravel the different reaction pathways of hydration and carbonation, so that guidelines on how to select, handle, and process LLZO powders can be derived. Moreover, an investigation of the reaction time dependency, i.e., of the reaction kinetics, could give valuable insights into the reaction sequence as well as possible interaction of the reaction steps.

The degradation of LLZO including Li^+/H^+ exchange and formation of Li_2CO_3 was proven to have a negative impact on the material properties and battery performance. It impairs the ionic conductivity of sintered LLZO[12,22−24] and the Li^+ transport at the interface anode or cathode materials because of the insulating properties of the passivating Li_2CO_3 layer.[15,16,19,25] Regarding HSEs, this surface layer immensely hinders the ion transport pathway from the polymer matrix into the LLZO powder particles, thereby reducing the overall electrochemical performance, i.e., ionic conductivity, electrochemical window, and transference number.[26−29] Therefore, an uncontaminated LLZO powder surface is crucial for achieving required HSE performance, especially when the particle size of the incorporated LLZO powder is small and the specific surface area is large. However, only a few studies deal with the hydration/carbonation process of powder surfaces. Instead, mainly sintered pellets were subject of the investigations as well as the correlation of degradation with their microstructure.[30−32]

This study aims to clarify the reaction pathway of the hydration/carbonation mechanism in ambient air and its kinetics in dependence of the specific surface area of Ta-doped LLZO (LLZTO, $Li_{6.5}La_3Zr_{1.5}Ta_{0.5}O_{12}$) powders as representative material system. In order to study the influence of particle size, which correlates inversely with the specific surface area, we selected three powders of different particle sizes that are relevant for battery application, i.e., particle sizes from sub-μm to a few microns. Besides the investigation of morphological and structural changes on the powder surfaces, kinetic data were gained from *in situ* Raman spectroscopy that allows simultaneously following the hydration and carbonation of LLZTO. The mechanism is further elucidated by performing the analyses in different synthetic air atmospheres to investigate the influence of H_2O and CO_2. This study gives a profound insight into the hydration/carbonation mechanism of LLZTO and allows suggestions for its processing, thereby making an important contribution to the development of next-generation lithium batteries.

2. EXPERIMENTAL SECTION

2.1. Materials. Garnet-type Ta-doped $Li_{6.5}La_3Zr_{1.5}Ta_{0.5}O_{12}$ was manufactured via a unique and industrially scalable melting route at the SCHOTT AG to give glass−ceramic LLZTO. The metal oxide raw materials in stoichiometric ratio were melted in an inductively heated skull crucible implemented by a radio frequency induction coil (~1600 °C). After homogenization of the melt, samples were taken from the crucible in order to realize fast cooling. Further details can be found elsewhere.[33] Upon cooling, an amorphous phase is generated intrinsically, whose fraction and composition can be adjusted during the process. In this study, LLZTO with an almost negligible fraction of amorphous phase (<0.1 wt %) was chosen to simulate stoichiometric LLZTO powders that are widely used in the literature. The melting block was first pre-crushed on a jaw crusher, pre-ground to a particle size <1 mm using a ball mill, and brought to the final particle sizes and particle size distributions by using an opposed jet mill with a downstream classifier. N_2 was used as the process gas in the latter case. By different rotation speeds of the downstream classifier, different particle sizes as given in Table 1 were realized. Further details can be found elsewhere.[34] The median particle size *D*50 was measured by static light scattering (CILAS 1064, Quantachrome) and the specific surface area was determined by the BET method (QUADRASROB evo, Anton Paar). Bulk densities ρ of the powders were calculated by eq 1 using the density of the crystalline phase ($\rho_{cryst.}$, determined by Rietveld refinement of the lattice parameter by XRD), the estimated density of the amorphous phase, i.e., lithium excess, (therefore estimated from Li_2O: $\rho_{am.} \approx 2$ g cm^{-3}), and the corresponding fractions of crystalline and amorphous phase in vol %.

Table 1. Characterization of the Starting LLZTO Powders with Fine (f), Medium (M), and Coarse (c) Particle Sizes Including Mean Particle Size *D*50, Surface Area S_{BET}, and Density ρ as Well as the Ionic Conductivity σ of Sintered Pellets

sample	*D*50 (μm)	S_{BET} (m^2 g^{-1})	ρ (g cm^{-3})	σ (mS cm^{-1})
f-LLZTO	0.40	5.62	5.32	0.96
m-LLZTO	0.83	2.73	5.37	0.97
c-LLZTO	4.93	0.76	5.40	0.83

$$\rho = \frac{\text{vol\%}_{cryst.} \cdot \rho_{cryst.} + \text{vol\%}_{am.} \cdot \rho_{am.}}{100} \quad (1)$$

The crystalline phase fractions were determined by chemical analysis (fractions of ZrO_2, La_2O_3, and Ta_2O_5 were analyzed by X-ray fluorescence spectroscopy and Li_2O by atomic absorption spectroscopy). The fraction of amorphous phase, i.e., lithium excess, was calculated by subtracting the ideal stoichiometry of LLZTO assuming that the elements Zr, Ta, and La fully contribute to the crystalline phase. All powders were stored in a N_2-filled glovebox (MBraun) with O_2 and H_2O contents <1 ppm.

2.2. Materials Characterization. Scanning electron microscopy (SEM) was performed with a ZEISS LEO1550 and LEO1530 equipped with a field emission gun (FEG) to capture the SEM images with a secondary electron detector operated at 10 keV acceleration voltage. Prior to analysis, powders were prepared in an argon-filled glovebox (MBraun,

https://doi.org/10.1021/acs.jpcc.3c01027
J. Phys. Chem. C 2023, 127, 8320−8331

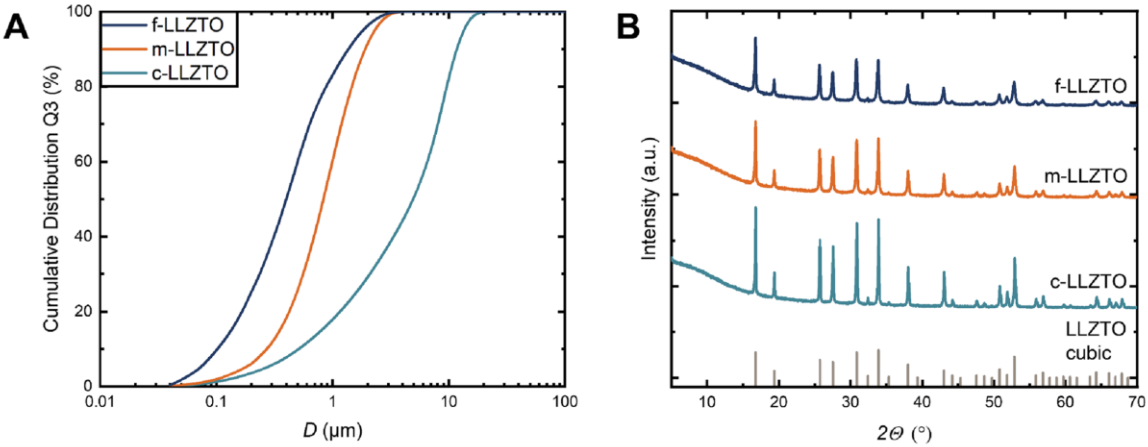

Figure 1. Characterization of the starting LLZTO powders with fine (f-), medium (m-), and coarse (c-) particle sizes including (A) particle size distributions measured by static light scattering and (B) X-ray diffraction patterns together with the reference reflections of cubic LLZTO.

O_2 and H_2O content <1 ppm) and poured on SEM stubs equipped with carbon adhesive discs. Samples at t = 0 h were transferred directly to a sputter coater. After about 8 nm Pt were sputtered onto the samples, to avoid charging during the SEM analyses, the samples were transferred into the SEM chamber. All other samples were, prior to Pt sputtering, exposed to ambient air (40−45% RH, T = 25 °C) for the defined durations of 6 and 32 h, respectively. The exposition was done in the Raman measuring cell in order to ensure the same gas flow and distribution as for the Raman experiment.

Energy-dispersive X-ray spectroscopy (EDX) was carried out on particle agglomerates with a ZEISS LEO1550 equipped with a Noran System Six EDX system from Thermo Fisher Scientific GmbH. EDX spectra were taken at 10 keV accelerating voltage.

X-ray diffraction (XRD) spectra were collected using a PANalytical X'Pert PRO MPD (Malvern Panalytical) in Bragg−Brentano geometry from 10−70° 2Θ in increments of 0.013° using Cu Kα radiation operating at 45 kV and 40 mA. To ensure diffraction from multiple grains, samples were spun during XRD. Prior to analysis, powder samples were transferred from the glovebox to the XRD directly after preparation to ensure minimal contact time with ambient air (<1 min). For time-dependent analysis, a diffraction pattern (duration of about 35 min) was collected every 60 min for 32 h or 60 h at T = 25 °C in ambient air. For qualitative analysis, the software HighScore Plus (Malvern Panalytical) was used and reference crystallographic information files were from ICDD PDF-2 (Li_2CO_3: JCPDS #87-0729) and Crystallography Open Database (COD) (cubic LLZTO: COD #1545083). Rietveld refinement was performed with the same software. Only cubic LLZTO was refined, reflection intensities of the other phases were too low to be fitted. Unit cell parameter, zero point, scale factor, peak shape, and profile parameters were refined for the respective data sets.

Confocal Raman spectroscopy was performed on an Alpha300 M+ (WITec, Oxford Instruments) using a Nd-YAG laser with a wavelength of 532 nm and a power of 0.5 W. Prior to analysis, powder samples were transferred into a self-built airtight measuring cell in a N_2-filled glovebox (MBraun, O_2 and H_2O content <1 ppm) so that the first measurement at t = 0 h was done under a glovebox atmosphere. The cell was equipped with two valves on opposite sides that were opened after the first measurement. One of them is connected to a gas line (either ambient air (40−45% RH, 400 ppm-mol CO_2), synthetic air (Air Liquide, ≤ 0.5 ppm mol H_2O, ≤ 0.1 ppm-mol CO_2), dry air containing CO_2 (Air Liquide, ≤ 0.5 ppm-mol H_2O, 400 ppm mol CO_2) or humid air (Air Liquide, 40−45% RH, ≤ 0.1 ppm mol CO_2)), and the other one was left open during the experiment to ensure continuous gas flow. All measurements were done at T = 25 °C. Raman maps (500 × 500 μm^2, 144 measurement points) were collected every 20 min and averaged. The peak areas of Li_2CO_3 (1087 cm^{-1}), LiOH (3660 cm^{-1}), and one of the protonated LLZO bands (295 cm^{-1}) were extracted after baseline correction for each time and normalized to the LLZO bands (150−1000 cm^{-1}) at t = 0 h.

Absolute water and carbon contents were determined with a LECO RC612 multiphase determinator using IR spectroscopy (LECO Instrumente) from 100−1100 °C with a rate of 120 K/min and held at 1100 °C for about 5 min. Samples at t = 0 h were transferred directly from the glovebox to the instrument, and the other samples were exposed to the different atmospheres (as described in the section above) for 32 h in the Raman measuring cell to ensure the same gas flow and distribution as for the Raman experiment. The software RC 612 version 1.31 was used for analysis, and water and carbon content was normalized to a defined mass of powder sample.

Electrochemical impedance spectroscopy (EIS) was performed with an Alpha A-High Analyzer (Novocontrol) on the sintered LLZTO pellets produced via sintering in mother powder (1130 °C, 0.5 h, O_2 atmosphere). Gold electrodes with a diameter of 6.5 mm were sputter coated on both sides of each pellet using a sputter coater (EM SDC050, Leica). EIS was carried out at T = 25 °C for room temperature conductivity in a frequency range from 100 mHz to 20 MHz with a 20 mV perturbation amplitude. EIS data were fitted using Z-View software. The thickness d of each pellet and electrode area A together with impedance R were used for calculation of the specific ionic conductivity σ:

$$\sigma = \frac{1}{R} \cdot \frac{d}{A} \tag{2}$$

https://doi.org/10.1021/acs.jpcc.3c01027
J. Phys. Chem. C 2023, 127, 8320−8331

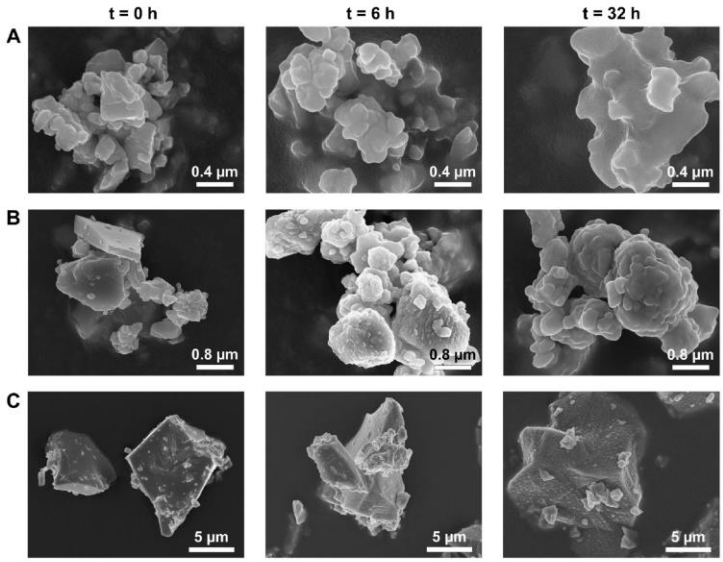

Figure 2. SEM images of the pristine powder samples (A) f-LLZTO, (B) m-LLZTO, and (C) c-LLZTO exposed to ambient air for 0, 6, and 32 h.

Measurements were performed in triplicate giving an experimental error <10%.

3. RESULTS AND DISCUSSION

3.1. Characterization of Pristine LLZTO Powders. The garnet-type LLZTO was synthesized via an industrially scalable melting route at the SCHOTT AG.[33] Upon fast cooling, an amorphous phase is formed whose fraction and composition can be adjusted during the process. Herein, LLZTO with a negligible fraction of amorphous phase was chosen as a model system in order to compare the findings to stoichiometric LLZTO produced via the conventional solid-state reaction. Three different powders of which particle sizes ranged from fine (f-) over medium (m-) to coarse (c-) were obtained from milling using different processing parameters. In Figure 1A, the particle size distributions of the three samples are shown. f- and m-LLZTO exhibit a monomodal distribution, while a slight shoulder is visible for c-LLZTO, indicating the presence of finer particles.

The corresponding $D50$ values are given in Table 1, together with the specific surface areas S_{BET} and the densities ρ. The S_{BET} differ by a factor of about 2 for f- and m-LLZTO and 3.5 for m- and c-LLZTO. The densities ρ of the three samples are all in the same range of 5.32−5.40 g cm^{-3}, a typical value for cubic LLZTO.[35] Additionally, the powder samples were cold-pressed and sintered in order to determine the ionic conductivity. The respective values in Table 1 are close to 1 mS cm^{-1}, which is outstandingly high compared with other LLZTO materials (ref 36 and refs therein) and makes them suitable SEs for battery applications. The reasons for such high conductivity are due to superior microstructure realized by the help of the amorphous phase. The latter acts as a sintering additive promoting liquid phase sintering and high density.

Figure 1B shows the XRD patterns of the pristine powders. All match well with the reflections of the reference pattern of cubic LLZTO. No reflections of impurities are observed for any of the samples, which proves that the melting route and the milling process are robust against the formation of secondary phases, such as $La_2Zr_2O_7$, that often arise due to lithium loss.[37]

3.2. Temporal Changes of Powder Morphology and Particle Surface Properties. SEM analysis was performed in order to study morphological changes due to the hydration/carbonation of the three LLZTO samples. Figure 2 shows the SEM images of f-, m-, and c-LLZTO powder particles exposed to ambient air for 0, 6, and 32 h.

The estimated particle sizes are in agreement with the $D50$ values given in Table 1. For c-LLZTO, finer particles on top of larger particles are evident, which corresponds well with the bimodal particle size distribution observed in Figure 1A. At t = 0 h, the particles of all three samples are cullet-shaped with sharp edges due to the milling process. After exposition to ambient air for 6 h, the particle surfaces differ from the pristine state. The surface of f-LLZTO powder particles appears to be homogeneously coated and the former sharp edges of the particles appear to be softened. In contrast, the surfaces of m- and c-LLZTO exhibit a spot-like secondary phase with a size of about 0.1−0.3 μm. At t = 32 h, the coated appearance of f-LLZTO remains unchanged. Yet, the surface of the m-LLZTO particles display a similar coating as observed for the f-LLZTO particles. For c-LLZTO, the observations are comparable to those at t = 6 h, i.e., the spots of a secondary phase are still visible. Hence, the formation of a potential secondary phase, as coating or spot-like particles, seems fastest for f-LLZTO and slowest for c-LLZTO. This temporal evolution of particle surface morphology coincides qualitatively with the increase in intensity of the carbon peak at 0.28 keV in EDX analysis (see Figure S1). Therefore, we believe that the different morphologies relate to the state of hydration according to eq 3 and carbonation in eq 4 and the associated formation of LiOH and Li_2CO_3. The formation of Li_2CO_3 can also take place via the formation of the intermediate LiOH·H_2O (eqs 5 and 6).[14,15,17]

https://doi.org/10.1021/acs.jpcc.3c01027
J. Phys. Chem. C 2023, 127, 8320−8331

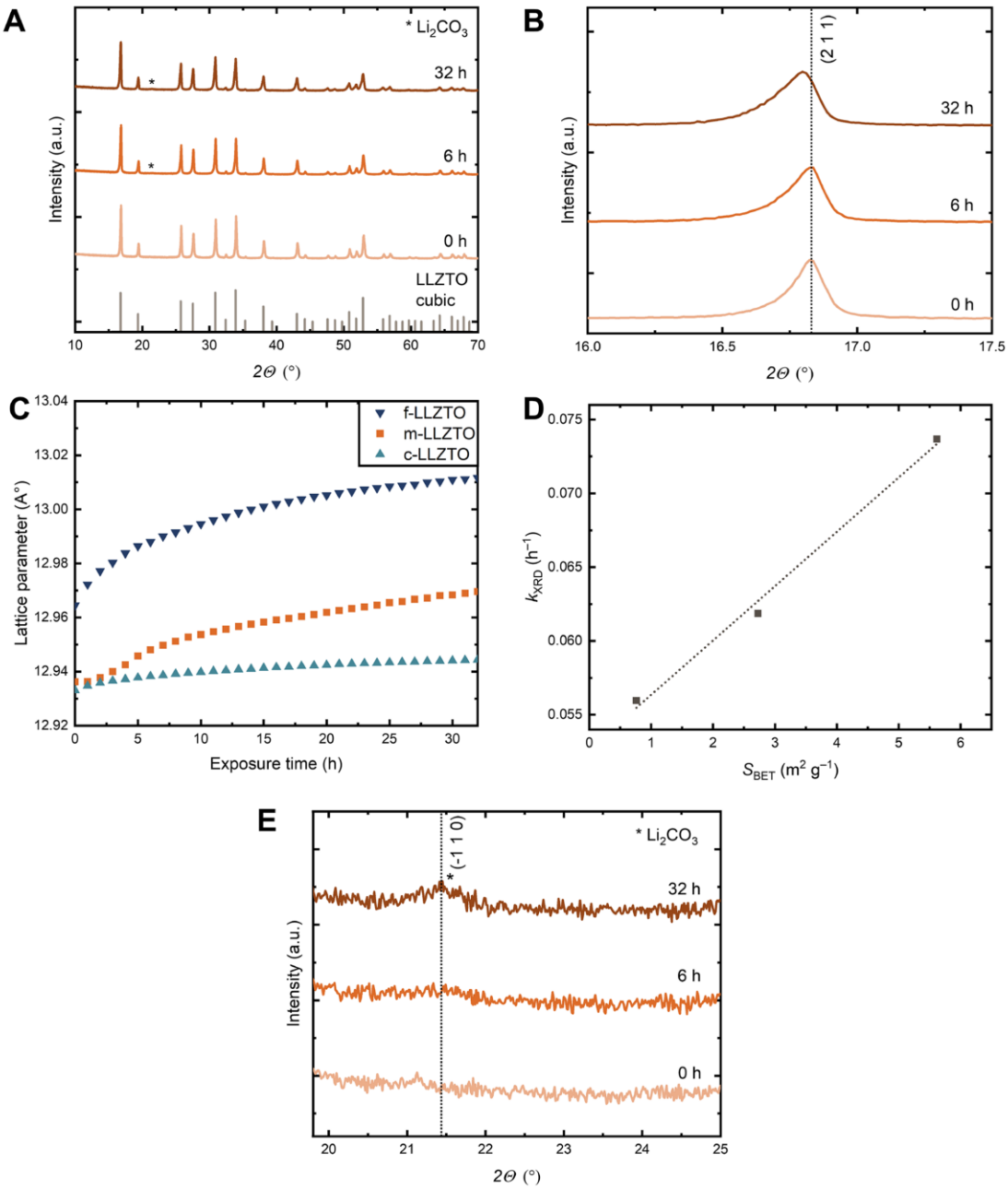

Figure 3. (A) XRD patterns of the powder sample m-LLZTO exposed to ambient air for 0, 6, and 32 h. The respective data for f- and c-LLZTO can be found in Figure S2. (B) Magnification of the reflection of the (211) lattice plane. (C) Temporal evolution of the LLZTO lattice parameter of the powder samples f-LLZTO, m-LLZTO, and c-LLZTO. (D) Calculated rate constants according to eq 8 of the Li^+/H^+ exchange observed in (C) for the powder samples f-LLZTO, m-LLZTO, and c-LLZTO as a function of the surface area S_{BET}. The dotted line is only for visualization. (E) Magnification of the reflection of the (−110) lattice plane of Li_2CO_3.

$$Li_{6.5}La_3Zr_{1.5}Ta_{0.5}O_{12\,(s)} + xH_2O_{(g)} \rightarrow Li_{6.5-x}H_xLa_3Zr_{1.5}Ta_{0.5}O_{12\,(s)} + xLiOH_{(s)} \quad (3)$$

$$2LiOH_{(s)} + CO_{2\,(g)} \rightarrow Li_2CO_{3\,(s)} + H_2O \quad (4)$$

$$LiOH_{(s)} + H_2O_{(g)} \rightarrow LiOH{\cdot}H_2O_{(s)} \quad (5)$$

$$2LiOH{\cdot}H_2O_{(s)} + CO_{2\,(g)} \rightarrow Li_2CO_{3\,(s)} + eH_2O \quad (6)$$

The morphology of the secondary phase, e.g., the spots on m- and c-LLZTO as well as the "coating" of f- and m-LLZTO,

https://doi.org/10.1021/acs.jpcc.3c01027
J. Phys. Chem. C 2023, 127, 8320−8331

resembles the morphologies that have been observed in studies on the surface of sintered pellets.[14,38,39] Depending on the surface area of the powder samples, the hydration/carbonation has progressed to a different extent for a given time. While f-LLZTO has already almost fully reacted at t = 6 h, it takes up to 32 h for m-LLZTO to get the particles' surfaces covered. Only small changes are observed in c-LLZTO over time.

3.3. Temporal Changes of the Crystal Structure. Time-resolved XRD analysis was performed in order to investigate the evolution of the crystal structure due to degradation reactions. In Figure 3A, the diffraction patterns of the powder sample m-LLZTO exposed to ambient air for 0, 6, and 32 h are given. The respective data of the f- and c-LLZTO powder samples are shown in Figure S2A,B.

At each time of exposure to ambient air, all samples retain the cubic LLZTO structure with the space group $Ia\bar{3}d$. However, the diffraction patterns exhibit a slight shift to lower diffraction angles as well as a growing reflection asymmetry over time, as demonstrated for the reflection of the (211) lattice plane in Figure 3B. The shift of the reflection maximum indicates an increase of the lattice parameter, which originates from the partial substitution of lithium ions with protons from H_2O in ambient air following eq 3. The lattice expansion can be explained by the replacement of strong Li−O bonds by weaker O−H···O bonds together with a non-discrete spread of the lattice parameter causing the asymmetry of the reflection. The stability of the cubic $Ia\bar{3}d$ phase and the correlated lattice expansion is in agreement with previous reports, in which LLZO has been exposed to ambient air.[23−25] A phase transformation to the slightly distorted non-centrosymmetric space group $I\bar{4}3d$ is not observed, as suggested by some authors for deep Li^+/H^+ exchange (>75%) in protic solvents.[10,18] The diffraction patterns of f- and c-LLZTO show a similar trend over time, f-LLZTO having the strongest shift and asymmetry and c-LLZTO the lowest compared with m-LLZTO (refer to Figure S2C,D).

The lattice expansion over time is demonstrated for the three samples in Figure 3C. At t = 0 h, f-LLZTO appears to have a larger lattice parameter compared with the other two samples. We assume that this is due to the faster Li^+/H^+ exchange of f-LLZTO compared to m- and c-LLZTO, and finite time that is required to record a diffractogram (35 min). The curves all exhibit an initial increase of the lattice parameter that slowly reaches an apparent plateau reflecting that the Li^+/H^+ exchange is decelerating. Such behavior has been observed before, but was not further discussed in terms of a kinetic model.[40,41] Arinicheva *et al.* proposed a mechanism of the hydration kinetics as investigated by thermogravimetry and gas sorption analysis.[42] According to their work, the hydration mechanism is based on the unreacted core shrinking model that describes the proceeding exchange reaction into the core of the particle toward the unreacted LLZTO. It is limited by the diffusion of water molecules through the LiOH layer (and Li_2CO_3 at a later stage) that is formed at the surface of the LLZTO particles. The core shrinking model has been intensively investigated for the isothermal hydration process in humid air of other oxides, e.g., for calcium oxide. There are various complex mathematical models considering material properties, e.g., porosity, molar flux, diffusivity of gas educts, and changes of particle size during the reaction. Details including the required assumptions can be found in elsewhere.[43−45]

Here, the kinetic model of Avrami was used in order to describe the kinetics of the diffusion-controlled LLZO hydration in Figure 3C as a simplified model, which will be described below. The Avrami equation is widely adopted to model the crystallization kinetics in solids comprising nucleation and growth, as given in eq 7 where $f(t)$ is the fraction of transformed material as a function of time t, k is the reaction rate, and n is the so-called Avrami exponent representing the dimensionality of crystal growth.[46,47]

$$f(t) = 1 - e^{-(kt)^n} \tag{7}$$

The Avrami equation is also commonly used for the description of solid−gas reactions including hydration reactions.[48,49] Please note that this approach relies on the assumption of a two-phase system of non-hydrated and hydrated material, which is greatly simplified for the hydration considered within this study. In fact, the composition of the hydrated $Li_{6.5-x}H_xLa_3Zr_{1.5}Ta_{0.5}O_{12}$ is distributed from the surface to the core of the particles dependent on the state of hydration. The latter is determined by several diffusion processes: (i) H^+ diffusion in the $LiOH/Li_2CO_3$ layers on the particle surface, (2) H^+ diffusion in the LLZTO particles, and also (3) Li^+ diffusion in the $LiOH/Li_2CO_3$ layers. Therefore, the Avrami equation describes the time-dependent change in lattice parameter in a simplified manner. However, we applied it as a useful way to semi-quantitatively describe the different hydration behavior of the distinct powders.

In order to account for the fact that nucleation occurs heterogeneously at the surface of solid particles instead of homogeneously in the bulk,[50,51] we applied a modified first-order Avrami model (n = 1) that considers the consecutive occupation of available reaction sites on the surface of the particles. Equation 8 gives the lattice parameter a as a function of time t, a_0 is the lattice parameter at t = 0 h, $a_{plateau}$ is the lattice parameter after reaching the apparent plateau, and k_{XRD} is the rate constant of the reaction.

$$a(t) = a_0 + (a_{plateau} - a_0)(1 - e^{-k_{XRD}t}) \tag{8}$$

The fitted data from experimental results in Figure 3C can be found in Figure S3 and Table S1, revealing R^2 values >0.99, i.e., close to 1. The rate constants k_{XRD} differ significantly between the powder samples f-LLZTO, m-LLZTO, and c-LLZTO. Figure 3D shows the linear dependence of the calculated rate constants k_{XRD} from S_{BET}. The rate of Li^+/H^+ exchange is directly correlated to the specific surface area and available surface reaction sites. This is in agreement with the studies related to the core shrinking model. The authors explained the slow reaction kinetics of larger particles by the larger surface area and the correlated increase of the diffusion path for the reactant gas to reach the unreacted core.[43,44,52] Therefore, this correlation allows a useful estimation of the Li^+/H^+ exchange rate for different particle sizes.

Besides the lattice parameter expansion, the evolution of a weak reflection at a diffraction angle of about 21.5° in 2Θ over time can be seen in Figure 3A. It can be assigned to the (−110) lattice plane of Li_2CO_3 that forms upon the carbonation of the formed LiOH throughout the Li^+/H^+ exchange reaction (eq 4). The respective data of f- and c-LLZTO can be found in Figure S2E,F. Considering that lithium has a very low X-ray scattering factor, Raman spectroscopy was employed next as a complementary

https://doi.org/10.1021/acs.jpcc.3c01027
J. Phys. Chem. C 2023, 127, 8320−8331

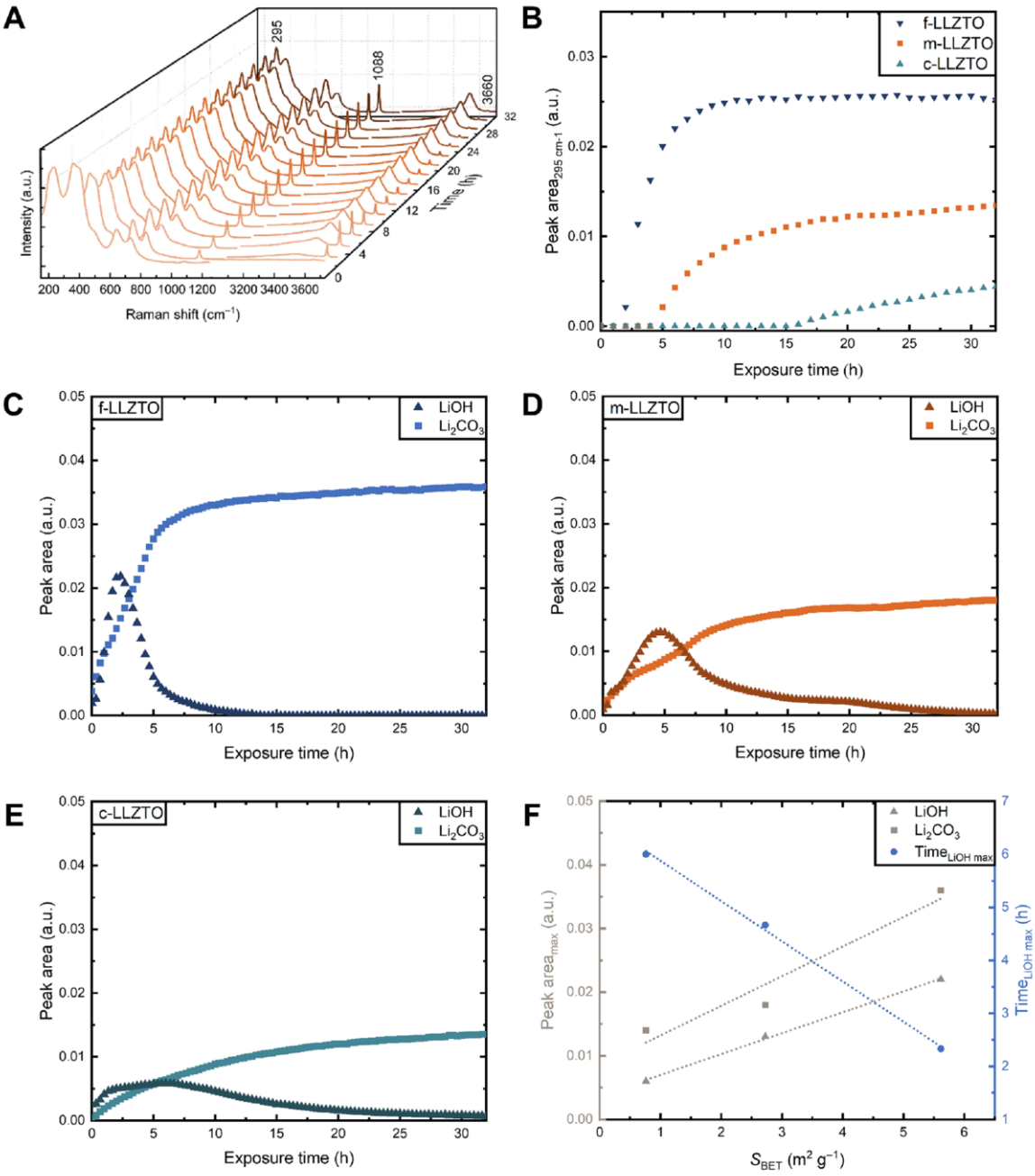

Figure 4. (A) Averaged Raman spectra (mapping) of the m-LLZTO powder sample exposed to ambient air as a function of time. The respective data for f- and c-LLZTO powder samples can be found in Figures S3. (B) Evolution of the normalized peak area at 295 cm^{-1} as a function of time for the f-, m-, and c-LLZTO powder samples. Evolution of the normalized peak areas of Li_2CO_3 (1088 cm^{-1}) and LiOH (3660 cm^{-1}) as a function of time for (C) f-LLZTO, (D) m-LLZTO, and (E) c-LLZTO. (F) Extracted maximum peak areas of Li_2CO_3 and LiOH as well as point in time of the maximum LiOH signal as a function of S_{BET} of the powder samples with dotted lines as a guide to the eye.

technique to study the formation of Li-containing secondary phases.

3.4. Temporal Changes of Chemical Composition. In contrast to XRD, Raman spectroscopy is very sensitive to Li-containing secondary phases and probes only the surface of the particles compared to bulk penetration in XRD. Raman spectroscopy was performed on the f-, m-, and c-LLZTO powder samples over time. To get good statistics, average spectra were obtained from Raman mapping of 500 × 500 μm^2 areas, as demonstrated exemplary in Figure 4A for m-LLZTO.

https://doi.org/10.1021/acs.jpcc.3c01027
J. Phys. Chem. C 2023, 127, 8320−8331

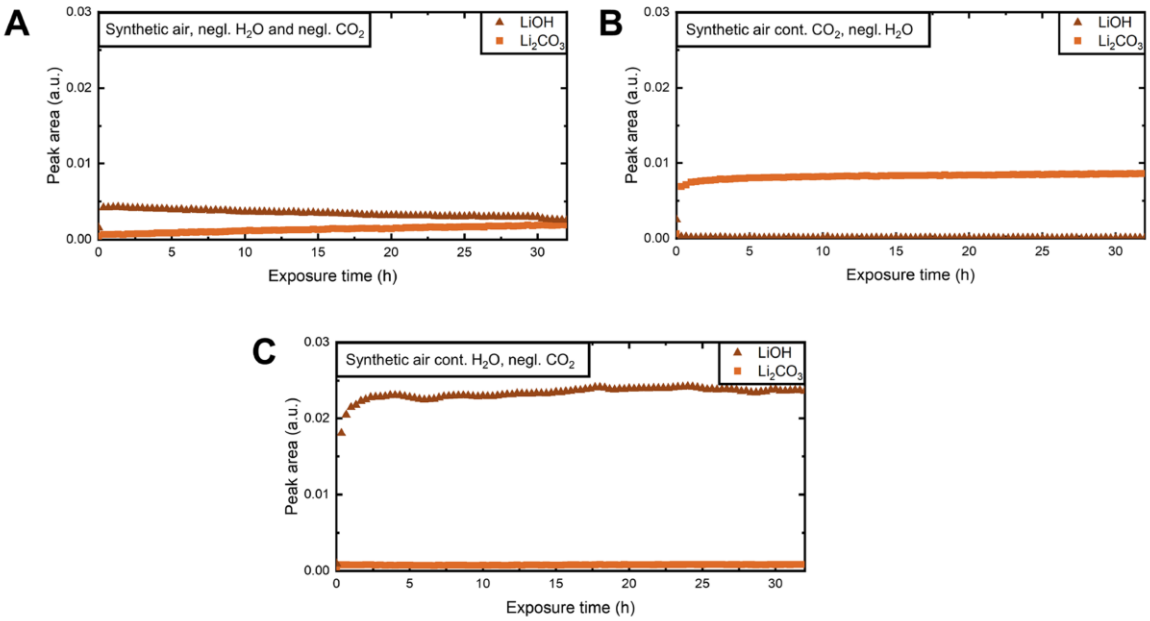

Figure 5. Averaged Raman mapping spectra of the powder sample m-LLZTO in dependence of exposure time in (A) synthetic air (mixture of N_2 and O_2 in the volume ratio of 78/21 with a negligible amount of CO_2 and H_2O (negl. CO_2, negl. H_2O), (B) synthetic air containing CO_2 in an equal amount to the amount in ambient air (400 ppm-mol), but negligible amount of H_2O (negl. H_2O), and (C) synthetic air containing a defined amount of moisture (40−45% RH), but negligible amount of CO_2 (negl. CO_2).

The Raman spectrum at t = 0 h agrees well with the spectra of cubic LLZO reported in the literature.[13−15,53] Qualitatively, the bands between 180 and 300 cm^{-1} can be assigned to internal modes of the LiO_6 octahedron, whereas the internal modes of LiO_4 tetrahedra are expected in the range of 300 to 500 cm^{-1}. The band at about 640 cm^{-1} is due to the Zr−O bond stretching vibration in the ZrO_6 octahedron as well as the Ta−O stretching vibration in the TaO_6 octahedron at about 750 cm^{-1}. Over time, the double peak between 180 and 400 cm^{-1} changes significantly in shape and intensity distribution. Most predominantly, a new band arises at 295 cm^{-1} with two shoulders at each side. Additionally, the Zr−O and Ta−O stretching modes are slightly shifted to higher wavenumbers. We assume that this transformation can be assigned to a protonated form of LLZTO due to the occurring Li^+/H^+ exchange over time following eq 3. A similar peak shape has been observed before for aged LLZO samples.[11,54] The spectra of f- and c-LLZTO show analogous trends, but the transformation onset is different for f-LLZTO and c-LLZTO compared with m-LLZTO (Figure S4). Therefore, the evolution of the most intense band at 295 cm^{-1} as a function of time is given in Figure 4B for the three samples. Please note that no signal can be evaluated within the first hours because of the strong overlap of the 295 cm^{-1} band with the already existing bands. Hence, it cannot be excluded that the transformation has already started before. However, it gets clear that the Li^+/H^+ exchange is faster for f-LLZTO and delayed for c-LLZTO compared with m-LLZTO. The curves qualitatively resemble those of the XRD results and thus are in good agreement with the kinetic model and its surface area dependence.

Besides the changes in the bands attributed to LLZTO, a band at 3660 cm^{-1} appears in the first few hours and then decreases again over time. We assign this band to the stretching vibrations of O−H bonds in LiOH, which agrees well with reference values of the pure compound.[55,56] Regarding studies on LLZO, such high wavenumber regions have rarely been considered,[17] but it provides useful information about the kinetics of the Li^+/H^+ exchange reaction. Furthermore, a band at 1088 cm^{-1} increases over time, which can be assigned to Li_2CO_3. Its appearance has been observed in several studies; however, those studies lacked high time resolution and mostly only studied pellet surfaces.[11,14,15,39] Additionally, a broad band from 3200 to 3600 cm^{-1} is emerging over time that is attributed to water loosely adsorbed on the LLZTO surface.[57,58] It can also stem from crystal water in $LiOH{\cdot}H_2O$, but has probably minor influence as the most prominent band of $LiOH{\cdot}H_2O$ at 3572 cm^{-1}[59] is not observed.

In Figure 4C−E, the normalized peak areas related to Li_2CO_3 and LiOH are plotted versus time for the three f-, m-, and c-LLZTO samples. Qualitatively, all curves exhibit the same peak shape. While the LiOH signal reaches a maximum after a certain amount of time and then vanishes, the Li_2CO_3 signal increases within the first hours and reaches an apparent saturation within the considered time period. We conclude that hydration and carbonation are strongly coupled consecutive reaction pathways that are overall determined by the postulated core shrinking model. At the beginning, the hydration via eq 3 takes place at the free surface reaction sites following an Avrami-like behavior, as observed by the XRD results. It is directly followed by the carbonation following eq 4. Once the surface is fully covered by the reaction products LiOH and Li_2CO_3, impeding the diffusion of water molecules to the unreacted core, the hydration reaction is decelerated as also demonstrated by the XRD results. The

https://doi.org/10.1021/acs.jpcc.3c01027
J. Phys. Chem. C 2023, 127, 8320−8331

reaction mechanism then proceeds solely via the carbonation that is controlled by the available LiOH reaction sites from eq 3 as well as the diffusivity of CO_2 molecules through the product layer. Thus, the rate-limiting step of the overall reaction mechanism is the diffusion process of H_2O and CO_2. This is typical for two-step consecutive reactions and has been investigated for calcium oxide in detail[45,60] as well as for other compounds, such as calcium silicate.[61] For LLZO, such detailed kinetic studies of both hydration and carbonation have not been reported before. Only studies considering specific air exposure times can be found in the literature,[14,15,38] e.g., Lu *et al.* studied the temporal evolution of the Li_2CO_3 reflection by XRD and observed a linear dependence. However, the study was performed on a pellet surface and the kinetics differs substantially from our study.[25]

As can be seen from Figure 4C−E, the three investigated samples show significantly different two-step reaction kinetics. The rate constant of the hydration reaction decreases from f- to m- and c-LLZTO, which causes a shift of the time, at which the LiOH signal is at its maximum (f-LLZTO: ∼2.5 h, m-and LLZTO: ∼4 h, c-LLZTO: ∼5 h). Due to the consecutive reaction pathway, the rate constant of the carbonation reaction shows a similar behavior for the different samples. In the same manner, the maxima of the LiOH signal as well as the plateau of the Li_2CO_3 signal qualitatively decline from f-LLZTO to m-LLZTO and c-LLZTO. Figure 4F shows the extracted values as a function of S_{BET} of the powder samples. They all show a linear dependence on surface area, which is in good agreement with the observations made by XRD (Figure 3D). Not only the hydration mechanism but also the carbonation reaction is dominated by the core shrinking mechanism that is strongly influenced by the available surface reaction sites. As the extracted intensities of the Raman spectra are not absolute values, the absolute carbon and water contents of the three samples after an exposure time of 32 h were measured by a multiphase determinator using IR spectroscopy and are given in Tables S2 and S3, confirming the linear dependence. Please note that the water content not only stems from LiOH but also from adsorbed water and crystal water. The investigation of the degradation of LLZO powders with different particle sizes provides an important contribution for the processability of powders, e.g., for the incorporation in polymer matrices for HE application. Especially, submicrometer powders need to be handled with care.

In order to confirm the postulated two-step consecutive reaction mechanism of hydration and carbonation, the process atmosphere was systematically varied from (i) ambient air to (ii) synthetic air, i.e., a mixture of N_2 and O_2 in the volume ratio of 78/21 with a negligible amount of CO_2 and H_2O (named negl. CO_2 and negl. H_2O in the following), (iii) synthetic air containing CO_2 in an amount equal to the amount in ambient air (400 ppm-mol), but negligible amount of H_2O (negl. H_2O), and (iv) synthetic air containing a defined amount of moisture (40−45% RH), but negligible amount of CO_2 (negl. CO_2). In Figure 5, the time-dependent peak areas of LiOH and Li_2CO_3 from Raman spectroscopy are given for m-LLZTO in the different process atmospheres.

In a synthetic air (N_2/O_2 mixture) atmosphere, only slight changes in the LiOH and Li_2CO_3 signal are observed. At t = 0 h, the LiOH signal is above zero, which we attribute to unavoidable brief exposure to ambient air during sample transfer after the milling process (Figure 5A). It slowly diminishes over time, while the Li_2CO_3 signal slightly increases. Therefore, we assume that the CO_2 traces in synthetic air (≤ 0.1 ppm-mol) are sufficient to cause a reaction from LiOH (present at the beginning) to Li_2CO_3. Such high sensitivity toward CO_2 (and H_2O) is in accordance with other reports in which the authors examined the surface species on LLZO pellets in a glove box atmosphere, also revealing hydration and carbonation products.[62,63] The LLZTO remains unaffected, as shown by negligible lattice expansion in XRD (Figure S5).

In comparison, the reaction proceeds much faster in dry air (CO_2 amount equal to ambient air: 400 ppm mol) due to the larger content of the reactant CO_2 (Figure 5B). As known from the literature, the reaction from LiOH to Li_2CO_3 is thermodynamically highly favored,[21] which confirms that it is not the rate-limiting step of the overall degradation mechanism. Another possible reaction pathway contrarily discussed in other studies[14,15,20,21] is the direct carbonation of LLZO via eq 9:

$$Li_7La_3Zr_2O_{12\,(s)} + xCO_{2\,(g)} \rightarrow Li_{7-2x}La_3Zr_2O_{12-x\,(s)} + xLi_2CO_{3\,(s)} \quad (9)$$

This reaction includes only a single step, and the final product is a non-protonated LLZO in contrast to the two-step mechanism in eqs 3 and 4. As the Li_2CO_3 signal saturates after the LiOH present at the beginning has converted, we hypothesize that the direct carbonation of LLZTO does not take place. Hence, the protonation of LLZTO and the resulting formation of the intermediate LiOH is an essential step of the degradation mechanism. This is in agreement with the work by Sharafi *et al.*[15] and Xia *et al.*,[14] who both demonstrated experimentally and theoretically that the direct carbonation in eq 9 is thermodynamically unfavored, i.e., endergonic, while both the protonation of LLZO in eq 3 and the following reaction from LiOH to Li_2CO_3 in eq 4 are exergonic. However, the authors did not specify the exact CO_2 content of dry air used in their studies.

In humid air (40−45% RH, Figure 5C), only the hydration reaction via eq 3 occurs, i.e., the LiOH signal increases and stays constant as soon as the surface is saturated, furthermore proving that the reaction is diffusion-controlled by H_2O diffusion through the LiOH layer. The results were all confirmed by determination of the absolute carbon and water content after 32 h compared with the results in ambient air (Tables S2 and S3).

Overall, the hydration of LLZO is the prerequisite step for its degradation and should therefore be avoided when handling LLZO. Synthetic air or dry air containing CO_2 (in an amount equal to ambient air) are preferred. The systematic variation of the process atmosphere provides useful information for work environments like dry rooms and their specifications.

4. CONCLUSIONS

In this study, the degradation mechanism of LLZTO powders under ambient air was investigated in a time-resolved manner. The kinetics of hydration and carbonation are unraveled in detail for three different particle sizes ranging from fine (f-; 0.4 μm) to mid-range (m-; 0.8 μm) and coarse LLZTO particles (c-; 5 μm). Regarding hydration, the kinetics was found to follow the Avrami model examined by lattice expansion of the LLZTO crystal upon Li^+/H^+ exchange. The reaction rate is limited by the diffusion of water through the developing LiOH

https://doi.org/10.1021/acs.jpcc.3c01027
J. Phys. Chem. C 2023, 127, 8320−8331

layer. The corresponding rate constants increase linearly with the surface area of the particles. Raman spectroscopy was chosen as a useful technique to analyze both hydration and carbonation by monitoring LiOH and Li_2CO_3 bands over time. It could be demonstrated that the degradation mechanism is a two-step consecutive reaction pathway with the hydration as a prerequisite intermediate step. Degradation kinetics is in accordance with the core shrinking model and is faster with a larger specific surface area, which is in agreement with the results of powder morphology investigations, which revealed a faster Li_2CO_3 evolution for f-LLZTO than for m-LLZTO and c-LLZTO. The reaction mechanism was further elucidated by systematic variation of the process atmosphere from (i) ambient air to (ii) synthetic air (N_2/O_2 mixture, negligible amounts of H_2O and CO_2), (iii) dry air (containing CO_2 in an amount equal to ambient air, negligible amount of H_2O), and (iv) humid synthetic air (containing defined amount of H_2O, negligible amount of CO_2). Indeed, the direct carbonation of LLZTO is excluded, making an important contribution to handling conditions of LLZTO powders. Overall, this work clarifies the degradation mechanism and kinetics of LLZTO and provides crucial information on the processability of LLZTO powders with different particle sizes, facilitating its practical application in SSBs.

■ ASSOCIATED CONTENT

Supporting Information

The Supporting Information is available free of charge at https://pubs.acs.org/doi/10.1021/acs.jpcc.3c01027.

Additional details including EDX spectra of particle agglomerates after air exposure, full set of data for f- and c-LLZTO including time-dependent XRD and Raman measurements, and absolute carbon and water contents of all powder samples determined by IR spectroscopy in a multiphase determinator (PDF)

■ AUTHOR INFORMATION

Corresponding Authors

Andreas Roters − *SCHOTT AG, Mainz D-55122, Germany*; Email: andreas.roters@schott.com

Jürgen Janek − *Center for Materials Research (ZfM) and Institute of Physical Chemistry, Justus Liebig University, Giessen D-35392, Germany*; orcid.org/0000-0002-9221-4756; Email: juergen.janek@pc.jlug.de

Authors

Nina Hoinkis − *SCHOTT AG, Mainz D-55122, Germany*; *Center for Materials Research (ZfM) and Institute of Physical Chemistry, Justus Liebig University, Giessen D-35392, Germany*

Jörg Schuhmacher − *SCHOTT AG, Mainz D-55122, Germany*

Sebastian Leukel − *SCHOTT AG, Mainz D-55122, Germany*

Christoph Loho − *SCHOTT AG, Mainz D-55122, Germany*

Felix H. Richter − *Center for Materials Research (ZfM) and Institute of Physical Chemistry, Justus Liebig University, Giessen D-35392, Germany*; orcid.org/0000-0002-6587-7757

Complete contact information is available at: https://pubs.acs.org/10.1021/acs.jpcc.3c01027

Notes

The authors declare no competing financial interest.

■ ACKNOWLEDGMENTS

N.H., J.S., and A.R. acknowledge funding by the European Union's Horizon 2020 research and innovation programme under the project "SAFELiMOVE", Grant Agreement no. 875189. F.H.R. and J.J. acknowledge funding by the BMBF (Federal Ministry for Education and Research) under the project LiSi-2 (03XP0509B).

■ REFERENCES

(1) Hatzell, K. B.; Chen, X. C.; Cobb, C. L.; Dasgupta, N. P.; Dixit, M. B.; Marbella, L. E.; McDowell, M. T.; Mukherjee, P. P.; Verma, A.; Viswanathan, V.; et al. Challenges in Lithium Metal Anodes for Solid-State Batteries. *ACS Energy Lett.* **2020**, *5*, 922−934.

(2) Samson, A. J.; Hofstetter, K.; Bag, S.; Thangadurai, V. A Bird's-Eye View of Li-Stuffed Garnet-Type Li7La3Zr2O12 Ceramic Electrolytes for Advanced All-Solid-State Li Batteries. *Energy Environ. Sci.* **2019**, *12*, 2957−2975.

(3) Janek, J.; Zeier, W. G. A Solid Future for Battery Development. *Nat. Energy* **2016**, *1*, 16141.

(4) Wang, C.; Fu, K.; Kammampata, S. P.; McOwen, D. W.; Samson, A. J.; Zhang, L.; Hitz, G. T.; Nolan, A. M.; Wachsman, E. D.; Mo, Y.; et al. Garnet-Type Solid-State Electrolytes: Materials, Interfaces, and Batteries. *Chem. Rev.* **2020**, *120*, 4257−4300.

(5) Murugan, R.; Thangadurai, V.; Weppner, W. Fast Lithium Ion Conduction in Garnet-Type Li7La3Zr2O12. *Am. Ethnol.* **2007**, *46*, 7778−7781.

(6) Hitz, G. T.; McOwen, D. W.; Zhang, L.; Ma, Z.; Fu, Z.; Wen, Y.; Gong, Y.; Dai, J.; Hamann, T. R.; Hu, L.; et al. High-Rate Lithium Cycling in a Scalable Trilayer Li-Garnet-Electrolyte Architecture. *Mater. Today* **2019**, *22*, 50−57.

(7) Li, L.; Deng, Y.; Chen, G. Status and Prospect of Garnet/Polymer Solid Composite Electrolytes for All-Solid-State Lithium Batteries. *J. Energy Chem.* **2020**, *50*, 154−177.

(8) Jin, Y.; McGinn, P. J. Li7La3Zr2O12 Electrolyte Stability in Air and Fabrication of a Li/Li7La3Zr2O12/Cu0.1V2O5 Solid-State Battery. *J. Power Sources* **2013**, *239*, 326−331.

(9) Ma, C.; Rangasamy, E.; Liang, C.; Sakamoto, J.; More, K. L.; Chi, M. Excellent Stability of a Llithium-Ion-Conducting Solid Electrolyte upon Reversible Li(+) /H(+) Exchange in Aqueous Solutions. *Am. Ethnol.* **2015**, *54*, 129−133.

(10) Galven, C.; Suard, E.; Mounier, D.; Crosnier-Lopez, M.-P.; Le Berre, F. Structural Characterization of a New Acentric Protonated Garnet: Li6−xHxCaLa2Nb2O12. *J. Mater. Res.* **2013**, *28*, 2147−2153.

(11) Rosen, M.; Ye, R.; Mann, M.; Lobe, S.; Finsterbusch, M.; Guillon, O.; Fattakhova-Rohlfing, D. Controlling the Lithium Proton Exchange of LLZO to Enable Reproducible Processing and Performance Optimization. *J. Mater. Chem. A* **2021**, *9*, 4831−4840.

(12) Grissa, R.; Payandeh, S.; Heinz, M.; Battaglia, C. Impact of Protonation on the Electrochemical Performance of Li7La3Zr2O12 Garnets. *ACS Appl. Mater. Interfaces* **2021**, *13*, 14700−14709.

(13) Larraz, G.; Orera, A.; Sanjuán, M. L. Cubic Phases of Garnet-Type Li7La3Zr2O12: the Role of Hydration. *J. Mater. Chem. A* **2013**, *1*, 11419.

(14) Xia, W.; Xu, B.; Duan, H.; Tang, X.; Guo, Y.; Kang, H.; Li, H.; Liu, H. Reaction Mechanims of Lithium Garnet Pellets in Ambient Air: The Effect of Humidity and CO2. *J. Am. Ceram. Soc.* **2017**, 1−8.

(15) Sharafi, A.; Yu, S.; Naguib, M.; Lee, M.; Ma, C.; Meyer, H. M.; Nanda, J.; Chi, M.; Siegel, D. J.; Sakamoto, J. Impact of Air Exposure and Surface Chemistry on Li−Li7La3Zr2O12 Interfacial Resistance. *J. Mater. Chem. A* **2017**, *5*, 13475−13487.

(16) Cheng, L.; Liu, M.; Mehta, A.; Xin, H.; Lin, F.; Persson, K.; Chen, G.; Crumlin, E. J.; Doeff, M. Garnet Electrolyte Surface Degradation and Recovery. *ACS Appl. Energy Mater.* **2018**, *1*, 7244−7252.

(17) Orera, A.; Larraz, G.; Rodríguez-Velamazán, J. A.; Campo, J.; Sanjuán, M. L. Influence of Li(+) and H(+) Distribution on the Crystal Structure of Li(7-x)H(x)La3Zr2O12 ($0 \leq x \leq 5$) Garnets. *Inorg. Chem.* **2016**, *55*, 1324−1332.
(18) Liu, X.; Chen, Y.; Hood, Z. D.; Ma, C.; Yu, S.; Sharafi, A.; Wang, H.; An, K.; Sakamoto, J.; Siegel, D. J.; et al. Elucidating the Mobility of H+ and Li+ Ions in (Li6.25−xHxAl0.25)La3Zr2O12 via Correlative Neutron and Electron Spectroscopy. *Energy Environ. Sci.* **2019**, *12*, 945−951.
(19) Huo, H.; Luo, J.; Thangadurai, V.; Guo, X.; Nan, C.-W.; Sun, X. Li 2 CO 3 : A Critical Issue for Developing Solid Garnet Batteries. *ACS Energy Lett.* **2020**, *5*, 252−262.
(20) Cheng, L.; Crumlin, E. J.; Chen, W.; Qiao, R.; Hou, H.; Franz Lux, S.; Zorba, V.; Russo, R.; Kostecki, R.; Liu, Z.; et al. The Origin of High Electrolyte-Electrode Interfacial Resistances in Lithium Cells Containing Garnet Type Solid Electrolytes. *Phys. Chem. Chem. Phys.* **2014**, *16*, 18294−18300.
(21) Li, Y.; Prabhu, A. M.; Choksi, T. S.; Canepa, P. H2O and CO2 Surface Contamination of the Lithium Garnet Li7La3Zr2O12 Solid Electrolyte. *J. Mater. Chem. A* **2022**, *10*, 4960−4973.
(22) Wang, Y.; Lai, W. Phase Transition in Lithium Garnet Oxide Ionic Conductors Li7La3Zr2O12: The Role of Ta Substitution and H2O/CO2 Exposure. *J. Power Sources* **2015**, *275*, 612−620.
(23) Kun, R.; Langer, F.; Delle Piane, M.; Ohno, S.; Zeier, W. G.; Gockeln, M.; Colombi Ciacchi, L.; Busse, M.; Fekete, I. Structural and Computational Assessment of the Influence of Wet-Chemical Post-Processing of the Al-Substituted Cubic Li7La3Zr2O12. *ACS Appl. Mater. Interfaces* **2018**, *10*, 37188−37197.
(24) Brugge, R. H.; Hekselman, A. K. O.; Cavallaro, A.; Pesci, F. M.; Chater, R. J.; Kilner, J. A.; Aguadero, A. Garnet Electrolytes for Solid State Batteries: Visualization of Moisture-Induced Chemical Degradation and Revealing Its Impact on the Li-Ion Dynamics. *Chem. Mater.* **2018**, *30*, 3704−3713.
(25) Lu, W.; Wang, T.; Xue, M.; Zhang, C. Improved Li6.5La3Zr1.5Nb0.5O12 Electrolyte and Effects of Atmosphere Exposure on Conductivities. *J. Power Sources* **2021**, *497*, No. 229845.
(26) Gupta, A.; Sakamoto, J. Controlling Ionic Transport through the PEO-LiTFSI/LLZTO Interface. *Electrochem. Soc. Interface* **2019**, *28*, 63−69.
(27) Keller, M.; Appetecchi, G. B.; Kim, G.-T.; Sharova, V.; Schneider, M.; Schuhmacher, J.; Roters, A.; Passerini, S. Electrochemical Performance of a Solvent-Free Hybrid Ceramic-Polymer Electrolyte Based on Li7La3Zr2O12 in P(EO)15LiTFSI. *J. Power Sources* **2017**, *353*, 287−297.
(28) Guo, Y.; Cheng, J.; Zeng, Z.; Li, Y.; Zhang, H.; Li, D.; Ci, L. Li2CO3 : Insights into Its Blocking Effect on Li-Ion Transfer in Garnet Composite Electrolytes. *ACS Appl. Energy Mater.* **2022**, *5*, 2853−2861.
(29) Huo, H.; Li, X.; Sun, Y.; Lin, X.; Doyle-Davis, K.; Liang, J.; Gao, X.; Li, R.; Huang, H.; Guo, X.; et al. Li2CO3 Effects: New Insights into Polymer/Garnet Electrolytes for Dendrite-Free Solid Lithium Batteries. *Nano Energy* **2020**, *73*, No. 104836.
(30) Brugge, R. H.; Pesci, F. M.; Cavallaro, A.; Sole, C.; Isaacs, M. A.; Kerherve, G.; Weatherup, R. S.; Aguadero, A. The Origin of Chemical Inhomogeneity in Garnet Electrolytes and its Impact on the Electrochemical Performance. *J. Mater. Chem. A* **2020**, *8*, 14265−14276.
(31) Cheng, L.; Wu, C. H.; Jarry, A.; Chen, W.; Ye, Y.; Zhu, J.; Kostecki, R.; Persson, K.; Guo, J.; Salmeron, M.; et al. Interrelationships among Grain Size, Surface Composition, Air Stability, and Interfacial Resistance of Al-Substituted Li7La3Zr2O12 Solid Electrolytes. *ACS Appl. Mater. Interfaces* **2015**, *7*, 17649−17655.
(32) Cheng, L.; Park, J. S.; Hou, H.; Zorba, V.; Chen, G.; Richardson, T.; Cabana, J.; Russo, R.; Doeff, M. Effect of Microstructure and Surface Impurity Segregation on the Electrical and Electrochemical Properties of Dense Al-Substituted Li7La3Zr2O12. *J. Mater. Chem. A* **2014**, *2*, 172−181.
(33) Schneider, M.; Hochrein, O.; Wolfgang, S.; Kunze, M. Ionenleitende Glaskeramik mit Granatartiger Kristallstruktur. DE102014100684A1, 2015.
(34) Schuhmacher, J.; Treis, P.; Drewke, J.; Schmitt, H. J.; Samsinger, R. F.; Roters, A.; Schneider, M. Solid-State Lithium-Ion Conductor Materials, Powder made of Solid-State Ion Conductor Materials and Method for Producing Same. US 20,220,328,817 A1. 2022.
(35) Liu, J.; Gao, X.; Hartley, G. O.; Rees, G. J.; Gong, C.; Richter, F. H.; Janek, J.; Xia, Y.; Robertson, A. W.; Johnson, L. R.; et al. The Interface between Li6.5La3Zr1.5Ta0.5O12 and Liquid Electrolyte. *Joule* **2020**, *4*, 101−108.
(36) Yi, M.; Liu, T.; Wang, X.; Li, J.; Wang, C.; Mo, Y. High Densification and Li-Ion Conductivity of Al-Free Li7-xLa3Zr2-xTaxO12 Garnet Solid Electrolyte Prepared by Using Ultrafine Powders. *Ceram. Int.* **2019**, *45*, 786−792.
(37) Geng, H.; Chen, K.; Di, Y.; Mei, A.; Huang, M.; Lin, Y.; Nan, C. Formation Mechanism of Garnet-Like Li7La3Zr2O12 Powder Prepared by Solid State Reaction. *Rare Metal Mater. Eng.* **2016**, *45*, 612−616.
(38) Leng, J.; Wang, H.; Liang, H.; Xiao, Z.; Wang, S.; Zhang, Z.; Tang, Z. Storage of Garnet Solid Electrolytes: Insights into Air Stability and Surface Chemistry. *ACS Appl. Energy Mater.* **2022**, *5*, 5108−5116.
(39) Xia, W.; Xu, B.; Duan, H.; Guo, Y.; Kang, H.; Li, H.; Liu, H. Ionic Conductivity and Air Stability of Al-Doped $Li_7La_3Zr_2O_{12}$ Sintered in Alumina and Pt Crucibles. *ACS Appl. Mater. Interfaces* **2016**, *8*, 5335−5342.
(40) Redhammer, G. J.; Tippelt, G.; Portenkirchner, A.; Rettenwander, D. Aging Behavior of Al- and Ga- Stabilized Li7La3Zr2O12 Garnet-Type, Solid-State Electrolyte Based on Powder and Single Crystal X-ray Diffraction. *Crystals* **2021**, *11*, 721.
(41) Yow, Z. F.; Oh, Y. L.; Gu, W.; Rao, R. P.; Adams, S. Effect of Li +/H+ exchange in water treated Ta-doped Li7La3Zr2O12. *Solid State Ionics* **2016**, *292*, 122−129.
(42) Arinicheva, Y.; Guo, X.; Gerhards, M.-T.; Tietz, F.; Fattakhova-Rohlfing, D.; Finsterbusch, M.; Navrotsky, A.; Guillon, O. Competing Effects in the Hydration Mechanism of a Garnet-Type Li 7 La 3 Zr 2 O 12 Electrolyte. *Chem. Mater.* **2022**, *34*, 1473−1480.
(43) Blamey, J.; Zhao, M.; Manovic, V.; Anthony, E. J.; Dugwell, D. R.; Fennell, P. S. A Shrinking Core Model for Steam Hydration of CaO-Based Sorbents Cycled for CO2 Capture. *Chem. Eng. J.* **2016**, *291*, 298−305.
(44) Criado, Y. A.; Alonso, M.; Abanades, J. C. Kinetics of the CaO/Ca(OH) 2 Hydration/Dehydration Reaction for Thermochemical Energy Storage Applications. *Ind. Eng. Chem. Res.* **2014**, *53*, 12594−12601.
(45) Gravogl, G.; Birkelbach, F.; Müller, D.; Lengauer, C. L.; Weinberger, P.; Miletich, R. Pressure Dependence of the Low Temperature Carbonation Kinetics of Calcium Oxide for Potential Thermochemical Energy Storage Purposes and Sustainable CO 2 Fixation. *Adv. Sustainable Syst.* **2021**, *5*, 2100022.
(46) Avrami, M. Kinetics of Phase Change. I General Theory. *J. Chem. Phys.* **1939**, *7*, 1103−1112.
(47) Khawam, A.; Flanagan, D. R. Solid-State Kinetic Models: Basics and Mathematical Fundamentals. *J. Phys. Chem. B* **2006**, *110*, 17315−17328.
(48) Fedunik-Hofman, L.; Bayon, A.; Donne, S. W. Kinetics of Solid-Gas Reactions and Their Application to Carbonate Looping Systems. *Energies* **2019**, *12*, 2981.
(49) Sun, Y.; Wang, Z. H.; Park, D. J.; Kim, W. S.; Kim, H. S.; Yan, S. R.; Lee, H. S. Analysis of the Isothermal Hydration Heat of Cement Paste Containing Mechanically Activated Fly Ash. *Thermochim. Acta* **2022**, *715*, No. 179273.
(50) Pang, E. L.; Vo, N. Q.; Philippe, T.; Voorhees, P. W. Modeling Interface-Controlled Phase Transformation Kinetics in Thin Films. *J. Appl. Phys.* **2015**, *117*, 175304.
(51) Dri, M.; Sanna, A.; Maroto-Valer, M. M. Dissolution of Steel Slag and Recycled Concrete Aggregate in Ammonium Bisulphate for

https://doi.org/10.1021/acs.jpcc.3c01027
J. Phys. Chem. C 2023, 127, 8320−8331

CO2 Mineral Carbonation. *Fuel Process. Technol.* **2013**, *113*, 114−122.
(52) Rehmat, A.; Saxena, S. c. Single Nonisothermal Noncatalytic Solid-Gas Reaction. Effect of Changing Particle Size. *Ind. Eng. Chem. Proc. Des. Dev.* **1976**, *15*, 343−350.
(53) Thompson, T.; Wolfenstine, J.; Allen, J. L.; Johannes, M.; Huq, A.; David, I. N.; Sakamoto, J. Tetragonal vs. Cubic Phase Stability in Al-Free Ta Doped Li7La3Zr2O12 (LLZO). *J. Mater. Chem. A* **2014**, *2*, 13431−13436.
(54) Dhivya, L.; Karthik, K.; Ramakumar, S.; Murugan, R. Facile Synthesis of High Lithium Ion Conductive Cubic Phase Lithium Garnets for Electrochemical Energy Storage Devices. *RSC Adv.* **2015**, *5*, 96042−96051.
(55) Gorelik, V. S.; Vodchits, A. I.; Bi, D.; Koltashev, V. V.; Plotnichenko, V. G. Raman Scattering in LiOH and LiOD Polycrystals. *Inorg. Mater.* **2019**, *55*, 271−276.
(56) Walrafen, G. E.; Douglas, R. T. W. Raman Spectra from very Concentrated Aqueous NaOH and from Wet and Dry, Solid, and Anhydrous Molten, LiOH, NaOH, and KOH. *J. Chem. Phys.* **2006**, *124*, 114504.
(57) Li, F.; Li, Z.; Wang, Y.; Wang, S.; Wang, X.; Sun, C.; Men, Z. A Raman Spectroscopy Study on the Effects of Intermolecular Hydrogen Bonding on Water Molecules Absorbed by Borosilicate Glass Surface. *Spectrochim. Acta, Part A* **2018**, *196*, 317−322.
(58) de Ligny, D.; Guillaud, E.; Gailhanou, H.; Blanc, P. Raman Spectroscopy of Adsorbed Water in Clays: First Attempt at Band Assignment. *Proc. Earth Planet. Sci.* **2013**, *7*, 203−206.
(59) Tyutyunnik, V. I. Lithium Hydroxide Monohydrate Single Crystals: Infrared Reflectivity and Raman Study. *J. Raman Spectrosc.* **2000**, *31*, 559−563.
(60) Morales-Flórez, V.; Santos, A.; Romero-Hermida, I.; Esquivias, L. Hydration and Carbonation Reactions of Calcium Oxide by Weathering: Kinetics and Changes in the Nanostructure. *Chem. Eng. J.* **2015**, *265*, 194−200.
(61) Wang, T.; Yi, Z.; Guo, R.; Huang, H.; Garcia, S.; Maroto-Valer, M. M. Particle Carbonation Kinetics Models and Activation Methods under Mild Environment: The Case of Calcium Silicate. *Chem. Eng. J.* **2021**, *423*, No. 130157.
(62) Zhu, Y.; Connell, J. G.; Tepavcevic, S.; Zapol, P.; Garcia-Mendez, R.; Taylor, N. J.; Sakamoto, J.; Ingram, B. J.; Curtiss, L. A.; Freeland, J. W.; et al. Dopant-Dependent Stability of Garnet Solid Electrolyte Interfaces with Lithium Metal. *Adv. Energy Mater.* **2019**, *9*, 1803440.
(63) Yamada, H.; Ito, T.; Kammampata, S. P.; Thangadurai, V. Toward Understanding the Reactivity of Garnet-Type Solid Electrolytes with H2O/CO2 in a Glovebox Using X-ray Photoelectron Spectroscopy and Electrochemical Methods. *ACS Appl. Mater. Interfaces* **2020**, *12*, 36119−36127.

https://doi.org/10.1021/acs.jpcc.3c01027
J. Phys. Chem. C 2023, 127, 8320−8331

3.2 Publication 2: "Amorphous phase induced lithium dendrite suppression in glass-ceramic garnet-type solid electrolyte"

Publication 2 of this thesis covers the application of glass-ceramic LLZO as sintered SE. The influence of the intrinsically contained amorphous phase on the sintering process and the electrochemical performance was studied. In addition, the formation and propagation of lithium dendrites at the LLZO/lithium interface were studied in detail and data were correlated with the microstructure of the sintered bodies. A LLZO variant with a high volume fraction of amorphous phase (4 wt%) was used and compared to LLZO with a low volume fraction of amorphous phase (0.1 wt%), similar to that investigated in publication 1.

Regarding the sintering process, the amorphous phase was identified as intrinsic sintering aid promoting liquid phase sintering. Therefore, both sintering time and sintering temperature were effectively reduced compared with conventional synthesis routes. Moreover, the amorphous phase was found to have an effect on the microstructure of the sintered body by segregating into the grain boundaries and open pores. This highly decreased the susceptibility to dendrite propagation expressed by a high critical current density $> 1\ \mathrm{mA\ cm^{-2}}$. Moreover, *in situ* lithium plating measurements confirmed the superior dendrite stability by suppressed crack formation upon lithium plating.

In conclusion, this work gives insights into the unique properties of the novel glass-ceramic LLZO variant. In addition to the industrially scalable manufacturing and favorable sintering conditions, the superior dendrite stability makes it a promising candidate for future SSB applications.

The concept of this study was developed by the first author together with J. Schuhmacher and A. Roters. C. Loho performed and assisted the SEM/EDX and ToF-SIMS analysis at the SCHOTT AG. T. Fuchs and the first author carried out the *in situ* SEM experiments at the University of Giessen. The other experiments were performed by the first author, partially in cooperation with the analytics division of the SCHOTT AG. Data were analyzed by the first author and discussed with the input of J. Schuhmacher, S. Leukel, F. H. Richter and J. Janek. The first author wrote the manuscript that was edited by seven co-authors.

The manuscript has been accepted for publication in ACS Applied Materials Interfaces **2023**, DOI: https://doi.org/10.1021/acsami.3c01667.

ACS APPLIED MATERIALS & INTERFACES

www.acsami.org Research Article

Amorphous Phase Induced Lithium Dendrite Suppression in Glass-Ceramic Garnet-Type Solid Electrolytes

Nina Hoinkis, Jörg Schuhmacher, Till Fuchs, Sebastian Leukel, Christoph Loho, Andreas Roters,* Felix H. Richter, and Jürgen Janek*

Cite This: https://doi.org/10.1021/acsami.3c01667 Read Online

ACCESS | Metrics & More | Article Recommendations | Supporting Information

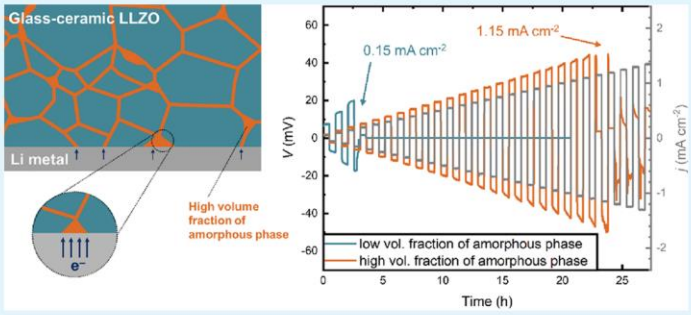

ABSTRACT: Lithium metal-based solid-state batteries (SSBs) have attracted much attention due to their potentially higher energy densities and improved safety compared with lithium-ion batteries. One of the most promising solid electrolytes, garnet-type $Li_7La_3Zr_2O_{12}$ (LLZO), has been investigated intensively in recent years. It enables the use of a lithium metal anode, but its application is still challenging because of lithium dendrites that grow at voids, cracks, and grain boundaries of sintered bodies during cycling of the battery cell. In this work, glass-ceramic Ta-doped LLZO produced in a unique melting process was investigated. Upon cooling, an amorphous phase is generated intrinsically, whose composition and fraction are adjusted during the process. Herein, it was set to about 4 wt % containing Li_2O and a $Li_2O–SiO_2$ phase. During sintering, it was shown to segregate into the grain boundaries and decrease porosity via liquid phase sintering. Sintering temperature and sintering time were found to be reduced compared with the LLZO fabricated by a solid-state reaction while maintaining high density and ionic conductivity. The glass-ceramic sintered at 1130 °C for 0.5 h showed a room-temperature ionic conductivity of 0.64 mS cm^{-1}. Most importantly, the evenly distributed amorphous phase along the grain boundaries effectively hinders lithium dendrite growth. Besides mechanically blocking pores and voids, it helps to prevent inhomogeneous distribution of current density. The critical current density (CCD) of the LiI LLZTO|Li symmetric cell was determined as 1.15 mA cm^{-2}, and *in situ* lithium plating experiments in a scanning electron microscope revealed superior dendrite stability properties. Therefore, this work provides a promising strategy to prepare a dense and dendrite-suppressing solid electrolyte for future implementation in SSBs.

KEYWORDS: *solid electrolyte, solid-state battery, LLZO, glass-ceramics, sintering aid, lithium metal anode, lithium dendrite*

1. INTRODUCTION

Solid-state batteries (SSBs) are considered to be the potential next-generation lithium batteries to advance the progress of vehicle electrification. Conventional flammable liquid electrolytes are replaced in these batteries by solid electrolytes (SEs) that have excellent thermal stability. Furthermore, solid materials are mechanically stable intrinsically and have the ability to suppress the growth of lithium dendrites, which are detrimental for battery operation as they lead to internal short circuit. Most importantly, SEs enable the use of a lithium metal anode with the highest theoretical specific capacity of all anodes (3860 mA h g^{-1}), provided that they are electrochemically stable against lithium metal. Thus, SSBs are a likely candidate to overcome the challenges of the safety issue and the limitation of the energy density of lithium-ion batteries.[1,2]

Among various SEs, the ceramic garnet-type $Li_7La_3Zr_2O_{12}$ (LLZO) in its cubic modification is one of the most promising candidates because of its high room-temperature ionic conductivity, chemical stability against lithium metal, and

Received: February 5, 2023
Accepted: May 21, 2023

wide electrochemical window plus the comprehensive properties named above.[3,4] In principle, LLZO can be applied as a SE in different concepts, e.g., by incorporation of LLZO particles into a lithium-ion conductive polymer matrix (hybrid electrolyte[5]) or by sintering to dense ceramics, which results in a completely inorganic SE, the latter being the focus of this study. However, for sintered SEs, there are still major obstacles to overcome for their large-scale application. Most importantly, stable lithium cycling at relevant current densities remains challenging because of lithium dendrite growth, leading to a short circuit of the cell. One of the manifold reasons is the poor contact at LilLLZO interfaces caused by surface impurities, voids, or defects at the interface, leading to uneven deposition of lithium by current focusing, which ultimately accelerates lithium dendrite growth.[6,7] Void formation is also promoted by continuous lithium stripping because of the limited self-diffusion coefficient of lithium metal, i.e., the flux of Li^+ away from the interface exceeds the flux of Li^0 to the interface.[8−11] Strategies to suppress interfacial issues include surface cleaning approaches,[12] lithiophilic coating layers,[13−15] alloy layers,[16,17] and high stack pressures, as well as elevated temperatures to increase the lithium self-diffusion coefficient.[8,10] Even though these approaches can effectively reduce interfacial impedance, the issue of lithium dendrite growth at moderate current densities remains.

In fact, the density and the intrinsic microstructure of LLZO are crucial for the ability to suppress dendrite formation. Lithium dendrites preferably grow along grain boundaries in polycrystalline LLZO, revealing dendritic and whisker growth, as shown by several *in situ* and *ex situ* techniques.[18−20] The high local ionic resistivity at grain junctions and the lower shear modulus, i.e., softening in elastic properties, of the grain boundary are discussed as possible reasons.[21,22] Furthermore, interconnected pores and preexisting cracks in the microstructure facilitate lithium dendrite formation. Once a crack is penetrated by lithium metal, it promotes further lithium insertion by pressure-driven crack-propagation, which has been modeled by an electro-chemo-mechanical approach.[23−25]

Therefore, the development of dense LLZO with superior grain boundary strength and low porosity is crucial for lithium dendrite suppression. The production of dense LLZO is demanding and cost-intensive, especially via a conventional solid-state reaction and subsequent sintering. It requires high sintering temperatures (up to 1200−1300 °C) and long sintering times (about 12 h), leading to severe lithium loss at such high temperatures and the risk of mismatch of stoichiometry.[26,27] Strategies for reducing sintering temperature and time while achieving high density include hot press sintering,[28] ultrafast high-temperature sintering (UHS),[29] and field-assisted sintering technique (FAST) also known as spark plasma sintering (SPS).[30,31] Although the obtained electrolytes can reach high relative densities up to 97% and even a high critical current density (CCD) of 3.2 mA cm^{-2} in cycling experiments for the UHS method, these methods require sophisticated setups and are not feasible for large-scale application.

Another strategy is the use of the liquid phase sintering method, in which a sintering additive with a lower melting point than the ceramic is added to the starting powder. During the actual sintering step, the liquid phase already formed before tends to wet the surfaces of the ceramic grains, and as a result, it fills the grain boundaries and thus leads to improved densification. As sintering additives, mostly lithium compounds like Li_2O,[32] LiOH,[33] Li_3PO_4,[34] Li_3BO_3,[35,36] $LiAlO_2$ (by an uncontrolled reaction of excess Li_2CO_3 with an Al_2O_3 crucible[37] or by atomic layer deposition coating of Al_2O_3[38]), and lithium-containing glass systems (e.g., $Li_2O-B_2O_3-SiO_2$[39] and $3Li_2O-2GeO_2$[40]) have been investigated. Even though the sintering temperature can effectively be reduced to around 1000 °C by these methods, the sintering time is still long (10 h up to 36 h[34−39]), and, if measured, CCD values are relatively low (0.3 to 0.6 mA cm^{-1}[33,36,38,40]), indicating poor lithium dendrite suppression.

In this work, we used Ta-doped LLZO with an (X-ray) amorphous phase to improve the microstructure quality and lithium dendrite stability of the sintered bodies. LLZTO is produced by a unique melting route of the SCHOTT AG[41] that intrinsically leads to the presence of an amorphous phase, whose fraction can be tuned during the process. Throughout this study, we compare LLZTO having a high fraction of amorphous phase with LLZTO that has a negligible fraction of amorphous phase. We examined the effect of the amorphous phase on the densification behavior via liquid phase sintering by varying the sintering temperature and sintering time systematically. Electrochemical properties, i.e., the ionic conductivity, were measured by electrochemical impedance spectroscopy (EIS) and linked with density and microstructure. Last, we investigated the dendrite stability and growth mechanisms by measuring the CCD with galvanostatic cycling tests and *in situ* lithium plating experiments. This study enables the correlation of microstructures with the capability for dendrite suppression, making a fundamental contribution to the development of next-generation solid-state lithium batteries.

2. EXPERIMENTAL SECTION

2.1. Material Synthesis. Garnet-type Ta-doped LLZO was manufactured via a unique and industrially scalable melting route at SCHOTT AG. The metal oxide raw materials were melted in an inductively heated skull crucible implemented by a radio frequency induction coil. After homogenization of the melt, samples were taken from the crucible to realize fast cooling. Further details can be found in ref 41. Besides the highly lithium-ion conductive cubic phase, the powders include an amorphous phase whose fraction and composition can be adjusted during the processing route. Powders were milled, and the median particle size D_{50} was measured by static light scattering (CILAS 1064). The powders were analyzed by chemical analysis; fractions of ZrO_2, La_2O_3, and Ta_2O_5 were analyzed by X-ray fluorescence spectroscopy (RFA), Li_2O by atomic absorption spectroscopy (AAS), and SiO_2 by inductively coupled plasma optical emission spectroscopy (ICP-OES). The fraction of amorphous phase, i.e., lithium excess, was calculated by subtracting the ideal stoichiometry of LLZTO, assuming that the elements Zr, Ta, and La fully contribute to the crystalline phase. The amorphous phase reduces the skeleton density ρ compared with a pure crystalline material. Densities ρ of the powders were calculated based on the density $\rho_{cryst.}$ as determined from the XRD lattice parameter, the estimated density of the amorphous phase ($\rho_{am.} \sim 2$ g cm^{-3}), and the corresponding fractions of the crystalline and amorphous phase in vol %:

$$\rho = \frac{\text{vol\%}_{cryst.} \cdot \rho_{cryst.} + \text{vol\%}_{am.} \cdot \rho_{am.}}{100} \quad (1)$$

Here, two types of LLZTO were chosen, one with negligible fraction of amorphous phase (low-am) and one with a high fraction of amorphous phase (high-am). The latter additionally contains the glass-forming agent SiO_2. The exact compositions, particle sizes, and densities are given in Table 1.

https://doi.org/10.1021/acsami.3c01667
ACS Appl. Mater. Interfaces XXXX, XXX, XXX−XXX

Table 1. Composition, D_{50} Values of Particle Size Distribution, and Bulk Densities ρ of the Initial LLZTO Powders Having Low and High Amorphous Phase Mass Fractions (low-am and high-am, Respectively)

sample	amorphous phase (wt %)	SiO_2 (wt %)	D_{50} (μm)	ρ (g cm^{-3})
low-am	0.1	0.02	0.8	5.37
high-am	4.4	0.7	1.0	5.04

Prior to sintering, the powders were cold-pressed at 382 MPa into a green pellet with 10 mm diameter using a stainless-steel die. The relative green density (RD) was calculated by dividing the measured geometric density of the pellet by the skeleton density of the corresponding powder. All green pellets had a RD in the range from 59 to 63%. Green pellets were sintered in a tube furnace under an O_2 flow in ZrO_2 crucibles covered in mother powder to prevent lithium loss. Sintering temperatures were varied from 930 and 1030 °C to 1130 °C for a constant sintering time of 0.5 h. The sintering time was also varied from 0.5, 2, and 6 to 14.5 h at a constant sintering temperature of 1130 °C. Typical dimensions of the pellets were about 1 mm thickness and 8.4 mm in diameter, which were used for RD calculation along with the mass and skeleton density, giving RDs > 90% ± 2%. For electrochemical characterization, the pellets were polished using #600 SiC sandpaper in an argon-filled glovebox (MBraun) with O_2 and H_2O contents <1 ppm. For scanning electron microscopy (SEM), energy-dispersive X-ray spectroscopy (EDX), and time-of-flight secondary ion mass spectrometry (ToF-SIMS), additional polishing steps with #1200, #2500, and #4000 SiC sandpaper were carried out.

2.2. Material Characterization. X-ray diffraction patterns (XRD) were collected using a PANalytical X'Pert PRO MPD (Malvern Panalytical) from 5° < 2θ < 70° in increments of 0.013° using CuKα radiation operating at 45 kV and 40 mA. To ensure diffraction from multiple grains, samples were spun during XRD. For qualitative analysis, the software HighScore Plus (Malvern Panalytical) was used and reference crystallographic information files were used from Crystallography Open Database (COD) (cubic LLZTO: COD #1545083). Rietveld refinement was performed for determination of the lattice parameter and calculation of the density (see eq 1).

Differential scanning calorimetry (DSC) was performed with a DSC 404F1 Pegasus (NETZSCH) in Pt-Rh crucibles from 23 to 1150 °C at a heating rate of 5 K min^{-1}. Ar was chosen as a processing gas to prevent side reactions. Heating microscopy (EM301, Hesse Instruments) was run with a heating rate of 20 K min^{-1} up to 550 °C and 5 K min^{-1} up to max. 1300 °C. The software EMIII (Hesse Instruments) was used for analysis of the geometric area of the pellet. Before the measurement, powders were pressed into green pellets (diameter 5 mm, 700 MPa).

Scanning electron microscopy (SEM) was performed on the polished surfaces of LLZTO pellets as well as on pristine cross sections that have been manually fractured using a carbide glass cutter. A ZEISS LEO1550 equipped with a field emission gun (FEG) was used to capture the SEM images with a secondary electron detector operated at 10 and 20 keV accelerating voltages.

Energy-dispersive X-ray spectroscopy (EDX) was carried out on a ZEISS NEON40 FEG-SEM equipped with an Oxford Instruments EDX System in mapping mode. EDX maps were taken at 5 keV accelerating voltage with a magnification of about 2000, resulting in a field of view of about 160 μm × 120 μm. The samples for EDX mapping have been transferred to the SEM directly after completion of ToF-SIMS analyses. The EDX maps were collected at the same position on the LLZTO surface at which preceding ToF-SIMS maps were collected to ensure complementary analyses of the same grains.

Time-of-Flight Secondary ion mass spectrometry (ToF-SIMS) was performed on a TOF.SIMS 4 instrument (ION-TOF GmbH) with a non-linear time-of-flight analyzer under the following conditions: The primary ion source was a liquid metal ion gun with Ga^+, and the primary ion energy was 25 keV. The primary ion mode was "burst alignment" with lateral resolution of approximately 500 nm, and the image raster was 256 pixel × 256 pixel. Charge compensation was achieved by an electron flood gun, and surface cleaning was done by ion sputtering with Ca^+ for negative polarity and O_2^+ for positive polarity. Data were processed with the software SurfaceLab 7. Please note that combined EDX and ToF-SIMS analyses for the high-am sample were conducted on a high-am sample that was manufactured from a high-am powder with a larger initial particle size (5 μm). This is because the grain boundary domains are larger in this case, showing an improved recognizability with higher resolvability compared with those of the high-am sample manufactured from the 1 μm powder.

Electrochemical impedance spectroscopy (EIS) was performed with an Alpha A-High Analyzer (Novocontrol) on the sintered LLZTO pellets. Beforehand, gold electrodes with a diameter of 6.5 mm were sputter-coated on both sides of each pellet using a sputter coater (EM SDC050, Leica). EIS was carried out either at 25 °C for room-temperature conductivity or at −40 to 80 °C (heating rate: 1 K min^{-1}) for temperature-dependent measurements in the frequency range from 20 MHz to 100 mHz with a 20 mV perturbation amplitude. EIS data were fitted with Z-View software using equivalent circuits with impedance (R) and capacitance elements (constant phase element (CPE)) for each bulk and grain boundary process. The thickness d of each pellet and electrode area A together with total impedance R_t were used for calculation of total ionic conductivity σ_t:

$$\sigma_t = \frac{1}{R_t} \cdot \frac{d}{A} \tag{2}$$

Measurements were at least triplicated, giving an experimental error < 10%. The contribution of the grain boundary resistance to the total conductivity was calculated by dividing the grain boundary resistance R_{gb} by the total resistance R_t. Activation energies were calculated according to the Arrhenius equation:

$$\sigma T = \sigma_0 \exp\left(-\frac{E_a}{k_B T}\right) \tag{3}$$

Galvanostatic cycling tests with step-up current densities were carried out to determine the critical current density (CCD) using lithium symmetric cells. Prior to assembly, polished LLZTO pellets were cleaned with lithium foil (Goodfellow, 99.9%) by multiple contacting and removing steps and subsequently heated to 180 °C on a heating plate inside an Ar-filled glovebox (MBraun, $p(H_2O)/p$ and $p(O_2)/p$ < 1 ppm). Fresh lithium foil was prepared by cutting off a piece from a lithium rod (Sigma-Aldrich, 99.9%) using a ceramic knife and pressing it with a self-built hand press to a thickness of about 50–100 μm. Lithium electrodes with a diameter of 6 mm were punched out and applied on the pellets by the help of a soldering iron at a temperature of about 190 °C. Copper foil was used as a current collector. EIS was measured at 25 °C to determine the interface resistance R_{int} between LLZO and lithium by normalizing the EIS spectra to the contact area (0.28 cm^2). For all cells, R_{int} was in the range from 20 to 30 Ω cm^2. For galvanostatic cycling, the cells were transferred into CompreCells (rhd instruments) with tungsten carbide electrodes suitable for the uniaxial laboratory press CompreDrive (rhd instruments) with a high-resolution servo drive for active pressure regulation. The applied pressure was 11 MPa, and the temperature was set at 60 °C with the built-in temperature control. Current densities between 0.05 and 2 mA cm^{-2} with an increment of 0.05 mA cm^{-2} and a constant temperature of 60 °C were chosen. One cycle per current density was performed with a half cycle time of 30 min (60 min in total per cycle). Cycling was continued until a sudden drop in polarization voltage occurred, indicating short-circuiting of the cell. *In situ* potentiostatic plating experiments were carried out according to Krauskopf *et al.*[42] A lithium electrode was applied on only one side of the pellet following the procedure above. It inherently acts as counter and reference electrodes. Pellets were manually fractured by using a carbide glass cutter into two semicircular pieces. One of those pieces was then transferred into the micromanipulator setup (Kammrath & Weiss GmbH) using a

https://doi.org/10.1021/acsami.3c01667
ACS Appl. Mater. Interfaces XXXX, XXX, XXX−XXX

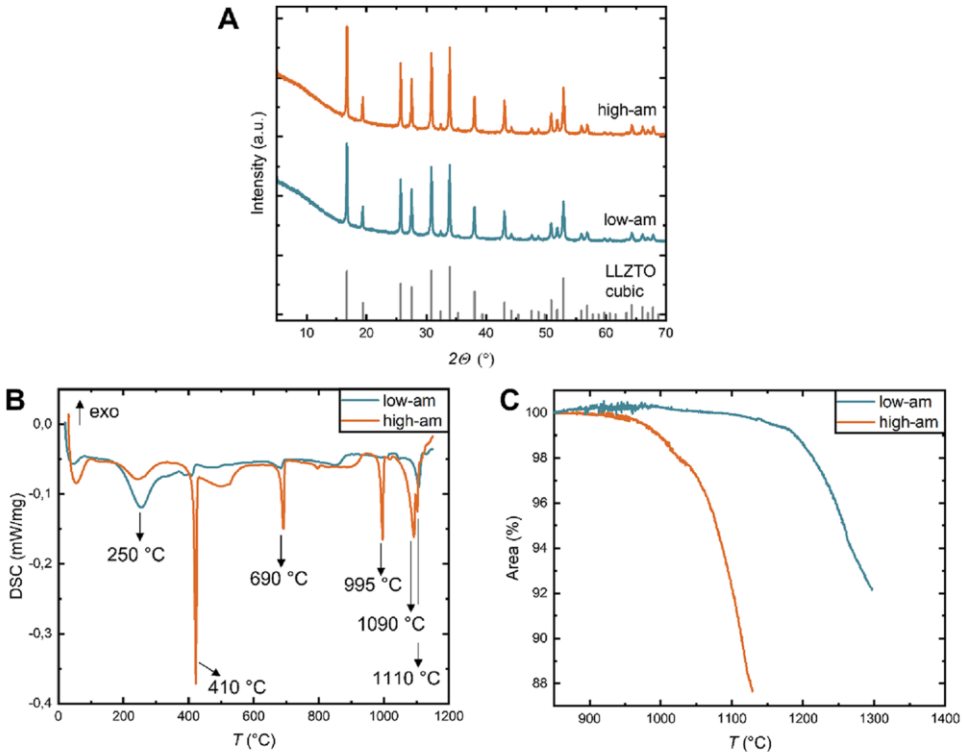

Figure 1. Characterization of the initial LLZTO powders having low and high amorphous phase mass fractions (low-am and high-am, respectively): (A) XRD patterns and the reference reflections of cubic LLZTO. (B) DSC analysis and indication of specific temperatures. (C) Shrinkage of green pellet area as a function of temperature measured by heating microscopy.

tungsten needle as a microelectrode inside the SEM chamber (Carl Zeiss Ultrafield emission SEM, Merlin). The microelectrode, which acts as a working electrode, was contacted with the cross-sectional surface of the pellet piece. An SP-200 potentiostat (Bio-Logic) with an implemented impedance analyzer was used to apply step potentials from −0.1 V up to −1.5 V with 0.1 V increments and a duration of 30 s per step. Resulting current was recorded as a function of time.

3. RESULTS AND DISCUSSION

3.1. Powder Characterization. The garnet-type solid electrolyte LLZTO was synthesized via a unique melting route at the SCHOTT AG,[41] in which an additional amorphous phase comprising Li_2O was formed. Additionally, the glass-forming agent SiO_2 was included into the amorphous phase as it is well-known to form amorphous lithium silicate together with Li_2O upon fast cooling.[43] It is expected to act as a sintering agent, as shown before for crystalline Li_4SiO_4,[44] as well as to increase the dendrite suppression ability of LLZTO due to its glassy properties. Two distinct initial powders having a low and high mass fraction of amorphous phase (denoted by "low-am" and "high-am") were compared in this study. The calculation of the amorphous phase fraction is based on the Li_2O excess used during the process (see the Experimental Section). The compositions in Table 1 indicate a difference in amorphous phase fraction by a factor of about 40 (0.1 wt % for low-am compared with the 4.4 wt % for high-am). The SiO_2 content in the high-am sample is 0.7 wt % and almost negligible for low-am (decrease by a factor of about 35). The bulk densities decrease according to the fraction of the amorphous phase as the latter has a lower density than LLZTO. The particle size distributions of the powder samples are monomodal in both cases and exhibit D_{50} values of about 1 μm (Figure S1).

The XRD diffraction patterns of the initial powders are shown in Figure 1A. The reflections of both powders match well with the diffraction pattern of cubic LLZTO. The patterns do not display reflections related to impurities such as $La_2Zr_2O_7$ that often arise due to lithium loss.[45] Thus, the melting process and subsequent milling is robust against the formation of secondary phases and changes in crystal structure. Furthermore, the abovementioned additional phase that forms during the melting process does not show any reflections in the XRD patterns and hence is X-ray amorphous. We therefore simply denote it as "amorphous phase" from now on.

To investigate the sintering of the two types of samples, thermal analyses, i.e., DSC and heating microscopy measurements, were conducted. DSC curves up to a temperature of 1150 °C are shown in Figure 1B. In both cases, an endothermic peak appears at about 250 °C that can be ascribed to the evaporation of adsorbed H_2O. The reason for this is that sample preparation for DSC cannot be done under an inert atmosphere. Consequently, LLZTO readily reacts with moisture and CO_2 in air to form LiOH and Li_2CO_3 as reaction products.[46] This can be verified by the two endothermic peaks detectable at 410 °C (melting of LiOH[47]) and at 690 °C (melting of Li_2CO_3[48]). Because of the higher amorphous phase fraction, i.e., Li_2O excess, the peaks are more pronounced for

https://doi.org/10.1021/acsami.3c01667
ACS Appl. Mater. Interfaces XXXX, XXX, XXX−XXX

the high-am sample. The three endothermic peaks in the high-temperature range (>900 °C) are not expected for pure crystalline LLZTO and therefore can be attributed to the amorphous phase. Regarding the first peak at 995 °C, we believe that it is due to a Li_2O-SiO_2 phase. According to the Li_2O-SiO_2 phase diagram, the peak can be assigned to the eutectic temperature of a Li_4SiO_4 phase.[49] It is only present in the case of high-am, which is consistent with the composition of high-am, i.e., a 40-fold higher fraction of amorphous phase and 35-fold higher content of SiO_2 compared with low-am (see Table 1). Regarding the two endothermic peaks at 1090 and 1110 °C, we assume that these are due to excess Li_2O that can form a Li_2O-ZrO_2 phase, i.e., Li_8ZrO_6, that has a eutectic point at that temperature range.[50] For high-am, the peak at 1090 °C is much more pronounced than the peak at 1110 °C. A possible reason is that it rather forms a ternary $Li_2O-ZrO_2-SiO_2$ system instead of a binary Li_2O-ZrO_2 system due to the presence of SiO_2 in the high-am sample. For low-am, only the peak at 1110 °C is observed. It has lower intensity compared with high-am, which is in agreement with the distinct fraction of amorphous phase in the two types of samples. To the best of our knowledge, such a high temperature range of the DSC measurement has not been reported for LLZO in the literature before.

The endothermic peak of the eutectic Li_2O-SiO_2 phase (at 995 °C) together with the strong endothermic peak of the Li_2O-ZrO_2 phase (at 1090 °C and 1110 °C) influences the sintering of high-am compared with low-am, as shown by heating microscopy measurements. The shrinkage in the high temperature range, represented by the onset of densification during the sintering process, is given in Figure 1C. It reveals a shrinkage onset of high-am at about 950 °C compared with 1100 °C in the case of low-am. These onset temperatures directly correlate with the DSC measurements. The liquefaction of the amorphous phase promotes densification at lower temperatures via liquid phase sintering. It thereby gradually spreads, wets the surfaces of LLZO grains, and fills grain boundaries and voids.

3.2. Microstructure. To study the influence of the amorphous phase on the microstructure, we systematically varied the sintering temperature and sintering time. Besides the microstructure, the sintered bodies were also analyzed with respect to inhomogeneities correlating to different structural features that are observable within the microstructural investigations. Regarding the sintering temperature variation, Figure S2 shows the XRD patterns of the pellets sintered for 0.5 h at different temperatures ranging from 930 °C, over 1030 °C, to 1130 °C. For both low-am and high-am, they indicate the crystal structure of cubic LLZTO without any crystalline impurity phases. This shows that the sintering process is stable over a wide temperature range and robust against phase changes, e.g., due to lithium loss.

The microstructure and morphology of the sintered samples investigated by SEM are presented in Figure 2A,B. At 930 °C, both low-am and high-am show insufficient densification. The initial particles are still apparent, showing no recognizable merging. This is in agreement with the results of the DSC and heating microscopy, indicating the absence of densification below 995 °C. At 1030 °C, coalesced particle networks occur noticeably for high-am compared with low-am, indicating an advanced sintering stage (see the inset). The sintering temperature exceeds the first DSC melting peak of high-am, and densification is promoted. This is also in agreement with

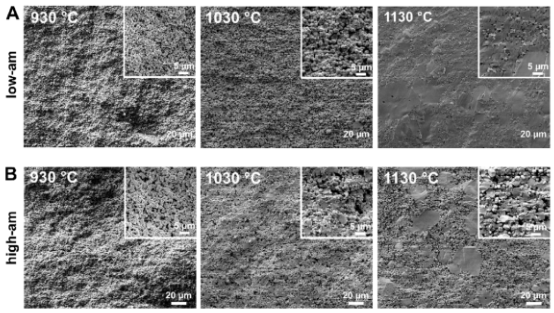

Figure 2. SEM images of pristine (i.e., nonpolished) cross sections of the samples having (A) low and (B) high amorphous phase mass fractions (low-am and high-am, respectively) synthesized at different sintering temperatures of 930, 1030, and 1130 °C at a constant sintering time of 0.5 h.

the result of heating microscopy. When increasing the sintering temperature to 1130 °C, low-am is reasonably dense, revealing large grains of about 40−50 μm size among coalesced particles, but some porosity remains. For high-am, grains of similar size are visible, but the particles in between seem not to be coalesced, suspecting open porosity at first glance. Another interpretation is that the particles are surrounded by a second phase that is darker in appearance, presumably the amorphous phase connecting the grains, caused by the proposed liquid phase sintering mechanism.

To test such hypothesis, the darker second phase in between the grains was examined by SEM/EDX elemental maps with complementary ToF-SIMS maps of the sample with a high amorphous phase mass fraction (Figure 3). To ensure the same positions in both analyses, a SiC particle stemming from sandpaper polishing was used as a marker (Figure S3).

The EDX maps show that the grains around the white circles consist of the four elements O, Zr, La, and Ta, confirming that

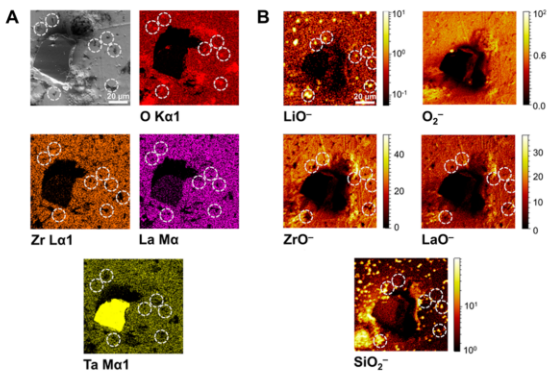

Figure 3. (A) Top-view SEM image and corresponding EDX elemental maps of the LLZTO sample having a high fraction of amorphous phase (high-am) sintered at a sintering temperature of 1130 °C for 0.5 h. (B) ToF-SIMS analysis at the same position and corresponding selected negative secondary ion maps. The second phase in between the grains is marked with white circles. A SiC particle was used as a marker (for related EDX and ToF-SIMS maps, see Figure S3). The Ta signal of EDX is increased for the SiC particle because of an overlap of the Ta Mα1 and Si Kα1 line at an acceleration voltage of 5 keV.

https://doi.org/10.1021/acsami.3c01667
ACS Appl. Mater. Interfaces XXXX, XXX, XXX−XXX

they are LLZTO. The darker second phase marked by the white circles is rich in O, revealing that the supposed porosity is indeed filled by a second phase. It does not contain Zr, La, and Ta, indicating that it has a different chemical composition. As lithium cannot be detected by EDX due to its light mass, ToF-SIMS analysis was performed as a complementary method to also map the lithium distribution in the pellet. In Figure 3B, the LiO^- secondary ion map clearly shows an increased signal at the positions of the second phase in between the grains compared with the surrounding grains that are composed of LLZTO. The ZrO^- and LaO^- maps do not show any signal at these positions, which is in agreement with the EDX results. Furthermore, the SiO_2^- map mostly overlaps with the lithium-rich second phase observed in the LiO^- map. Therefore, we conclude that the supposed porosity is filled by a second phase in between the grains, that is, the amorphous phase mainly composed of Li_2O as well as a Li_2O–SiO_2 phase, e.g., Li_4SiO_4. This confirms that the proposed process of liquid phase sintering takes place, which induces spreading of the amorphous phase due to liquefaction as well as filling of the grain boundaries and voids. This is in accordance with the results of the DSC, which has shown that high-am has much more intense endothermic peaks at 1090 and 1110 °C, respectively. To check for a part or even full loss of the amorphous phase during sintering, the chemical composition of the sintered pellets was analyzed (Table S1). The fraction of the amorphous phase only slightly decreased compared with the initial powder, confirming that such a phase is still present in the sintered pellet.

As a comparison, the microstructure of low-am was also investigated by EDX spectroscopy and ToF-SIMS (Figure S4). The EDX spectroscopy maps do not display any features in any of the elemental maps. Since the darker phase in between the grains is much narrower compared with that of high-am, EDX spectroscopy could not resolve these regions. Regarding ToF-SIMS, the LiO^- map does also not show any signal amplifications at the darker positions in between the grains. This indicates that there is zero or very little volume of amorphous phase in between the grains, i.e., there is porosity. We believe that the amorphous phase mass fraction of low-am is that small that it only coats the grains instead of forming a distinct phase in between the grains, which is the case for high-am. This confirms our assumption, stated above in the discussion of SEM results, that low-am has some porosity, whereas the supposed porosity of high-am is filled with the amorphous phase. A schematic representation of amorphous phase distribution will be discussed in Section 3.5.

Such segregation of sintering aids in the grain boundaries has been observed for liquid phase sintering before, e.g., for Li_2O,[32] LiOH,[51] and Li_2CO_3,[37] and were identified to form a glassy-like phase in the grain boundaries. However, this is because of the formation of a Li–Al–O phase due to an uncontrolled reaction with the aluminum crucible. In the experimental work related to this paper, ZrO_2 crucibles were used to suppress such side reactions. SiO_2 as a sintering additive revealed formation of Li_4SiO_4, which segregated into the grain boundaries as well, and was identified to be mostly crystalline.[52]

Considering the results from sintering temperature variation, a sintering temperature of 1130 °C gives the optimal densification and was chosen to be kept constant for the variation of sintering time. XRD analysis shows that all of the sintered pellets of low-am and high-am with varying sintering times of 2, 6, and 14.5 h contain only the cubic LLZTO phase (Figure S5). Thus, phase changes due to prolonged sintering do not occur.

The SEM images of the microstructure are given in Figure 4. Compared with the samples sintered for 0.5 h in Figure 2,

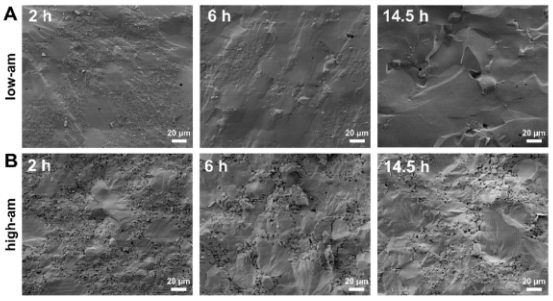

Figure 4. SEM images of pristine (i.e., nonpolished) cross sections of the samples having (A) low and (B) high amorphous phase mass fractions (low-am and high-am, respectively) synthesized at a constant sintering temperature of 1130 °C for different sintering times of 2, 6, and 14.5 h.

grain growth is strongly promoted for low-am with longer sintering times. At 14.5 h, different grains, i.e., grain boundaries, can no longer be localized and very little porosity is visible. In contrast, high-am also shows grain growth for 2 and 6 h compared with 0.5 h, but it seems to stop at 6 h, as no further grain growth is observed at 14.5 h. The darker amorphous phase in the grain boundaries is still present at longer sintering times. However, since large grains are growing, the amorphous phase seems to accumulate in the grain boundaries and is confined to a smaller area. Such redistribution supports a liquid phase sintering mechanism. Chemical analysis of high-am sintered at 14.5 h reveals that the amorphous phase mass fraction has decreased by about 50%, compared with the high-am sintered for 0.5 h, due to Li_2O evaporation and/or leaking of the amorphous phase during the long sintering time. However, it is still significantly higher than that for low-am (Table S1).

3.3. Ionic Conductivity. Figure 5 summarizes the results of ionic conductivity measurements of the pellets prepared at varying sintering temperatures and using different sintering times. Impedance was extracted from corresponding Nyquist plots to calculate the ionic conductivity. An exemplary Nyquist plot at room temperature is shown in Figure 5C for high-am sintered at 1030 and 1130 °C. Two semicircles in the high frequency range are visible, which can be attributed to bulk (b) and grain boundary (gb) processes. The spike in the low frequency range is due to the use of blocking electrodes. Data were fitted with the specified equivalent circuit using parallel R-CPE elements for bulk and grain boundaries. While the impedance for the bulk processes is similar, the grain boundary impedance noticeably differs. These impedance contributions were used to calculate the ratio χ_{gb} that is defined as the quotient of R_{gb} divided by total R_t. They are shown in Figure 5A,B (low-am and high-am, respectively) along with total conductivities σ_t and relative densities RD of the samples synthesized at varying sintering temperatures. Both samples show a significant increase in σ_t and RD with decreasing χ_{gb} ratio. At 930 °C, sintering is in the early stage for both samples, which is indicated by a very low σ_t and high χ_{gb} ratio. From

https://doi.org/10.1021/acsami.3c01667
ACS Appl. Mater. Interfaces XXXX, XXX, XXX–XXX

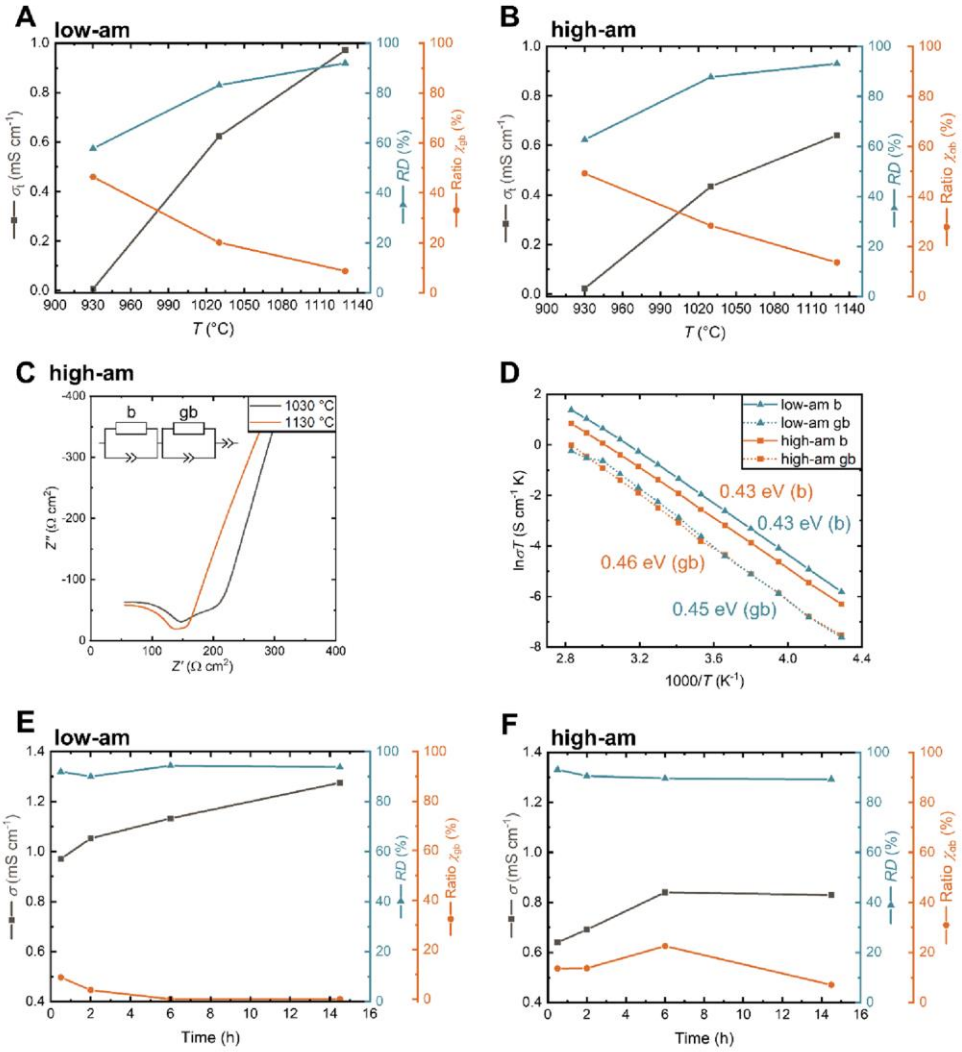

Figure 5. Total RT ionic conductivity σ_t, relative density RD, and ratio of grain boundary resistance χ_{gb} as a function of sintering temperature T for the samples having a (A) low and (B) high amorphous phase mass fraction (low-am and high-am, respectively) at a constant sintering time of 0.5 h. (C) Exemplary RT Nyquist plot of high-am sintered at sintering temperatures of 1030 and 1130 °C for 0.5 h. Equivalent circuit used for fitting is depicted. (D) Arrhenius plots of low-am and high-am of bulk (solid line) and grain boundary processes (dotted line) sintered at 1130 °C for 0.5 h. Corresponding values as a function of sintering time are given in (E) for low-am and in (F) for high-am at a constant sintering time of 0.5 h.

1030 to 1130 °C, the increase in σ_t of 60% for low-am is larger than that for high-am with an increase of 45%. This is consistent with the observed microstructures in Figure 2, in which high-am shows a more advanced sintering stage already at 1030 °C, compared with low-am due to liquid phase sintering of the amorphous phase. The RD values further confirm this observation, namely, 88% at 1030 °C for high-am compared with 83% for low-am. At 1130 °C, the total ionic conductivities are 0.97 mS cm^{-1} for low-am and 0.64 mS cm^{-1} for high-am at RD values of 92 and 93%, respectively. The comparable RD values of low-am and high-am corroborate the conclusions drawn from the EDX and ToF-SIMS results (Figure 3) that the grain boundaries are filled with the amorphous phase resulting in a dense glass-ceramic. Compared with reference works, these are outstandingly high values considering that both the sintering temperature of 1130 °C and especially the sintering time of 0.5 h have been massively reduced in comparison to conventional LLZO synthesis routes (ref 53 and ref. therein).

When comparing the ionic conductivity between the two samples, high-am has a lower σ_t and higher χ_{gb} ratio. This is because the amorphous phase volume in the grain boundaries is higher compared with low-am, as seen from the microstructure and its analysis. The grain boundary conductivity σ_{gb} can also be calculated by taking into account the dimension of its thickness according to the brick layer model (see Table S2). Figure 5D indicates that the σ_{gb} values for high-am and low-am are similar (~0.02 mS cm^{-1} at room temperature) as well as the activation energies of the grain boundary process (~0.46 eV). This reveals that the nature of the grain boundaries

https://doi.org/10.1021/acsami.3c01667
ACS Appl. Mater. Interfaces XXXX, XXX, XXX−XXX

(mainly Li_2O and Li_2O–SiO_2 for high-am) is nearly identical, but the thickness, i.e., volume, of the amorphous phase differs, which is in agreement with the microstructures. The observed bulk activation energies are consistent with reference values.[53]

In Figure 5E,F, the total RT ionic conductivities σ_t, RD, and χ_{gb} ratio of the samples synthesized for varying sintering times are given. For low-am, the steady increase in σ_t with increasing sintering time is in agreement with the densification observed by SEM. For 14.5 h, a σ_t of 1.27 mS cm^{-1} is reached. The decreasing χ_{gb} ratio to almost zero also matches well with the observation that grain boundaries almost disappear at 14.5 h. RD values do not increase significantly with sintering time (from 92% at 0.5 h to 94% at 14.5 h) revealing that even with a short sintering time, a high RD can be reached. For high-am, σ_t increases with sintering time as well, but it reaches a plateau at 6 h with a σ_t of 0.83 mS cm^{-1}. The χ_{gb} ratio moderately decreases from about 14% (0.5 h) to 7% (14.5 h). This is due to the continuous grain growth observed by SEM, which leads to less contribution of the grain boundary impedance. RD values only slightly decrease with varying sintering times (from 93% at 0.5 h to 89% at 14.5 h), reaching a plateau at 6 h. This confirms that a high RD can be reached with a very short sintering time.

3.4. Dendrite Stability. To study the influence of sintering time on the critical current density (CCD) that is used as a relative measure of dendrite stability, galvanostatic cycling experiments were carried out for the samples sintered for minimum and maximum sintering times (0.5 and 14.5 h). EIS of the symmetric lithium transference cells was measured before galvanostatic cycling. The Nyquist plots for low-am and high-am, both sintered for 0.5 and 14.5 h, show two semicircles that are assigned to bulk and interface impedance (Figure S6A,B). The bulk resistances differ according to the microstructure properties as observed in Section 3.2. However, the area specific resistance (ASR) for one Li|LLZTO interface is in the range of 20–30 Ω cm^2 and similar for all samples, which is outstandingly low compared with other works.[54,55] It is known that the ASR has a great impact on galvanostatic cycling of lithium and thus also on CCD values.[55,56] The resistance mainly originates from insufficient contact between lithium and LLZO, leading to constrictions in current distribution with locally high effective current densities.[8,57,58] Therefore, low ASRs are favorable to reach maximum CCDs as shown by the recent work by Flatscher *et al.*, who have investigated the influence of ASR on CCD without applying any external pressure.[55] ASRs observed in this work are well below 50 Ω cm^2, providing excellent conditions for lithium cycling. However, Flatscher *et al.* also found that, even with such a low ASR, voids at the Li|LLZTO interface will form during stripping when cycling at high current densities. This is due to the limited self-diffusion coefficient of Li^0 (Li^+ flux > Li^0 flux).[8,9] Therefore, CCD tests are determined not only by the material properties but also by the quality of the interface contact. To solely probe the material's ability to suppress lithium dendrite formation, the CCD tests in this study were carried out at an elevated temperature of 60 °C and an external pressure of 11 MPa was applied to ensure stable lithium cycling preferably without the influence of interfacial effects on the dendrite suppression ability of the material.

In Figure 6A, the results from galvanostatic cycling with step-up current densities of low-am and high-am sintered for 0.5 h are shown. Overall, ohmic behavior is observed for both cells with only slight deviations, demonstrating morphologically stable lithium stripping and plating. For low-am, a sudden drop in the voltage is visible at a current density of 0.15 mA cm^{-2}, which directly indicates that a dendrite has formed, short-circuiting the cell, i.e., the CCD of the sample. In contrast, high-am shows an approx. 8-fold higher CCD of 1.15 mA cm^{-2}. In comparison, the galvanostatic cycling results of the samples sintered for 14.5 h are given in Figure 6B. Again, high-am reveals a higher CCD of 0.45 mA cm^{-2} compared with the 0.2 mA cm^{-2} for low-am (about a factor of 2). The short circuit of the cells is confirmed by EIS measurements after galvanostatic cycling (Figure S6C,D). These results show that the microstructures containing the amorphous phase effectively suppress dendrite growth, which results in higher CCD values. Obviously, the CCD differences of high-am between sintering times of 0.5 and 14.5 h are due to the distinct microstructures that were discussed before. A detailed discussion and possible explanations are given at the end of this section.

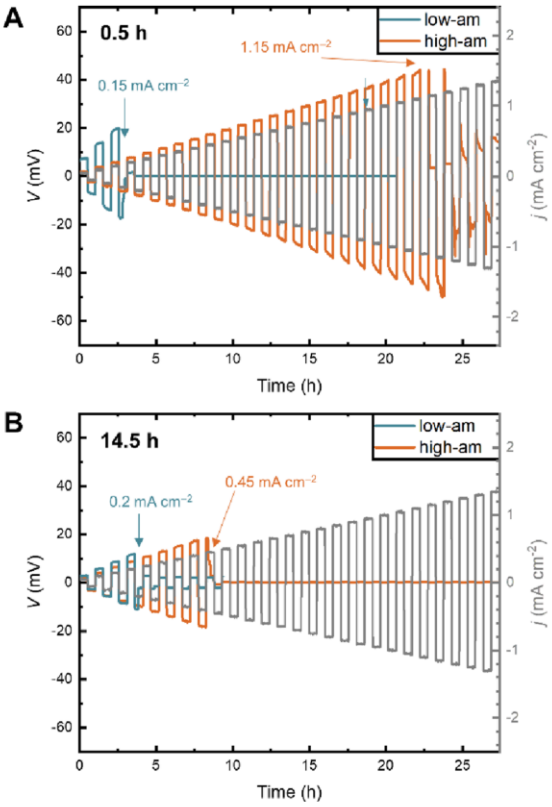

Figure 6. Galvanostatic cycling with increasing current density of the samples having a low and a high amorphous phase mass fraction (low-am and high-am, respectively) sintered for (A) 0.5 h and (B) 14.5 h at a pressure of 11 MPa and a temperature of 60 °C for comparison.

To gain further insights into the beneficial effect of the amorphous phase on dendrite stability, we conducted potentiostatic plating experiments, in which lithium plating can be observed *in situ* by SEM. Lithium electrodes are *in situ* generated using tungsten micromanipulators, which are deposited on a pristine LLZO cross section. By applying a stepwise external overpotential at the microelectrode, lithium

https://doi.org/10.1021/acsami.3c01667
ACS Appl. Mater. Interfaces XXXX, XXX, XXX–XXX

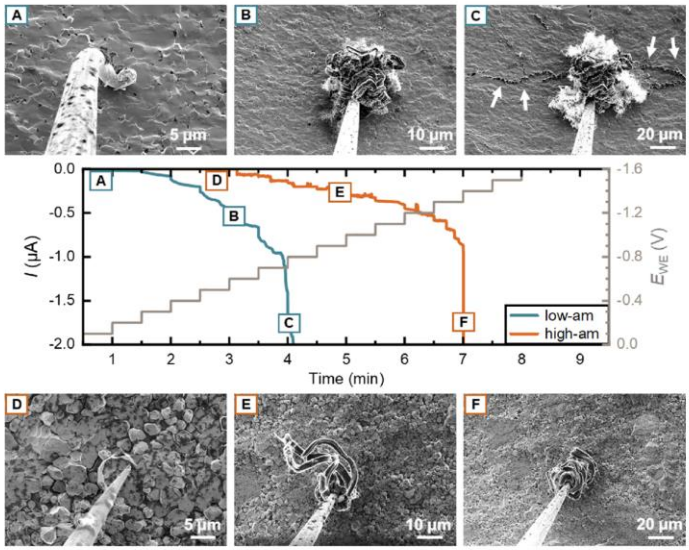

Figure 7. *In situ* potentiostatic lithium plating experiment on a microscopic working electrode for the samples having a low and a high amorphous phase mass fraction (low-am and high-am, respectively) sintered for 0.5 h. The overpotential E_{WE} at the working electrode was stepwise increased from −0.1 to −1.5 V (gray), and current profiles were collected for low-am (blue) and high-am (orange) as a function of time. The SEM images taken at different time intervals are indicated in the current profiles: (A−C) for low-am and (D−F) for high-am. The arrows indicate cracks in the pellet.

growth modes can be examined and information about dendrite stability is provided. Experimental details of this setup can be found in the work of Krauskopf *et al.*[42] Figure 7 shows the results for low-am and high-am sintered for 0.5 h including the applied overpotential from −0.1 to −1.5 V and the corresponding current profiles over time as well as selected SEM images at different potentials.

First, we like to emphasize that the electric field at the microelectrode with its radial distribution substantially differs from the potential distribution at planar electrodes. However, the experiment can simulate current focusing due to constriction resistances at the LilLLZO interface. The applied overpotentials are caused by the microelectrode (constriction) geometry and do not correspond to a charge transfer overpotential.

At the start of the experiment, the bare tungsten needle on the LLZTO cross section is visible for both samples (Figure 7A,D) and thus, a negligible current is observed. The lithium microelectrode is generated *in situ* by deposition of lithium metal at potentials of −0.2 V for low-am and −0.6 V for high-am, respectively. This can be seen in the videos recorded *in situ* that are provided in the Supporting Information (Video S1 at 1 s for low-am and Video S2 at 8 s for high-am). The generation of the lithium microelectrode is an important prerequisite for the investigation of lithium plating mechanisms, but the onset of lithium deposition itself does not correspond to the dendrite suppression ability of the two materials. The different onset potentials are rather due to distinct ionic and electronic conductivity, i.e., permittivity, of the LLZO material as well as the nucleation kinetics of lithium metal on the LLZO surface.[18] It could also be dependent on the microelectrode geometry.

Once the lithium microelectrode has formed, a signal in the current profile is observed. At the first potential step (−0.2 V), the current profile of low-am shows a constant zero dI/dt slope, indicating a stable Li metal plating. This corresponds to the vertical growth of lithium metal with whisker-like structures without any change of the contact area at the interface (Video S1 at 1−11 s). With increasing externally applied overpotentials, a nonzero slope is observable during each potentiostatic pulse for low-am, indicating the lateral growth of lithium metal, i.e., increasing contact area at the interface (Figure 7B and Video S1, starting from 11 s). Very fine lithium metal structures are observed that can be due to a fractal growth mode with branching lithium metal filaments (closeup in Figure S7A).[20,42] At an overpotential of −0.5 V, intergranular and intragranular crack formation occurs due to high mechanical stress (Video S1 at 14 s). The cracks are readily filled with lithium metal (see arrows in Figure 7C and Figure S7B), which then propagate to the counter electrode, leading to cell failure visible at the sudden increase in the current (at −0.7 V). Such crack formation and propagation in polycrystalline LLZO has been observed before, supporting the electro-chemical-mechanical concept of dendrite growth.[20,24,42] The fracture susceptibility is highly dependent on the microstructure, i.e., grain boundaries that are involved in intergranular fracture[19,59,60] as well as interconnected pores that are prone to dendrite growth.[23,61]

In contrast, high-am shows a substantially different behavior. After lithium microelectrode generation, only vertical (whisker-like) lithium metal growth is visible lasting for several overpotential steps (Figure 7E and Video S2, starting from 8 s). This corresponds to the estimated zero dI/dt slope in the current profile with slight deviations at high overpotentials. Cell failure is observed at an overpotential of −1.3 V, which is about a factor of 2 higher than for that for low-am, revealing superior dendrite suppression ability. This is in agreement with the results of the CCD measurements, in which an 8-fold higher CCD was observed for high-am compared with low-am. Most importantly, no cracking of the high-am pellet is visible at an overpotential of −1.3 V (Figure 7F). This implies a

https://doi.org/10.1021/acsami.3c01667
ACS Appl. Mater. Interfaces XXXX, XXX, XXX−XXX

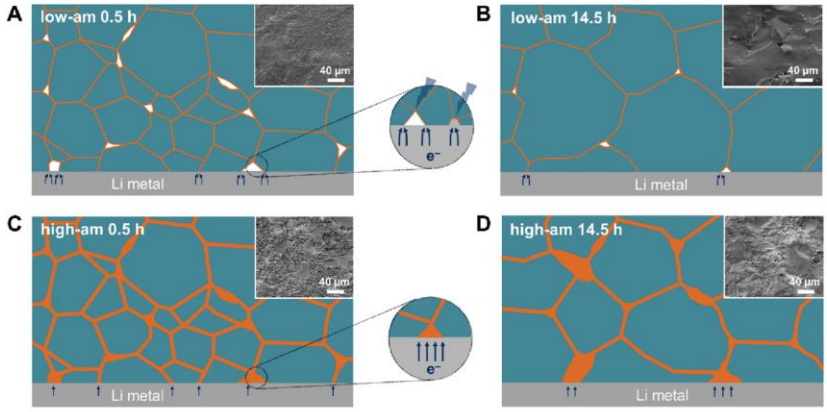

Figure 8. Schematic representation of different microstructures of the samples having a (A, B) low and a (C, D) high amorphous phase mass fraction (low-am and high-am, respectively) realized by distinct sintering times of 0.5 and 14.5 h in contact with a lithium metal anode. The fraction of amorphous phase in the grain boundaries (orange) is crucial for dendrite suppression ability. For the high-am sample, the amorphous phase fills the open porosity and suppresses current focusing at the interface.

completely different growth mechanism, presumably a rather straight lithium metal filament growth to the counter electrode.[20]

From the current profiles, the current densities at the Li| LLZTO interface together with an estimated contact area were calculated. For better comparison between the two samples, we analyze the beginning of the lithium metal plating as the whisker-root diameter is comparable for both samples (~4 μm). This demonstrates that local current densities of about 400 mA cm^{-2} for low-am and 800 mA cm^{-2} for high-am, respectively, are achieved during the measurement. This highlights that lithium plating is possible at very high rates, with high-am revealing a two-fold higher current density. The order of magnitude of these current densities is in agreement with the works of Krauskopf *et al.* confirming that stable plating at such high current densities is in principle achievable for the Li|LLZTO interface.[18,42] They found that the charge transfer kinetics at the interface is not rate-determining, but rather the nucleation kinetics on the crystal surface, i.e., the surface morphology and homogeneity of the LLZO substrate, and the ionic transport properties of the LLZO.[18,42] Therefore, we assume that high-am has superior surface microstructure properties that help to enable high lithium metal plating rates. Consequently, the microstructure of high-am with the amorphous phase located in the grain boundaries alters the dendrite growth mechanism compared with low-am. It significantly helps to suppress lateral growth of lithium metal as well as associated crack propagation.

3.5. Mechanism of Lithium Dendrite Suppression. Most recent research works agree that the formation of lithium dendrites is mainly caused by the inhomogeneous distribution of the current field, i.e., current focusing, which triggers lithium nucleation and growth into the garnet SE. The mechanism of dendrite penetration is proposed according to the following steps: (1) Lithium preferentially nucleates at voids at the interface and pores due to not fully dense sintered materials and grain boundaries, primarily at the Li|LLZO interface. Especially grain boundaries are prone to be nucleation sites due to their distinct electrochemical and mechanical properties.[21,22] The accumulation of lithium leads to extremely high local stresses and thus crack formation. (2) Lithium deposition into the crack is kinetically favored.[24] The lithium-filled cracks will propagate through grain boundaries and/or voids and interconnected pores inside the LLZO, eventually causing a short circuit of the cell. Hence, dendrite growth is an electro-chemo-mechanical degradation process. Therefore, the corresponding electro-chemo-mechanical properties of the SE are crucial for the application in SSBs. In our work, the intrinsic amorphous phase of glass-ceramic LLZTO is evenly distributed in the grain boundaries caused by liquid phase sintering. It has a high content of Li_2O for low-am and additionally contains a Li_2O−SiO_2 phase for high-am. Depending on its mass fraction as well as sintering conditions, i.e., sintering times of 0.5 and 14.5 h, the microstructure of the sintered pellets is altered. Indeed, the microstructure in terms of grain size and localization/distribution of the amorphous phase differs enormously between low-am and high-am sintered at different sintering conditions, resulting in the observed distinct dendrite stability. A schematic representation of the microstructures together with the SEM images and their effect on dendrite stability is given in Figure 8.

The low-am sample with an amorphous phase fraction of 0.1 wt % has shown very low CCD values of about 0.2 mA cm^{-2}, independent of sintering time and microstructure. The open porosity as well as the little fraction of amorphous phase in the grain boundaries, i.e., weak grain boundaries, result in current focusing at the interface and crack formation and propagation, which was confirmed by the *in situ* plating experiments. These results confirm the state-of-the-art mechanism described above. The higher density and larger grain sizes of the sample sintered for 14.5 h do not alter this behavior. This is in accordance with a study of Cheng *et al.* in which they postulated that the presence of fewer grain boundaries leads to inhomogeneous current distribution.[62]

In contrast, the high-am samples with a 40-fold higher amorphous phase fraction (4.4 wt % compared with 0.1 wt % of low-am) has demonstrated an 8-fold higher CCD than the low-am sample (1.15 mA cm^{-2} compared with 0.15 mA cm^{-2} for a sintering time of 0.5 h and 0.45 mA cm^{-2} for 14.5 h). This is a clear indication that a high amorphous phase fraction leads to a high CCD. Taking the microstructure of high-am into account, this seems to be counterintuitive as high-am

https://doi.org/10.1021/acsami.3c01667
ACS Appl. Mater. Interfaces XXXX, XXX, XXX−XXX

seems to be more porous than low-am at first glance and has more grain boundaries than low-am. According to a study by Wang et al., such microstructures with defects, i.e., pores and grain boundaries, are expected to have low CCD.[63] However, it could be shown by EDX and ToF-SIMS analysis (Figure 3) that the supposed pores are filled with the amorphous phase, resulting in a dense glass-ceramic. This is also confirmed by comparable relative densities of high-am and low-am samples (both samples have relative densities of about 92% ± 2%). A sole effect on the CCD by alteration of relative density of the distinct samples can therefore be excluded. We assume that the outstandingly high CCD of high-am is due to the superior electro-chemo-mechanical properties that are attributed to two major effects: (1) The mechanical strength of high-am is enhanced by the dense microstructure with filled grain boundaries and pores. We also assume that the amorphous phase has superior mechanical properties, preventing crack formation and crack propagation inside the LLZO. This was confirmed by the *in situ* plating experiments. (2) The current distribution at the interface is more homogeneous due to the amorphous phase in the grain boundaries. The insulating properties of the Li_2O-SiO_2 phase together with its moderate ionic conductivity[64] help to suppress electron injection in the LLZO and hinder current focusing. This hypothesis is corroborated by the results of other works that introduced lithium silicate phases as artificial interlayers. Even though theoretical calculations showed that the Li_2O-SiO_2 phases are not thermodynamically stable with lithium metal,[65] it could be experimentally proven that they are either chemically stable (in the case of Li_4SiO_4[66]) or that the reaction products are helpful to achieve a more homogeneous current distribution at the interface with the lithium metal anode (in the case of Li_3SiO_3[67]).

For high-am sintered for 14.5 h, the amorphous phase accumulates in between large grains leading to a less homogeneous current distribution. Therefore, its dendrite stability is lower than that for high-am sintered for 0.5 h. Small grain sizes are thus favorable. This is also supported by recent modeling studies that reveal that amorphous grain boundaries together with small grain sizes are favorable for high current densities.[68,69]

Such benefits of an amorphous phase (with a different chemistry compared to our work) in the grain boundaries on mechanical and electrochemical properties have been reported before, but often only relatively low CCD values of about 0.5 mA cm^{-2} were achieved.[38−40,70] The main difference to our approach is that the amorphous phase is formed by adding phases or glasses to the initial powders, which can result in inhomogeneous mixing of the powders. In our material, the amorphous phase is intrinsically incorporated in the powder due to the melting process promoting excellent distribution and outstanding dendrite stability.

4. CONCLUSIONS

In this work, the sintering and dendrite suppression ability of glass-ceramic LLZTO prepared by a melting route was investigated for the first time. The amorphous phase, mainly composed of Li_2O and a Li_2O-SiO_2 phase, acts as a sintering aid that is intrinsically incorporated into the initial powder. It is shown that the amorphous phase promotes liquid phase sintering, enabling a low sintering temperature and short sintering time. Hence, glass-ceramics could be well densified within 0.5 h at 1130 °C, which is a significant reduction compared with standard solid-state reaction approaches. A high room-temperature ionic conductivity of 0.64 mS cm^{-1} was reached. Galvanostatic cycling tests and *in situ* lithium plating experiments revealed a positive influence of the amorphous phase on the dendrite stability shown by CCD values up to 1.15 mA cm^{-2} and suppressed crack formation upon lithium plating. Superior electro-chemical-mechanical properties were given as a major reason: On the one hand, the amorphous phase fills the grain boundaries and mechanically blocks voids and pores, enhancing the mechanical strength. On the other hand, the amorphous phase with its moderate ionic conductivity helps to distribute the current field uniformly at the interface, suppressing current focusing and ultimately lithium deposition. It has also been shown that smaller grain sizes, i.e., more homogeneous distribution of the amorphous phase in the sintered material, are favorable for higher cycling stability. The current work reveals the superior properties of glass-ceramic LLZO with low-energy sintering conditions and enhanced electrochemical performance, which is attractive for future implementation in SSBs.

■ ASSOCIATED CONTENT

Supporting Information

The Supporting Information is available free of charge at https://pubs.acs.org/doi/10.1021/acsami.3c01667.

Additional details including particle size distributions of powders, XRD patterns, chemical composition, and impedance analysis of sintered pellets, additional EDX and ToF-SIMS analysis of the reference sample, detailed impedance analysis of Li-symmetric cells, and SEM images of samples after *in situ* lithium plating (PDF)

Video S1: *In situ* recorded video of lithium plating in low-am (MP4)

Video S2: *In situ* recorded video of lithium plating in high-am (MP4)

■ AUTHOR INFORMATION

Corresponding Authors

Andreas Roters − *SCHOTT AG, Mainz D-55122, Germany*; Email: andreas.roters@schott.com

Jürgen Janek − *Center for Materials Research (ZfM) and Institute of Physical Chemistry, Justus Liebig University, Giessen D-35392, Germany*; orcid.org/0000-0002-9221-4756; Email: juergen.janek@pc.jlug.de

Authors

Nina Hoinkis − *SCHOTT AG, Mainz D-55122, Germany; Center for Materials Research (ZfM) and Institute of Physical Chemistry, Justus Liebig University, Giessen D-35392, Germany*

Jörg Schuhmacher − *SCHOTT AG, Mainz D-55122, Germany*

Till Fuchs − *Center for Materials Research (ZfM) and Institute of Physical Chemistry, Justus Liebig University, Giessen D-35392, Germany*

Sebastian Leukel − *SCHOTT AG, Mainz D-55122, Germany*

Christoph Loho − *SCHOTT AG, Mainz D-55122, Germany*

Felix H. Richter − *Center for Materials Research (ZfM) and Institute of Physical Chemistry, Justus Liebig University, Giessen D-35392, Germany*; orcid.org/0000-0002-6587-7757

Complete contact information is available at:

https://doi.org/10.1021/acsami.3c01667
ACS Appl. Mater. Interfaces XXXX, XXX, XXX−XXX

https://pubs.acs.org/10.1021/acsami.3c01667

Notes

The authors declare no competing financial interest.

■ ACKNOWLEDGMENTS

T.F. and J.J. acknowledge the funding by the German Federal Ministry of Education and Research (BMBF) under the projects "LiSI" and "LiSI-2", grant identifiers 03XP0224E and 03XP0509B.

■ REFERENCES

(1) Hatzell, K. B.; Chen, X. C.; Cobb, C. L.; Dasgupta, N. P.; Dixit, M. B.; Marbella, L. E.; McDowell, M. T.; Mukherjee, P. P.; Verma, A.; Viswanathan, V.; et al. Challenges in Lithium Metal Anodes for Solid-State Batteries. *ACS Energy Lett.* **2020**, *5*, 922−934.
(2) Janek, J.; Zeier, W. G. A Solid Future for Battery Development. *Nat. Energy* **2016**, *1*, 16141.
(3) Wang, C.; Fu, K.; Kammampata, S. P.; McOwen, D. W.; Samson, A. J.; Zhang, L.; Hitz, G. T.; Nolan, A. M.; Wachsman, E. D.; Mo, Y.; et al. Garnet-Type Solid-State Electrolytes: Materials, Interfaces, and Batteries. *Chem. Rev.* **2020**, *120*, 4257−4300.
(4) Murugan, R.; Thangadurai, V.; Weppner, W. Schnelle Lithiumionenleitung in Granatartigem Li7La3Zr2O12. *Am. Ethnol.* **2007**, *119*, 7925−7928.
(5) Keller, M.; Varzi, A.; Passerini, S. Hybrid Electrolytes for Lithium Metal Batteries. *J. Power Sources* **2018**, *392*, 206−225.
(6) Yang, L.; Lu, Z.; Qin, Y.; Wu, C.; Fu, C.; Gao, Y.; Liu, J.; Jiang, L.; Du, Z.; Xie, Z.; Li, Z.; Kong, F.; Yin, G. Interrelated Interfacial Issues between Li7La3Zr2O12-Based Garnet Electrolyte and Li Anode in the Solid-State Lithium Battery: A Review. *J. Mater. Chem. A* **2021**, *9*, 5952−5979.
(7) Sharafi, A.; Yu, S.; Naguib, M.; Lee, M.; Ma, C.; Meyer, H. M.; Nanda, J.; Chi, M.; Siegel, D. J.; Sakamoto, J. Impact of Air Exposure and Surface Chemistry on Li−Li7La3Zr2O12 Interfacial Resistance. *J. Mater. Chem. A* **2017**, *5*, 13475−13487.
(8) Krauskopf, T.; Hartmann, H.; Zeier, W. G.; Janek, J. Toward a Fundamental Understanding of the Lithium Metal Anode in Solid-State Batteries - An Electrochemo-Mechanical Study on the Garnet-Type Solid Electrolyte Li6.25Al0.25La3Zr2O12. *ACS Appl. Mater. Interfaces* **2019**, *11*, 14463−14477.
(9) Kasemchainan, J.; Zekoll, S.; Spencer Jolly, D.; Ning, Z.; Hartley, G. O.; Marrow, J.; Bruce, P. G. Critical Stripping Current leads to Dendrite Formation on Plating in Lithium Anode Solid Electrolyte Cells. *Nat. Mater.* **2019**, *18*, 1105−1111.
(10) Kinzer, B.; Davis, A. L.; Krauskopf, T.; Hartmann, H.; LePage, W. S.; Kazyak, E.; Janek, J.; Dasgupta, N. P.; Sakamoto, J. Operando Analysis of the Molten Li|LLZO Interface: Understanding how the Physical Properties of Li affect the Critical Current Density. *Matter* **2021**, *4*, 1947−1961.
(11) Wang, M.; Wolfenstine, J. B.; Sakamoto, J. Temperature Dependent Flux Balance of the Li/Li7La3Zr2O12 Interface. *Electrochim. Acta* **2019**, *296*, 842−847.
(12) Huo, H.; Chen, Y.; Zhao, N.; Lin, X.; Luo, J.; Yang, X.; Liu, Y.; Guo, X.; Sun, X. In-situ Formed Li2CO3-Free Garnet/Li Interface by Rapid Acid Treatment for Dendrite-Free Solid-State Batteries. *Nano Energy* **2019**, *61*, 119−125.
(13) Lu, G.; Dong, Z.; Liu, W.; Jiang, X.; Yang, Z.; Liu, Q.; Yang, X.; Wu, D.; Li, Z.; Zhao, Q.; Hu, X.; Xu, C.; Pan, F. Universal Lithiophilic Interfacial Layers towards Dendrite-Free Lithium Anodes for Solid-State Lithium-Metal Batteries. *Sci. Bull.* **2021**, *66*, 1746−1753.
(14) Wang, C.; Gong, Y.; Liu, B.; Fu, K.; Yao, Y.; Hitz, E.; Li, Y.; Dai, J.; Xu, S.; Luo, W.; et al. Conformal, Nanoscale ZnO Surface Modification of Garnet-Based Solid-State Electrolyte for Lithium Metal Anodes. *Nano Lett.* **2017**, *17*, 565−571.
(15) Han, X.; Gong, Y.; Fu, K. K.; He, X.; Hitz, G. T.; Dai, J.; Pearse, A.; Liu, B.; Wang, H.; Rubloff, G.; Mo, Y.; Thangadurai, V.; Wachsman, E. D.; Hu, L. Negating Interfacial Impedance in Garnet-Based Solid-State Li Metal Batteries. *Nat. Mater.* **2017**, *16*, 572−579.
(16) Luo, Y.; Feng, W.; Meng, Z.; Wang, Y.; Jiang, X.; Xue, Z. Interface Modification in Solid-State Lithium Batteries based on Garnet-Type Electrolytes with High Ionic Conductivity. *Electrochim. Acta* **2021**, *397*, No. 139285.
(17) Tsai, C.-L.; Roddatis, V.; Chandran, C. V.; Ma, Q.; Uhlenbruck, S.; Bram, M.; Heitjans, P.; Guillon, O. Li7La3Zr2O12 Interface Modification for Li Dendrite Prevention. *ACS Appl. Mater. Interfaces* **2016**, *8*, 10617−10626.
(18) Krauskopf, T.; Dippel, R.; Hartmann, H.; Peppler, K.; Mogwitz, B.; Richter, F. H.; Zeier, W. G.; Janek, J. Lithium-Metal Growth Kinetics on LLZO Garnet-Type Solid Electrolytes. *Joule* **2019**, *3*, 2030−2049.
(19) Cheng, E. J.; Sharafi, A.; Sakamoto, J. Intergranular Li Metal Propagation through Polycrystalline Li6.25Al0.25La3Zr2O12 Ceramic Electrolyte. *Electrochim. Acta* **2017**, *223*, 85−91.
(20) Kazyak, E.; Garcia-Mendez, R.; LePage, W. S.; Sharafi, A.; Davis, A. L.; Sanchez, A. J.; Chen, K.-H.; Haslam, C.; Sakamoto, J.; Dasgupta, N. P. Li Penetration in Ceramic Solid Electrolytes: Operando Microscopy Analysis of Morphology, Propagation, and Reversibility. *Matter* **2020**, *2*, 1025−1048.
(21) Raj, R.; Wolfenstine, J. Current Limit Diagrams for Dendrite Formation in Solid-State Electrolytes for Li-Ion Batteries. *J. Power Sources* **2017**, *343*, 119−126.
(22) Yu, S.; Siegel, D. J. Grain Boundary Softening: A Potential Mechanism for Lithium Metal Penetration through Stiff Solid Electrolytes. *ACS Appl. Mater. Interfaces* **2018**, *10*, 38151−38158.
(23) Shen, F.; Dixit, M. B.; Xiao, X.; Hatzell, K. B. Effect of Pore Connectivity on Li Dendrite Propagation within LLZO Electrolytes Observed with Synchrotron X-ray Tomography. *ACS Energy Lett.* **2018**, *3*, 1056−1061.
(24) Porz, L.; Swamy, T.; Sheldon, B. W.; Rettenwander, D.; Frömling, T.; Thaman, H. L.; Berendts, S.; Uecker, R.; Carter, W. C.; Chiang, Y.-M. Mechanism of Lithium Metal Penetration through Inorganic Solid Electrolytes. *Adv. Energy Mater.* **2017**, *7*, 1701003.
(25) Lewis, J. A.; Tippens, J.; Cortes, F. J. Q.; McDowell, M. T. Chemo-Mechanical Challenges in Solid-State Batteries. *Trends Chem.* **2019**, *1*, 845−857.
(26) Chen, R.; Li, Q.; Yu, X.; Chen, L.; Li, H. Approaching Practically Accessible Solid-State Batteries: Stability Issues Related to Solid Electrolytes and Interfaces. *Chem. Rev.* **2020**, *120*, 6820−6877.
(27) Paolella, A.; Zhu, W.; Bertoni, G.; Savoie, S.; Feng, Z.; Demers, H.; Gariepy, V.; Girard, G.; Rivard, E.; Delaporte, N.; Guerfi, A.; Lorrmann, H.; George, C.; Zaghib, K. Discovering the Influence of Lithium Loss on Garnet Li 7 La 3 Zr 2 O 12 Electrolyte Phase Stability. *ACS Appl. Energy Mater.* **2020**, *3*, 3415−3424.
(28) Li, J.; Zhang, J.; Zhai, H.; Tang, X.; Tan, G. Rapid Synthesis of Garnet-Type Li7La3Zr2O12 Solid Electrolyte with Superior Electrochemical Performance. *J. Eur. Ceram. Soc.* **2021**, *42*, 1568−1575.
(29) Wang, C.; Ping, W.; Bai, Q.; Cui, H.; Hensleigh, R.; Wang, R.; Brozena, A. H.; Xu, Z.; Dai, J.; Pei, Y.; et al. A General Method to Synthesize and Sinter Bulk Ceramics in Seconds. *Science* **2020**, *368*, 521−526.
(30) Zhang, Y.; Chen, F.; Tu, R.; Shen, Q.; Zhang, L. Field Assisted Sintering of Dense Al-Substituted Cubic Phase Li7La3Zr2O12 Solid Electrolytes. *J. Power Sources* **2014**, *268*, 960−964.
(31) Botros, M.; Djenadic, R.; Clemens, O.; Möller, M.; Hahn, H. Field Assisted Sintering of Fine-Grained Li7-3xLa3Zr2AlxO12 Solid Electrolyte and the Influence of the Microstructure on the Electrochemical Performance. *J. Power Sources* **2016**, *309*, 108−115.
(32) Li, Y.; Cao, Y.; Guo, X. Influence of Lithium Oxide Additives on Densification and Ionic Conductivity of Garnet-Type Li6.75La3Zr1.75Ta0.25O12 Solid Electrolytes. *Solid State Ionics* **2013**, *253*, 76−80.
(33) Basappa, R. H.; Ito, T.; Morimura, T.; Bekarevich, R.; Mitsuishi, K.; Yamada, H. Grain Boundary Modification to Suppress Lithium Penetration through Garnet-Type Solid Electrolyte. *J. Power Sources* **2017**, *363*, 145−152.

https://doi.org/10.1021/acsami.3c01667
ACS Appl. Mater. Interfaces XXXX, XXX, XXX−XXX

(34) Xu, B.; Li, W.; Duan, H.; Wang, H.; Guo, Y.; Li, H.; Liu, H. Li 3 PO 4 -added Garnet-Type Li 6.5 La 3 Zr 1.5 Ta 0.5 O 12 for Li-Dendrite Suppression. *J. Power Sources* **2017**, *354*, 68−73.
(35) Tadanaga, K.; Takano, R.; Ichinose, T.; Mori, S.; Hayashi, A.; Tatsumisago, M. Low Temperature Synthesis of Highly Ion Conductive Li7La3Zr2O12−Li3BO3 Composites. *Electrochem. Commun.* **2013**, *33*, 51−54.
(36) Hosokawa, H.; Takeda, A.; Inada, R.; Sakurai, Y. Tolerance for Li Dendrite Penetration in Ta-Doped Li7La3Zr2O12 Solid Electrolytes Sintered with Li2.3C0.7B0.3O3 Additive. *Mater. Lett.* **2020**, *279*, No. 128481.
(37) Liu, K.; Ma, J.-T.; Wang, C.-A. Excess Lithium Salt Functions more than Compensating for Lithium Loss when Synthesizing Li6.5La3Ta0.5Zr1.5O12 in Alumina Crucible. *J. Power Sources* **2014**, *260*, 109−114.
(38) Chen, S.; Hu, X.; Bao, W.; Wang, Z.; Yang, Q.; Nie, L.; Zhang, X.; Zhang, J.; Jiang, Y.; Han, Y.; et al. Low-Sintering-Temperature Garnet Oxides by Conformal Sintering-Aid Coating. *Cell Rep. Phys. Sci.* **2021**, *2*, No. 100569.
(39) Rosero-Navarro, N. C.; Yamashita, T.; Miura, A.; Higuchi, M.; Tadanaga, K. Effect of Sintering Additives on Relative Density and Li-Ion Conductivity of Nb-Doped Li7La3ZrO12 Solid Electrolyte. *J. Am. Ceram. Soc.* **2017**, *100*, 276−285.
(40) Wang, C.; Liu, Z.-G.; Lin, P.-P.; Xu, X.; Lu, F.-G.; Lin, J.-C.; He, P.; Lin, T.-S. Liquid Sintering of Garnet Electrolytes by Lithium Germanate: Properties and Interfacial Performance with Lithium Anode. *Appl. Surf. Sci.* **2022**, *575*, No. 151762.
(41) Schneider, M.; Hochrein, O.; Wolfgang, S.; Kunze, M. Ionenleitende Glaskeramik mit Granatartiger Kristallstruktur. DE102014100684A1, 2015.
(42) Krauskopf, T.; Mogwitz, B.; Hartmann, H.; Singh, D. K.; Zeier, W. G.; Janek, J. The Fast Charge Transfer Kinetics of the Lithium Metal Anode on the Garnet-Type Solid Electrolyte Li6.25Al0.25-La3Zr2O12. *Adv. Energy Mater.* **2020**, *10*, 2000945.
(43) Charles, R. J. Some Structural and Electrical Properties of Lithium Silicate Glasses. *J. Am. Ceram. Soc.* **1963**, *46*, 235−238.
(44) Janani, N.; Deviannapoorani, C.; Dhivya, L.; Murugan, R. Influence of Sintering Additives on Densification and Li+ Conductivity of Al Doped Li7La3Zr2O12 Lithium Garnet. *RSC Adv.* **2014**, *4*, 51228−51238.
(45) Geng, H.; Chen, K.; Yi, D.; Mei, A.; Huang, M.; Lin, Y.; Nan, C. Formation Mechanism of Garnet-Like Li7La3Zr2O12 Powder Prepared by Solid State Reaction. *Rare Met. Mater. Eng.* **2016**, *45*, 612−616.
(46) Huo, H.; Luo, J.; Thangadurai, V.; Guo, X.; Nan, C.-W.; Sun, X. Li2CO3: A Critical Issue for Developing Solid Garnet Batteries. *ACS Energy Lett.* **2020**, *5*, 252−262.
(47) Maiti, G. C.; Baerns, M. Dehydration of Sodium Hydroxide and Lithium Hydroxide dispersed over Calcium Oxide Catalysts for the Oxidative Coupling of Methane. *Appl. Catal., A* **1995**, *127*, 219−232.
(48) Zhang, Y.; Cai, J.; Chen, F.; Tu, R.; Shen, Q.; Zhang, X.; Zhang, L. Preparation of Cubic Li7La3Zr2O12 Solid Electrolyte Using a Nano-Sized Core−Shell Structured Precursor. *J. Alloys Compd.* **2015**, *644*, 793−798.
(49) Kim, S. S.; Sanders, T. H. Thermodynamic Modeling of Phase Diagrams in Binary Alkali Silicate Systems. *J. Am. Ceram. Soc.* **1991**, *74*, 1833−1840.
(50) Wyers, G. P.; Cordfunke, E. H. P. Phase Relations in the System Li2O-ZrO2. *J. Nucl. Mater.* **1989**, *168*, 24−30.
(51) Dobretsov, E. A.; Mateyshina, Y. G.; Uvarov, N. F. Influence of Lithium Oxide Excess and Alumina on Grain Boundary Resistance of Li6.75La3Zr1.75Nb0.25O12 Solid Electrolyte. *Solid State Ionics* **2017**, *299*, 55−59.
(52) Zhang, S.; Zhao, H.; Wang, J.; Xu, T.; Zhang, K.; Du, Z. Enhanced Densification and Ionic Conductivity of Li-Garnet Electrolyte: Efficient Li2CO3 Elimination and Fast Grain-Boundary Transport Construction. *Chem. Eng. J.* **2020**, *393*, No. 124797.
(53) Yi, M.; Liu, T.; Wang, X.; Li, J.; Wang, C.; Mo, Y. High Densification and Li-Ion Conductivity of Al-Free Li7-xLa3Zr2-xTaxO12 Garnet Solid Electrolyte Prepared by Using Ultrafine Powders. *Ceram. Int.* **2019**, *45*, 786−792.
(54) Wang, D.; Zhu, C.; Fu, Y.; Sun, X.; Yang, Y. Interfaces in Garnet-Based All-Solid-State Lithium Batteries. *Adv. Energy Mater.* **2020**, *10*, 2001318.
(55) Flatscher, F.; Philipp, M.; Ganschow, S.; Wilkening, H. M. R.; Rettenwander, D. The Natural Critical Current Density Limit for Li7La3Zr2O12 Garnets. *J. Mater. Chem. A* **2020**, *8*, 15782−15788.
(56) Sharafi, A.; Kazyak, E.; Davis, A. L.; Yu, S.; Thompson, T.; Siegel, D. J.; Dasgupta, N. P.; Sakamoto, J. Surface Chemistry Mechanism of Ultra-Low Interfacial Resistance in the Solid-State Electrolyte Li7La3Zr2O12. *Chem. Mater.* **2017**, *29*, 7961−7968.
(57) Wang, M. J.; Choudhury, R.; Sakamoto, J. Characterizing the Li-Solid-Electrolyte Interface Dynamics as a Function of Stack Pressure and Current Density. *Joule* **2019**, *3*, 2165−2178.
(58) Eckhardt, J. K.; Klar, P. J.; Janek, J.; Heiliger, C. Interplay of Dynamic Constriction and Interface Morphology between Reversible Metal Anode and Solid Electrolyte in Solid State Batteries. *ACS Appl. Mater. Interfaces* **2022**, *14*, 35545−35554.
(59) Zhang, L. C.; Yang, J. F.; Li, C. L.; Gao, Y. X.; Wang, X. P.; Fang, Q. F. Intragranular Growth and evenly Distribution Mechanism of Li Metal in Li7La3Zr2O12 Electrolyte. *J. Power Sources* **2020**, *449*, No. 227610.
(60) Manalastas, W.; Rikarte, J.; Chater, R. J.; Brugge, R.; Aguadero, A.; Buannic, L.; Llordés, A.; Aguesse, F.; Kilner, J. Mechanical Failure of Garnet Electrolytes during Li Electrodeposition observed by In-Operando Microscopy. *J. Power Sources* **2019**, *412*, 287−293.
(61) Ren, Y.; Shen, Y.; Lin, Y.; Nan, C.-W. Direct Observation of Lithium Dendrites inside Garnet-Type Lithium-Ion Solid Electrolyte. *Electrochem. Commun.* **2015**, *57*, 27−30.
(62) Cheng, L.; Chen, W.; Kunz, M.; Persson, K.; Tamura, N.; Chen, G.; Doeff, M. Effect of Surface Microstructure on Electrochemical Performance of Garnet Solid Electrolytes. *ACS Appl. Mater. Interfaces* **2015**, *7*, 2073−2081.
(63) Wang, H.; Gao, H.; Chen, X.; Zhu, J.; Li, W.; Gong, Z.; Li, Y.; Wang, M.-S.; Yang, Y. Linking the Defects to the Formation and Growth of Li Dendrite in All-Solid-State Batteries. *Adv. Energy Mater.* **2021**, *11*, 2102148.
(64) Nakagawa, A.; Kuwata, N.; Matsuda, Y.; Kawamura, J. Characterization of Stable Solid Electrolyte Lithium Silicate for Thin Film Lithium Battery. *J. Phys. Soc. Jpn.* **2010**, *79*, 98−101.
(65) Zhu, Y.; He, X.; Mo, Y. First Principles Study on Electrochemical and Chemical Stability of Solid Electrolyte−Electrode Interfaces in All-Solid-State Li-Ion Batteries. *J. Mater. Chem. A* **2016**, *4*, 3253−3266.
(66) Kim, J. Y.; Kim, A.-Y.; Liu, G.; Woo, J.-Y.; Kim, H.; Lee, J. K. Li4SiO4-Based Artificial Passivation Thin Film for Improving Interfacial Stability of Li Metal Anodes. *ACS Appl. Mater. Interfaces* **2018**, *10*, 8692−8701.
(67) Rosero-Navarro, N. C.; Kajiura, R.; Jalem, R.; Tateyama, Y.; Miura, A.; Tadanaga, K. Significant Reduction in the Interfacial Resistance of Garnet-Type Solid Electrolyte and Lithium Metal by a Thick Amorphous Lithium Silicate Layer. *ACS Appl. Energy Mater.* **2020**, *3*, 5533−5541.
(68) Barai, P.; Ngo, A. T.; Narayanan, B.; Higa, K.; Curtiss, L. A.; Srinivasan, V. The Role of Local Inhomogeneities on Dendrite Growth in LLZO-Based Solid Electrolytes. *J. Electrochem. Soc.* **2020**, *167*, 100537.
(69) Li, G.; Monroe, C. W. Dendrite Nucleation in Lithium-Conductive Ceramics. *Phys. Chem. Chem. Phys.* **2019**, *21*, 20354−20359.
(70) Tian, Y.; Ding, F.; Zhong, H.; Liu, C.; He, Y.-B.; Liu, J.; Liu, X.; Xu, Q. Li6.75La3Zr1.75Ta0.25O12@Amorphous Li3OCl Composite Electrolyte for Solid State Lithium-Metal Batteries. *Energy Storage Mater.* **2018**, *14*, 49−57.

https://doi.org/10.1021/acsami.3c01667
ACS Appl. Mater. Interfaces XXXX, XXX, XXX−XXX

3.3 Manuscript: "The role of ceramic/polymer interfaces in garnet-polymer hybrid electrolytes: Understanding the influence of phase compatibility on electrochemical performance"

In the manuscript of this thesis, the application of glass-ceramic LLZO variants in HSEs was studied. The focus was on the correlation between the phase compatibility of LLZO/polyethylene oxide (PEO)-based PSE and the corresponding interface resistance. Thus, the objective is to understand how such interfaces influence the electrochemical performance of HSEs. The compatibility was altered by different LLZO chemistry as well as surface modifications. The two Ta-doped LLZO variants with low and high volume fraction of amorphous phase studied in publication 1 and 2 were used. Additionally, an Al-doped LLZO variant was considered as alternative LLZO chemistry. The latter was also subjected for surface modification by milling in PEO-analogous solvents and annealing in different atmospheres.

The results of this study revealed that the compatibility with the PEO-based PSE matrix was enhanced for the Ta-doped LLZO variants in comparison with the Al-doped variant. In terms of surface modification, the variants milled in solvents analogous to the PEO monomer showed strongly enhanced compatibility, while for the annealed powders lower compatibilities compared with the pristine one were obtained. However, the ionic conductivities of all variants were found to be lower than the reference samples of the pure PSE and HSEs containing the passive filler Al_2O_3. By determination of the interface resistance in a trilaminar four-point measurement setup, it could be confirmed that the interface resistance limits the ion transport across the interface and the ionic conductivity solely takes place through the PSE matrix. Therefore, a positive correlation between enhanced compatibility and lowered interface resistance could not be found in the case of PEO-based PSEs.

Overall, this work emphasizes the influence of ceramic/polymer interfaces on the ion transport in HSEs, which needs to be considered for the manufacturing of HSEs. Furthermore, it expands the knowledge of the interplay between phase compatibility and electrochemical performance, providing useful information for the application of LLZO particles in HSEs.

The concept of this manuscript was developed by the first author under the supervision of J. Schuhmacher. All experiments were performed and analyzed by the first author, partially with the support of the analytics division at the SCHOTT AG. Four-point measurements were carried out at the University of Giessen. J. Schuhmacher, S. Leukel, F. H. Richter and J. Janek assisted the scientific discussion of the data. The manuscript was written by the first author and edited by five co-authors.

The role of ceramic/polymer interfaces in garnet-polymer hybrid electrolytes: Understanding the influence of phase compatibility on electrochemical performance

Nina Hoinkis, Jörg Schuhmacher, Sebastian Leukel, Andreas Roters, Felix H. Richter, and Jürgen Janek**

N. Hoinkis, Dr. J. Schuhmacher, Dr. S. Leukel, Dr. C. Loho, Dr. A. Roters
SCHOTT AG
Hattenbergstrasse 10, 55122 Mainz, Germany
E-mail: andreas.roters@schott.com

N. Hoinkis, Dr. F. H. Richter, Prof. J. Janek
Institute of Physical Chemistry
Justus Liebig University Giessen
Heinrich-Buff-Ring 17, 35392 Giessen, Germany
E-Mail: juergen.janek@phys.chemie.uni-giessen.de

Keywords

hybrid electrolytes, composites, garnet, interface, solid-state battery

Abstract

Hybrid solid electrolytes (HSEs) composed of ceramic fillers embedded in a polymer solid electrolyte matrix are considered as possible solid electrolytes for high energy density solid-state batteries (SSBs). By benefitting from the properties of both components, they have the potential to realize high lithium ion conductivity, wide electrochemical window, sufficient mechanical strength, and ability to prevent lithium dendrite formation. However, in terms of ionic conductivity of the HSE, the results reported in the literature are contradictory. It remains unclear whether the filler contributes to the ionic conductivity, which is strongly dependent on the filler/polymer interface resistance. We hypothesize that the compatibility between the two phases is a key factor in achieving low interface resistances and thus enabling ion transfer through the highly conductive fillers. In this study, the compatibility of different garnet-type $Li_7La_3Zr_2O_{12}$ (LLZO) fillers with a PEO-based matrix was quantified by sedimentation analysis, revealing slight changes due to distinct LLZO chemistry (distinct doping elements (Al, Ta) and amorphous phase in glass-ceramic LLZO) and strong enhancement by surface modification, i.e., milling in solvents analogous to the PEO monomer. However, the ionic conductivities of the corresponding HSEs were all found to decrease with increasing LLZO volume fraction in comparison with the pure polymer electrolyte and HSEs containing the passive filler Al_2O_3. By a trilaminar four-point measurement setup, it could be confirmed that the LLZO|PEO interface resistance of all variants is in the range of a few hundred $\Omega\,cm^2$ at 20 °C, hindering ion transport through the LLZO particles. According to the results, the observed enhancement in compatibility is insufficient to achieve a low interface resistance. This work clarifies the influence of the ceramic/polymer interface on the ionic conductivity of HSEs and therefore provides important insights for their future application in SSBs.

3.3.1 Introduction

Solid-state batteries (SSBs) are promising alternatives to conventional lithium-ion batteries, as they can overcome severe safety issues, such as flammability and leakage, due to the replacement of liquid electrolytes by solid electrolytes. Besides the safety aspect, SSBs have the potential to significantly increase the energy density of the battery, which is of special interest for electric vehicle application.[1–3] They enable the use of lithium metal as anode material that has the highest theoretical specific capacity, i.e., 3860 mAh g^{-1} compared with 372 mAh g^{-1} of conventional graphite anodes.[4] In combination with liquid electrolytes, lithium metal anodes (LMAs) are impracticable due to inherent instabilities and growth of lithium dendrites during cell cycling.[5] Solid electrolytes (SEs) with their intrinsic high mechanical stability are considered to have the ability to solve these limitations.

Both inorganic (ceramic) solid electrolytes (ISE) and polymer solid electrolytes (PSE) have attracted great interest as potential SEs.[3,6] Among ISEs, the oxide-based garnet lithium lanthanum zirconium oxide $Li_7La_3Zr_2O_{12}$ (LLZO) has emerged as the most promising choice due to its high room-temperature ionic conductivity, wide electrochemical stability window, and chemical stability against lithium metal.[7] Nonetheless, several drawbacks remain such as their sensitivity to moisture and related formation of insulating lithium carbonate[8] and their intrinsic brittleness, causing poor interfacial contact with lithium metal, which induces current focusing and lithium dendrite generation.[9,10] In contrast, PSEs, of which polyethylene oxide (PEO)-based PSEs are the most extensively studied [11], offer flexibility and good wetting properties with lithium metal due to their soft nature. However, their low room-temperature ionic conductivity along with low lithium ion transference number and small electrochemical window impede their application. Moreover, the lithium dendrite issue also applies to PSEs due to their low mechanical strength.[12]

Due to the current challenges of both ceramic ISEs and PSEs, an alternative approach has attracted increasing attention.[13,14] The hybrid solid electrolyte (HSE) approach combines both SEs to benefit from the respective advantages. Typically, ceramic ISE particles are embedded in a flexible ion-conducting polymer matrix. Among various studies combining different types of ISEs and PSEs, PEO-based HSEs containing garnet fillers are the most prominent ones.[15] It has been shown that HSEs exhibit an enhanced electrochemical stability window as well as more stable lithium cycling compared with the pure PSEs due to their superior mechanical strength and uniform lithium deposition at the Li|HSE interface.[16–21] However, in terms of ionic conductivity, the investigations reported so far show substantial discrepancies for a wide range of different ceramic filler contents.

In principle, HSEs can be classified into "polymer-rich" (< 50 vol%) and "inorganic-rich" (> 50 vol%) composites, which strongly influences the ionic transport mechanism inside the HSE.[22] For both systems, some HSEs show an increased ionic conductivity with an optimal filler

content[17,19,23–26], while for others, a monotonic decrease upon increased ISE content is observed compared with the pure PSE.[16,20,27,28] Most authors ascribe the positive effect to the plasticizing effect of the fillers, i.e., decrease of crystallinity of the polymer and enhanced ion transport at the particle surface along an interphase, e.g., due to Lewis acid-base interactions. Such behavior has also been observed for passive, non-ion-conducting fillers, such as SiO_2, TiO_2, and Al_2O_3.[29,30] The contribution of active (ion-conducting) fillers to the ion transport is controversially discussed. There are reports confirming the pathway inside the ISE particles experimentally[31], but other authors state that the ion transport takes place mainly via the polymer matrix.[20,27] Moreover, it could be shown that the size and the shape of the filler particles have significant influence on the ion transport properties, e.g., nano-sized and rod-shaped structures can enhance the ionic conductivity.[17,21,32,33]

The differences between the manifold reports remain poorly understood and comparability is low because of the large number of parameters that influence the electrochemical performance of the HSEs. Among them, the synthesis route via solvent-cast method[17,19,23,26] has potentially crucial influence, as it could be shown that residual solvent leads to overestimation of ionic conductivity and potential side reactions.[29] Especially in the case of LLZO, which is very sensitive to water or protic solvents, this can be detrimental.[34,35] Often the consideration and investigation of the lithium ion pathway across the inorganic/organic interface is neglected, even though this is essential to understand the different ionic transport pathways. A few reports exist that investigate the interfacial resistance of the PSE|ISE interface by a trilaminar setup.[36–39] However, there is a lack of profound analyses, especially in terms of composition of the ISE as well as consideration of chemical compatibility between the inorganic and organic phase.

In this study, we synthesized LLZO/PEO:LiTFSI HSEs by using a solvent-free three roll mill process. According to the hypothesis that high chemical compatibility of the LLZO/PEO phases leads to low interface resistance between them, enhancement in ionic conductivity of the corresponding HSE is expected. To study such a correlation, we used LLZO with different doping elements (Ta, Al) and glass-ceramic LLZO containing an amorphous phase with modified chemistry to increase the compatibility with the PEO matrix. In the same manner, the surfaces of LLZO particles were modified by milling in solvents analogous to the PEO monomer or by annealing in oxidizing (O_2), reducing (H_2/N_2), and inert (N_2) atmosphere. Solvent-based methods such as sedimentation analysis were applied to study the chemical compatibility between the LLZO variants and the PEO matrix, and were correlated with ionic conductivities of the corresponding HSEs. The LLZO content was varied from 0–20 vol% and compared to both the pure PSE and the passive filler Al_2O_3. Moreover, we determined the LLZO|PEO:LiTFSI interfacial resistance using two approaches of which one is an in-house-developed four-point (4P) trilaminar measurement setup enabling the direct assessment of the interface. A simple brick-layer model was used to understand the influence of the LLZO|PEO:LiTFSI interfacial resistance on the ionic conductivity.

3.3.2 Experimental

3.3.2.1 Materials

Garnet-type Al- and Ta-doped LLZO (LALZO and LLZTO, respectively) were manufactured by a unique and industrially scalable melting process at the SCHOTT AG.[40] Glass-ceramic LLZO is formed that contains an amorphous phase formed intrinsically upon cooling, whose volume fraction and composition is adjustable during the process. In this study, LALZO and LLZTO with very low volume fraction of amorphous phase (LA-LALZO and LA-LLZTO, respectively) were chosen to simulate stoichiometric LLZO powders produced via conventional solid-state reaction. Additionally, LLZTO with high amorphous phase content (HA-LLZTO) containing the glass former SiO_2 was used. The composition of the LLZO variants was determined by chemical analysis: ZrO_2, La_2O_3, Ta_2O_5 by X-ray fluorescence spectroscopy (RFA); Li_2O by atomic absorption spectroscopy (AAS) and SiO_2 by inductively coupled plasma optical emission spectroscopy (ICP-OES). The amorphous phase content, i.e., Li excess, was calculated by the difference between the ideal stoichiometry of LALZO or LLZTO and the Li excess under the assumption that the elements Zr, La, and Ta or 0.2 pfu Al fully contribute to the crystalline phase. Bulk densities ρ of the powders were calculated by Equation (3.3.1) using the density of the crystalline phase ($\rho_{\text{cryst.}}$, determined by Rietveld refinement of the lattice parameter bye XRD), the estimated density of the amorphous phase ($\rho_{\text{am.}} \sim 2$ g cm^{-3}), and the corresponding volume fractions of crystalline and amorphous phase in vol%:

$$\rho = \frac{\text{vol\%}_{\text{cryst.}} \cdot \rho_{\text{cryst.}} + \text{vol\%}_{\text{am.}} \cdot \rho_{\text{am.}}}{100} \tag{3.3.1}$$

All powders were milled under inert gas atmosphere in order to avoid side reactions with ambient air. The median particle size *D50* was measured by static light scattering (CILAS 1064, Quantachrome) and the specific surface area was determined by the BET method (QUADRASORB evo, Anton Paar).

The surface-modified LA-LALZO powders were prepared either by milling in solvents analogous to the PEO monomer or by annealing in distinct atmospheres. For the milling approach, 110 g of LA-LALZO powder with an initial particle size of *D90* < 20 µm were dissolved in 200 g ethylene glycol dimethyl ether (EGDME) and milled in an attritor (R41-55/2, NETZSCH) containing 1,47 kg of ZrO_2 grinding beads at a speed of 1000 rpm until a *D50* value of 0.6 µm was reached. The solution was centrifuged, the solvent decanted, and subsequently washed with isopropanol (Sigma-Aldrich), which was repeated three times in total. In the final step, the isopropanol was evaporated in a rotary evaporator. For the annealing approach, the LA-LALZO powder was filled in a self-built, sealed glass tube with a gas inlet and outlet. Either nitrogen, oxygen or forming gas (N_2: 95%, H_2: 5%)) was

flowed through the tube (1 L min^{-1}). The tube was placed in a tube furnace (R170/750/12, Nabertherm) and annealed at 700 °C with a heating rate of 10 K min^{-1} for 12 h.

Prior to HSE preparation, PEO (M_v = 10^6 g mol^{-1}, Sigma-Aldrich) and lithium bis(trifluoro-methanesulfonyl)imide (LiTFSI, ≥99%, Sigma-Aldrich) were dried in vacuum at 55 °C for PEO and 110 °C for LiTFSI for 48 h. The inert filler Al_2O_3 (AKP3000, ≥99.99%, Sumitomo Chemical) was also vacuum-dried at 250 °C for 24 h. All materials were stored in a N_2-filled glovebox (MBraun) with O_2 and H_2O content < 1 ppm.

3.3.2.2 Hybrid solid electrolyte preparation

PEO, LiTFSI, and fillers (either LLZO or Al_2O_3) were mixed in different volume ratios (5, 10, 15, and 20 vol% of filler, named filler *x*/PEO:LiTFSI) in an airtight container. The particle size of the reference Al_2O_3 was similar to the used LLZO variants (*D50* = 0.7 µm according to datasheet Sumitomo Chemical). For the reference solid polymer electrolyte, no filler was added (named PEO:LiTFSI). The molar ratio of *n*(EO):*n*(Li^+) was set to 14:1. The mixtures were homogenized in a dual asymmetric centrifuge mixer at 3000 rpm for 2 min (SpeedMixer DAC 150 FVZ, Hauschild), annealed at 60 °C for 24 h and processed on a three roll mill (Exakt, Modell 80S) with a roll temperature of about 60 °C. The mixtures were processed three times on the three roll mill in order to ensure sufficient dispersion of the fillers in the thermoplastic PEO matrix. All steps were performed under inert nitrogen atmosphere.

3.3.2.3 Characterization methods

As chemical compatibility tests, calorimetric determination of the heat of dispersion as well as sedimentation analysis were developed. Both methods were performed under inert nitrogen atmosphere. For the first one, three PEO-analogous solvents with decreasing acidity, i.e., decreasing δ_{Hdon} value, were chosen: ethylene glycol (EG, δ_{Hdon} = 20.5 $(MPa)^{0.5}$), ethylene glycol monomethyl ether (EGMME, δ_{Hdon} = 9.9 $(MPa)^{0.5}$), and ethylene glycol dimethyl ether (EGDME, δ_{Hdon} = 0.1 $(MPa)^{0.5}$). All values were extracted from the HSPiP software.[41] In a self-built mixing calorimeter setup (see Figure A3.1A), 5 mL of the PEO-analogous solvent were filled into the thermally insulated container and stirred on a stirring plate until the temperature was constant. The temperature was recorded every second with a temperature sensor inside the liquid (Pt1000, ALMEMO). 0.5 g of the LLZO powder was added at once and the temperature was monitored until the temperature was constant again. The temperature curve is given in Figure A3.1B, which shows the temperature increase upon adding the LLZO powder. The offset between the temperature plateau at the beginning and at the end of the measurement is due to heat loss of the not perfectly insulated container. The curve was fitted with the function given in Equation (3.3.2) to determine the heat of dispersion ΔT:

$$f(t) = \Delta T \frac{k_1}{k_2 - k_1}\left(e^{-k_1(t-t_0)} - e^{k_2(t-t_0)}\right) + T_0 \qquad (3.3.2)$$

It is composed of two exponential function describing first-order reactions, of which the first one is related to the heat of dispersion with the rate constant k_1 and the second one the heat loss to the exterior of the calorimeter with the rate constant k_2. The starting temperature is T_0 and the point of time of adding the LLZO powder is t_0.

For the second compatibility test (sedimentation analysis), 0.015 g of the LLZO powder was added to 10 g of the PEO-analogous solvent EGDME. The mixture was homogenized using an ultrasonic finger (Hielscher UP400S, amplitude 70%, cycle 0.7) for 30 s and transferred into an analytical centrifuge (LUMiSizer, LUM GmbH) that measures transmitted light over the entire sample length over time (space- and time-resolved extinction). The rotation speed was set to 1500 rpm (equivalent to 270 rcf (relative centrifugal force) and the temperature to 25 °C. The extinction profiles were integrated using the software SEPView Version 6.4. The sedimentation time τ was defined as the time necessary to reach a value 15% above the final value of integral extinction reached at the end of centrifugation (full separation)[42] and normalized (τ_{norm}) using the density and the particle size *D50* of the corresponding LLZO powder ρ_{LLZO} (see Table 3.3.1), the density of EGDME (ρ_{EGDME} = 0.87 g mL^{-1}), and the viscosity of EGDME (η_{EGDME} = 0.47 mPas) as given by the adapted Stokes equation in Equation (3.3.3):

$$\tau_{\text{norm}} = \frac{\tau(\rho_{\text{LLZO}} - \rho_{\text{EGDME}})}{\eta_{\text{EGDME}}} D50 \qquad (3.3.3)$$

Room-temperature X-ray diffraction (XRD) spectra were collected using a PANalytical X'Pert PRO MPD (Malvern Panalytical) in Bragg-Brentano geometry from 10–70° *2Θ* in increments of 0.013° using CuKα radiation operating at 45 kV and 40 mA. Samples were spun during XRD in order to ensure diffraction from multiple grains. Powder samples were directly transferred from the glovebox to the XRD and HSE samples were hot-pressed (Bürkle LA4.5, 50 MPa, 60 °C) prior to analysis to get HSE foils. Diffraction patterns were analyzed qualitatively using the software HighScore Plus (Malvern Panalytical) and reference crystallographic information files were from the Crystallography Open Database (COD) (cubic LLZO: COD #1545083). Rietveld refinement was performed with the same software for determination of the lattice parameter used for the determination of the density (see Equation (3.3.1)).

Differential scanning calorimetry (DSC) were measured with a DSC 404F1 Pegasus (NETZSCH) in Pt-Rh crucibles from 23–130 °C at a heating rate of 5 K min^{-1}. Ar was chosen as processing gas to prevent side reactions. Together with the melting enthalpies ΔH_{m} of the corresponding DSC curves, the degree of crystallinity χ_{c} was calculated as given in Equation (3.3.4) with the melting enthalpy

$\Delta H_{m,PEO}$ of PEO being completely crystallized (196.6 J g^{-1})[43] and f_{PEO} the weight fraction of PEO in the HSE:

$$\chi_c = \frac{\Delta H_m}{\Delta H_{m,PEO} f_{PEO}} \cdot 100\% \quad (3.3.4)$$

Scanning electron microscopy (SEM) was performed with a LEO1530 equipped with field emission gun (FEG) to record the SEM images with a secondary electron detector operated at 5 keV accelerating voltage. Prior to analysis, HSEs were pressed between PTFE foils (Bola) with a hot-press (Bürkle LA4.5, 50 MPa, 60 °C) and were sputtered coated with carbon.

For the determination of the ionic conductivities, electrochemical impedance spectroscopy (EIS) was performed on the PSE and HSE samples as well as on sintered LLZO pellets. For the PSE and HSE samples, an airtight measuring cell with stainless steel electrodes (diameter of 12 mm) equipped with a spacer ring for defined thickness (0.2 mm) was used (TSC battery cell, rhd instruments). About 40 mg of sample were filled into the cell. For the LLZO pellets, a self-built airtight measuring cell with gold electrodes was used. The LLZO pellets were produced via sintering in mother powder (1130 °C, 0.5 h, O_2 atmosphere) and were sputter coated with gold electrodes with a diameter of 6.5 mm on both sides of each pellet using a sputter coater (EM SDC050, Leica).

For the determination of the interface resistance LLZO|PEO:LiTFSI, two methods were applied. For the 2-point subtraction method, sintered LLZO pellets (diameter of about 8.4 mm) were polished (SiC sandpaper #1200) and sandwiched between two PSE foils (thickness of about 100 µm) with a diameter of 8 mm (hot-pressed prior to analysis (Bürkle LA4.5, 50 MPa, 60 °C)). Lithium metal electrodes were freshly prepared by cutting off a piece from a Li rod (Sigma-Aldrich, 99.9%) using a ceramic knife and pressing it with a self-built hand press to a thickness of about 50–100 µm. Li electrodes with a diameter of 6 mm were punched out and applied to the trilaminar stack together with copper foil (diameter of 8 mm) as current collector. The complete stack was hot-pressed at about 200 MPa at 60 °C. In a similar manner, a stack without the LLZO pellet was prepared to determine solely the Li|PEO:LiTFSI interface resistance that can be subtracted from the full stack including both the Li|PEO:LiTFSI and LLZO|PEO:LiTFSI interface resistance to give the LLZO|PEO:LiTFSI interface resistance (see details in Figure 3.3.5 and corresponding explanation). For the 4-point method, a procedure following the work of Simon *et al.* was adopted.[44] The same symmetrical cell setup as for the subtraction method was used but gold-plated tungsten wires (diameter of 25 µm) were placed between two layers of PSE foil, and lithium was plated onto the wire to obtain a stable potential. Using this four-point setup, the sole LLZO|PEO:LiTFSI interface resistance could be measured directly without the influence of other interfaces.

EIS was carried out with an Alpha A-High Analyzer (Novocontrol) in a frequency range from 20 MHz to 100 mHz with a 20 mV perturbation amplitude either at 70 °C or temperature-dependent from 20 °C to 70 °C (increment of 10 °C) with a heating rate of 1 K min^{-1}. Prior to the measurement,

the system was kept at the chosen temperature for at least 2 h. EIS data were fitted with Z-View software using equivalent circuits with impedance (*R*) and capacitance elements (constant phase element (*CPE*)). The effective capacitance *C* were calculated by converting the *CPE* together with fitting the alpha value *α* following Equation (3.3.5):

$$C = \left(\frac{CPE}{R^{1-\alpha}}\right)^{1/\alpha} \tag{3.3.5}$$

The thickness *d* of the sample and the electrode area *A* together with impedance *R* were used for calculation of the ionic conductivity *σ* as given by Equation (3.3.6):

$$\sigma = \frac{1}{R} \cdot \frac{d}{A} \tag{3.3.6}$$

Measurements were performed in triplicates giving an experimental error of about 7%. Activation energies were calculated according to the Arrhenius equation in Equation (3.3.7):

$$\sigma T = \sigma_0 \exp\left(-\frac{E_a}{k_B T}\right) \tag{3.3.7}$$

3.3.3 Results and Discussion

3.3.3.1 LLZO powder characterization

In order to study the influence of LLZO composition on the electrochemical performance of the HSE, three different garnet compositions were used. All of them were synthesized via a unique glass-ceramic melting process at the SCHOTT AG in which an amorphous phase is formed upon cooling that can be adjusted in terms of volume fraction and composition.[40] Here, two aliovalently doped LLZO glass-ceramics with very low amorphous phase content (i.e., Ta-doped LLZO (LA-LLZTO) and Al-doped LLZO (LA-LALZO)) were chosen in order to compare the findings with stoichiometric LLZO manufactured using the conventional solid-state reaction route. For LA-LLZTO, the particle size was also varied to fine particles (f-LA-LLZTO) and coarse particles (c-LA-LLZTO). Additionally, LLZTO with high volume fraction of amorphous phase was used (HA-LLZTO). The latter is mainly composed of an excess of Li_2O and a small volume fraction of the glass former SiO_2. Table 3.3.1 gives the exact compositions (see Experimental section for calculation), the mean particle size *D50*, as well as the bulk densities *ρ* of the starting glass-ceramic powders.

Table 3.3.1. Composition, *D50* values of the particle size distribution and bulk densities ρ of the LLZO glass-ceramic powders doped with Al (LALZO) and Ta (LLZTO), either having low (LA-) and high volume fraction of amorphous phase (HA-). For LA-LLZTO, two additional particle sizes are given from fine (sub-µm, f-) to coarse (a few µm, c-).

Sample	Amorphous (wt%)	SiO_2 (wt%)	*D50* (µm)	ρ (g cm^{-3})	S_{BET} (m^2 g^{-1})
LA-LALZO	0.1	0.1	0.7	5.19	3.9
LA-LLZTO	0.1	0.02	0.8	5.37	2.7
f-LA-LLZTO	0.3	0.03	0.4	5.32	5.6
c-LA-LLZTO	0.0	0.02	4.9	5.40	0.8
HA-LLZTO	4.4	0.7	1.0	5.04	3.5

The compositions indicate a 40-fold higher amorphous phase content for HA-LLZTO and a significantly higher SiO_2 content in comparison with the two LA-LLZO variants. The particle size distributions of all powders are monomodal; only c-LA-LLZTO shows a slight bimodality due to a second mode of finer particles (Figure A3.2A). The *D50* values of the three LLZO variants are in the same range (0.7 µm, 0.8 µm, and 1.0 µm). The fine and coarse LA-LLZTO samples obviously have differing *D50* values in the sub-µm (0.4 µm) and a few microns (4.9 µm) range. The S_{BET} values agree well with the *D50* values; merely the LA-LLZTO exhibits slightly lower surface area (2.7 m^2 g^{-1} *vs.* 3.9 m^2 g^{-1} and 3.5 m^2 g^{-1} for the two other LLZO variants). The bulk densities ρ are comparable for the stoichiometric LLZO variants LA-LALZO and LA-LLZTO (including particle size variation) and slightly lower for HA-LLZTO due to the presence of the amorphous phase that has lower density.

The XRD patterns of the three starting powders are presented in Figure A3.2B. They all match well with the reference pattern of cubic LLZO and are all free of impurity phases as no additional reflections are observed.

3.3.3.2 Chemical compatibility between LLZO powders and PEO matrix

In order to verify the correlation between the chemical compatibility of LLZO particle surfaces with the PEO matrix and the ionic conductivity of the corresponding HSE, two methods to study the compatibility were evaluated. Both are solvent-based and use PEO-analogous solvents to model the PEO matrix. In Figure 3.3.1, the results of both methods are demonstrated for the samples LA-LALZO, LA-LLZTO, and HA-LLZTO.

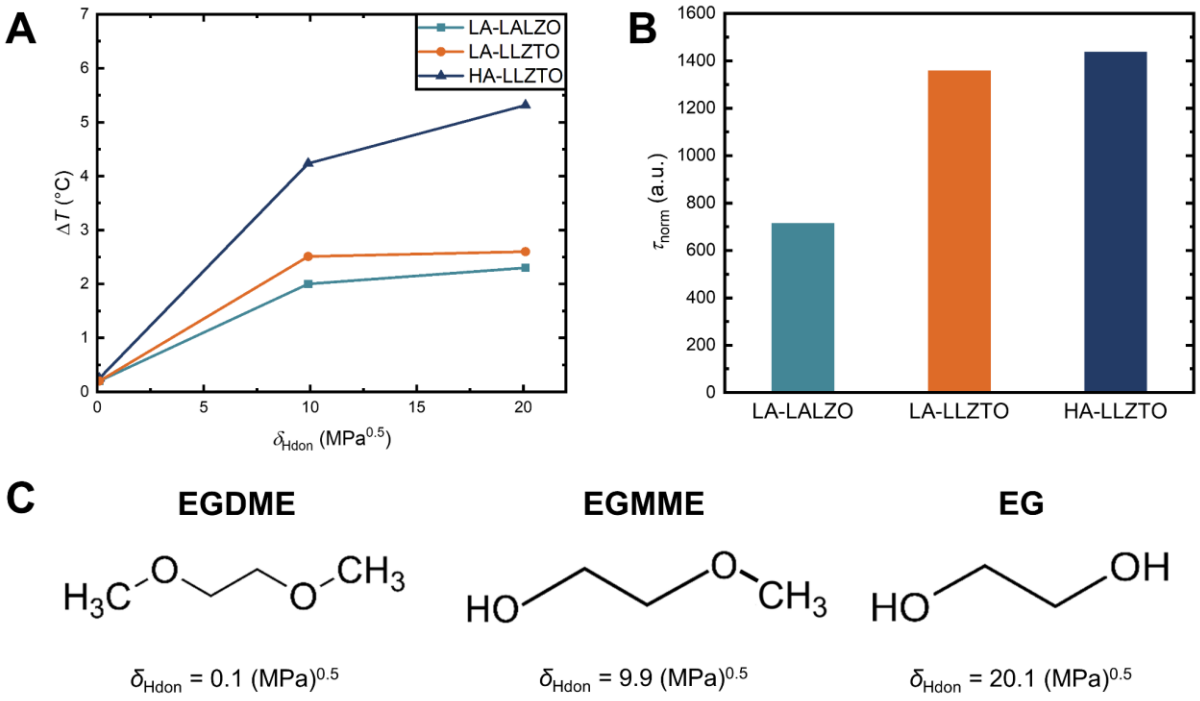

Figure 3.3.1. (A) Calorimetric determination of the heat of dispersion of LA-LALZO, LA-LLZTO, and HA-LLZTO powders in PEO-analogous solvents with distinct acidity. (B) Normalized sedimentation times of LA-LALZO, LA-LLZTO, and HA-LLZTO powders in EGDME determined with the help of an analytical centrifuge. (C) Structural chemical formula and δ_{Hdon} values of the used PEO-analogous solvents: ethylene glycol dimethyl ether (EGDME), ethylene glycol monomethyl ether (EGMME), and ethylene glycol (EG).

The first method calorimetrically measures the heat of dispersion when the LLZO particles are dispersed into PEO-analogous solvents with different acidities. Ethylene glycol (EG), which is the monomer of PEO, ethylene glycol monomethyl ether (EGMME), as well as ethylene glycol dimethyl ether (EGDME) were chosen (structural chemical formulas in Figure 3.3.1C). The acidity of the solvents decreases in the given order due to the methylation of the free OH groups, which is quantified with the help of the δ_{Hdon} value derived from the Hansen parameter concept. It describes the donor contribution of the cohesive energy of hydrogen bonds (see ref. [45] for detailed information). As can be seen from Figure 3.3.1A, the heat of dispersion (ΔT) steadily increases with acidity of the solvent for all LLZO variants. For EGDME, which has no free protons, ΔT is accordingly low for all LLZO variants. For EGMME and EG, LA-LALZO and LA-LLZTO show comparable ΔT values, while HA-LLZTO exhibits about two-fold higher values. We suppose that the heat of dispersion ΔT is due to exothermic reaction between the alkaline surface of LLZO and the acidity function of the solvent according to the Brønsted acid-base concept. It is thus a measure of the alkalinity of the LLZO variant. Hence, HA-LLZTO appears to be more alkaline and to have stronger interactions with the solvents (EGMME and EG) compared with LA-LALZO and LA-LLZTO. This can be ascribed to its high volume fraction of amorphous phase that is mainly composed of alkaline Li_2O. The glass former SiO_2 also contained in the amorphous phase apparently has minor influence on

lowering the alkalinity of LLZO due to its small content. In order to evaluate the compatibility with the PEO matrix, the results of EGDME can be used as comparison due to its similar δ_{Hdon} value (δ_{Hdon} (PEO) = 0.1 $(MPa)^{0.5}$). Due to the observed similar ΔT values in EGDME for all LLZO variants, differences between the LLZO variants in terms of the compatibility with the PEO matrix cannot be determined.

The second method quantifies the sedimentation time for LLZO particles in the PEO-analogous solvent EGDME with the help of an analytical centrifuge. The sedimentation time highly depends on the interaction between the particle surface and the surrounding solvent matrix. Besides the (Brønsted) acid-base interactions observed in the calorimetric method, also Lewis acid-base as well as dipole-dipole interactions play an important role in the sedimentation analysis. If the interaction is strong, i.e., chemical compatibility is high, a stable dispersion is formed and the particles take longer to sediment. If the compatibility is poor, the particle-particle interaction becomes dominating and agglomerates form that sediment faster. Due to its strong dependence on particle size and material properties such as density, the sedimentation time needs to be corrected for comparable results (see Experimental for details). As demonstrated in Figure 3.3.1C, LA-LALZO has a sedimentation time about half as long as LA-LLZTO and HA-LLZTO, the latter having similar values. Evidently, the doping element has greater influence on the dispersion stability, i.e., compatibility, than the amorphous phase. A possible explanation is that the Lewis-acid dopant Ta^{5+} and its location within the structure at the surface presumably leads to a stronger interaction with the PEO backbone than the dopant Al^{3+}. The amorphous phase of HA-LLZTO only slightly influences the sedimentation time compared to LA-LLZTO and thus has marginal effect on the particle/matrix interactions, probably due to the low amorphous phase content compared to the crystalline volume fraction. According to the results, HA-LLZTO and LA-LLZTO should have the strongest interaction with the PEO matrix. Therefore, a positive influence on the LLZO|PEO:LiTFSI interfacial resistance and thus on the ionic conductivity of the corresponding HSE might result.

3.3.3.3 Structural and thermal characterization of HSEs

HSEs incorporating the three LLZO variants were manufactured with increasing LLZO volume fractions from 5–20 vol% (named LLZO*x*/PEO:LiTFSI) in a solvent-free process using a three roll mill. In order to ensure degradation-free processing, XRD of the HSEs was measured. Figure 3.3.2A shows the XRD patterns of pure PEO, the PSE sample PEO:LiTFSI, and the HSE samples LA-LLZTO*x*/PEO:LiTFSI.

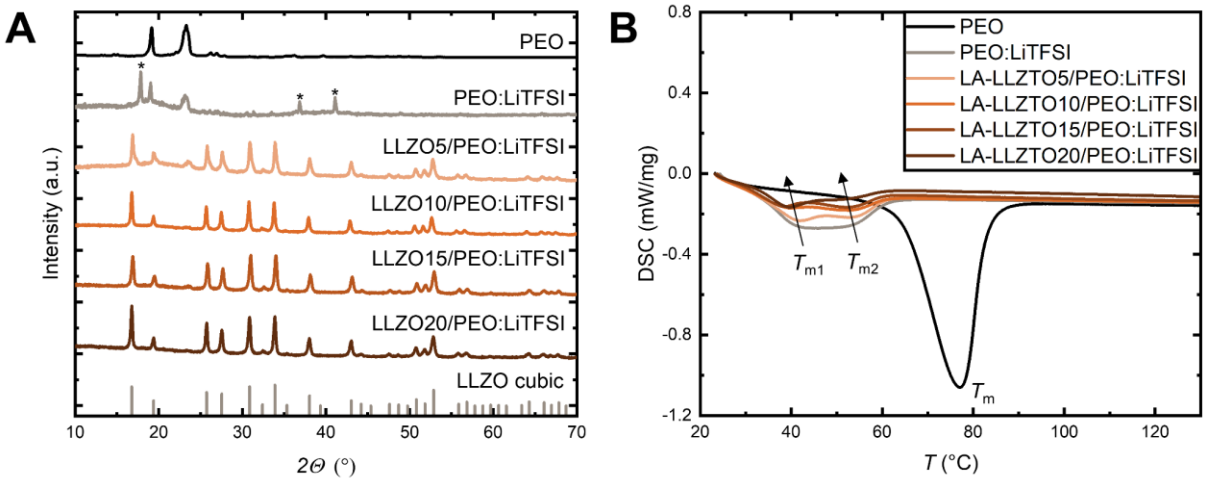

Figure 3.3.2. (A) XRD patterns of pure PEO, the PSE PEO:LiTFSI, and the HSEs LA-LLZTO*x*/PEO:LiTFSI (*x*=5, 10, 15, and 20) together with the reference pattern of cubic LLZO. The reflections marked with an asterisk (*) stem from the underlying substrate made of PTFE. (B) DSC curves of pure PEO, the PSE PEO:LiTFSI, and the HSEs LA-LLZTO*x*/PEO:LiTFSI (*x*=5, 10, 15, and 20).

The XRD pattern of PEO can be ascribed to the mostly crystalline nature of the pure polymer. Upon incorporation of the lithium salt LiTFSI, no additional reflections related to LiTFSI are observable, which can be explained by the solvation of LiTFSI in the PEO matrix.[46] The reflections marked with an asterisk are due to the underlying PTFE substrate that was used during the measurement because of the low viscosity of the PEO:LiTFSI sample. As LA-LLZTO is introduced in the PEO:LiTFSI matrix, the characteristic reflections of cubic LLZO emerge increasing in intensity with increasing LA-LLZTO content, while the PEO-related reflections decrease in intensity. For all samples besides pure PEO, the background of the diffractograms is increased, indicating the lower degree of crystallinity of the PEO. It is well known that the incorporation of inorganic fillers in the polymer matrix hinders polymer crystallization, promoting the formation of amorphous regions.[19,28,47] This is also in agreement with the results from the DSC measurements that are presented in Figure 3.3.2B for the same set of samples. The reference sample of pure PEO exhibits one endothermic peak at about 77 °C that is attributed to the melting of crystalline PEO (T_m).[20] It shifts to lower temperatures and splits into two peaks upon incorporation of the lithium salt LiTFSI and the filler LA-LLZTO. These can be assigned to the melting process of the HSE. The one at higher temperatures (T_{m2}) stems from the melting of the crystalline complex between PEO and LiTFSI and the one at lower temperatures (T_{m1}) from the melting of a eutectic PEO:LiTFSI mixture.[25] The corresponding values are given in Table 3.3.2 together with the melting enthalpies ΔH_m obtained from the melting peaks. Both the T_{m1}, T_{m2} and the ΔH_m values are shifted to lower values with increasing LA-LLZTO content, which is due to the plasticizing effect of the lithium salt and/or the LA-LLZTO particles, decreasing the crystalline phase content of the polymer. With the help of Equation (3.3.4) the degree of

crystallinity χ_c of the PSE and HSEs was calculated (Table 3.3.2), confirming the decreasing crystallinity of the samples, which is in accordance with the findings of other studies.[25–27]

Table 3.3.2. Extracted values from the DSC analysis (Figure 3.3.2B) of pure PEO, the PSE PEO:LiTFSI, and the HSEs LA-LLZTO5/PEO:LiTFSI, LA-LLZTO10/PEO:LiTFSI, LA-LLZTO15/PEO:LiTFSI, and LA-LLZTO20/PEO:LiTFSI, including the melting temperatures T_m of pure PEO, T_{m2} and T_{m1} of the PSE and HSEs, the melting enthalpy ΔH_m and the degree of crystallinity χ_c.

Sample	T_m **(°C)**	T_{m2} **(°C)**	T_{m1} **(°C)**	ΔH_m **(J g^{-1})**	χ_c **(%)**
PEO	77	--	--	136.2	69.3
PEO:LiTFSI	--	43.4	53.1	37.0	27.6
LA-LLZTO5/PEO:LiTFSI	--	41.8	52.9	30.0	27.4
LA-LLZTO10/PEO:LiTFSI	--	39.3	52.5	16.6	18.3
LA-LLZTO15/PEO:LiTFSI	--	38.1	52.4	17.2	22.5
LA-LLZTO20/PEO:LiTFSI	--	38.0	52.0	15.8	24.4

In order to examine the dispersing quality and distribution of the LLZO particles in the PEO matrix, SEM was carried out on the set of LA-LALZO HSEs. In Figure 3.3.3A, the PSE sample PEO:LiTFSI without filler exhibit a smooth and continuous film. For the samples with 5 and 10 vol% LA-LALZO content (Figure 3.3.3B–C), the PEO is the dominant phase and the particles are found to be well dispersed, as their original cullet shape can be well identified (see Figure A3.3 for SEM image of the powder particles). For the sample with the highest LLZO content in Figure 3.3.3D (LA-LALZO20/PEO:LiTFSI), the particles have a significantly higher volume fraction but the particles are still well distributed within the PEO matrix. Some agglomerates are observable, e.g., in the bottom right corner. However, considering the results of the different characterization methods, it can be concluded that the solvent-free mixing with the three roll mill leads to well dispersed, impurity-free HSEs that have lower crystallinity upon the introduction of the LLZO particles.

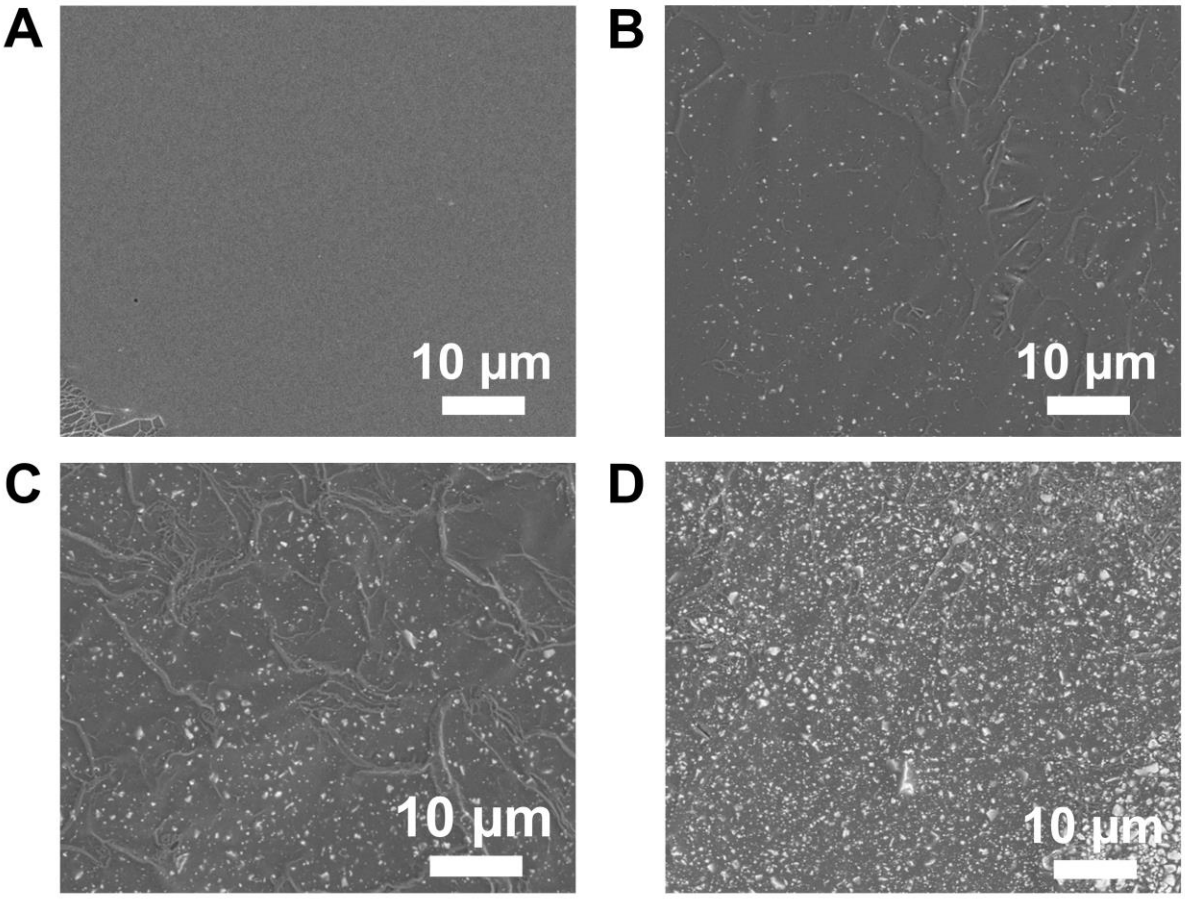

Figure 3.3.3. Top-view SEM images of (A) the PSE PEO:LiTFSI without filler and the HSEs with increasing filler volume fraction: (B) LA-LALZO5/PEO:LiTFSI, (C) LA-LALZO10/PEO:LiTFSI, and (D) LA-LALZO20/PEO:LiTFSI.

3.3.3.4 Electrochemical characterization of HSEs

The HSEs were evaluated for their ionic conductivities using EIS. The associated Nyquist plots at 20 °C are shown in Figure 3.3.4A representatively for the LLZO variant LA-LALZO with a volume fraction of 10 vol% and compared to the pure PSE PEO:LiTFSI as well as the pure ISE manufactured via sintering of LA-LALZO. One semicircle, i.e., capacitive resistance, in the high frequency range and a capacitive tail at low frequencies due to the blocking electrodes can be observed for the three samples. The data were fitted with an equivalent circuit including (*R*-*CPE*)(*CPE*) elements. With the help of Equation (3.3.5), the effective capacitances C_{bulk} were calculated (Table 3.3.3) revealing capacitances in the range of 25–39 pF, which are typical values for bulk capacitances.[48] Therefore, these capacitances can be assigned to the ionic conductivity in the bulk polymer (for PEO:LiTFSI) or in the sintered grains (for the sintered LA-LALZO pellet). For the HSE, contributions from both the bulk polymer and the LA-LALZO particles are to be expected, but no distinguishable semi-circles can be observed in the Nyquist plot. On the contrary, it can be assumed that the lithium ion transport might mainly take place through the polymer matrix, as the resistance of the pure PEO:LiTFSI is close to the resistance of the HSE, while the resistance of the sintered LA-LALZO pellet is almost

negligible. Since no further semicircles are observed, ion conduction through the LLZO|PEO:LiTFSI interface (µF range) cannot be proven.

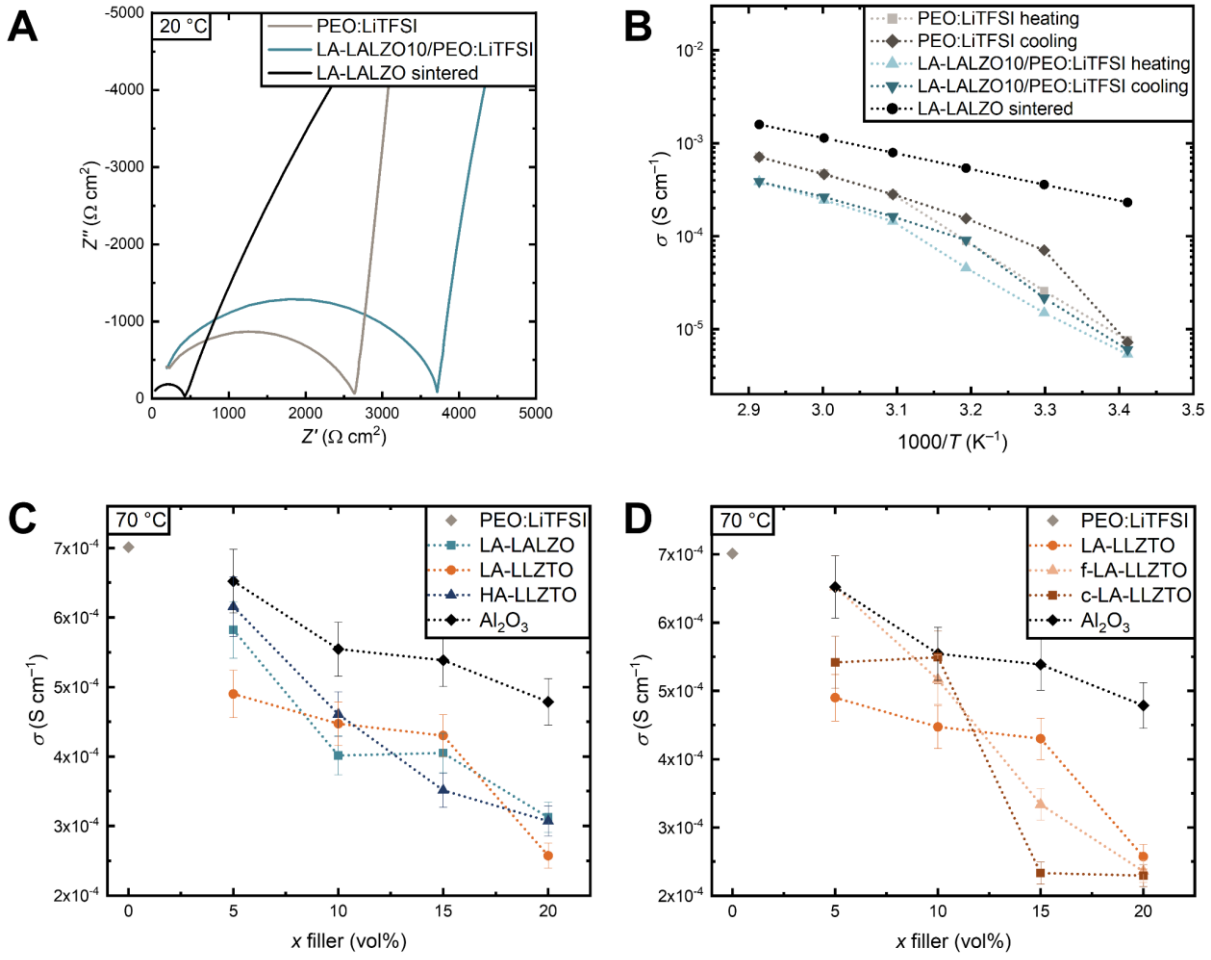

Figure 3.3.4. (A) Temperature-dependent ionic conductivities as Arrhenius plots for PEO:LiTFSI (PSE), LA-LALZO10/PEO:LiTFSI (HSE), and LA-LALZO (sintered pellet). Both heating and cooling scans are presented for the PSE and the HSE. The corresponding activation energies can be found in Table 3.3.3. (B) Nyquist plots at 20 °C from the heating cycle for the same set of samples as in (A). (C) Ionic conductivities of the HSEs LA-LALZO*x*/PEO:LiTFSI, LA-LLZTO*x*/PEO:LiTFSI, and HA-LLZTO*x*/PEO:LiTFSI in dependence of the volume fraction *x* of the LLZO filler at 70 °C. (D) Ionic conductivities of the HSEs with varying particle size LA-LLZTO*x*/PEO:LiTFSI, f-LA-LLZTO*x*/PEO:LiTFSI, c-LA-LLZTO*x*/PEO:LiTFSI in dependence of the volume fraction *x* of the LLZO filler at 70 °C. In (C) and (D), the ionic conductivities of the pure PSE PEO:LiTFSI (filler content *x* = 0 vol%) and the HSE containing the passive filler Al_2O_3 (Al_2O_3*x*/PEO:LiTFSI) are given as reference.

The temperature-dependency of the ionic conductivity is given in Arrhenius plots for the same set of samples in the temperature range from 20 to 70 °C in Figure 3.3.4B. The ionic conductivities were determined by Equation (3.3.6) using the corresponding thickness, electrode area, and impedance *R* extracted from the Nyquist plots in Figure 3.3.4A. The ionic conductivity values as well as the activation energy (determined by Equation (3.3.7), values seeTable 3.3.3) of the pure sintered LA-LALZO pellet are in good agreement with reported values in literature for LALZO ($2.3 \cdot 10^{-4}$ S cm^{-1} at 20 °C and 0.36 eV, respectively).[49] The same applies for the ionic conductivity of the pure PSE

PEO:LiTFSI, i.e., $7.6 \cdot 10^{-6}$ S cm^{-1} at 20 °C, which is in accordance with values from other works.[50] We only compare the values to PSEs also manufactured by solvent-free processing in order to exclude the influence of residual solvents.

The results in Figure 3.3.4B give evidence that the ionic conductivities of the sintered pellet are higher than those of the pure PSE, and the latter being higher than those of the HSE LA-LALZO10/PEO:LiTFSI. This indicates that the LA-LALZO particles likely do not contribute to the ionic conductivity of the HSE. Instead, the ion conduction appears to occur mainly within the polymer matrix. For both the PSE and the HSE, data were collected upon heating and consecutive cooling temperature scans, as the ionic conductivity of polymer electrolytes is known to be highly dependent on the thermal history. The pure PSE shows a strong hysteresis within the 20–50 °C range, with the conductivity values of the cooling scan being significantly higher than the values of the heating scan. No hysteresis is observed at a temperature > 50 °C because above the melting temperature of the PSE (observed by DSC), recrystallization of the polymer upon cooling has minor influence. Below the melting temperature, hysteresis occurs due to the slow recrystallization kinetics upon cooling. The HSE shows a similar behavior, which hints that lithium ion conduction in the polymer matrix has a strong contribution to the ionic conductivity of the HSE. For practical applications, only the conductivity values from the heating scan, i.e., near-equilibrium values should be used. This is often overlooked in the literature and most studies do not specify heating and cooling scans.

Both the PSE and the HSE show two linear regimes in the heating scan between 20–50 °C and 50–70 °C with a knee around 50 °C, which is in agreement with the melting temperatures (T_{m2} at about 52 °C and T_{m1} at about 40 °C) observed by DSC measurements (Figure 3.3.2B). The activation energies for the two linear temperature regimes of PSE and HSE are presented inTable 3.3.3. Both samples show significantly lower activation energies above the observed melting temperatures (0.47 eV and 0.50 eV for T = 50–70 °C *vs*. 1.01 eV and 0.92 eV for T = 20–50 °C), which is due to the much larger amorphous phase content, supporting fast ion movement. The values are in agreement with other reported values.[20] The activation energies for the cooling scan are also given inTable 3.3.3, revealing an analogous trend, but slightly higher values for the low-temperature regime due to hysteresis. Overall, the activation energies of both PSE and HSE are similar, indicating that the ion conduction through the polymer dominates the temperature-dependent behavior.

Table 3.3.3. Bulk capacities C_{bulk} (exemplary at 20 °C for the Nyquist plots in Figure 3.3.4A) and activation energies E_a of the Arrhenius plots in Figure 3.3.4B for PEO:LiTFSI (PSE), LA-LALZO10/PEO:LiTFSI (HSE), and LA-LALZO (sintered pellet). For the PSE and HSE, both heating and cooling cycles are distinguished as well as low and high temperature ranges.

Sample	C_{bulk} **@20 °C (pF)**	E_a **heating (eV)**	E_a **cooling (eV)**
PEO:LiTFSI	39	1.01 (20–50 °C) 0.47 (50–70 °C)	1.25 (20–40 °C) 0.50 (40–70 °C)
LA-LALZO10/ PEO:LiTFSI	34	0.92 (20–50 °C) 0.50 (50–70 °C)	1.10 (20–40 °C) 0.48 (40–70 °C)
LA-LALZO sintered	25	0.36	–

Figure 3.3.4C shows the ionic conductivities for the LA-LALZO*x*/PEO:LiTFSI, LA-LLZTO*x*/PEO:LiTFSI, HA-LLZTO*x*/PEO:LiTFSI, and Al_2O_3*x*/PEO:LiTFSI in dependence of the filler volume fraction *x*. As reference, the ionic conductivity of the PSE PEO:LiTFSI is given as well. Ionic conductivities were measured at 70 °C in order to avoid comparability issues due to crystallinity effects of the polymer. The corresponding Nyquist plots together with the bulk capacitances of the four samples can be found in Figure A3.4 and Table A3.1 with a volume fraction of 10 vol% as example. They all exhibit solely one semicircle with a capacitance in the pF range that can be ascribed to the bulk conductivity of the HSE. Interface processes cannot be observed. In agreement with the results in Figure 3.3.4B, the ionic conductivities of all HSEs are well below the ionic conductivity of the unfilled PSE, and they all decrease with increasing filler content. Interestingly, the ionic conductivities of all LLZO variants are even lower than the reference HSEs containing the passive filler Al_2O_3. The characterization of the latter can be found in Figure A3.5, demonstrating well-distributed Al_2O_3 particles with a similar particle size as the used LLZO particles. Among the LLZO variants, no significant differences can be observed as the values are approximately within the given error range. The results indicate that the incorporation of either passive or active filler leads to a decrease in ionic conductivity of the pure PSE, with the particles not contributing to the transport of lithium ions. Thus, the ion conduction is considered to take place mainly through the polymer matrix. The monotonic decrease of ionic conductivity can be understood considering the lower cross-sectional area and higher tortuosity of the polymer matrix, causing longer ion conduction pathways. Accordingly, the chemistry of the active filler, i.e., the doping element (LALZO *vs*. LLZTO) as well as the amorphous phase of HA-LLZTO do not have an effect on the ionic conductivity of the HSE.

These results are in agreement with previous reports on other PEO/garnet-based HSEs.[16,20,27,28] However, the majority of other studies describe contrasting results.[17,19,23–26] Such discrepancies can potentially be caused by the variety of parameters (polymer type, polymer/salt ratio, filler type, and

particle size) and synthesis conditions (solvent-based or solvent-free) used in the literature. Table A3.2 summarizes the most important properties of several PEO/garnet-based HSEs (exceptional structures such as rod-like or 3D structures were omitted), indicating no clear trend which parameter determines a positive effect on the ionic conductivity of the pure PSE. Another important parameter that is rarely described in the given references is the shape of the fillers, which can highly influence the ion transport pathways. This could be an explanation for the contrary results. Presumably, the cullet-shaped LLZO particles used in our study are ineffective in terms of ionic transport enhancement.

Furthermore, please note that almost all studies solely use the unfilled PSE as reference system and disregard the comparison with a passive filler. However, such comparison contains crucial information on the contribution to the ion conduction. As demonstrated by our results, the LLZO-containing HSEs have even lower ionic conductivities than the Al_2O_3-containing HSEs, presumably indicating the formation of a potential insulating interphase at the LLZO surface, which increases the effective radii and thus lowers the ionic conductivity more effectively. For this reason, passive fillers should also be considered when discussing ion conduction contributions of the fillers.

To further evaluate how the shape and the size of the LLZO particles affect the electrochemical performance of the HSE, we investigated the ionic conductivities of LA-LLZTO*x*/PEO:LiTFSI with varying *D50* values (Figure 3.3.4D). A similar trend to the results in Figure 3.3.4B–C can be observed, as the ionic conductivities are also all below the ionic conductivity of the pure PSE and the HSE reference containing Al_2O_3. Merely two HSEs (f-LA-LLZTO5/PEO:LiTFSI and c-LA-LLZTO10/PEO:LiTFSI) are close to the values of the Al_2O_3-containing reference. The varying surface area of the particles apparently does not have a significant effect on the ionic conductivity. Therefore, conduction pathways along the interface and/or interphases can be excluded in all probability. This confirms the results from Figure 3.3.4B–C, but is in stark contrast to other studies that reported enhanced interface/interphase ionic conductivities with increasing surface area of the filler.[17,21]

In order to understand why the LLZO particles considered in this study do not contribute to the ionic conductivity of the HSE, interface resistance studies were performed. Figure 3.3.5A–B schematically shows the two methods for electrochemical determination of the LLZO|PEO:LiTFSI interface using lithium metal electrodes. The 2-point subtraction method uses a trilaminar and a bilaminar cell setup, i.e., Li|PEO:LiTFSI|LLZO|PEO:LiTFSI|Li and Li|PEO:LiTFSI|Li, with the LLZO pellet being manufactured via sintering. The corresponding Nyquist plots of the sample LA-LLZTO are also demonstrated for both setups, each revealing two semicircles. The first one can be attributed to the sum of bulk resistance of the PSE and the LLZO pellet in the case of the trilaminar setup and only of the PSE in the case of the bilaminar setup, according to the bulk capacitances in the pF range given in Table A3.3. The second semicircle is related to interface processes with capacitances in the µF

range (Table A3.3). The interface resistance of the bilaminar setup only includes contributions of the Li|PEO:LiTFSI interface ($R_{Li|PEO}$), which is subtracted from the interface resistance from the trilaminar setup (including both the LLZO|PEO:LiTFSI and the Li|PEO:LiTFSI interface resistances, i.e., $R_{LLZO|PEO}$ and $R_{Li|PEO}$), giving the LLZO|PEO:LiTFSI interface resistance ($R_{LLZO|PEO}$). The 4-point direct method uses reference electrodes, thereby solely measuring the LLZO|PEO:LiTFSI interface ($R_{LLZO|PEO}$) and excluding contributions from the Li|PEO:LiTFSI interface. In the corresponding Nyquist plot of LA-LLZTO, the sum of bulk resistance of the PSE and the LLZO pellet is obtained as well as the interface resistance of the LLZO|PEO:LiTFSI interface with µF range capacitance (see Table A3.3). As two LLZO|PEO:LiTFSI interfaces are measured simultaneously in both methods, the single LLZO|PEO:LiTFSI interface resistance is calculated by dividing the $R_{LLZO|PEO}$ by factor 2.

Figure 3.3.5C shows the temperature-dependent LLZO|PEO:LiTFSI interface resistances ($R_{LLZO|PEO}$) for the LLZO variants LA-LALZO, LA-LLZTO, and HA-LLZTO, determined by the 2-point subtraction method. For LA-LLZTO, the results of the 4-point direct method are also shown. The extracted $R_{LLZO|PEO}$ values at 70 °C and 20 °C are presented in Table 3.3.4. The values are in the kΩ cm^2 range at 20 °C, while they are in the range of a few hundred Ω cm^2 at 70 °C due to the temperature-dependency of the interface resistance. LA-LALZO exhibits the lowest interface resistance (34 kΩ cm^2 at 20 °C and 0.30 kΩ cm^2 at 70 °C) and HA-LLZTO the highest (59 kΩ cm^2 at 20 °C and 0.66 kΩ cm^2 at 70 °C). The values at 70 °C are in agreement with values from a study that also implemented a 4-point setup[39], but lower compared with the values measured in other works, e.g., Langer *et al.* determined 9 kΩ cm^2 between LALZO and PEO:$LiClO_4$[36] and Zagórski *et al.* 11.5 kΩ cm^2 between Ga-doped LLZO and PEO:LiTFSI[16]. They both used 2-point trilaminar setups with blocking electrodes that can also have contributions from other interface resistances. With the help of the methods used in this study, such contributions can be excluded, providing the sole LLZO|PEO:LiTFSI interface resistance. The results in Figure 3.3.5C confirm that both the 2-point subtraction method and the 4-point direct method are suitable for the determination of the LLZO|PEO:LiTFSI interface resistance, as the interface resistances are in good agreement. Table 3.3.4 also gives the activation energies E_a of the interface resistances for the different samples. They all exhibit values in the range from 0.81–0.85 eV, which are in agreement with the activation energy reported by Trevisanello *et al.* (0.72 eV)[39] and Langer *et al.* (0.9 eV)[36]. Thus, the activation energy of the interface process is much higher compared with bulk ion conduction processes (Table 3.3.3).

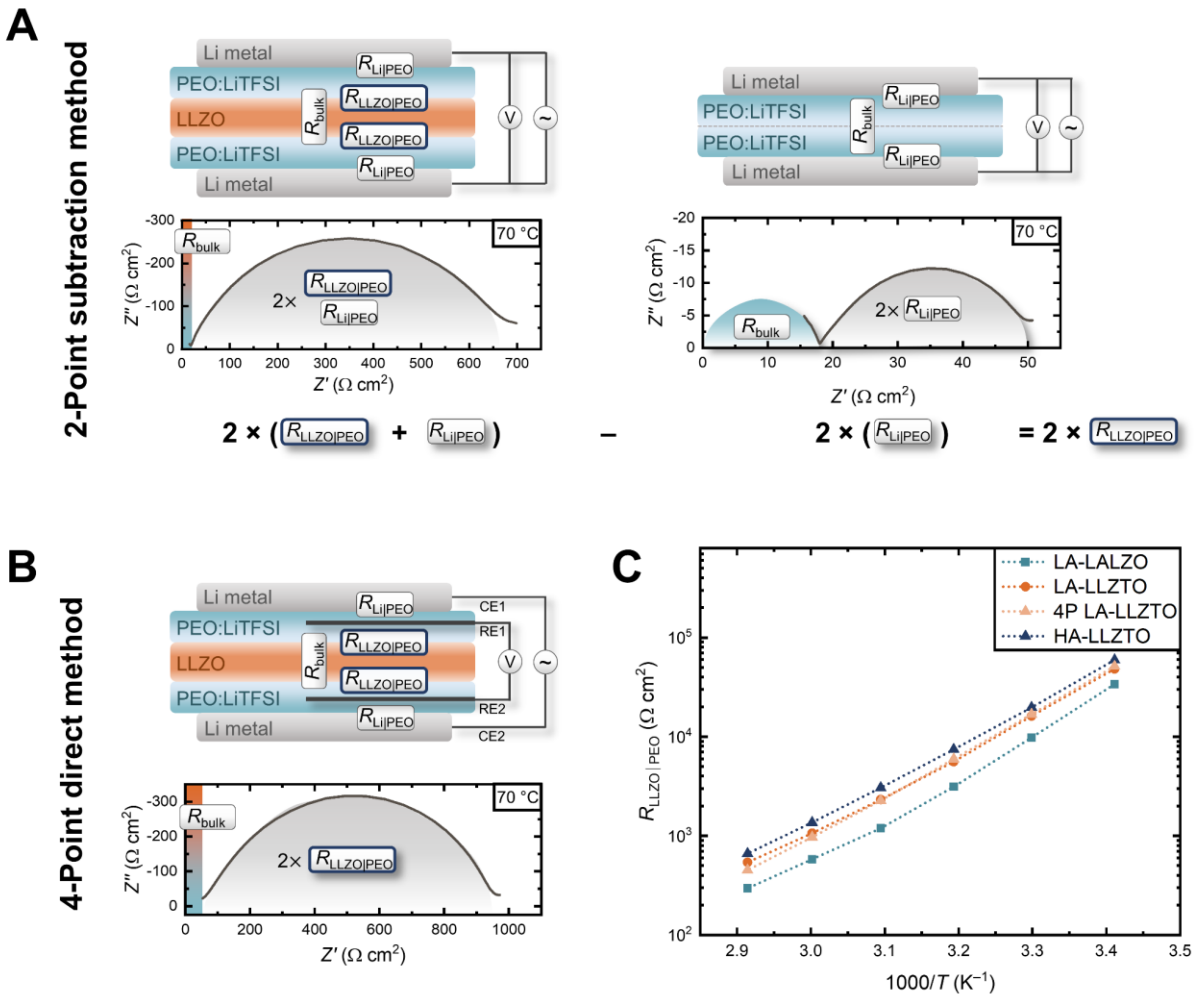

Figure 3.3.5. Schematics of the methods used to study the LLZO|PEO:LiTFSI interface: (A) The subtraction method involves two cell setups in 2-point configuration (Li|PEO:LiTFSI|LLZO|PEO:LiTFSI|Li and Li|PEO:LiTFSI|Li). The corresponding Nyquist plots at 70 °C for the sample LA-LLZTO are given below each schematic. The grey semicircles can be attributed to the interface resistance, of which the interface resistance of the Li|PEO:LiTFSI|Li setup ($R_{Li|PEO}$) is subtracted from the other one ($R_{LLZO|PEO}$ and $R_{Li|PEO}$) to give solely the LLZO|PEO:LiTFSI interface. (B) The direct method uses the Li|PEO:LiTFSI|LLZO|PEO:LiTFSI|Li setup with two additional reference electrodes (RE) in the PEO:LiTFSI layers. The Nyquist plot given below has only contributions from the LLZO|PEO:LiTFSI interface ($R_{LLZO|PEO}$). In both (A) and (B), the first semicircle of the Nyquist plots can be assigned to bulk processes (R_{bulk}), either from the PEO:LiTFSI or the LLZO pellet. (C) Temperature-dependent resistance of the LLZO|PEO:LiTFSI interface ($R_{LLZO|PEO}$) as Arrhenius plots for the LLZO variants LA-LALZO, LA-LLZTO, and HA-LLZTO measured with the 2-point subtraction method given in (A). For LA-LLZTO, the 4-point direct method in (B) was used additionally (designated as 4P LA-LLZTO). The corresponding activation energies can be found in Table 3.3.4.

Table 3.3.4. LLZO|PEO:LiTFSI interface resistances ($R_{LLZO|PEO}$) at 70 °C and 20 °C and the corresponding activation energies E_a of the Arrhenius plots in Figure **3.3.5**C for the samples LA-LALZO, LA-LLZTO, and HA-LLZTO determined by either 2-point subtraction method (2P) or 4-point direct method (4P).

Sample	$R_{LLZO\|PEO}$ **@70 °C** ($k\Omega\ cm^2$)	$R_{LLZO\|PEO}$ **@20 °C** ($k\Omega\ cm^2$)	E_a **(eV)**
2P LA-LALZO	0.30	34	0.85
2P LA-LLZTO	0.54	48	0.81
4P LA-LLZTO	0.45	51	0.85
2P HA-LLZTO	0.66	59	0.81

The obtained high interface resistances of all samples together with the high activation energies indicate that the LLZO|PEO:LiTFSI interface is a limiting barrier for the lithium ion transport across the interface. The lithium ion transfer comprises distinct processes, including the desolvation of the lithium ion at the interface. According to other studies, this is considered to be the rate-determining step of the whole transfer process.[51,52] The desolvation process and its activation energy is highly influenced by the chemical potential difference of the lithium ions in the polymer matrix and in the ISE particles. The chemical potential depends on the lithium ion activity that is higher in the ISE particles by more than one order of magnitude.[22] Due to such high differences, the transfer across the interface is hindered. Another factor for the observed high interface resistance is the formation of a resistive solid polymer electrolyte interphase (SPEI) upon decomposition of the polymer.[39] For these reasons, the lithium ion transport in the HSEs investigated in this study only takes place via the polymer matrix. In order to investigate the influence of the interface resistance on the ionic conductivity of the HSEs, we applied a simple series brick layer model (SBLM). It models the ionic conductivity of a two-phase composite, taking the ionic conductivities of the single phases as well as the interface resistance between the two phases into account. The embedded particles are modeled as cubes with an edge length equivalent to the particle size of the powder particles. Details can be found in Figure A3.6. The results of the SBLM at a temperature of 70 °C for the three samples LA-LALZO, LA-LLZTO, and HA-LLZTO are presented in Figure A3.7, using the ionic conductivities from the pure PSE and sintered LLZO pellet, the particle sizes from Table 3.3.1 and the interface resistances $R_{LLZO|PEO}$ from Table 3.3.4.

In all cases, the modeled ionic conductivities describe well the observed decrease in ionic conductivity of the HSE, confirming that the LLZO|PEO:LiTFSI interface resistances are a barrier for the ion transport through the LLZO particles. The filler only lead to a decrease of the effective cross-sectional area of the conductive polymer matrix. Moreover, we evaluated a lower limit of the interface resistance for achieving an increase in ionic conductivity compared to the pure PSE.

According to our results, it must be lower than 0.05 $\Omega\,cm^2$ in order to be enhance the ionic conductivity of the HSE. This emphasizes that a low interface resistance is extremely important to achieve a contribution of ionic conductivity from the LLZO particles. Interestingly, the modeled ionic conductivities match well with the measured conductivities of the Al_2O_3-containing HSEs, but not with the LLZO-containing HSEs, as the measured ionic conductivities of the latter are below the modeled ionic conductivities. This indicates that the SBLM apparently does not account for the behavior of LLZO particles embedded in the polymer matrix, e.g., formation of interphases are not considered in the SBLM. Moreover, it does not account for changes in the lithium ion transference number (about 0.5 in PSEs vs. close to unity in ISEs) and possible local fluctuations in the PSE upon incorporation of LLZO particles.

In summary, the HSEs all show decreasing ionic conductivities compared with the pure PSE with increasing LLZO volume fraction, caused by the high LLZO|PEO:LiTFSI interface resistance. This is similar for all the LLZO variants used, indicating that the observed slight differences in compatibility with the PEO matrix (determined by the sedimentation analysis) do not have an influence on the electrochemical performance of the HSE. Therefore, we investigated different surface modification approaches in order to significantly increase the compatibility of the LLZO with the polymer matrix.

3.3.3.5 Characterization of HSEs containing surface-modified LLZO

Two different approaches of surface modification were applied to LA-LALZO powders to increase the compatibility with the polymer matrix and thus, to lower the LLZO|PEO:LiTFSI interface resistance achieving enhancement in ionic conductivity. The first approach includes wet milling in PEO-analogous solvents, i.e., ethylene glycol monomethyl ether (EGMME) and ethylene glycol dimethyl ether (EGDME). In analogy to other examples[53,54], the LLZO surface is activated due to the high-energy input during milling, promoting the grafting/adsorption of solvent molecules at the particle surface via van-der-Waals or even covalent chemical bonding. The samples are designated as “milled EGMME” and “milled EGDME”. The second approach uses surface activation via annealing in reducing (H_2/N_2), inert (N_2), and oxidizing (O_2) atmosphere at a temperature of 700 °C, which is well below the sintering temperature of LLZO. The reducing or oxidizing conditions can promote the formation or reduction of oxygen vacancies, respectively[55], which can influence the lithium ion transport pathway at the LLZO|PEO: LiTFSI interface. Annealing in inert atmosphere can help to reduce residual contaminations at the LLZO surface, e.g., lithium carbonate due to reaction of LLZO with water and carbon dioxide from ambient air.[20] The samples are labeled as “annealed H_2/N_2”, “annealed N_2”, and “annealed O_2”.

To check for structural changes upon surface modification, XRD was performed on the five samples (Figure A3.8). The patterns of all samples are not changed compared with the XRD pattern of the

pristine LA-LALZO powder (Figure A3.2) and match well with cubic LLZO reference. Solely the "milled EGDME" sample shows peak broadening, which is probably due to the reduction of crystallite sizes upon milling. The particle sizes, i.e., *D50* values of the surface-modified powders are in the same range or slightly higher than the *D50* value of the pristine LA-LALZO powder (see Table A3.4), which is of high importance for comparability.

Figure 3.3.6A demonstrates the results of the chemical compatibility test via sedimentation analysis of the surface-modified powders together with the pristine LA-LALZO powder as reference. The sedimentation times, i.e., compatibility with the PEO matrix of the "milled EGMME" and "milled EGDME" powders have approximately doubled compared with the pristine LA-LALZO powder. This clearly indicates that the surface modification by grafting PEO-analogous solvent molecules on the LA-LALZO surface was successful, strongly enhancing the compatibility with the PEO matrix. Contrary to this, the annealed powders all exhibit lower sedimentation times by a factor of 0.5 for the "annealed H_2/N_2" sample, 0.7 for "annealed N_2", and 0.4 for "annealed O_2". This implies that the annealing (and hypothesized formation/reduction of oxygen vacancies, and removal of lithium carbonate potentially present at the surface) does not improve the chemical compatibility with the PEO matrix, but the opposite.

EIS was performed on the HSEs containing the surface-modified samples in order to study the influence of the significantly altered compatibility with the PEO matrix on the LLZO|PEO:LiTFSI interface resistance and the ion transport pathway in the HSEs. Figure 3.3.6B shows the corresponding EIS results of the HSEs with the powders milled in PEO-analogous solvents and Figure 3.3.6C those with the annealed powders in different atmospheres, both in dependence of the filler content at a temperature of 70 °C. The values of the HSE including the pristine LA-LALZO powder as well as the pure PSE PEO:LiTFSI and the Al_2O_3-containing HSEs are given as a reference in both graphs.

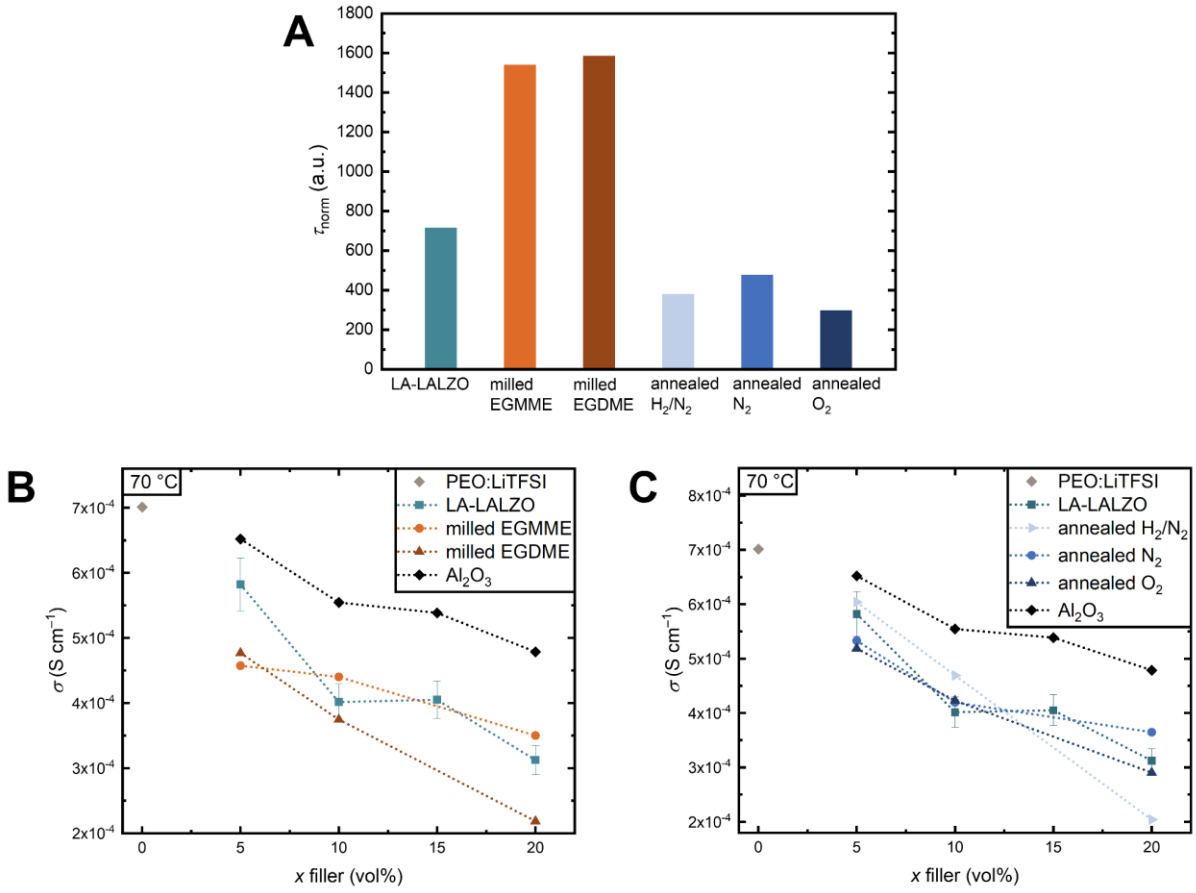

Figure 3.3.6. (A) Normalized sedimentation times of the surface-modified LA-LALZO powders in EGDME determined with the help of an analytical centrifuge. They were modified either by milling in PEO-analogous solvents (ethylene glycol monomethyl ether (EGMME) and ethylene glycol dimethyl ether (EGDME)), or by annealing in reducing (H_2/N_2), inert (N_2), and oxidizing (O_2) atmosphere. The pristine LA-LALZO powder is shown as a reference. (B) Ionic conductivities of the HSEs LA-LALZO*x*/PEO:LiTFSI and the HSEs containing the LA-LALZO powders milled in PEO-analogous solvents (milled EGMME and milled EGDME) in dependence of the volume fraction *x* of the LLZO filler at 70 °C. (C) Ionic conductivities of the HSEs LA-LALZO*x*/PEO:LiTFSI and the HSEs containing the LA-LALZO powders annealed in reducing (H_2/N_2), inert (N_2), and oxidizing (O_2) atmosphere in dependence of the volume fraction *x* of the LLZO filler at 70 °C. In (B) and (C), the ionic conductivities of the pure PSE PEO:LiTFSI (filler content x = 0 vol%) and the HSE containing the passive filler Al_2O_3 (Al_2O_3*x*/PEO:LiTFSI) are given as reference. Moreover, the experimental error of 7% is given only for one sample each for reasons of clarity.

The ionic conductivities of the surface-modified samples were extracted from the corresponding Nyquist plots (Figure A3.9), which all exhibit one semicircle attributed to the bulk ionic conductivity of the HSE. The ionic conductivities are all well below the references PEO:LiTFSI and Al_2O_3-containing HSEs, indicating no contribution of the surface-modified LA-LALZO particles to the ion transport, neither by interface and/or interphase processes or by direct contribution through the LA-LALZO particle itself, probably due to high LLZO|PEO:LiTFSI interface resistances. Similar to the HSE with the pristine LA-LALZO particles embedded, the ionic conductivities of all samples decrease with increasing filler content, which further confirms that the ion transport solely takes place via the polymer matrix. Only slight differences between the surface-modified samples can be

observed, as most of the values are within the range of the experimental error. Overall, the results are similar to those of the unmodified, pristine LLZO powders. In summary, the surface modifications and the related altered compatibilities with the PEO matrix do not positively affect the ionic conductivity of the HSEs and the LLZO|PEO:LiTFSI interface resistance. Presumably, there are other factors more strongly determining the LLZO|PEO:LiTFSI interface resistance besides the sole compatibility such as the high difference in lithium ion chemical potential in the two phases, hindering the transfer across the interface. Methods to equalize this difference can potentially help to lower the interface resistance, e.g., by etching of the LLZO surface (lowering lithium ion concentration in the ISE) or increasing the lithium ion concentration in the polymer matrix.

3.3.4 Conclusions

In this work, the correlation between the ionic conductivities of hybrid solid electrolytes (HSEs) and the phase compatibility of the components, i.e., glass-ceramic garnet-type fillers LLZO and the PEO:LiTFSI polymer matrix was investigated in detail. The chemical compatibility quantified by two solvent-based methods altered slightly upon variation of LLZO chemistry (Al-doped < Ta-doped < Ta-doped LLZO with high content of amorphous phase), but surface modification, i.e., milling in solvents analogous to the PEO monomer, was found to increase compatibitility significantly due to solvent molecules grafted at the particle surface. However, in the case of all of the investigated powders, the ionic conductivities of HSEs prepared thereof were lower compared with the references, i.e., pure polymer electrolyte as well as HSEs containing the passive filler Al_2O_3. Ionic conductivities were also found to decrease with increasing LLZO content, indicating that the LLZO particles do not contribute to the ion transport but instead decrease the effective cross-sectional area of the polymer electrolyte. The LLZO|PEO:LiTFSI interface resistances of all variants (0.3–0.6 kΩ cm^2 at 20 °C, activation energies ~0,8 eV) confirmed that the ion transfer across the interface is hindered. Modeling of the data with a simple brick layer model was in accordance with the observed results. In summary, the enhanced LLZO/PEO compatibility observed in this study does not have a positive effect on lowering the interface resistance, disproving the hypothesis of this study. However, it emphasized the importance of understanding ceramic/polymer interfaces for the design of HSEs, which are a very attractive solution approach in future solid-state battery applications, especially due to their mechanical flexibility.

Associated Content

Supporting information

Additional details on experimental setups, data of pristine powder characterization, detailed analysis of Nyquist plots including capacitances of selected HSE samples, key parameters of other PEO/garnet systems from literature, schematics and analysis of the used brick layer modeling, powder characterization of powders with modified surfaces and Nyquist plot analysis of HSE made thereof.

Author information

Corresponding Authors

*E-mail: juergen.janek@phys.chemie.uni-giessen.de

*E-mail:: andreas.roters@schott.com

ORCID

Nina Hoinkis: 0000-0003-3517-3174

Felix H. Richter: 0000-0002-6587-7757

Jürgen Janek: 0000-0002-9221-4756

Notes

The authors declare no competing financial interest.

3.3.5 References

(1) Janek, J.; Zeier, W. G. A Solid Future for Battery Development. *Nat. Energy* **2016**, *1*, 16141.

(2) Schnell, J.; Günther, T.; Knoche, T.; Vieider, C.; Köhler, L.; Just, A.; Keller, M.; Passerini, S.; Reinhart, G. All-Solid-State Lithium-Ion and Lithium Metal Batteries – Paving the Way to Large-Scale Production. *J. Power Sources* **2018**, *382*, 160–175.

(3) Albertus, P.; Babinec, S.; Litzelman, S.; Newman, A. Status and Challenges in Enabling the Lithium Metal Electrode for High-Energy and Low-Cost Rechargeable Batteries. *Nat. Energy* **2017**, *3*, 16–21.

(4) Boaretto, N.; Garbayo, I.; Valiyaveettil-SobhanRaj, S.; Quintela, A.; Li, C.; Casas-Cabanas, M.; Aguesse, F. Lithium Solid-State Batteries: State-of-the-art and Challenges for Materials, Interfaces and Processing. *J. Power Sources* **2021**, *502*, 229919.

(5) Yoshimatsu, I.; Hirai, T.; Yamaki, J. Lithium Electrode Morphology during Cycling in Lithium Cells. *J. Electrochem. Soc.* **1988**, *135*, 2422–2427.

(6) Chen, R.; Li, Q.; Yu, X.; Chen, L.; Li, H. Approaching Practically Accessible Solid-State Batteries: Stability Issues Related to Solid Electrolytes and Interfaces. *Chem. Rev.* **2020**, *120*, 6820–6877.

(7) Liu, Q.; Geng, Z.; Han, C.; Fu, Y.; Li, S.; He, Y.; Kang, F.; Li, B. Challenges and Perspectives of Garnet Solid Electrolytes for All Solid-State Lithium Batteries. *J. Power Sources* **2018**, *389*, 120–134.

(8) Leng, J.; Wang, H.; Liang, H.; Xiao, Z.; Wang, S.; Zhang, Z.; Tang, Z. Storage of Garnet Solid Electrolytes: Insights into Air Stability and Surface Chemistry. *ACS Appl. Energy Mater.* **2022**, *5*, 5108–5116.

(9) Wang, C.; Fu, K.; Kammampata, S. P.; McOwen, D. W.; Samson, A. J.; Zhang, L.; Hitz, G. T.; Nolan, A. M.; Wachsman, E. D.; Mo, Y.*; et al.* Garnet-Type Solid-State Electrolytes: Materials, Interfaces, and Batteries. *Chem. Rev.* **2020**, *120*, 4257–4300.

(10) Hatzell, K. B.; Chen, X. C.; Cobb, C. L.; Dasgupta, N. P.; Dixit, M. B.; Marbella, L. E.; McDowell, M. T.; Mukherjee, P. P.; Verma, A.; Viswanathan, V.*; et al.* Challenges in Lithium Metal Anodes for Solid-State Batteries. *ACS Energy Lett.* **2020**, *5*, 922–934.

(11) Yao, P.; Yu, H.; Ding, Z.; Liu, Y.; Lu, J.; Lavorgna, M.; Wu, J.; Liu, X. Review on Polymer-Based Composite Electrolytes for Lithium Batteries. *Front. Chem.* **2019**, *7*, 522.

(12) Ding, P.; Lin, Z.; Guo, X.; Wu, L.; Wang, Y.; Guo, H.; Li, L.; Yu, H. Polymer Electrolytes and Interfaces in Solid-State Lithium Metal Batteries. *Mater. Today* **2021**, *51*, 449–474.

(13) Li, S.; Zhang, S.-Q.; Shen, L.; Liu, Q.; Ma, J.-B.; Lv, W.; He, Y.; Yang, Q.-H. Progress and Perspective of Ceramic/Polymer Composite Solid Electrolytes for Lithium Batteries. *Adv. Sci.* **2020**, *7*, 1903088.

(14) Sen, S.; Trevisanello, E.; Niemöller, E.; Shi, B.-X.; Simon, F. J.; Richter, F. H. The Role of Polymers in Lithium Solid-State Batteries with Inorganic Solid Electrolytes. *J. Mater. Chem. A* **2021**, *9*, 18701–18732.

(15) Li, L.; Deng, Y.; Chen, G. Status and Prospect of Garnet/Polymer Solid Composite Electrolytes for All-Solid-State Lithium Batteries. *J. Energy Chem.* **2020**, *50*, 154–177.

(16) Zagórski, J.; Del López Amo, J.; Cordill, M. J.; Aguesse, F.; Buannic, L.; Llordés, A. Garnet-Polymer Composite Electrolytes: New Insights on Local Li-Ion Dynamics and Electrodeposition Stability with Li Metal Anodes. *ACS Appl. Energy Mater.* **2019**, 1734–1746.

(17) Zhang, J.; Zhao, N.; Zhang, M.; Li, Y.; Chu, P. K.; Guo, X.; Di, Z.; Wang, X.; Li, H. Flexible and Ion-Conducting Membrane Electrolytes for Solid-State Lithium Batteries: Dispersion of Garnet Nanoparticles in Insulating Polyethylene Oxide. *Nano Energy* **2016**, *28*, 447–454.

(18) Wang, C.; Yang, Y.; Liu, X.; Zhong, H.; Xu, H.; Xu, Z.; Shao, H.; Ding, F. Suppression of Lithium Dendrite Formation by Using LAGP-PEO (LiTFSI) Composite Electrolyte and Lithium Metal Anode Modified by PEO (LiTFSI) in All-Solid-State Lithium Batteries. *ACS Appl. Mater. Interfaces* **2017**, 13694–13702.

(19) Chen, F.; Yang, D.; Zha, W.; Zhu, B.; Zhang, Y.; Li, J.; Gu, Y.; Shen, Q.; Zhang, L.; Sadoway, D. R. Solid Polymer Electrolytes Incorporating Cubic $Li_7La_3Zr_2O_{12}$ for All-Solid-State Lithium Rechargeable Batteries. *Electrochim. Acta* **2017**, *258*, 1106–1114.

(20) Keller, M.; Appetecchi, G. B.; Kim, G.-T.; Sharova, V.; Schneider, M.; Schuhmacher, J.; Roters, A.; Passerini, S. Electrochemical Performance of a Solvent-Free Hybrid Ceramic-Polymer Electrolyte Based on $Li_7La_3Zr_2O_{12}$ in $P(EO)_{15}LiTFSI$. *J. Power Sources* **2017**, *353*, 287–297.

(21) Huo, H.; Chen, Y.; Luo, J.; Yang, X.; Guo, X.; Sun, X. Rational Design of Hierarchical "Ceramic-in-Polymer" and "Polymer-in-Ceramic" Electrolytes for Dendrite-Free Solid-State Batteries. *Adv. Energy Mater.* **2019**, *9*, 1804004.

(22) Keller, M.; Varzi, A.; Passerini, S. Hybrid Electrolytes for Lithium Metal Batteries. *J. Power Sources* **2018**, *392*, 206–225.

(23) Cheng, S. H.-S.; He, K.-Q.; Liu, Y.; Zha, J.-W.; Kamruzzaman, M.; Ma, R. L.-W.; Dang, Z.-M.; Li, R. K.; Chung, C. Y. Electrochemical Performance of All-Solid-State Lithium Batteries Using Inorganic Lithium Garnets Particulate Reinforced PEO/$LiClO_4$ Electrolyte. *Electrochim. Acta* **2017**, *253*, 430–438.

(24) Zhang, Z.; Huang, Y.; Gao, H.; Huang, J.; Li, C.; Liu, P. An All-Solid-State Lithium Battery Using the $Li_7La_3Zr_2O_{12}$ and $Li_{6.7}La_3Zr_{1.7}Ta_{0.3}O_{12}$ Ceramic Enhanced Polyethylene Oxide Electrolytes with Superior Electrochemical Performance. *Ceram. Int.* **2020**, *46*, 11397–11405.

(25) Zhuang, H.; Ma, W.; Xie, J.; Liu, X.; Li, B.; Jiang, Y.; Huang, S.; Chen, Z.; Zhao, B. Solvent-Free Synthesis of PEO/Garnet Composite Electrolyte for High-Safety All-Solid-State Lithium Batteries. *J. Alloys Compd.* **2021**, *860*, 157915.

(26) Buvana, P.; Vishista, K.; Shanmukaraj, D.; Murugan, R. Lithium Garnet Oxide Dispersed Polymer Composite Membrane for Rechargeable Lithium Batteries. *Ionics* **2017**, *23*, 541–548.
(27) Langer, F.; Bardenhagen, I.; Glenneberg, J.; Kun, R. Microstructure and Temperature Dependent Lithium Ion Transport of Ceramic–Polymer Composite Electrolyte for Solid-State Lithium Ion Batteries Based on Garnet-Type $Li_7La_3Zr_2O_{12}$. *Solid State Ionics* **2016**, *291*, 8–13.
(28) Waidha, A. I.; Ferber, T.; Donzelli, M.; Hosseinpourkahvaz, N.; Vanita, V.; Dirnberger, K.; Ludwigs, S.; Hausbrand, R.; Jaegermann, W.; Clemens, O. Compositional Dependence of Li-Ion Conductivity in Garnet-Rich Composite Electrolytes for All-Solid-State Lithium-Ion Batteries-Toward Understanding the Drawbacks of Ceramic-Rich Composites. *ACS Appl. Mater. Interfaces* **2021**, *13*, 31111–31128.
(29) Xi, J.; Qiu, X.; Ma, X.; Cui, M.; Yang, J.; Tang, X.; Zhu, W.; Chen, L. Composite Polymer Electrolyte Doped with Mesoporous Silica SBA-15 for Lithium Polymer Battery. *Solid State Ionics* **2005**, *176*, 1249–1260.
(30) Croce, F.; Appetecchi, G. B.; Persi, L.; Scrosati, B. Nanocomposite Polymer Electrolytes for Lithium Batteries. *Nature* **1998**, *394*, 456–458.
(31) Zheng, J.; Tang, M.; Hu, Y.-Y. Lithium Ion Pathway within $Li_7La_3Zr_2O_{12}$-Polyethylene Oxide Composite Electrolytes. *Angew. Chem.* **2016**, *128*, 12726–12730.
(32) Fu, K. K.; Gong, Y.; Dai, J.; Gong, A.; Han, X.; Yao, Y.; Wang, C.; Wang, Y.; Chen, Y.; Yan, C.*; et al.* Flexible, Solid-State, Ion-Conducting Membrane with 3D Garnet Nanofiber Networks for Lithium Batteries. *Proceedings of the National Academy of Sciences of the United States of America* **2016**, *113*, 7094–7099.
(33) Yang, T.; Zheng, J.; Cheng, Q.; Hu, Y.-Y.; Chan, C. K. Composite Polymer Electrolytes with $Li_7La_3Zr_2O_{12}$ Garnet-Type Nanowires as Ceramic Fillers: Mechanism of Conductivity Enhancement and Role of Doping and Morphology. *ACS Appl. Mater. Interfaces* **2017**, *9*, 21773–21780.
(34) Grissa, R.; Payandeh, S.; Heinz, M.; Battaglia, C. Impact of Protonation on the Electrochemical Performance of $Li_7La_3Zr_2O_{12}$ Garnets. *ACS Appl. Mater. Interfaces* **2021**, *13*, 14700–14709.
(35) Brugge, R. H.; Hekselman, A. K. O.; Cavallaro, A.; Pesci, F. M.; Chater, R. J.; Kilner, J. A.; Aguadero, A. Garnet Electrolytes for Solid State Batteries: Visualization of Moisture-Induced Chemical Degradation and Revealing Its Impact on the Li-Ion Dynamics. *Chem. Mater.* **2018**, *30*, 3704–3713.
(36) Langer, F.; Palagonia, M. S.; Bardenhagen, I.; Glenneberg, J.; La Mantia, F.; Kun, R. Impedance Spectroscopy Analysis of the Lithium Ion Transport through the $Li_7La_3Zr_2O_{12}$/$P(EO)_{20}Li$ Interface. *J. Electrochem. Soc.* **2017**, *164*, A2298-A2303.
(37) Gupta, A.; Sakamoto, J. Controlling Ionic Transport through the PEO-LiTFSI/LLZTO Interface. *Electrochem. Soc. Interface* **2019**, *28*, 63–69.

(38) Brogioli, D.; Langer, F.; Kun, R.; La Mantia, F. Space-Charge Effects at the $Li_7La_3Zr_2O_{12}$/Poly(Ethylene Oxide) Interface. *ACS Appl. Mater. Interfaces* **2019**, *11*, 11999–12007.

(39) Trevisanello, E.; Ates, T.; Passerini, S.; Richter, F. H.; Janek, J. Influence of the Polymer Structure and its Crystallization on the Interface Resistance in Polymer-LATP and Polymer-LLZO Hybrid Electrolytes. *J. Electrochem. Soc.* **2022**, *169*, 110547.

(40) Schneider, M.; Hochrein, O.; Wolfgang, S.; Kunze, M. Ionenleitende Glaskeramik mit Granatartiger Kristallstruktur. DE102014100684A1, **2015**.

(41) Steven Abbott. *HSPiP Software*:*Hansen Solubility Parameters in Practice*. https:// www.hansen-solubility.com/HSPiP/.

(42) D. Lerche, S. Horvat, T. Sobisch. Efficient Instrument Based Determination of the Hansen Solubility Parameters for Talc-Based Pigment Particles by Multisample Analytical Centrifugation: Zero to One Scoring. *Dispersion Letters* **2015**, *6*, 13–18.

(43) Dreezen, G. Nano-Structured Polymer Blends: Phase Structure, Crystallisation Behaviour and Semi-Crystalline Morphology of Phase Separated Binary Blends of Poly(ethylene oxide) and Poly(ether sulphone). *Polymer* **2000**, *41*, 1395–1407.

(44) Simon, F. J.; Hanauer, M.; Henss, A.; Richter, F. H.; Janek, J. Properties of the Interphase Formed between Argyrodite-Type Li_6PS_5Cl and Polymer-Based PEO_{10}:LiTFSI. *ACS Appl. Mater. Interfaces* **2019**, *11*, 42186–42196.

(45) Hansen, C. M. *Hansen solubility parameters*:*A user's handbook*, 2nd ed.; CRC Press. **2007**.

(46) Edman, L. Ion Association and Ion Solvation Effects at the Crystalline−Amorphous Phase Transition in PEO−LiTFSI. *J. Phys. Chem. B* **2000**, *104*, 7254–7258.

(47) Li, Z.; Huang, H.-M.; Zhu, J.-K.; Wu, J.-F.; Yang, H.; Wei, L.; Guo, X. Ionic Conduction in Composite Polymer Electrolytes: Case of PEO:Ga-LLZO Composites. *ACS Appl. Mater. Interfaces* **2019**, *11*, 784–791.

(48) Irvine, J. T. S.; Sinclair, D. C.; West, A. R. Electroceramics: Characterization by Impedance Spectroscopy. *Adv. Mater.* **1990**, *2*, 132–138.

(49) Krauskopf, T.; Hartmann, H.; G. Zeier, W.; Janek, J. Toward a Fundamental Understanding of the Lithium Metal Anode in Solid-State Batteries - An Electrochemo-Mechanical Study on the Garnet-Type Solid Electrolyte $Li_{6.25}Al_{0.25}La_3Zr_2O_{12}$. *ACS Appl. Mater. Interfaces* **2019**, *11*, 14463–14477.

(50) Huang, Z.; Tong, R.; Zhang, J.; Chen, L.; Wang, C.-A. Blending Poly(ethylene oxide) and $Li_{6.4}La_3Zr_{1.4}Ta_{0.6}O_{12}$ by Haake Rheomixer without Any Solvent: A Low-Cost Manufacture Method for Mass Production of Composite Polymer Electrolyte. *J. Power Sources* **2020**, *451*, 227797.

(51) Sagane, F.; Abe, T.; Iriyama, Y.; Ogumi, Z. Li^+ and Na^+ Transfer Through Interfaces Between Inorganic Solid Electrolytes and Polymer or Liquid Electrolytes. *J. Power Sources* **2005**, *146*, 749–752.

(52) Abe, T.; Sagane, F.; Ohtsuka, M.; Iriyama, Y.; Ogumi, Z. Lithium-Ion Transfer at the Interface Between Lithium-Ion Conductive Ceramic Electrolyte and Liquid Electrolyte-A Key to Enhancing the Rate Capability of Lithium-Ion Batteries. *J. Electrochem. Soc.* **2005**, *152*, A2151.
(53) Liu, W.; Xie, Z.; Yang, X.; Wu, Y.; Jia, C.; Bo, T.; Wang, L. Surface Modification Mechanism of Stearic Acid to Zirconia Powders Induced by Ball Milling for Water-Based Injection Molding. *Journal of the American Ceramic Society* **2011**, *94*, 1327–1330.
(54) Kim, H.; Lee, J. E.; Jo, S.-M.; Wooh, S. Universal Large-Scale and Solvent-Free Surface Modification of Inorganic Particles via Facile Mechanical Grinding. *ACS Sustainable Chem. Eng.* **2022**, *10*, 9679–9686.
(55) Yang, H.; Abdullah, M.; Bright, J.; Hu, W.; Kittilstved, K.; Xu, Y.; Wang, C.; Zhang, X.; Wu, N. Polymer-Ceramic Composite Electrolytes for All-Solid-State Lithium Batteries: Ionic Conductivity and Chemical Interaction Enhanced by Oxygen Vacancy in Ceramic Nanofibers. *J. Power Sources* **2021**, *495*, 229796.

4 Conclusions and Outlook

This thesis examined the novel class of glass-ceramic LLZO solid electrolyte with a unique amorphous phase manufactured at the SCHOTT AG for the potential application in SSBs. The focus was on the investigation of surface and interface-related properties of such powder particles as well as of components manufactured thereof, e.g., sintered pellets or hybrid electrolyte membranes. These are current obstacles to be overcome regarding their manufacturing, processing and integration into SSBs based on LMA. Accordingly, the investigation of pristine powder surfaces showing specific degradation reactions during storage in different atmospheres were highlighted in publication 1. In addition, the application as an ISE manufactured by sintering of such powders and as polymer-based HSEs manufactured by embedding those into a polymer electrolyte matrix was investigated. In this context, the focus was on the influence of the amorphous phase on the interfacial properties with a LMA and the polymer matrix, respectively. Both approaches are outlined in detail in publication 2 and the manuscript.

One central conclusion that can be drawn from the results and can not be emphasized enough, is that detailed consideration of surface and interface properties is vital for the application of SEs in SSBs. In contrast to conventional liquid electrolytes, that are mainly characterized by their bulk properties, typical powder properties such as morphology, shape, specific surface area, and surface chemistry need to be taken into account. They are crucial for manufacturing and further processing of both ISE and HSE components, their integration into battery cells together with electrode materials considering both the anode and the cathode, as well as for their electrochemical performance. For sintered ISEs, which have high brittleness and hardness compared to the inherently good wetting abilities of liquid electrolytes, sufficient contact at the electrode interfaces and optimized microstructure of the ISE are essential. This applies especially for LMAs, where such interface properties determine the cycling stability. Concerning the application of ISE powders in HSEs, the additional ISE/polymer interface has tremendous influence on the ion transport properties and overall performance of such composites.

Accordingly, the surface properties of glass-ceramic LLZO powders were studied in detail within publication 1. Since the focus was on the elucidation of the degradation mechanism in ambient air, powders with very low amorphous phase content were chosen to prevent side effects and to ensure

the transferability of the results to conventional LLZO materials. By kinetic measurements, the degradation mechanism could be identified as diffusion-limited with the hydration as a prerequisite intermediate step. The reaction rate is found to increase linearly with increasing specific surface area of the powder. From the results, important conclusions for the handling conditions of LLZO powders can be drawn in order to achieve optimum surface properties for further processing. As the degradation, i.e., protonation of LLZO and lithium carbonate formation, took place readily within the first twenty minutes of the experiment for all powders, contact with ambient air should be avoided at any time. This applies especially for nano-scale powders highly demanded for battery applications. Indeed, powders should be processed in moisture-free atmospheres in order to prevent the intermediate hydration step. Dry, CO_2-free as well as or dry room conditions (under which the CO_2 of the conditioned ambient air is still present) are favored. In addition, heat treatment of LLZO powders can help to remove any degradation products.

The interface properties of glass-ceramic LLZO with other battery components were examined regarding two potential applications. On the one hand, the interface between sintered LLZO glass-ceramics (ISE) and a LMA and the related dendrite stability were highlighted. On the other hand, glass-ceramic LLZO powders were embedded in a PSE matrix (HSE) and the corresponding LLZO/PSE interface was investigated. For both applications, the focus was on the influence of the amorphous phase on the interface properties and thus, the amorphous phase content was varied from very low (~0.1 wt%) to high content (~4 wt%). The overall conclusion is that a high volume fraction of amorphous phase is highly beneficial for the application in the case of the sintered ISE when it is combined with a LMA. In sintered bodies, the dendrite stability was found to be enhanced by the amorphous phase, as it fills grain boundaries and pores and thereby mechanically and electrochemically suppresses lithium dendrite formation at the LMA interface. It also prevents cracking of the LLZO material upon lithium plating. In contrast, no positive effect of the amorphous phase on the performance could be proven in the case of PEO-based HSEs into which glass-ceramic LLZO particles with low and high amorphous phase content were incorporated. In both cases, the HSEs exhibited similar electrochemical properties and investigations on the LLZO/PSE interface confirmed such behavior. The ionic conductivities of the HSEs are lower compared with the unfilled PSE indicating no positive influence of the amorphous phase chemistry on the lithium ion transport across the LLZO/PSE interface in the case of PEO-based PSEs.

In summary, this thesis outlines the high importance of surface and interface properties for the implementation of solid electrolytes in SSBs, with respect to the novel class of glass-ceramic LLZO produced at the SCHOTT AG. Besides fundamental insights into its surface degradation mechanism, providing the basis on how to select, handle and process LLZO in future production scenarios, the unique properties of glass-ceramic LLZO at the LMA interface make it a very promising material for the application as sintered ISE. Moreover, the intrinsically contained amorphous phase helps to

achieve high density and high ionic conductivity at lower temperatures and shorter dwelling times compared with conventional syntheses due to liquid phase sintering, enabling its cost-effective processing. Together with the scalability of the manufacturing at the SCHOTT AG, it is well-suited for the large-scale application in future SSBs.

Several ideas evolve from the present thesis that should be considered for future work. They are divided into three distinct subject areas, presented in the following section.

i. Precautions during manufacturing and processing of LLZO

For future large-scale production scenarios of LLZO, its high sensitivity against moisture and the related degradation should be considered carefully. The preparation of LLZO usually is a multi-step process that includes the handling and processing of LLZO powders. Especially upon milling, the powder surfaces are highly reactive. Therefore, all of these steps should take place in dry conditions in an ideal case. Since the surface properties of LLZO are crucial for its performance, methods may be evaluated how to reliably track the condition of the LLZO surface in between processing steps and just before final assembly, which is often neglected in the literature. For example, Raman spectroscopy may be a useful technique as it is fast and easy to implement.

ii. Further development of glass-ceramic LLZO

As sintered glass-ceramic LLZO has shown promising properties for the application with LMAs, several ideas arise how to further enhance its performance. First, the instrinsically contained amorphous phase could be further modified in terms of its electrochemical properties in order to boost its ability to prevent lithium dendrite formation. Several studies on artificial interlayers on LLZO have shown that the ideal interlayer would be highly ionically conducting but electronically insulating. Therefore, further adjustment of the amorphous phase in such direction could be fruitful, e.g., by replacing or combining the present lithium silicate glass with lithium phosphate compounds. Second, the superior microstructure of glass-ceramic LLZO was found to prevent cracking of the sintered body upon lithium plating. Hence, a detailed understanding of the mechanical properties should be the focus of further developments, including elastic, plastic and fracture properties. This may help to further tailor the amorphous phase. As a third idea, the microstructure with the grain boundaries and pores filled with the amorphous phase could be used as a template for a structured 3D LLZO framework with extremely high surface, e.g., by etching of the amorphous phase. This can be beneficial for stable lithium stripping/plating and prolonged cycling stability.

iii. Investigation and modification of the ceramic/polymer interface

For the application of glass-ceramic LLZO powders in HSEs, the LLZO/PSE interface was identified as bottleneck for high performance due to its high interface resistance in the case of PEO-based PSE. This might be different for other PSE systems due to the huge variety of different polymers used and

should therefore be investigated for other PSEs. Such SE/polymer interface effects are often neglected in the literature. Therefore, a profound understanding of the origin of such high interface resistances is vital. For example, surface-sensitive techniques such as ToF-SIMS or X-ray photoelectron spectroscopy should be considered for future investigations, as they can resolve the chemical species at the interface, e.g., due to chemical reaction of the two phases. Furthermore, this may help to develop strategies to lower the interface resistance, for example, by tailored interphase layers.

In conclusion, the results of this thesis prove the high potential of the novel class of glass-ceramic LLZO for the application in SSBs. Especially its amorphous phase arising from the manufacturing via melting route at the SCHOTT AG provide unique properties. Moreover, due to the scalability of the manufacturing process, glass-ceramic LLZO is a very promising candidate for the large-scale application of next-generation batteries with high energy density.

Appendix

A1 Supporting Information of section 3.1

Supporting Information

Particle Size-Dependent Degradation Kinetics of Garnet-Type $Li_{6.5}La_3Zr_{1.5}Ta_{0.5}O_{12}$ Solid Electrolyte Powders in Ambient Air

Nina Hoinkis[†,‡], Jörg Schuhmacher[†], Sebastian Leukel[†], Christoph Loho[†], Andreas Roters[,†], Felix H. Richter[‡], and Jürgen Janek*[,‡]*

[†] SCHOTT AG, Hattenbergstrasse 10, Mainz D-55122, Germany

[‡] Center for Materials Research (ZfM) and Institute of Physical Chemistry, Justus Liebig University, Giessen D-35392, Germany

Corresponding Authors

E-mail: juergen.janek@pc.jlug.de

E-mail: andreas.roters@schott.com

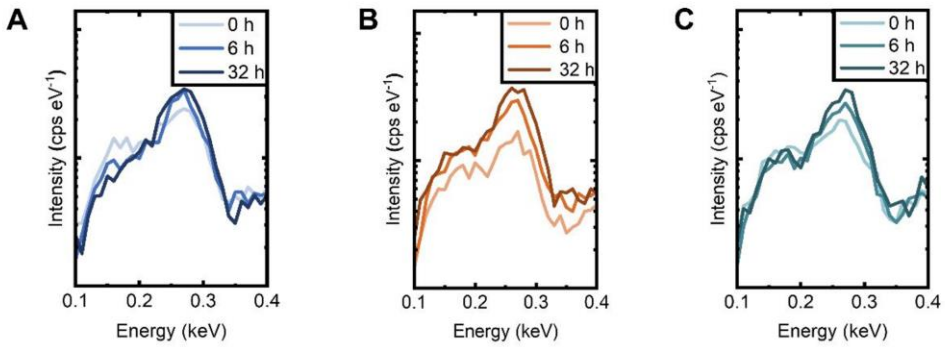

Figure S1. Temporal evolution of carbon peaks in EDX spectra taken from particle agglomerates after 0 h, 6 h and 32 h air exposure. The increment in carbon peak intensity between 0 h and 6 h in relation to the increment between 6 h and 32 h is higher for (A) f-LLZTO than for (B) m-LLZTO than for (C) c-LLZTO. Please note that the carbon signal at t = 0 h is assumed to originate from sample preparation.

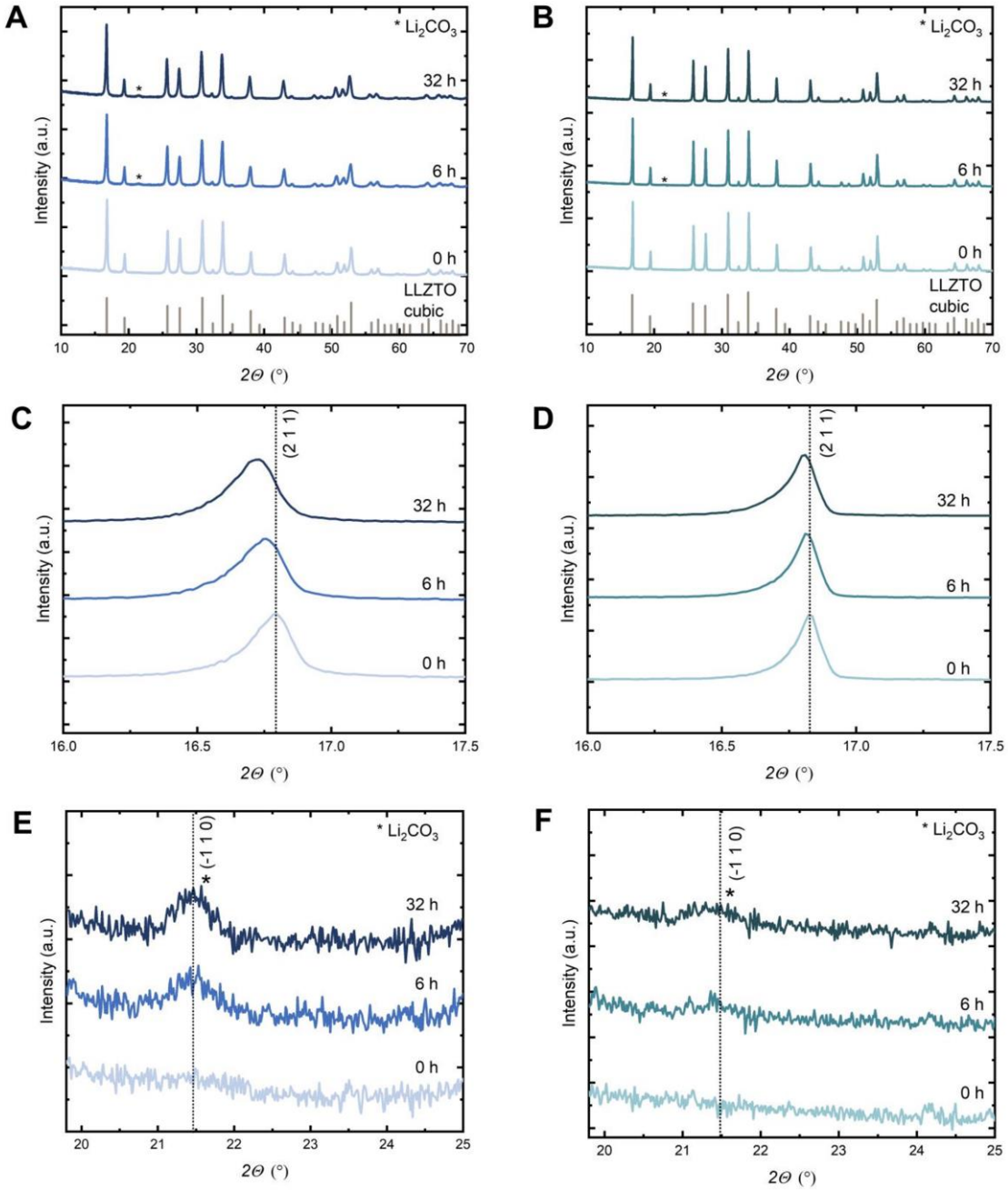

Figure S2. XRD patterns of the powder samples (A) f-LLZTO and (B) c-LLZTO exposed to ambient air for 0 h, 6 h, and 32 h. Magnification of the reflection of the (2 1 1) lattice plane as well as of the Li_2CO_3 reflection of the (–1 1 0) lattice plane for (C), (E) f-LLZTO and (D), (F) c-LLZTO exposed for the same durations.

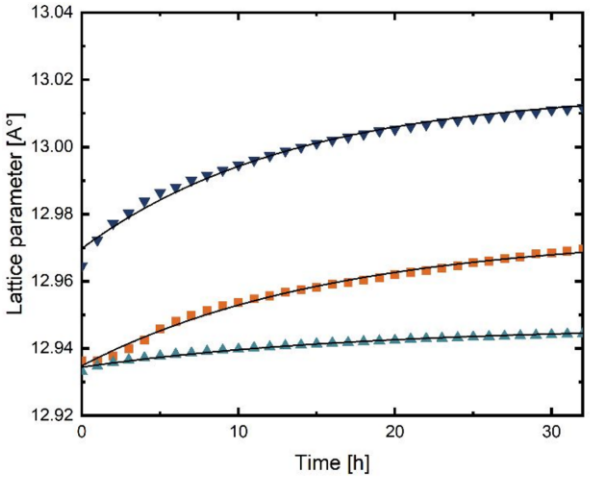

Figure S3. Temporal evolution of the LLZTO lattice parameter in Figure 3C fitted according to the modified Avrami equation (Equation (8)). The fitting parameters can be found in Table S2.

Table S1. Fitting parameters of the fit described in Figure S3.

Sample	a_0	$a_{plateau}$	k_{XRD}	R^2
f-LLZTO	12.97	13.02	0.074	0.99
m-LLZTO	12.93	12.97	0.062	0.99
c-LLZTO	12.93	12.95	0.056	0.99

Table S2. Absolute carbon content of the powder samples f-, m-, and c-LLZTO exposed to different atmospheres for 32 h, determined by IR spectroscopy in a multiphase determinator.

	C content (wt %)			
Sample	**Ambient air**	**Dry air**	**Dry air + CO_2**	**Dry air + H_2O**
f-LLZTO	0.37	–	–	–
m-LLZTO	0.23	0.05	0.19	0.06
c-LLZTO	0.14	–	–	–

Table S3. Absolute water content of the powder samples f-, m-, and c-LLZTO exposed to different atmospheres for 32 h, determined by IR spectroscopy in a multiphase determinator.

	H_2O content (wt %)			
Sample	**Ambient air**	**Dry air**	**Dry air + CO_2**	**Dry air + H_2O**
f-LLZTO	10.26	–	–	–
m-LLZTO	8.65	0.66	0.75	10.39
c-LLZTO	3.67	–	–	–

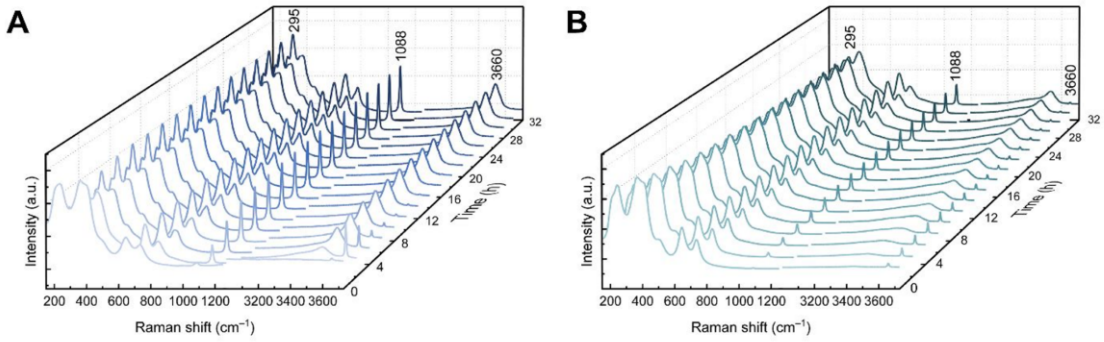

Figure S4. Averaged Raman mapping spectra of the powder samples (A) f-LLZTO, and (B) c-LLZTO exposed to ambient air in dependence of time.

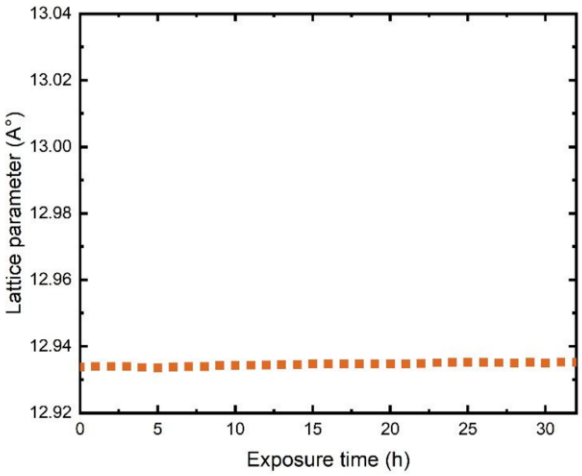

Figure S5. Temporal evolution of the LLZTO lattice parameter of the powder sample m-LLZTO exposed to dry atmosphere, determined via Rietveld refinement of the XRD data.

A2 Supporting Information of section 3.2

Supporting Information

Amorphous phase induced lithium dendrite suppression in glass-ceramic garnet-type solid electrolyte

Nina Hoinkis[†,‡], Jörg Schuhmacher[†], Till Fuchs[‡], Sebastian Leukel[†], Christoph Loho[†], Andreas Roters[,†], Felix H. Richter[‡], and Jürgen Janek*[,‡]*

[†] SCHOTT AG, Hattenbergstrasse 10, Mainz D-55122, Germany

[‡] Center for Materials Research (ZfM) and Institute of Physical Chemistry, Justus Liebig University, Giessen D-35392, Germany

Corresponding Authors

E-mail: juergen.janek@pc.jlug.de

E-mail: andreas.roters@schott.com

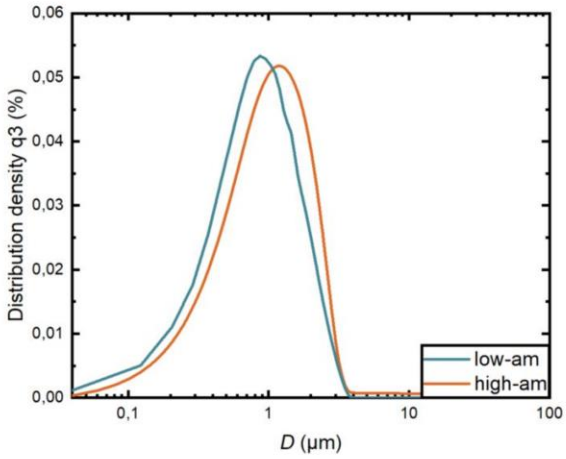

Figure S1. Particle size distribution measured by static light scattering of initial powders low-am and high-am.

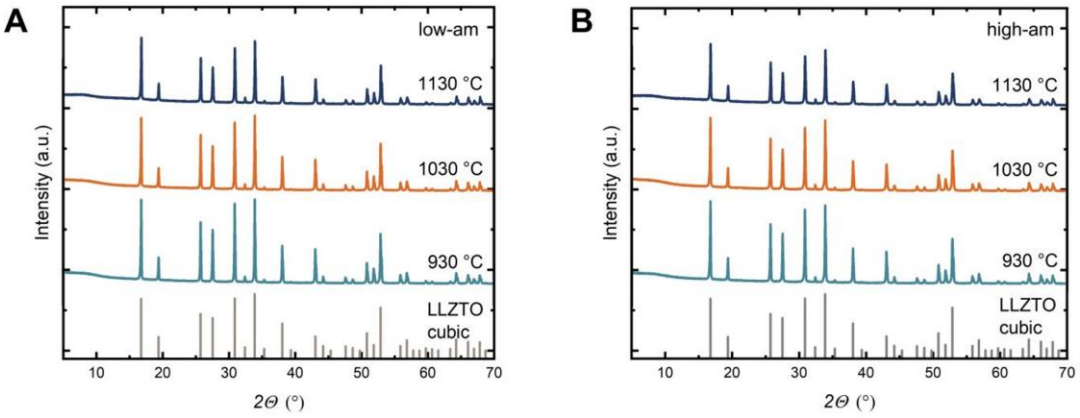

Figure S2. XRD patterns of the samples (A) low-am and (B) high-am sintered at different sintering temperatures (930 °C, 1030 °C, and 1130 °C) for a constant sintering time of 0.5 h.

Table S1. Content of amorphous phase and SiO_2 of the sintered pellets low-am and high-am synthesized at different sintering temperatures.

Sample	Sintering temperature (°C)	Sintering time (h)	Amorphous phase (wt%)	SiO_2 (wt%)
low-am	1130	0.5	0.1*	0.04
	1130	14.5	0.0*	0.04
	1030	0.5	0.4*	0.03

	1130	0.5	3.0	0.6
high-am	1130	14.5	1.4	0.5
	1030	0.5	3.7	0.7

* Due to the experimental error of chemical analysis, values close to the detection limit have higher uncertainty.

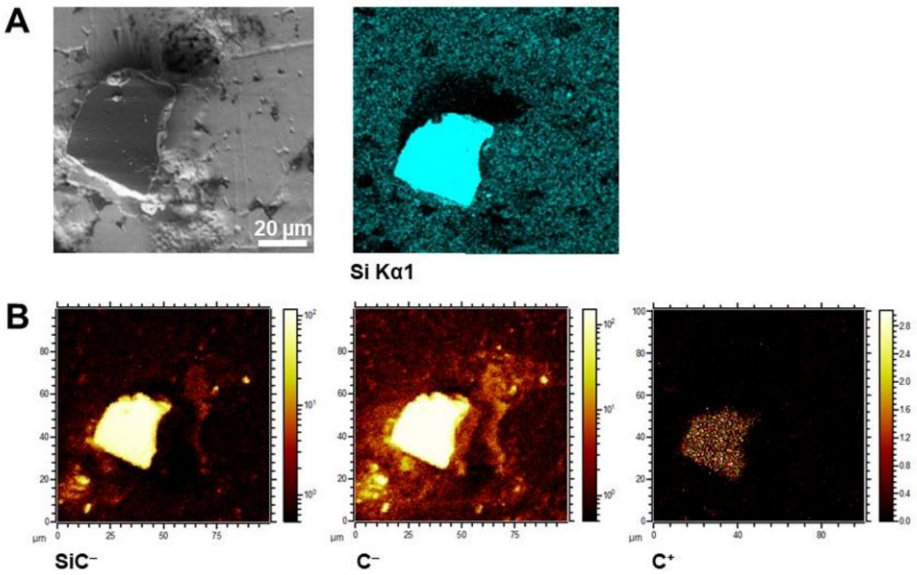

Figure S3. For the complementary SEM/EDX and ToF-SIMS analysis a SiC particle from the polishing paper was used as a landmark. (A) Top-view SEM image and corresponding EDX elemental maps of the sample high-am sintered at a sintering temperature of 1130 °C for 0.5 h. (B) ToF-SIMS analysis at the same position and selected positive and negative secondary ion maps.

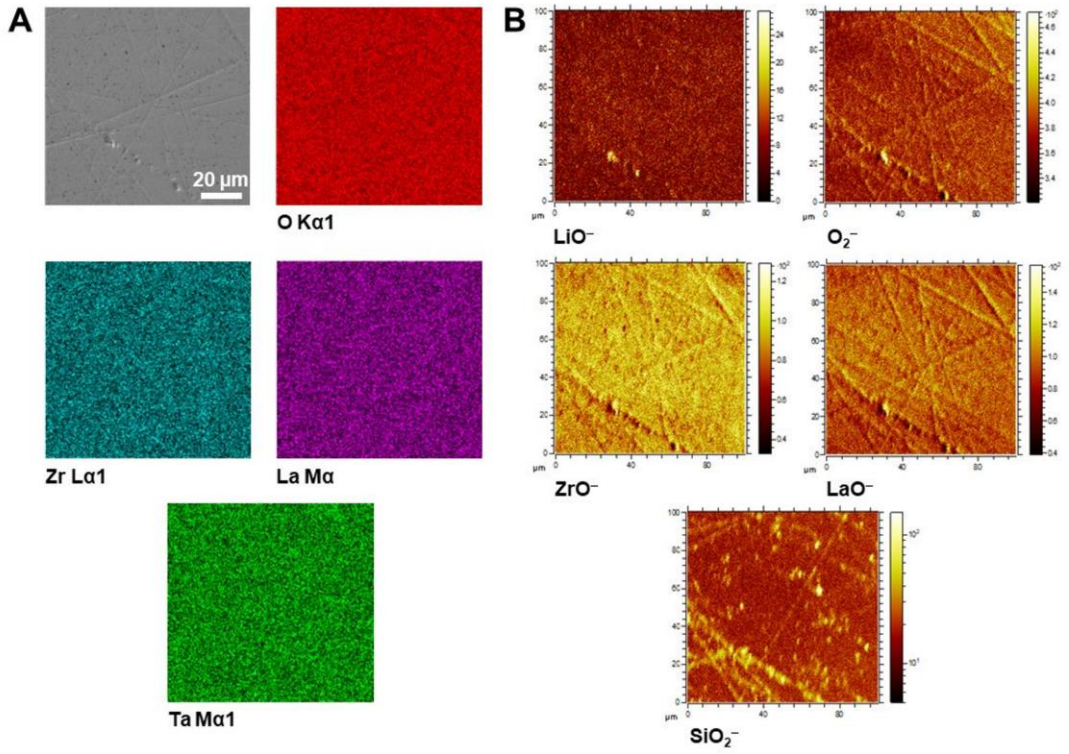

Figure S4. (A) Top-view SEM image and corresponding EDX elemental maps of the sample low-am sintered at a sintering temperature of 1130 °C for 0.5 h. (B) ToF-SIMS analysis at the same position and selected negative secondary ion maps. The scratches are from a diamond scriber used as a landmark.

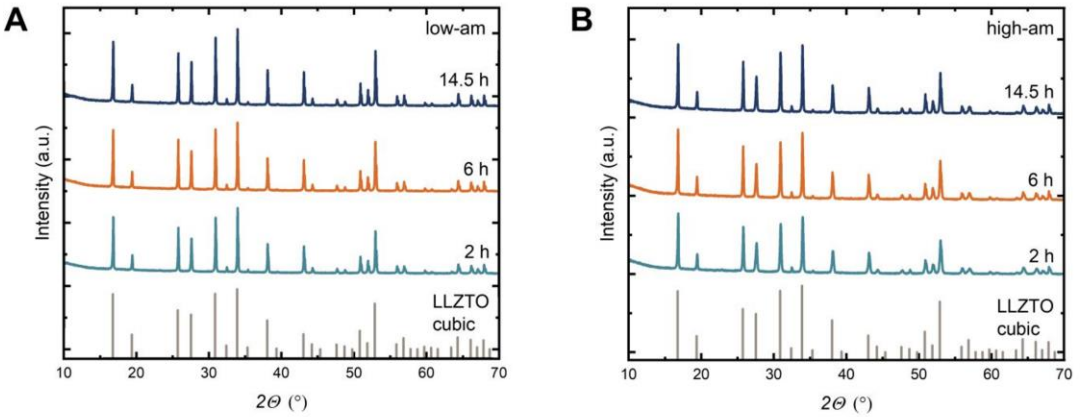

Figure S5. XRD patterns of the samples (A) low-am and (B) high-am sintered for different sintering times (2 h, 6 h and 14.5 h) at constant sintering temperature of 1130 °C.

Table S2. Detailed impedance analysis of the samples low-am and high-am sintered at different sintering temperature (at constant sintering time of 0.5 h) including the total ionic conductivity σ_t, the bulk conductivity σ_b, and grain boundary conductivity σ_{gb} at room temperature. The activation energies of bulk and grain boundary process $E_{a,b}$ and $E_{a,gb}$ and the capacity of the grain boundary C_{gb} are given as well.

Sample	Sintering temp. (°C)	σ_t (mS cm^{-1})	σ_b * (mS cm^{-1})	$E_{a,b}$ (eV)	σ_{gb} (mS cm^{-1})	C_{gb} (F)✦	$E_{a,gb}$ (eV)
low-am	1130	0.97	0.99	0.43	0.023	1.2E-08	0.45
	1030	0.62	0.77	-	0.013	7.7E-09	-
	930	0.006	0.01	-	0.001	1.2E-09	-
high-am	1130	0.65	0.75	0.43	0.021	6.2E-09	0.46
	1030	0.43	0.61	-	0.010	3.9E-09	-
	930	0.02	0.05	-	0.001	1.0E-09	-

* The ionic conductivity of the grain boundaries was estimated by using a simple brick layer model with $\sigma_{gb} = \frac{1}{R_{gb}} \cdot \frac{d}{A} \cdot \frac{C_b}{C_{gb}}$ assuming a similar permittivity ε_r of the grains and grain boundaries.[1] R_{gb} is the impedance of the grain boundary, C_b and C_{gb} the capacities of the bulk and grain boundary. The thickness of the pellet is given by d and the electrode area by A.

✦ Effective capacitance C values were calculated by converting the constant phase element (CPE) Q together with the fitted value α using $C = \left(\frac{Q}{R^{1-\alpha}}\right)^{1/\alpha}$.

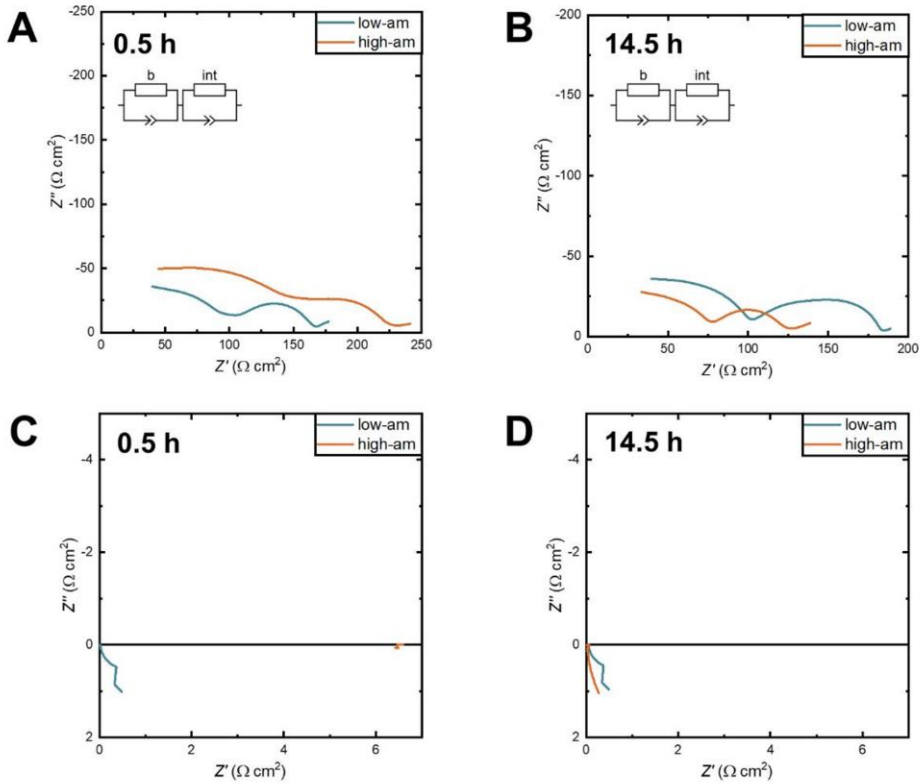

Figure S6. RT Nyquist plots of Li|Ta-LLZO|Li symmetric cells for the samples low-am and high-am sintered at 1130 °C for (A) 0.5 h and (B) 14.5 h before galvanostatic cycling and (C) and (D) after galvanostatic cycling.

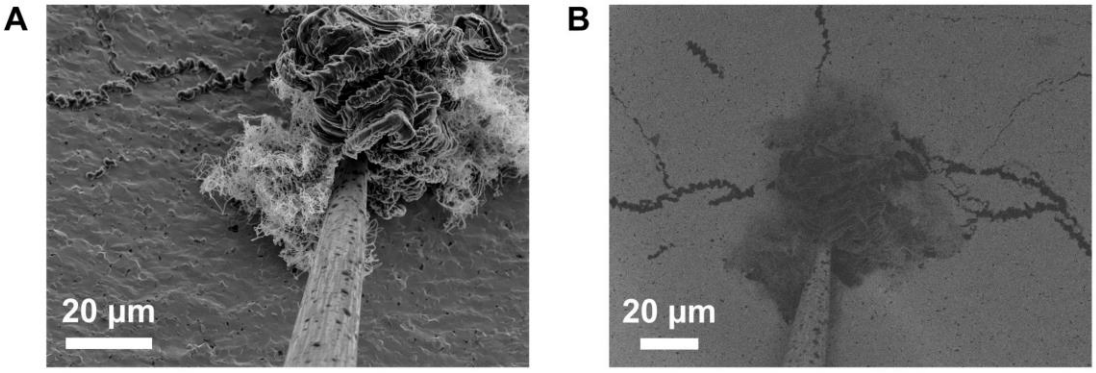

Figure S7. SEM images after *in situ* lithium plating for the sample low-am. (A) Close-up of fine lithium filaments and cracks filled with lithium metal. (B) Backscattered electrons (BSE)

image of the lithium filaments and lithium metal-filled cracks confirming the presence of lithium metal due to the strong elemental contrast.

References

(1) Guo, X.; Waser, R. Electrical properties of the grain boundaries of oxygen ion conductors: Acceptor-doped zirconia and ceria. *Prog. Mater. Sci.* **2006**, *51* (2), 151–210.

A3 Supporting Information of section 3.3

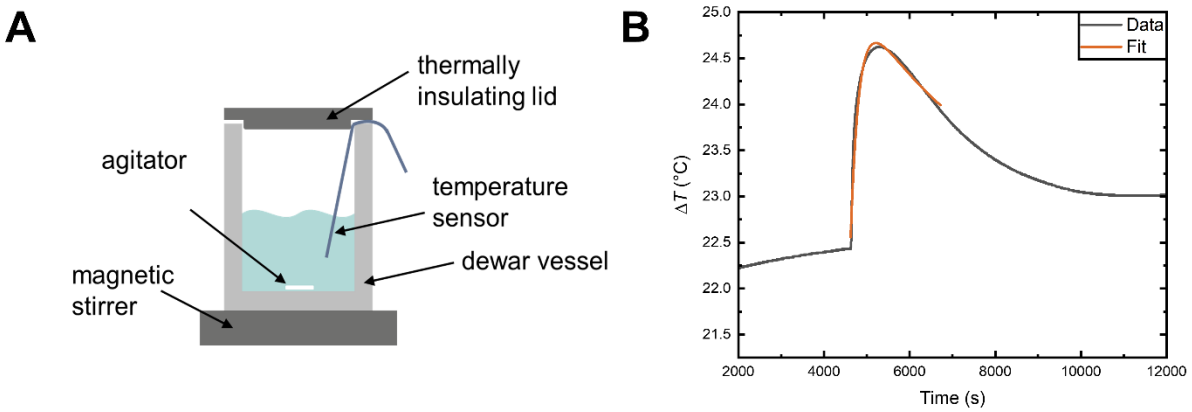

Figure A3.1. (A) Schematics of the setup used for calorimetric determination of the heat of dispersion upon dispersing LLZO particles into PEO-analogous solvents. (B) Exemplary temperature curve (grey) determined with the setup given in (A) for the sample LA-LLZTO dispersed in EGMME. Data were fitted using Equation (3.3.2) (orange).

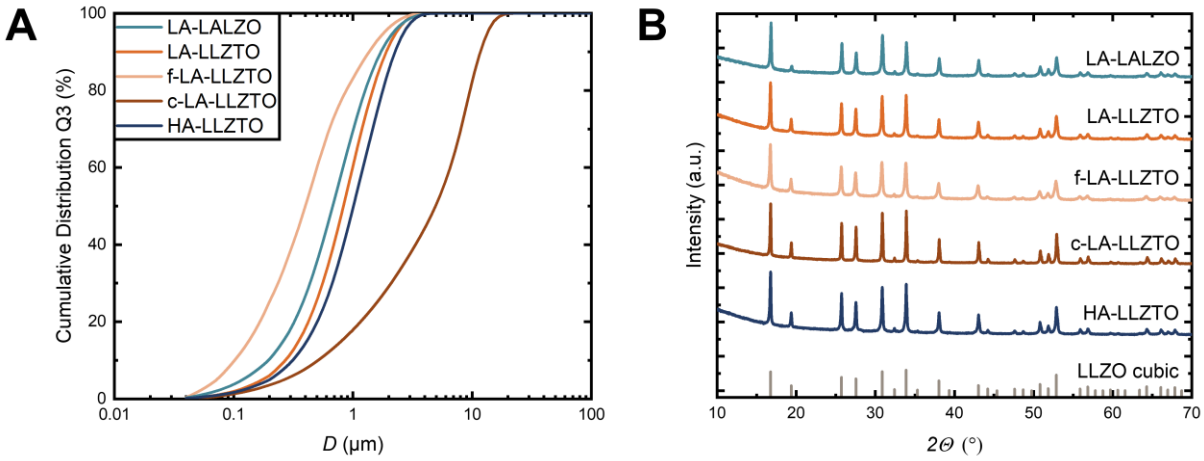

Figure A3.2. (A) Particle size distribution measured by static light scattering and (B) XRD patterns of the LLZO glass-ceramic powders doped with Al (LALZO) and Ta (LLZTO), either having low (LA-) and high amount (HA-) of amorphous phase. For LA-LLZTO, two additional particle sizes are given from fine (sub-µm, f-LA-LLZTO) to coarse (a few µm, c-LA-LLZTO).

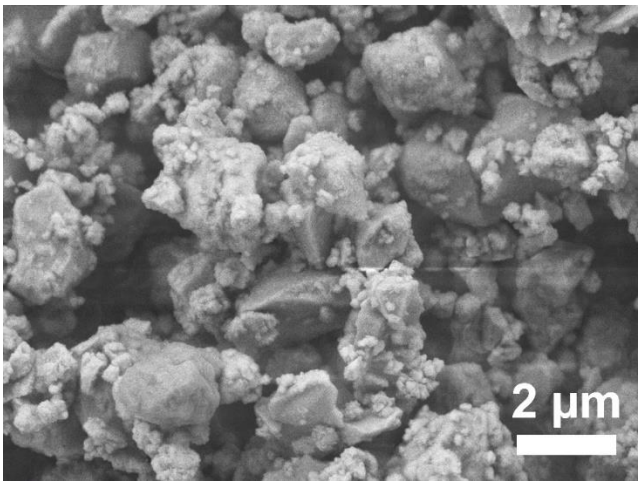

Figure A3.3. Top-view SEM image of the powder particles LA-LALZO.

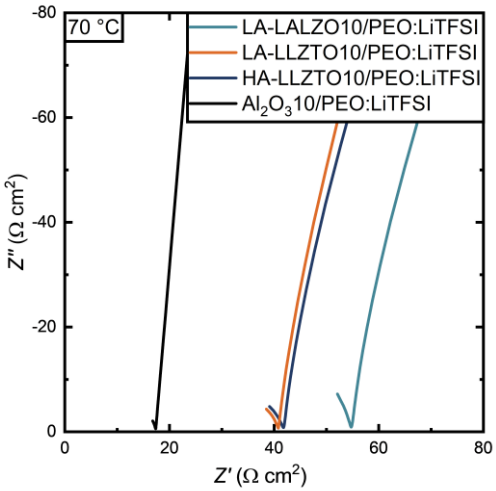

Figure A3.4. Nyquist plots of the HSE samples LA-LALZO10/PEO:LiTFSI, LA-LLZTO10/PEO:LiTFSI, HA-LALZO10/PEO:LiTFSI, and Al_2O_310/PEO:LiTFSI with a volume fraction of 10 vol% of the filler at 70 °C.

Table A3.1. Bulk capacitances C_{bulk} from the Nyquist plots (Figure A3.4) of the HSE samples LA-LALZO10/PEO:LiTFSI, LA-LLZTO10/PEO:LiTFSI, HA-LALZO10/PEO:LiTFSI, and Al2O310/PEO:LiTFSI, exemplary with a volume fraction of 10 vol% of the filler at 70 °C.

Sample	**C_{bulk} @70 °C (pF)**
LA-LALZO10/PEO:LiTFSI	31
LA-LLZTO10/PEO:LiTFSI	28
HA-LLZTO10/PEO:LiTFSI	30
Al_2O_310/PEO:LiTFSI	88

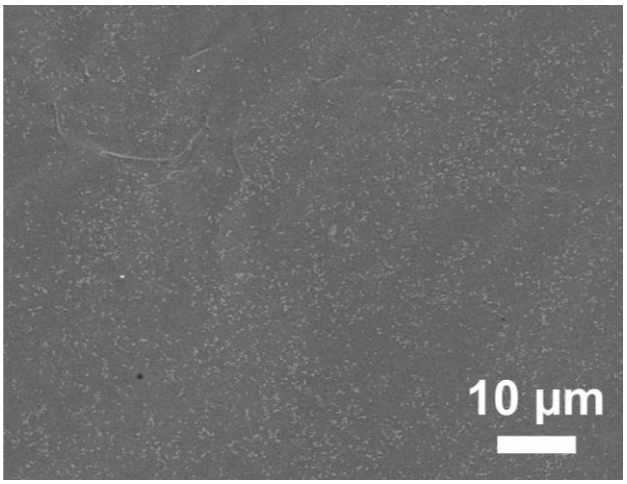

Figure A3.5. Top-view SEM image of the HSE Al_2O_310/PEO:LiTFSI.

Table A3.2. Summary of key properties of PEO/garnet-based HSEs described in the literature.

Polymer	Lithium salt	Molar ratio (EO:Li)	Filler type	Particle size (µm)	Increase of σ *vs.* pure PSE	Filler content @max. σ (vol%)	Synthesis	Solvent-based	Reference
PEO400,000	$LiClO_4$	8:1	Al- LLZO	----	+	14	tape casting	yes	[1]
PEO600,000	$LiClO_4$	18:1	Ta-LLZO	5	+	20	tape casting	yes	[2]
PEO	LiTFSI	18:1	Ta-LLZO	1	+	10	tape casting	yes	[3]
PEO300,000	LiTFSI	10:1	Ta-LLZO	0.2; 5	+	20	tape casting	yes	[4]
PEO600,000	---	---	Ga-LLZO	0.05	+	16	tape casting	yes	[5]
PEO	$LiClO_4$	18:1	Al-LLZO	0.2	+	15	tape casting	yes	[6]
PEO5M	LiTFSI	20:1	Ga-LLZO	1.4	–	---	tape casting	yes	[7]
PEO600,000	LiTFSI	8:1	Al-LLZO	10	+	2	tape casting	yes	[8]
PEO500,000	$LiClO_4$	8:1	Ba-Ta-LLZO	few µm	+	6	tape-casting	yes	[9]
PEO100,000	$LiClO_4$	20:1	Al-LLZO	few µm	–	---	tape-casting	yes	[10]
PEO1M	---	---	Ta-LLZO	0.04	+	12	tape-casting	yes	[11]
PEO	$LiClO_4$	15:1	tet. LLZO	~0.3	+	20	tape-casting	yes	[12]
PEO4M	LiTFSI	15:1	LLZO	~1	–	---	hot pressing	no	[13]
PEO600,000	$LiClO_4$	15:1	Ta-LLZO	1.4	+	10	tape casting	no	[14]
PEO600,000	LiTFSI	8:1	Ta-LLZO	---	+	3	hot pressing	no	[15]
PEO100,000	LiTFSI	11:1	Al-/Ga-LLZO	1	–	---	cryo milling	no	[16]
PEO600,000	LiTFSI	12:1	Ta-LLZO	0.5	+	3	hot rolling	no	[17]
PEO600,000	LiTFSI	10:1	Ta-LLZO	~0.5	+	20	kneading	no	[18]

Table A3.3. Bulk and interface capacitances C_{bulk} and C_{int} of the Nyquist plots of the 2-point subtraction method and 4-point direct method for the sample LA-LLZTO described in Figure 3.3.5. For the 2-point method, two cell setups (trilaminar and bilaminar) were used and for the 4-point method, solely one cell setup.

Sample	C_{bulk} @70 °C (pF)	C_{int} @70 °C (µF)
2-point trilaminar setup	26	0.5
2-point bilaminar setup	36	0.7
4-point trilaminar setup	--	0.3

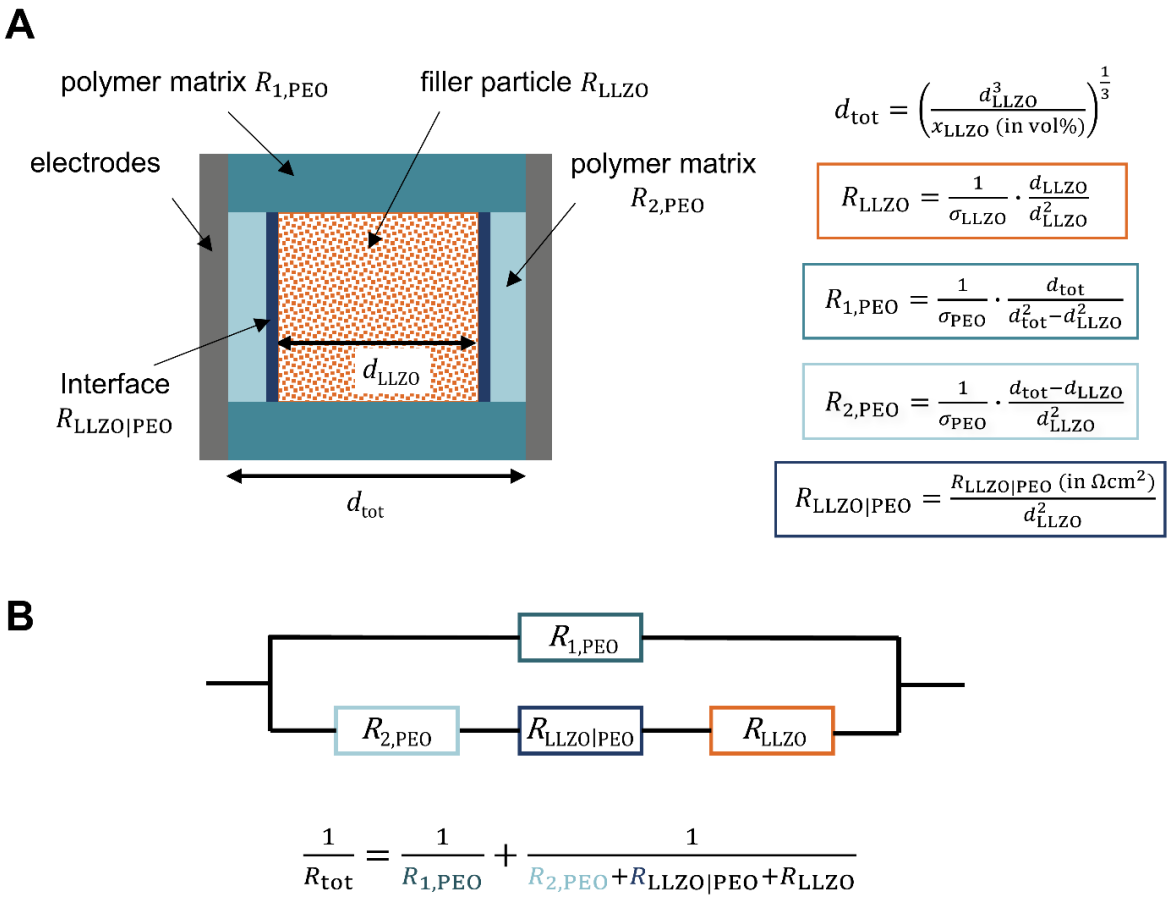

Figure A3.6. (A) Schematics of the series brick layer model (SBLM) used in this study to describe the ionic conductivity of the HSEs. It considers a cube-shaped LLZO particle with an edge length d_{LLZO} embedded in a polymer matrix PEO. The volume fraction of the LLZO x_{LLZO} is used to calculate the total length d_{tot} of the considered volume. The corresponding resistances are designated as R_{LLZO} and $R_{1,PEO}$/$R_{2,PEO}$, respectively. The interface resistance between LLZO and the PEO matrix is described by $R_{LLZO|PEO}$. The calculations of all resistances are given on the right-hand side. (B) The equivalent circuit used for the calculation of the total resistance R_{tot} described by the equation below. The R_{tot} is used to calculate the ionic conductivity of the HSE.

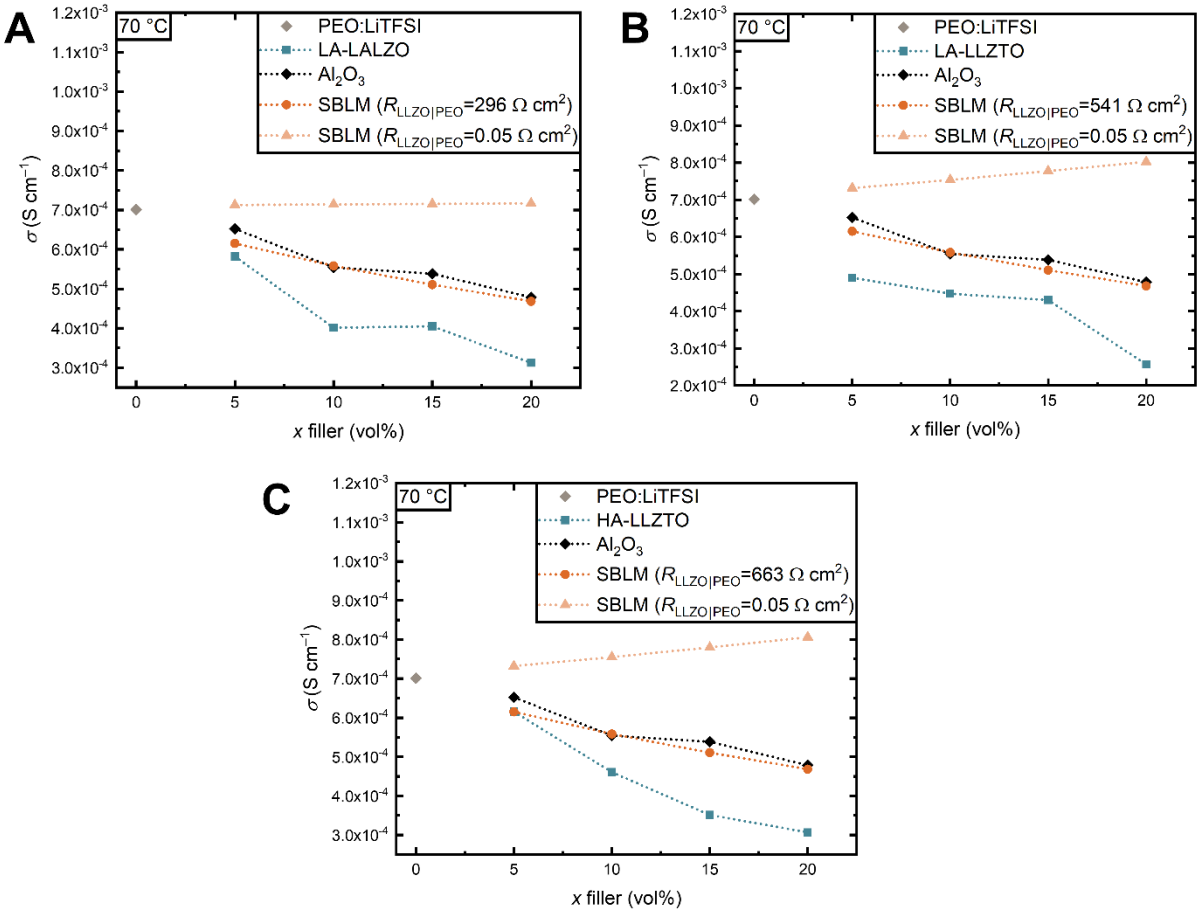

Figure A3.7. Results of the series brick layer modeling (SBLM) described in Figure **A3.6** as a function of filler content *x* at 70 °C for (A) LA-LALZO, (B) LA-LLZTO, and (C) HA-LLZTO using either the obtained interface resistance $R_{LLZO|PEO}$ from Figure **3.3.5** (orange) or a simulated $R_{LLZO|PEO}$ of 0.05 Ω cm^2 (bright-orange) that has been determined as lower limit for achieving an increase in ionic conductivity compared with the pure PSE. As references, the ionic conductivities of the pure PSE PEO:LiTFSI and the HSE containing the passive filler Al_2O_3 are given.

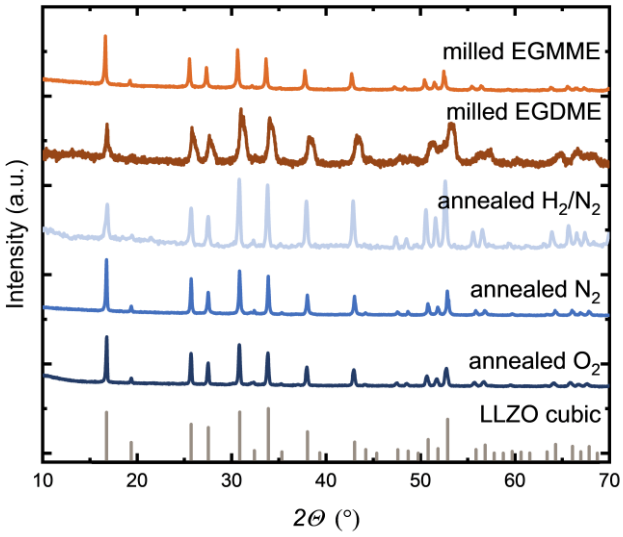

Figure A3.8. XRD patterns of the surface-modified LA-LALZO powders either by milling in PEO-analogous solvents (ethylene glycol monomethyl ether (EGMME) and ethylene glycol dimethyl ether (EGDME)) or by annealing in reducing (H_2/N_2), inert (N_2), and oxidizing (O_2) atmosphere.

Table A3.4. *D50* values of the surface-modified LA-LALZO powders either by milling in PEO-analogous solvents (ethylene glycol monomethyl ether (EGMME) and ethylene glycol dimethyl ether (EGDME)) or by annealing in reducing (H_2/N_2), inert (N_2), and oxidizing (O_2) atmosphere.

Sample	***D50* (µm)**
milled EGMME	0.7
milled EGDME	0.7
annealed H_2/N_2	0.9
annealed N_2	1.3
annealed O_2	1.3

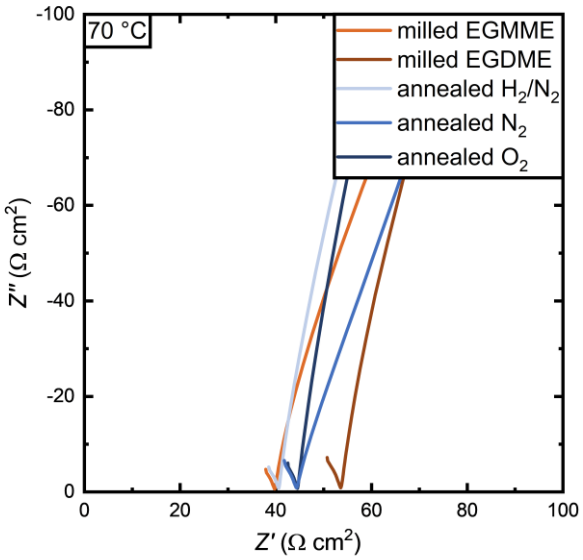

Figure A3.9. Nyquist plots of the HSEs containing the surface-modified LA-LALZO powders milled in PEO-analogous solvents (milled EGMME and milled EGDME) or annealed in reducing (H_2/N_2), inert (N_2), and oxidizing (O_2) atmosphere with a volume fraction of the filler of 10 vol% at 70 °C.

References

(1) Tian, G.; Li, H.; Khalid, B.; Zhao, Z. Optimization for Polyethylene Glycol/Garnet Oxide Composite Electrolyte Membrane for Solid-State Batteries. *Chem. Eng. J.* **2022**, *430*, 132803.

(2) Mei, X.; Wu, Y.; Gao, Y.; Zhu, Y.; Bo, S.-H.; Guo, Y. A Quantitative Correlation between Macromolecular Crystallinity and Ionic Conductivity in Polymer-Ceramic Composite Solid Electrolytes. *Mater. Today Commun.* **2020**, *24*, 101004.

(3) Zhang, Z.; Huang, Y.; Gao, H.; Huang, J.; Li, C.; Liu, P. An All-Solid-State Lithium Battery Using the $Li_7La_3Zr_2O_{12}$ and $Li_{6.7}La_3Zr_{1.7}Ta_{0.3}O_{12}$ Ceramic Enhanced Polyethylene Oxide Electrolytes with Superior Electrochemical Performance. *Ceram. Int.* **2020**, *46*, 11397–11405.

(4) Huo, H.; Chen, Y.; Luo, J.; Yang, X.; Guo, X.; Sun, X. Rational Design of Hierarchical "Ceramic-in-Polymer" and "Polymer-in-Ceramic" Electrolytes for Dendrite-Free Solid-State Batteries. *Adv. Energy Mater.* **2019**, *9*, 1804004.

(5) Li, Z.; Huang, H.-M.; Zhu, J.-K.; Wu, J.-F.; Yang, H.; Wei, L.; Guo, X. Ionic Conduction in Composite Polymer Electrolytes: Case of PEO:Ga-LLZO Composites. *ACS Appl. Mater. Interfaces* **2019**, *11*, 784–791.

(6) Zaman, W.; Hortance, N.; Dixit, M. B.; Andrade, V. de; Hatzell, K. B. Visualizing Percolation and Ion Transport in Hybrid Solid Electrolytes for Li–Metal Batteries. *J. Mater. Chem. A* **2019**, *7*, 23914–23921.

(7) Zagórski, J.; Del López Amo, J.; Cordill, M. J.; Aguesse, F.; Buannic, L.; Llordés, A. Garnet-Polymer Composite Electrolytes: New Insights on Local Li-Ion Dynamics and Electrodeposition Stability with Li Metal Anodes. *ACS Appl. Energy Mater.* **2019**, 1734–1746.

(8) Chen, F.; Yang, D.; Zha, W.; Zhu, B.; Zhang, Y.; Li, J.; Gu, Y.; Shen, Q.; Zhang, L.; Sadoway, D. R. Solid Polymer Electrolytes Incorporating Cubic $Li_7La_3Zr_2O_{12}$ for All-Solid-State Lithium Rechargeable Batteries. *Electrochim. Acta* **2017**, *258*, 1106–1114.

(9) Buvana, P.; Vishista, K.; Shanmukaraj, D.; Murugan, R. Lithium Garnet Oxide Dispersed Polymer Composite Membrane for Rechargeable Lithium Batteries. *Ionics* **2017**, *23*, 541–548.

(10) Langer, F.; Bardenhagen, I.; Glenneberg, J.; Kun, R. Microstructure and Temperature Dependent Lithium Ion Transport of Ceramic–Polymer Composite Electrolyte for Solid-State Lithium Ion Batteries Based on Garnet-Type $Li_7La_3Zr_2O_{12}$. *Solid State Ionics* **2016**, *291*, 8–13.

(11) Zhang, J.; Zhao, N.; Zhang, M.; Li, Y.; Chu, P. K.; Guo, X.; Di, Z.; Wang, X.; Li, H. Flexible and Ion-Conducting Membrane Electrolytes for Solid-State Lithium Batteries: Dispersion of Garnet Nanoparticles in Insulating Polyethylene Oxide. *Nano Energy* **2016**, *28*, 447–454.

(12) Choi, J.-H.; Lee, C.-H.; Yu, J.-H.; Doh, C.-H.; Lee, S.-M. Enhancement of Ionic Conductivity of Composite Membranes for All-Solid-State Lithium Rechargeable Batteries Incorporating Tetragonal $Li_7La_3Zr_2O_{12}$ into a Polyethylene Oxide Matrix. *J. Power Sources* **2015**, *274*, 458–463.

(13) Keller, M.; Appetecchi, G. B.; Kim, G.-T.; Sharova, V.; Schneider, M.; Schuhmacher, J.; Roters, A.; Passerini, S. Electrochemical Performance of a Solvent-Free Hybrid Ceramic-Polymer Electrolyte Based on $Li_7La_3Zr_2O_{12}$ in $P(EO)_{15}$LiTFSI. *J. Power Sources* **2017**, *353*, 287–297.

(14) Cheng, S. H.-S.; He, K.-Q.; Liu, Y.; Zha, J.-W.; Kamruzzaman, M.; Ma, R. L.-W.; Dang, Z.-M.; Li, R. K.; Chung, C. Y. Electrochemical Performance of All-Solid-State Lithium Batteries Using Inorganic Lithium Garnets Particulate Reinforced PEO/$LiClO_4$ Electrolyte. *Electrochim. Acta* **2017**, *253*, 430–438.

(15) Chen, L.; Li, Y.; Li, S.-P.; Fan, L.-Z.; Nan, C.-W.; Goodenough, J. B. PEO/Garnet Composite Electrolytes for Solid-State Lithium Batteries: From "Ceramic-in-Polymer" to "Polymer-in-Ceramic". *Nano Energy* **2018**, *46*.

(16) Waidha, A. I.; Ferber, T.; Donzelli, M.; Hosseinpourkahvaz, N.; Vanita, V.; Dirnberger, K.; Ludwigs, S.; Hausbrand, R.; Jaegermann, W.; Clemens, O. Compositional Dependence of Li-Ion Conductivity in Garnet-Rich Composite Electrolytes for All-Solid-State Lithium-Ion Batteries-Toward Understanding the Drawbacks of Ceramic-Rich Composites. *ACS Appl. Mater. Interfaces* **2021**, *13*, 31111–31128.

(17) Zhuang, H.; Ma, W.; Xie, J.; Liu, X.; Li, B.; Jiang, Y.; Huang, S.; Chen, Z.; Zhao, B. Solvent-Free Synthesis of PEO/Garnet Composite Electrolyte for High-Safety All-Solid-State Lithium Batteries. *J. Alloys Compd.* **2021**, *860*, 157915.

(18) Huang, Z.; Tong, R.; Zhang, J.; Chen, L.; Wang, C.-A. Blending Poly(ethylene oxide) and $Li_{6.4}La_3Zr_{1.4}Ta_{0.6}O_{12}$ by Haake Rheomixer without Any Solvent: A Low-Cost Manufacture Method for Mass Production of Composite Polymer Electrolyte. *J. Power Sources* **2020**, *451*, 227797.

Acknowledgements

First of all, I would like to thank my supervisor Prof. Jürgen Janek for realizing the preparation of this PhD thesis in collaboration with the SCHOTT AG. This was a very special opportunity for me, which I experienced as outstandingly fruitful. Especially the exchange between academia and industry helped me to develop professionally and personally, which would have not worked without the help of Prof. Janek. I would like to thank him for his curiosity and input into my research, the numerous discussions and his constant support throughout the whole time of my thesis.

I greatly thank Dr. Felix H. Richter for co-supervising this dissertation, his curious questions, always improving my work, and for his openness to answer all of my questions in return.

Special thanks also go to Prof. Maren Lepple for being the 2nd reviewer of this dissertation and Prof. Bernd Smarsly and Prof. Siegfried Schindler for being part of the examination committee of the defense.

I would like to express my deepest gratitude to Dr. Jörg Schuhmacher as my supervisor of the SCHOTT AG. I learned on so many levels from you – science, soft-skills, interaction with external partners, networking, and sometimes also questions of life (and good music). Thank you so much for your endless support, I could have not wished for a better supervisor.

From the SCHOTT AG, I would also like to thank my boss Dr. Adnan Adilovic for his support and encouragement that made me grow as a person, I really appreciated it. Furthermore, thanks to Dr. Andreas Roters, who as the project leader of the i-con "battery" project not only gave me the opportunity to realize this joint PhD thesis but also supported me repeatedly from a scientific point of view. Huge thanks to the whole i-con team including Philipp Treis, Kathrin Schellenberg, my office colleague Christoph Weber, David Steigenberger, Claudia Stolz, Denis Titow, Dr. Stefanie Stuckenholz, and Ralf-Dieter Werner for such an enjoyable and fruitful working atmosphere. I think especially the challenging Covid times made us grow closer as a team.

Special thanks go to all the students including Sven Jungblut, Mark Gumenjuk, and Roman Kurberg for the endless support in the lab, all of the discussions, our nice lunch breaks, and all the chats in-between. I really enjoyed working with you.

Moreover, I would like to thank all "Schottis" from the Material Development and Analytics Department for their openness, helpfulness and numerous measurements. Special thanks to Dr. Martin Letz for giving me (deep) insights into physics, to Dr. Bernd Rüdinger, Sonja Lauer, and Uwe Martens for countless XRD measurements, and to Dr. Christoph Loho and its team for support in SEM and ToF-SIMS measurements (and sometimes in-depth discussions on that). The Schottis Patrick, Florian, Jan-Oliver, Yeimy, Sebastian, and Julia receive particular thanks for the good times

of our “Jungwissenschaftlertreffen” and all the other fun activities besides work (often related to good food and wine).

Additionally, I would like to thank the whole working group of Prof. Janek for their open- and helpfulness. Even though my visits were rare due to Covid restrictions, I always felt very welcome and supported by them. I especially thank Dr. Enrico Trevisanello and Dr. Till Fuchs for the (sometimes long…) measurements and for answering all of my scientific and non-scientific questions.

Above all, a huge thanks to Janina and Maren, my two close friends from university, for enduring bachelor to PhD by my side, to Christian for being my biggest fan, and to all of my close friends from back home. You are like family to me and I deeply thank you for empowering me and keeping me alive in daily life. My deepest gratitude goes to my family, especially to my parents. You are certainly responsible for my way as “Chemikerin” or “Komikerin” as you would say, Dad (or expressed in the best english language: “The apple does not fall far from the tree”). I deeply thank you for your unconditional support and love. The same applies to you, Kevin. I do not know what I have done without you. Thank you for putting up with me, cooking for me, cheering me up and making me laugh every day.